The high-temperature pressure oxidation of a Witwatersrand pyrite concentrate

by

Jakolien Adriana Strauss

Thesis presented in partial fulfilment
of the requirements for the Degree

of

MASTER OF ENGINEERING
(EXTRACTIVE METALLURGICAL ENGINEERING)

in the Faculty of Engineering
at Stellenbosch University

Supervisors
Dr J.D.T. Steyl
Dr C. Dorfling

April 2019

DECLARATION

By submitting this thesis electronically, I declare that the entirety of the work contained therein is my own, original work, that I am the sole author thereof (save to the extent explicitly otherwise stated), that reproduction and publication thereof by Stellenbosch University will not infringe any third party rights and that I have not previously in its entirety or in part submitted it for obtaining any qualification.

Date: April 2019

PLAGIARISM DECLARATION

1. Plagiarism is the use of ideas, material and other intellectual property of another's work and to present is as my own.
2. I agree that plagiarism is a punishable offence because it constitutes theft.
3. I also understand that direct translations are plagiarism.
4. Accordingly, all quotations and contributions from any source whatsoever (including the internet) have been cited fully. I understand that the reproduction of text without quotation marks (even when the source is cited) is plagiarism.
5. I declare that the work contained in this assignment, except where otherwise stated, is my original work and that I have not previously (in its entirety or in part) submitted it for grading in this module/assignment or another module/assignment.

Initials and surname: J.A. Strauss

Date: April 2019

ABSTRACT

The oxidation of the pyrite present in gold and uranium ores is often desirable, to either liberate the gold present in the pyrite, or to generate iron(III) and acid for uranium extraction. The current study aimed to define a rate equation to describe the pressure oxidation (POX) kinetics of a Witwatersrand pyrite concentrate. Iron(III) and sulphuric acid, which is produced during POX of pyrite, may be used to leach uranium, which is also present in Witwatersrand ores. In addition, gold recovery from the POX residue may be improved significantly, especially if the gold ore is partially refractory, as is the case in many Witwatersrand tailings dumps. A rate equation to describe the pyrite oxidation kinetics will, thus, be important for reactor design purposes, as well as for operating and capital expenditure estimations to evaluate the feasibility of flow sheets incorporating POX.

The pyrite POX kinetics was investigated in terms of temperature (180 to 210°C), oxygen partial pressure (480 to 1100 kPa), acid concentration (10 to 50 g/L) and particle size (+38 to 150 μm) by using a batch 2 gallon Parr autoclave. A batch model was subsequently developed in MATLAB and employed to confirm the observed rate dependencies. The oxygen gas-liquid mass transfer coefficient was also measured independently during the study, to enable a quantitative description of the dissolved oxygen concentration during modelling of the batch oxidation process.

The activation energy was calculated as ~120 kJ/mol in relation to dissolved oxygen concentration, which indicated that the reaction was controlled by a chemical reaction at the surface of pyrite particles and that no diffusional limitations applied. The oxidation rate decreased with increasing acid concentration with a reaction rate order in acid concentration, ranging between -0.2 and -0.3. The oxidation kinetics was found to be relatively insensitive to particle size at oxygen partial pressures lower than 1000 kPa.

For all practical purposes, the pyrite oxidation rate was found to be first order in dissolved oxygen concentration; however, this assumption led to poor prediction of the iron(II) and iron(III) solution concentrations during modelling of the batch oxidation tests. Accurate quantification of the iron(II) and iron(III) solution concentrations would also be important to consider for reactor design purposes, as it will dictate the maximum quantities of iron(III) and acid that can be produced during POX.

Simulations showed that improved predictions of the iron(II) and iron(III) concentrations are obtained when a direct reaction between pyrite and iron(III) was allowed for. This means that both dissolved oxygen and iron(III) are responsible for the oxidation of pyrite at typical POX conditions, i.e., the pyrite could have a dual rate dependency on the oxygen and iron(III) concentrations in two additive rate-determining steps. Regression indicated that the experimental data may be represented by two additive rate equations with orders of ~0.6-1.0 in dissolved oxygen concentration and half-order in

iron(III) concentration. The relative contribution of the two reactions to the overall rate appears to be influenced by the slurry density, particle size, and oxygen partial pressure.

It is proposed that a follow-up study should be conducted to quantify the rate dependency of pyrite in solutions of varying iron(III) concentrations, at the temperatures employed during this study and in the absence of dissolved oxygen, that is, to provide an independently measured rate equation to the batch POX model. The homogenous iron(II) to iron(III) oxidation rate should also be measured independently to confirm whether the employed rate equation was correct. Furthermore, the possible effect of secondary minerals, in this case, pyrophyllite, should be clarified by conducting experimental work at higher slurry densities.

ABSTRAK

Die oksidasie van die piriet teenwoordig in goud- en uraniumerts is dikwels verkieslik om óf die goud teenwoordig in die piriet vry te stel, óf om yster(III) en suur vir uranium ontginning te genereer. Die huidige studie het beoog om ’n tempovergelyking te definieer om die drukoksidasie (DOX) kinetika van ’n Witwatersrand pirietkonsentraat te beskryf. Yster(III) en swaelsuur, wat gegenereer word gedurende die DOX van piriet, kan gebruik word om uranium uit te loog, wat ook teenwoordig is in Witwatersrand-erts. Daarby kan goudontginning van die DOX residu beduidend verbeter word, veral as die gouderts gedeeltelik refraktêr is, soos in die geval van baie Witwatersrand uitskothope. ’n Tempovergelyking om die piriet oksidasiekinetika te beskryf sal dus belangrik wees vir reaktorontwerp doeleindes, sowel as vir bedryfs- en kapitaaluitgawe beramings, om die uitvoerbaarheid van vleoidiagramme wat DOX insluit, te evalueer.

Die piriet DOX kinetika is ondersoek in terme van temperatuur (180 tot 210 °C), suurstof parsiële druk (480 tot 1100 kPa), suurkonsentrasie (10 tot 50 g/L) en partikelgrootte (+38 tot 150 µm) deur gebruik te maak van ’n lot 2 gallon Parr outoklaaf. ’n Lotmodel is daaropvolgend in MATLAB ontwikkel en gebruik om die tempo afhanklikhede wat waargeneem is, te bevestig. Die suurstof gas-vloeistof massa-oordrag-koëffisiënt is ook onafhanklik gemeet gedurende die studie om ’n kwantitatiewe beskrywing van die opgeloste suurstofkonsentrasie gedurende modellering van die lot oksidasieproses, moontlik te maak.

Die aktiveringsenergie is bereken as ~120 kJ/mol in verhouding met opgeloste suurstofkonsentrasie, wat aandui dat die reaksie deur ’n chemiese reaksie beheer is by die oppervlak van pirietpartikels en dat geen diffusie beperkinge van toepassing is nie. Die oksidasietempo het afgeneem met verhoogde suurkonsentrasie met ’n reaksietempo orde in suurkonsentrasie, met ’n bestek van tussen -0.2 en -0.3. Dis gevind dat die oksidasiekinetika relatief onsensitief is tot partikelgrootte by suurstof parsiële druk laer as 1000 kPa.

Vir alle praktiese doeleindes is die pirietoksidasie as eerste orde in opgeloste suurstofkonsentrasie gevind, alhoewel hierdie aanname tot swak voorspelling van die yster(II)- en yster(III)-oplossingkonsentrasies gedurende modellering van die lot oksidasie toets gelei het. Akkurate kwantifisering van die yster(II)- en yster(III)-oplossingkonsentrasies sal ook belangrik wees om in ag te neem vir reaktorontwerp doeleindes, aangesien dit die maksimum hoeveelhede yster(III) en suur wat geproduseer kan word tydens DOX, sal dikteer.

Simulasies het gewys dat verbeterde voorspellings van die yster(II)- en yster(III)-konsentrasies verkry word wanneer ’n direkte reaksie tussen piriet en yster(II) toegelaat word. Dit beteken dat beide opgeloste suurstof en yster(III) verantwoordelik is vir die oksidasie van piriet by tipiese DOX

kondisies, dit is, die piriet kon ’n duale tempo afhanklikheid op die suurstof- en yster(III)-konsentrasies in twee additiewe tempo bepalende stappe hê. Regressie het gewys dat die eksperimentele data verteenwoordig word deur twee additiewe tempovergelykings met ordes van ~0.6-1.1 in opgeloste suurstofkonsentrasies en half-orde in yster(III)-konsentrasie. Die relatiewe bydra van die twee reaksies tot die algehele tempo lyk of dit beïnvloed word deur die pulpdigtheid, partikelgrootte, en suurstof parsiële druk.

Dit word voorgestel dat ’n opvolg studie gedoen word om die tempo afhanklikheid van piriet in oplossings van wisselende yster(III)-konsentrasie te kwantifiseer, by temperature gebruik in hierdie studie en in die afwesigheid van opgeloste suurstof, sodat ’n gemete tempovergelyking, onafhanklik van die lot DOX model, verskaf kan word. Die homogene yster(II) na yster(III) oksidasietempo moet ook onafhanklik gemeet word om te bevestig dat die tempovergelyking wat gebruik is, korrek is. Verder moet die moontlike effek van sekondêre minerale, in hierdie geval pirofilliet, duidelik gemaak word deur eksperimentele werk by hoër pulpdigtheid te doen.

ACKNOWLEDGEMENTS

I would like to acknowledge MINTEK for the financial support, and MINTEK staff and colleagues, who have each assisted and contributed in some way during the course of my study.

I would like to express my sincerest gratitude to the following people for their support, motivation to excel in critical thinking, and overall guidance:

- Dr Johann Steyl (Dynamet Insights, formerly of University of Stellenbosch)
- Dr Christie Dorfling (University of Stellenbosch)
- Prof. Roelf Sandenbergh (MINTEK/University of Pretoria)
- Ing Christoph Pawlik (MINTEK)
- Mr Petrus van Staden (MINTEK)

Lastly, I would like to thank my family, especially my parents, to whom I dedicate this thesis, for their unfailing support, love and encouragement.

TABLE OF CONTENTS

LIST OF TABLES

LIST OF FIGURES

LIST OF SYMBOLS

Symbol	Description	Unit
a	Gas-liquid interfacial area	m^2
a_w	Water activity	mol/kg
$\bar{A}$	Pre-exponential factor	Dependent on unit of rate constant
B_i	Number of experimental data points	(-)
D_A	Diffusion coefficient	m^2/min
E_A	Activation energy of chemical reaction	J/mol.K
E_L	Enhancement factor	(-)
E_F	Objective/error function	%
E_{oc}	Mixed potential or open-circuit potential	V
E^o	Standard half-cell potential	V
E	Cell potential	V
F	Faraday's constant (96485 C/mol)	C/mol
H_A	Dimensionless Hatta number	(-)
i_C	Current density	A/m^2
J_A	Rate of absorption	mol.m/min.kg
k	Intrinsic reaction rate constant	Unit depending on order of chemical reaction $\frac{mol^{(1-n)}.kg^n}{m^2.min}$
k_s	Observed rate constant	1/min
k''	Apparent rate constant	Unit dependent on reaction orders $\frac{mol^{(1-n)}.kg^n}{min}$
$k_L a$	Overall oxygen mass transfer coefficient	1/min
k_m	Liquid side physical mass transfer coefficient	m/min
m_A	Molal concentration of species A	mol/kg
m	Molality	mol/kg
$m_A{}^0$	Bulk liquid molal concentration of diffusant A	mol/kg
m_A*	Concentration of diffusant A at gas-liquid interface	mol/kg
m_i	Molality of component i	mol/kg
M_i	Molarity of component i	mol/L
M_w	Molar weight of water	kg/mol
MW_i	Molar weight of component i	kg/mol
MW_s	Mineral molar weight	kg/mol
n	Indicates order of a chemical reaction	(-)
N_B	Total amount of moles in the unreacted spherical particle	mole
$N_{FeS_2:0}$	Initial pyrite concentration	mol/kg

P	Pressure	atm
$p_{1\text{-}3}$	Empirical parameter values to be used in Equation B.20 and 21	(-)
p_{O_2}	Partial pressure of oxygen	atm
p_s	Solution vapour pressure	bar
p_w	Water vapour pressure	bar
ψ	Fraction of water available to interact with oxygen	(-)
q	Fraction of the area of the surface which is replaced with fresh liquid in unit time	(-)
r_A	Chemical reaction rate of species A	mol/kg,min
r_{FeS_2}	Intrinsic reaction rate on mineral pyrite surface	mol/m^2.min
r_i	Intrinsic reaction rate of species, i, in solution	mol/kg.min
r_s	Intrinsic reaction rate on particle surface	mol/m^2.min
R_p	Particle diameter/unreacted core diameter	m
R_g	Ideal gas constant (8.314 J/mol.K or 0.08206 L.atm/mol.K)	J/mol.K L.atm/mol.K
R_{po}	Initial particle radius	m
t	Time	min
t_s	Time	second
T	Temperature	K
T_c	Temperature	°C
T_o	Unit temperature	°C
T_R	Reference temperature	K
V_g	Volume of gas phase	m^3
V_L	Volume of liquid phase	m^3
v	Ions released in solution upon electrolyte dissociation	(-)
w_i	Mass of species i	g
ΔW_k	Weight fraction of k monosize fraction	(-)
X	Fractional conversion	(-)
X_{mean}	Overall conversion of all size fractions	(-)
y_{O_2}	Mole fraction of oxygen in the gas phase	(-)
z_i	Experimental and predicted data points	(-)

Greek letters		
Symbol	**Description**	**Unit**
α	Dimensionless constant	(-)
β	Transfer coefficient	(-)
γ_{O_2}	Activity coefficient of oxygen in water	(-)
δ	Film thickness	m
ε	Empirical constant to be sued in Equation 2.29	(-)
η	empirical coefficient to be used in Eq. C.8	(-)
κ	Empirical coefficient to be sued in Eq. C.8	kg/mol
ρ	Density	kg/m^3
ρ_w	Density of water	kg/m^3
ρ_{sln}	Solution density	kg/L
ρ_{Fes2}	Mineral pyrite density	kg/m^3
ρ_s	Particle density	kg/m3
ρ_A	Density of diffusant A	kg/m^3
ψ_i	Fraction of the total water content available to interact with oxygen (modelling parameter in Eq C.6)	(-)
ψ_{eff}	Effective fraction of the total water content available to interact with oxygen (modelling parameter in Eq C.7)	(-)
$\hat{\phi}_{O_2}$	Fugacity coefficient of oxygen	(-)
$\emptyset$	Osmotic coefficient	(-)
$\mathcal{H}_{O_2}$	Henry's coefficient based on kg of solvent	atm.kg/mol
$\mathcal{H}_{MO_2}$	Henry's coefficient based on L of solvent	atm.L/mol
Y	Empirical coefficient to be used in Eq. C.8	(-)

LIST OF ABBREVIATIONS AND ACRONYMS

AARD	Absolute average relative deviation
AMD	Acid-mine drainage
CV	Coefficient of variation
EAC	Elemental accountability
EDS	Energy dispersive X-ray microanalysis
DI	Deionised
ICP-OES	Inductively-coupled plasma optical emission spectroscopy
LS	Lignosulphonate
POX	Pressure oxidation
PSD	Particle size distribution
RPV	Reaction progress variable
SEM	Scanning electron microscopy
USP	Unreacted shrinking particle
XRF	X-ray fluorescence

1. INTRODUCTION

1.1. Gold and uranium in Witwatersrand ores and tailings

It is well known that uranium and gold are important products from South Africa's Witwatersrand area (Fivaz, 1988; Ford, 1993; Kinnaird & Nex, 2016). Uranium production by gold-mining companies has been discontinues over the last few decades, due to fluctuating uranium prices and an irregular demand for uranium (Ford, 1993). However, using uranium for nuclear energy production is viewed as an environmentally clean technology for electricity supply. Compared to other energy sources, uranium has a significantly higher energy density, which ensures that only a small quantity of controllable waste is produced when it is used to generate electricity (World Nuclear Association, 2012).[a] On the other hand, the presence of uranium in Witwatersrand tailings dams poses health risks to urban communities located around the dams. Unreacted sulphides, mainly pyrite, also pose a serious acid-mine-drainage (AMD) problem (Ewart, 2011). Reprocessing tailings dumps to recover gold and uranium has, in many cases, become economically attractive, as the dumps are easily accessible and reprocessing, thus, has no related mining costs (Cornish, 2017). However, in some cases, gold present in Witwatersrand tailings dumps may be viewed as partially refractory, with associated gold recoveries lower than 80% via direct cyanidation (Fleming, Brown & Botha, 2010; Janse van Rensburg, 2016), thus, requiring pre-treatment if it is to be recovered effectively. Therefore, not only is gold and uranium production of strategic significance for South Africa from an economic perspective, but the removal of uranium and pyrite from the tailings to produce an environmentally benign mining waste is the responsibility of the South African government and local mining companies.

Various processing options may be considered for treating Witwatersrand ores and tailings to recover both gold and uranium. It is known that uranium can be recovered from these ores with the addition of sulphuric acid in the presence of a suitable oxidant. Since pyrite occurs naturally in Witwatersrand ores, it may be used to produce both sulphuric acid and iron(III), as oxidant, for a uranium leach by employing pressure oxidation (POX). In addition, POX has been shown to increase downstream gold recovery from tailings to above 90% (Fleming et al., 2010).

[a] Approximately 50 nuclear reactors are currently being constructed worldwide, which could favour the supply-demand ratio in favour of producers and lead to increasing uranium prices in the foreseeable future (Winde et al., 2017; World Nuclear Association, 2018). In addition, it is estimated that 7 000 Mt of uranium are associated with gold tailings in South Africa, which accounts for approximately 81% of the total global uranium tailings mass (Winde et al., 2017).

1.2. Problem statement

Even though the POX of pyrite-containing concentrates is of immense industrial importance, especially for the recovery of gold from refractory ores, its high-temperature oxidation behaviour is generally poorly understood. This means that its oxidation behaviour and reaction kinetics cannot, typically, be extrapolated to pyrites originating from different sources. The current investigation focussed on describing the pyrite oxidation behaviour at high temperatures for a typical Witwatersrand ore. Even though this was not the sole aim of the study, some contribution to the current understanding of pyrite POX kinetics was attempted.

1.3. Scope of work and research objective

This project specifically focussed on the pressure oxidation kinetics of a typical Witwatersrand pyrite flotation concentrate to characterise the pyrite oxidation behaviour at high temperatures (180-210°C). Currently, there exists no published information on the high-temperature oxidation kinetics of these pyrites. The specific objective of the project was to define a rate equation that may be used to predict pyrite pressure oxidation in terms of:

- Oxygen partial pressure,
- Acid concentration,
- Temperature, and
- Particle size.

Achieving these objectives would be critical for reactor design purposes and subsequent capital cost estimations, which are ultimately required to evaluate flow sheet economic feasibility.

1.4. Research approach

To quantify the parameters that influence the oxidation of pyrite mathematically by defining the relevant rate equations and associated rate constants, the experimental work will take the form of a typical lumped parametric study, wherein oxygen partial pressure, temperature, acid concentration and slurry density will be varied in a laboratory batch pressure reactor.

A dynamic simulation approach will be used to regress the rate constants of the proposed rate equation, by taking into consideration the transient change in variables. In addition to the batch pressure oxidation test work, oxygen gas-liquid mass transfer test work will be carried out to allow quantification of the dissolved oxygen concentration, which is difficult to measure at POX conditions. This methodology will enable a quantitative description of the system on a more fundamental level.

2. LITERATURE STUDY

2.1. Pressure oxidation

POX involves the oxidation of sulphide minerals at elevated temperatures[b], using oxygen in an acidic sulphate medium. The aqueous oxidation of pyrite and other sulphides by oxygen is slow at ambient conditions due to the high activation energies of the reactions involved. POX is attractive for this purpose, as it offers opportunities to increase the aqueous solubility of oxygen significantly by increasing the partial pressure of oxygen, as well as the rate of chemical reactions, to achieve faster conversions and form more stable residues (Forward & Halpern, 1955).

The oxidation products of sulphide in an acidic aqueous solution as a function of temperature are provided in Figure 2.1. Pressure oxidation, thus, offers the possibility to manipulate the sulphur product by operating at different temperatures. Oxidation of pyrite at temperatures exceeding ~180°C leads to complete oxidation of sulphides to sulphate, thus producing sulphuric acid.

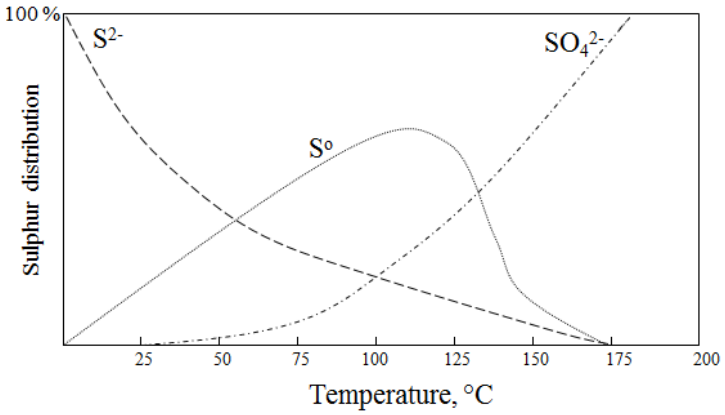

Figure 2.1: Sulphide oxidation as a function of temperature in acidic aqueous solutions (redrawn from Mackiw, Benz & Evans, 1966)

The choice of operating conditions is typically determined by the nature of the ore, the conversions and end products desired, and the operating and capital costs involved. In general, acidic conditions, i.e., > 10 g/L acid, relatively high temperatures, i.e., 170 to 225˚C, and high oxygen partial pressures, i.e., 300 to 750 kPa, are used to ensure full conversion of the sulphide to sulphate and iron to iron(III)

[b] In the hydrometallurgical sphere, “pressure oxidation” or “pressure leaching” are synonymous with leaching in an aqueous operation above the normal boiling point (i.e., elevated temperatures). Due to the saturation pressure exerted by the solution, operation at temperatures exceeding 100°C would inherently be associated with elevated (> 1 atm) pressures; therefore, the term “pressure leaching/oxidation”. “High-temperature oxidation” might have been a more suitable term for pressure leaching/oxidation.

(Berezowsky, Collins, Kerfoot & Torres, 1991), which would take very long at ambient conditions. Full conversion to sulphate also ensures maximum sulphuric acid production, which is a priority in the context of the current study, and ensures that solid products, such as elemental sulphur, which would be carried forward to gold leaching, does not consume cyanide in a possible downstream gold leaching circuit (Berezowsky et al., 1991; Thomas, 2005).

2.2. Witwatersrand ores

The Witwatersrand gold-uranium reef ores, which are located in quartz-pebble conglomerates, are relatively consistent in terms of the bulk minerals present (Janisch, 1986); they typically consist of pyrite and quartz, with varying proportions of the phyllosilicates/clay minerals pyrophyllite, muscovite and chlorite, as shown in Table 2.1 (Janisch, 1986; Von Rahden, 1970). Gold, uranium-containing minerals and pyrite are usually closely associated with one another (Lloyd, 1981). Since the mineralogical composition of the ores remains mainly unaltered during the conventional gold processing of these ores, the tailings dumps, compared to the original ores, contain similar minerals (Janse van Rensburg, 2016).

Table 2.1: Bulk mineralogical composition of typical Witwatersrand gold and uranium reef ores and tailings (Janse van Rensburg, 2016; Nengovhela, Yibas & Ogola, 2006; Stanley, 1987)

Mineral name	Chemical formula	Relative abundance
Pyrite	FeS_2	Minor
Quartz	SiO_2	Major
Pyrophyllite	$Al_2Si_4O_{10}(OH)_2$	Intermediate
Muscovite	$KAl_2(AlSi_3O_{10})(OH)_2$	Intermediate
Chlorite	$(Fe,Mg, Mn, Ni, Zn, Al, Li, Ti)_{4\text{-}6}(Si,Al)_4O_{10}(OH,O)_8$	Intermediate
Chloritoid	$(Fe^{2+},Mg,Mn^{2+})Al_2(SiO_4)O(OH)_2$	Intermediate
Uraninite[c]	UO_2	Trace
Major: >50 wt%, Intermediate, 10-50 wt%, Minor 3-5 wt%, trace 1-2 wt%		

The average gold and uranium grades of Witwatersrand ores are area/reef dependent and will be influenced by the extent of dilution that occurred during mining, thus, an estimate of the current average gold grade and associated uranium grade of the ores is difficult to provide. Some of the most recent figures provided by local gold producers are listed in Table 2.2. Typical uranium grades range

[c] Uraninite is the primary uranium-bearing mineral in Witwatersrand ores, however, other uranium-bearing minerals, such as coffenite and the more refractory brannerite, may also be present at varying levels (Feather & Snegg, 1978; Kinnaird & Nex, 2016; Lottering, Lorenzen, Phala, Smit & Schalkwyk, 2008).

between 150 and 1000 g/t in reef ores, with associated gold grades ranging between 4 to 20 g/t. Gold and uranium grades of various dumps as reported by Janse van Rensburg (2016) are also included.

Table 2.2: Gold and uranium grades of reef ores and tailings dumps

Mineral name	Gold grade g/t	Uranium grade g/t
Reef ore	2-20[a], 4.4-11.8[b], ~5[c], 3.6-11.6[d]	150-200 [a], 1074 [b], 300-500 [e]
Tailings dump/surface stockpiles	0.2-0.5[e], ~0.3[f], 0.2[c], 0.1-0.8[d], 0.3-0.4 [g]	670[f], 19-65[g]

[a] - Gold One International Limited, 2012; [b] – IRW Press, 2017; [c] – Gold Fields, 2017; [d] - Harmony, 2018;
[e] - AngloGoldAshanti, 2017; [f] – IRW Press, 2017; [g] - Janse van Rensburg, 2016

2.3. Process overview

A review of uranium leaching practices are provided by Venter and Boylett (2009) and Lunt, Boshoff, Boylett and El-Ansary (2007). Acidic POX has been considered in many cases, dating back to the 1950s, for the direct leaching of uranium concentrates, as well as for acid production to leach uranium, if sufficient pyrite (or other iron sulphide minerals) is present (Bovey & Stewart, 1979; Demopoulos, 1985; Forward & Halpern, 1955; Shatalov & Pirkovskii, 2007; Venter & Boylett, 2009; Warren, 1956). Witwatersrand ores have reasonably high sulphide content (~3 wt%), which allows POX to be used (Berezowsky et al., 1991) . Between the 1970s and 1980s the use of POX for the treatment of Witwatersrand uranium ores was considered by Anglo American Research Laboratories. This was followed by the installation of two pressure leaching plants at Vaal Reefs South and Rietkuil, following extensive piloting work at Vaal Reefs East and Western Deep Levels (Bovey & Stewart, 1979; Robinson, James, Van Zyl, Marsden & Bosman, 1958, Verster & Pieterse, 2008). However, according to Verster and Pieterse (2008), neither of the two plants was operated, due to a uranium price drop soon after the plants were built. More recently, the POX of uranium-containing concentrates has again been proposed for application on a commercial scale (Gold One International Limited, 2012, Goldwyer, 2007; Fleming et al., 2010, Shatalov & Pirkovskii, 2007, Verster & Pieterse, 2008).

The basis for using POX to recover uranium (and gold) from Witwatersrand pyritic ores is, in general, as follows:

- The oxidation of pyrite offers the opportunity for sufficient iron(III) and acid to be produced for the use in a parallel uranium leaching circuit, or in situ during the uranium leach (Forward & Halpern, 1955; Shatalov & Pirkovskii, 2007; Vezina & Gow, 1969; Warren, 1956).
- Heat produced by the exothermic sulphide oxidation reactions may be utilised in a parallel uranium leaching circuit (Verster & Pieterse, 2008).

- Subsequent gold recovery may be increased, especially from tailings dumps, where gold recovery by a second cyanidation step has been notoriously low, with associated recoveries less than 70% (Fleming et al., 2010; Janse van Rensburg, 2016).
- Products are environmentally friendly, as the sulphides are completely oxidised and, thus, the residue has zero AMD potential.
- The generation of acid could significantly lower reagent cost (associated with uranium extraction) if a large quantity of acid-consuming minerals are present in the feed (Fleming et al., 2010; Shatalov & Pirkovskii, 2007; Verster & Pieterse, 2008; Warren, 1956).

Based on the proposed flow sheets of Fleming et al. (2010), Gold One International Limited (2012) and Verster and Pieterse (2008), two high-level POX flow sheets for the treatment of Witwatersrand ores/tailings, to recover both gold and uranium, are shown in Figure 2.2. POX can be used to either produce acid and an oxidant for a parallel uranium leaching circuit (Figure 2.2a), or the entire uranium-bearing concentrate/ore can be treated “as is”, with no consideration of peripheral operations (Figure 2.2b). Gold may be recovered from the POX residue in a conventional cyanidation circuit after solid-liquid separation.

Inclusion of a sulphide flotation circuit in such a flow sheet is dependent on the sulphide grade of the ore. The sulphide flotation stage should target a sulphide grade in the concentrate, which would ensure autothermal POX operation, i.e., POX operation without the addition of external heat (Papangelakis & Demopoulos, 1992). A steady-state mass and energy balance has shown the required sulphide content to be around 5-6 wt% for sulphide concentrates, assuming a maximum slurry density of 40 wt% solids and complete sulphide oxidation in the autoclave (Conway & Gale, 1990; Papangelakis & Demopoulos, 1992).

Since a POX circuit is a very capital-intensive unit operation, careful consideration should be given to the Witwatersrand pyrite oxidation kinetics, which will determine the final autoclave size. From this perspective, a rate equation to describe the kinetics is important for reactor design and sizing purposes.

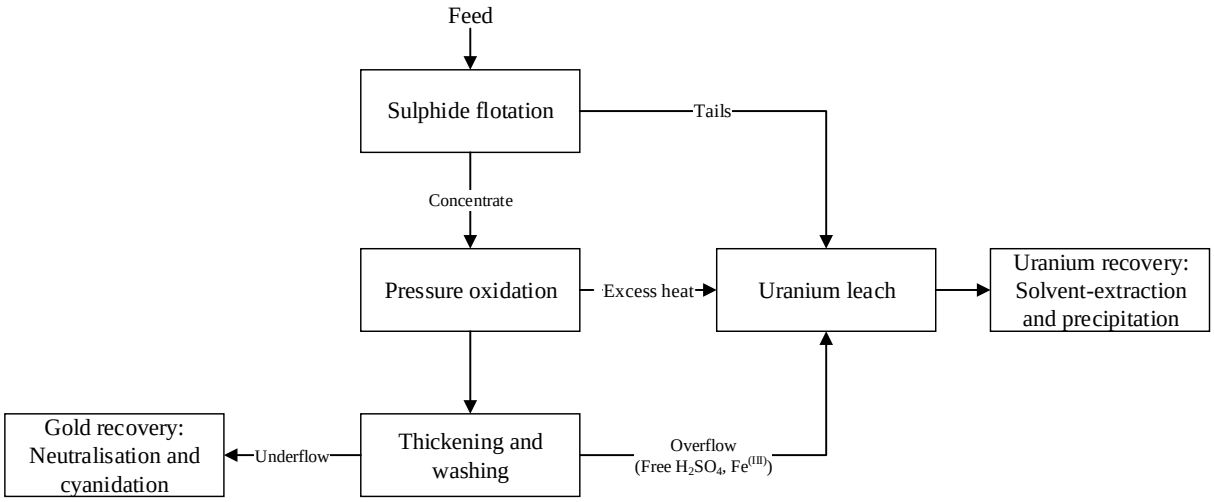

(a) Feed only amenable to sulphide flotation

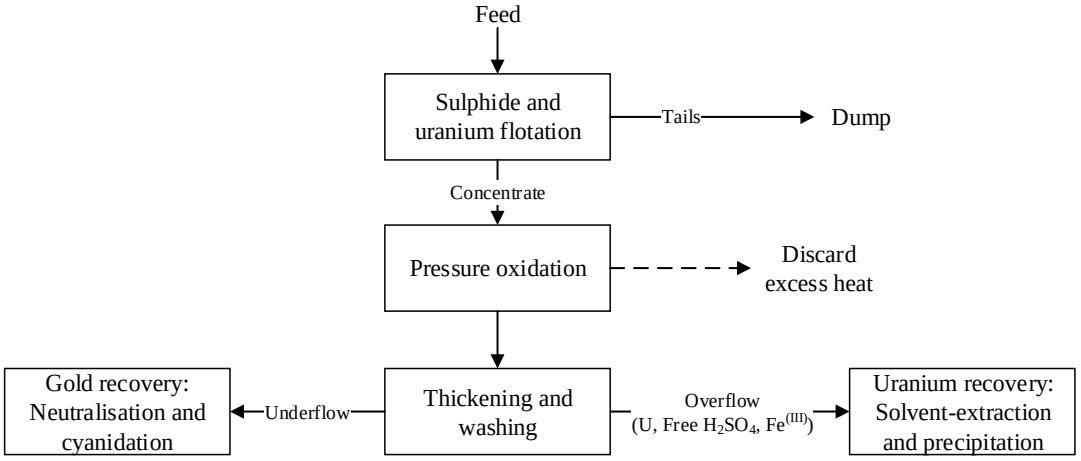

(b)Feed amenable to both sulphide and uranium flotation

Figure 2.2: Ore and tailings treatment options which includes POX (taken from flow sheets suggested by Fleming et al., 2010; Gold One International Limited, 2012; Verster & Pieterse, 2008)

2.4. Aqueous thermodynamic stability of pyrite

The aqueous stability of pyrite in terms of redox and hydrolysis processes is illustrated in Figure 2.3 by the Eh-pH (or Pourbaix) diagrams of the FeS_2-S-H_2O and FeS_2-Fe-H_2O systems, for temperatures of 25°C and 200°C.

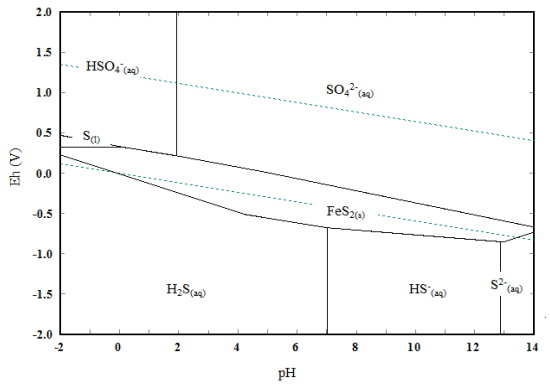

(a) FeS_2-S-H_2O system at 25°C

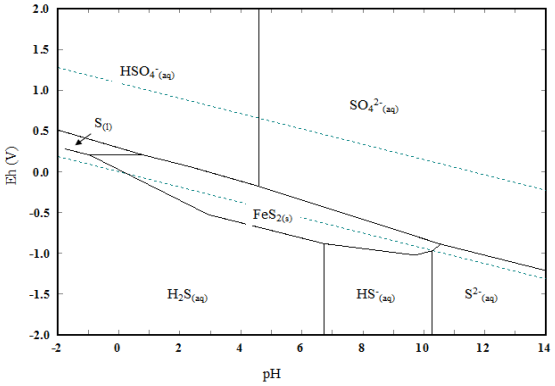

(b) FeS_2-S-H_2O system at 200°C

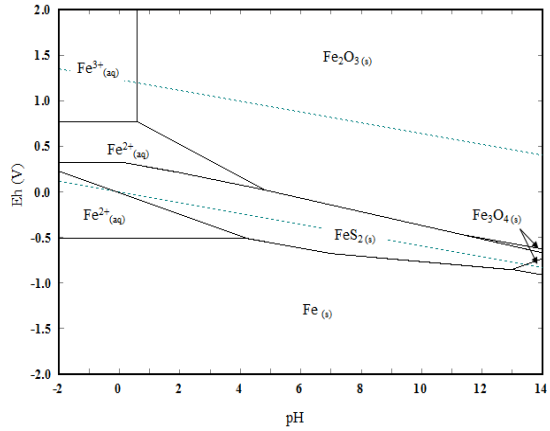

(c) FeS_2-Fe-H_2O system at 25°C

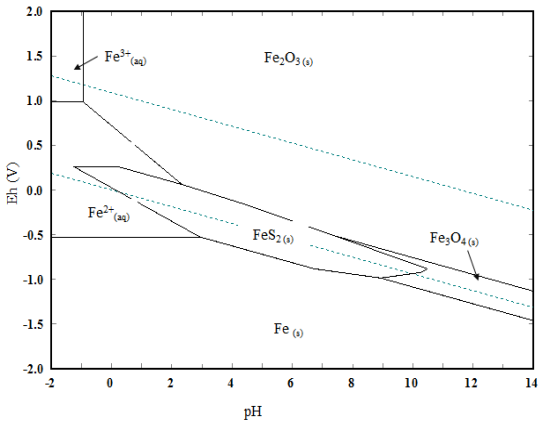

(d) FeS_2-Fe-H_2O system at 200°C

Figure 2.3: Eh-pH diagram of FeS_2-Fe-S-H_2O system ([Fe] = 0.05 mol/kg, [S] =0.5 mol/kg) (HSC Chemistry 6)

These diagrams show that pyrite is thermodynamically stable in oxygen-free water, except at extreme pH values, with its stability decreasing at higher temperatures. Pyrite is also relatively unreactive at ambient temperatures and will, typically, be stable beyond the Eh-pH domain indicated in Figure 2.3 (Kelsall, Yin, Vaughan, England & Brandon, 1999).

The stability area of elemental sulphur increases with increasing temperature, which means elemental sulphur could become an important intermediate product to consider under POX conditions. In terms of high-temperature iron precipitation, only hematite precipitation was included. Even though the formation of jarosites and basic iron sulphates are important iron products to consider at POX conditions (Fleuriault, Anderson & Shuey, 2016; Umetsu, Tozawa & Sasaki, 1977), they were omitted from the above diagrams, as these compounds are metastable, i.e., not stable over geological time frames.

The predominance diagrams show that the most prominent sulphur and iron species would be HSO_4^- and SO_4^{2-}, and Fe^{3+} and Fe_2O_3, respectively. Pyrite may thus be decomposed via four processes i.e., oxidation, reduction, acid decomposition or alkali decomposition. The favoured decomposition process will be dependent on the pyrite surface oxidation potential and the proton activity. The relevant equations for the four possible decomposition processes are provided below (Peters, 1976):

(a) Oxidation (with O_2) at low pH

$$FeS_2 + H_2O + 3.5O_2 \longrightarrow Fe^{2+} + 2SO_4^{2-} + 2H^+ \quad 2.1$$

$$FeS_2 + 0.5O_2 + 2H^+ \rightarrow Fe^{2+} + 2S^o + H_2O \quad 2.2$$

(b) Acid decomposition

$$FeS_2 + 2H^+ \rightarrow Fe^{2+} + H_2S + S^o \quad 2.3$$

(c) Reductive dissolution at low pH

$$FeS_2 + 4H^+ + 2R \rightarrow Fe^{2+} + 2H_2S + 2R^+ \quad 2.4$$

Where R^+ is a suitable reducing agent.

(d) Alkaline disproportionation

$$FeS_2 + 4OH^- \rightarrow 0.3Fe_3O_4 + 1.83\,S^{2-} + 0.16SO_4^{2-} + 2H_2O \quad 2.5$$

At high temperatures (180-220°C) in an acidic oxidative solution, typical of POX, the oxidative and acid decomposition routes would be expected to dominate. Since the oxidation of sulphides most likely occurs in single electron transfer steps (Basolo & Pearson, 1967: 473-474), it can be assumed that S_2^{2-} will be oxidised via species with intermediate oxidation states, that is, between elemental sulphur (S^o) and S^{6+} (or SO_4^{2-}) (Descostes, Vitorge & Beaucaire, 2004).

$$S° + H_2O + 1.5O_2 \rightarrow SO_4^{2-} + 2H^+ \quad 2.6$$

Any dissolved iron(II) will also be oxidised further to iron(III):

$$2Fe^{2+} + 0.5O_2 + 2H^+ \leftrightarrow 2Fe^{3+} + H_2O \quad 2.7$$

Once iron(III) is formed, pyrite may be oxidised by iron(III) (in addition to molecular oxygen) as follows:

$$FeS_2 + 14Fe^{3+} + 8H_2O \rightarrow 15Fe^{2+} + 16H^+ + 2SO_4^{2-} \quad 2.8$$

$$FeS_2 + 8Fe^{3+} + 4H_2O \rightarrow 9Fe^{2+} + 8H^+ + SO_4^{2-} + S° \quad 2.9$$

The direct acid (non-oxidative) decomposition (R.2.3) of pyrite is less likely, as iron-deficient sulphides have been shown to require reduction to stoichiometric Fe:S (i.e., 1:1 S to Fe ratio) compounds prior to the advent of spontaneous non-oxidative dissolution (Nicol & Scott, 1979). It is not expected that a reductant would exist at typical POX conditions where large oxygen over-pressures are employed. Lastly, it is expected that, if non-oxidative dissolution played a large role in the pyrite dissolution rate, the reaction rate would have a large positive order in proton concentration (Crundwell, 2013), which it does not have (see discussions in Section 2.6).

2.5. Properties of pyrite

Pyrite is the most abundant sulphide mineral and has been the topic of many scientific investigations, mainly because of its association with valuable metals, such as gold, copper and cobalt, and also because it is known to be the main cause of AMD. An extensive review on the oxidation of pyrite has been provided by Lowson (1982) and, more recently, by Chandra and Gerson (2010).

Iron (Fe) is a transition element and, in most cases, occurs naturally with surrounding ligand atoms. In the case of pyrite (transition metal sulphide), iron is bonded with sulphur atoms, giving rise to the ideal chemical formula FeS_2. XPS and Mössbauer spectroscopy has shown that iron is present as Fe^{2+} and sulphur as the $(S_2)^{2-}$ anion (Folmer, Jellinek & Calis, 1988). Each Fe^{2+} cation is surrounded by six neighbouring S_2 dimers in a rocksalt-type structure, with Fe^{2+} cations centred at the face-centres of each cubic cell. Each S atom is coordinated with three Fe atoms and one S atom. This configuration gives rise to a distorted tetrahedral arrangement, as shown in Figure 2.4 (Hung, Muscat, Yarovsky & Russo, 2002). Even though the ideal S:Fe ratio is 2, values of 1.978, 2.027 and 1.92 have also been cited (Chandra & Gerson, 2010).

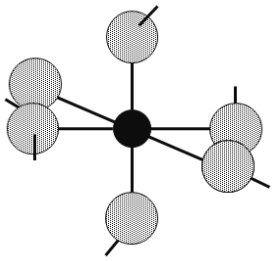

Figure 2.4: The bulk FeS_2 unit cell (black= Fe; light grey (big balls) = sulphur (redrawn from Mishra & Osseo-Asare, 1988)

Due to the large difference in electronegativity between the transition element and the ligands, covalent bonds are formed, and the resulting molecular orbitals may be described by the crystal field theory (Cotton, Wilkinson & Gaus, 1976). All electrons in the pyrite structure are paired (see Appendix A.1 for the molecular orbital scheme of pyrite), thus, no magnetic moment is displayed, i.e., it is diamagnetic. The disulphide group alone is also spin-paired (Kelsall et al., 1999).

Above properties pertain to pure pyrite, however, natural pyrite ores are polycrystalline, with some variability in surface and electrical properties (which may be due to the presence of impurity elements, i.e., lattice substitution with inorganic atoms) (Abraitis, Pattrick & Vaughan, 2004); therefore, it will be especially challenging to describe the pyrite oxidation rate by one single rate equation, under various conditions, unless the underlying processes that govern the observed leaching kinetics are properly understood and accounted for.

2.6. Observed pyrite leaching kinetics

In the present study, the pyrite dissolution system consists of several sub-processes that require consideration from a fundamental perspective. A schematic representation of the pyrite pressure oxidation system is provided in Figure 2.5.

The most important sub-processes that may have an influence on the observed pyrite pressure oxidation rate under typical industrial operating conditions, are as follows:

- Gas-liquid oxygen interfacial mass transfer;
- Mass transfer of solution species to the pyrite surface;
- Reactions occurring on the surface of pyrite, i.e., the intrinsic rate equation;
- Change of particle surface area during oxidation;
- Diffusion of reaction products away from the particle surface to the bulk of the solution; and
- Homogeneous iron(II) oxidation to iron(III) in the bulk solution.

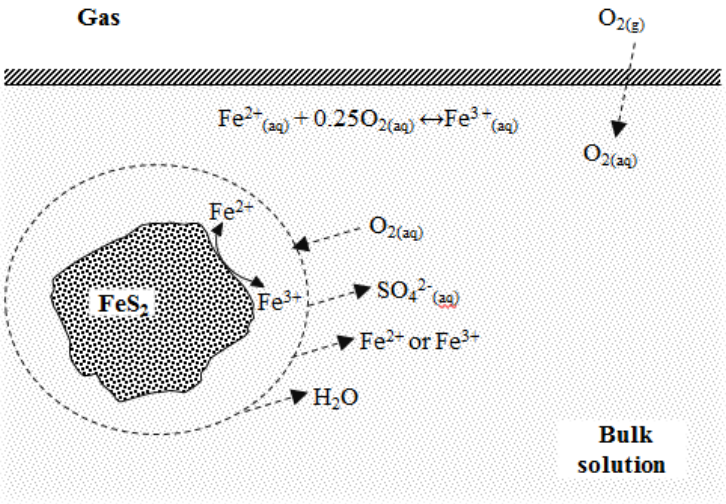

Figure 2.5: Schematic representation of pyrite dissolution during POX

Firstly, oxygen gas must diffuse through the gas-liquid interface into the bulk of the solution. It is assumed that the gas phase and the bulk of the solution are perfectly mixed, while the pyrite particles,

dissolved oxygen reagent and product species are homogenously dispersed throughout the slurry phase.

After oxygen has diffused from the bulk phase to the surface of the pyrite particle, it will interact with the surface of pyrite. The exact mechanism of the interaction of oxygen with pyrite is still unclear, i.e., whether it occurs via the iron(II)/iron(III), or via direct reaction with adsorbed oxygen. It is also unclear whether the iron leaves the surface as iron(III) or iron(II) species. The fact that iron is also a reaction product of the pyrite oxidation reactions complicates the understanding of the oxidation mechanism. For example, oxygen may simultaneously oxidise iron(II) on the surface of pyrite and in the bulk of the solution, which will occur at different reaction rates. What is important, however, is that, for the closed system around the pyrite particle (indicated in Figure 2.5), oxygen remains the primary oxidant and the ultimate electron acceptor, irrespective of whether these electrons are exchanged via the iron(II)/iron(III) couple. Since no iron is added externally, iron can only originate from the pyrite dissolution itself.

A summary of previously published kinetic studies of the aqueous oxidation of pyrite, relevant to the current work, are presented in Table 2.3. Studies concerning the oxidation of pyrite with iron(III) were also included in Table 2.3, as iron(III) is one of the important oxidation products that could also oxidise pyrite. In most of the reported work, both molecular oxygen and iron(III) were considered as oxidants. In addition, the effect of iron(II) and sulphuric acid on the rate of pyrite oxidation was also investigated. An increase in oxygen concentration (or oxygen partial pressure) resulted in an increase in the pyrite oxidation kinetics, with the order of the rate of pyrite in terms of oxygen concentration ranging from 0.5 to 1 (Holmes & Crundwell, 2000; Long & Dixon, 2004; McKibben & Barnes, 1986; Papangelakis & Demopoulos, 1991; Williamson & Rimstidt, 1994).

The pyrite oxidation reaction kinetics was also found to be strongly dependent on the iron(III) to iron(II) ratio, with an order in iron(III) ion concentration ranging between 0.5 and 1, and with a negative order in iron(II) concentration ranging mostly from 0.5 to 1 (Garrels & Thompson, 1960; McKibben & Barnes, 1986; Williamson & Rimstidt, 1994). Acid only weakly influenced the rate of pyrite oxidation, with a negative order in proton concentration ranging between -0.1 and -0.5 (Holmes & Crundwell, 2000; McKibben & Barnes, 1986; Williamson & Rimstidt, 1994).

In order to explain these observed dependencies and reaction orders, consideration should be given to the sub-processes occurring in the system. Each process will, therefore, be reviewed separately.

.

Table 2.3: Summary of pyrite pressure oxidation studies in the presence of iron(III) and molecular oxygen

Species investigated	Particle size	T, °C	Medium	$[O_2]$ and [Fe(III)] range	H^+ range	Rate equation	Activation energy	Reference
$[O_2]$	10-104 um	130-190	No acid added	~200-1300 kPa pO_2	n/a	$r = k[O_2]^{0.5}$	84 kJ/mol	Warren, 1956
$[O_2]$, $[H^+]$, [Fe(III)]	-325 um	100-130		0-4 atm	0-0.15 M H_2SO_4	$r = k[O_2]$ first order	56 kJ/mol	McKay & Halpern, 1958
Only [Fe(III)] and [Fe(II)] present. No oxygen	100-200 mesh	33	H_2SO_4 Eh adjusted with $KMnO_4$	$4.08x10^{-5}$ -1 $x10^{-3}$ mol/L Fe(III), Eh varied between 637 and 739 mV (SHE)	pH 0-2	$r = f([Fe^{(III)}])/[Fe^{(II)}])$ First order in $(Fe^{(III)}/Fe^{(II)})$ Independent of acid concentration	n/a	Garrels & Thompson, 1960
$[O_2]$	-65+200 mesh	85 - 130	H_2SO_4	12 - 66.4 atm	1 M H_2SO_4, 0.01 – 10 M H_2SO_4	$r = k[O_2]$ (12-22.2 atm) $r = k[O_2]^{<1 \text{ (approaching } 0.5)}$ (22.2-66.4 atm) Rate increased with decreasing acidity, no orders provided	51 kJ/mol	Bailey & Peters, 1976
[Fe(III)]	75-150 um	25-50	HCl	0.0004-0.0042 mol/kg Fe(III)	pH 2	$r = k[Fe^{(III)}]$ (assumed) Order in $[H^+]$ not investigated	92 kJ/mol	Wiersma & Rimstidt, 1984
[Fe(III)], $[O_2]$, $[H_2O_2]$	125-250 µm	20-40	HCl	~0.5-3.5 mM [Fe(III)], ~0.01-0.8 mM [Fe(II)] 1-0.21 atm pO_2	0.1-0.4 M $[H^+]$ and 0.02-0.1 M $[H^+]$	$r = k[Fe^{(III)}]^{0.5}[H^+]^{-0.5}$ $r = k[O_2]^{0.5}$, $r = k[H_2O_2]$	56.9 ± 7.5 kJ/mole $[O_2]$	McKibben & Barnes, 1986

Species investigated	Particle size	T, °C	Medium	$[O_2]$ and [Fe(III)] range	H^+ range	Rate equation	Activation energy	Reference
Fe(III)	-60+140 mesh		sulphate	Total Fe: 0.00895 to 0.0895 mol/L	0.102 mol/L	$r = k_1\text{-}k_2[Fe^{(II)}]^{0.5}[Fe^{(III)}]^{0.5}/((1/[Fe^{(III)}]^{0.5} + k_3 + k_4([Fe^{(II)}]/[Fe^{(III)}]^{0.5}))$		Zheng, Allen & Bautista, 1986
Both [Fe(III)] and $[O_2]$ tested	38-45 µm	23	Sulphate	67-104 µM [Fe(III)], $[O_2]$ saturated	Circum-neutral, pH 6 and 7	Positive in $[Fe^{(III)}]$, Positive in $[O_2]$ Negative in $[Fe^{(II)}]$ Order in $[H^+]$ not investigated	n/a	Moses & Herman, 1991
$[O_2]$	+37-147 um	140-180	H_2SO_4	5-20 atm 5-10 atm 10-20 atm	0.5 mol/L	$r = k[O_2]^{0.93}$ (5-10 atm, 150°C) $r= k[O_2]^{0.56}$ (10-20 atm, 170°C) $r= k[O_2]^{0.95}$ (5-10 atm, 170°C) Order in $[H^+]$ not investigated	46 kJ/mol (140-160 °C) 111 kJ/mol (160-180°C) 10atm	Papangelakis & Demo-poulos, 1991
[Fe(III)], $[O_2]$, [Fe(II)], $[H^+]$	150-250 um	25	HCl and H_2SO_4	$7.2x10^{-7}$-0.02 mol/kg $[O_2]$ $3.98x10^{-6}$-0.003 mol/kg [Fe(III)] & $1.12x10^{-6}$-0.002 mol/kg [Fe(II)]	$1 x10^{-10}$-0.03 mol/kg $[H^+]$; 0.003-0.03 mol/kg $[H^+]$	$r = k[O_2]^{0.5}/[H^+]^{0.11}$ $r = k[Fe^{(III)}]^{0.3}/[Fe^{(II)}]^{0.47}[H^+]^{0.32}$, N_2 purged solution $r = k[Fe^{(III)}]^{0.93}/[Fe^{(II)}]^{0.4}$, with $[O_2]$ present	n/a	Williamson & Rimstidt, 1994
$[H_2O_2]$	0.04-0.1 mm	20-50	H_2SO_4	0.5-5 M $[H_2O_2]$	0.1-3 M $[H_2SO_4]$	$r = k[H_2O_2][H^+]^{-0.36}$	68 kJ/mol	Antonijevic, Dimitrijevic & Jankovic, 1997

Species investigated	Particle size	T, °C	Medium	[O_2] and [Fe(III)] range	H^+ range	Rate equation	Activation energy	Reference
[O_2], [Fe(III)], [Fe(II)], [H^+]	Electrode	Not provided	H_2SO_4	0.005-0.2 M Fe(III) 3.2-21 mg/L O_2 Ranges of Fe(II) employed not provided	pH 1.5-3 0.2 M H_2SO_4 when Fe(III) was measured pH 0.6-1.8 and H_2SO_4 0.2 M when oxygen was measured	$r = k[H^+]^{-0.18}[O_2]^{0.5}$ $r = k[H^+]^{-0.5}(k_1[Fe^{(III)}]/(k_2[H^+]^{-0.5} + k_3[Fe^{(II)}]))^{0.5}$ Derived rate equations, individual half reactions were first order in O_2 and Fe(III) and negative first order in Fe(II)	Anodic half reaction: 80 kJ/mol Fe(III) reduction reaction: 45 kJ/mol	Holmes & Crundwell, 2000
[O_2]	49-125 um	170-230	H_2SO_4	345-1035 kPa pO_2	0.5 mol/L	$r = k[O_2]^{0.5}$ Order in [H^+] not investigated	33 kJ/mol	Long & Dixon, 2004
Not explicitly investigated	d50 ranged between 9.2 and 22.3 µm	150-155 145-155	sulphate	Not explicitly investigated	~25 g/L H_2SO_4	$r = k[H^+]^{-0.17}[O_2]^{0.5}$ (high slurry densities > 8 wt%) $r = k[H^+]^{-0.5}(k_1[Fe^{(III)}]/(k_2[H^+]^{-0.5} + k_3[Fe^{(II)}]))^{0.5}$ (low slurry densities < 2wt%)	75~139 kJ/mol (based on modal analyses) ~75-90 kJ/mol 71 kJ/mol	Steyl, 2012: 448
[Fe(III)], [H^+]	150-250 µm	30-75	sulphate	8 – 40 g/L Fe(III)	6-47 g/L	$r = k[Fe^{(III)}]^{0.36}$	51 kJ/mol	Zhong, 2015

2.6.1. Pyrite intrinsic rate equation

2.6.1.1. Electrochemical behaviour and dissolution of pyrite

There is general agreement that pyrite dissolution in acidic aerated aqueous solutions occurs via an electrochemical reaction mechanism (see references cited by Chandra & Gerson, 2010). An electrochemical reaction mechanism implies the potential-dependent transfer of electrons across the interface between the mineral and solution (Crundwell, 2013).

Strong evidence for the involvement of an electrochemical step in pyrite dissolution was identified by the isotope studies conducted by Bailey and Peters (1976), which confirmed that the majority of the oxygen in the final sulphate product originated via the anodic half-cell from the water, rather than from direct interaction with the dissolved molecular oxygen. Other support for the electrochemical mechanism includes the galvanic interaction of pyrite with other minerals (in which pyrite remains noble) (Lundström, Liipo, Karonen & Aromaa, 2009), and the effect of the redox potential on the reaction rate (Williamson & Rimstidt, 1994).

In this regard, the study of the oxidation behaviour of pyrite via electrochemical techniques may be considered as a valuable tool for investigating the reactions occurring on the surface of pyrite during its oxidation. Due to the electronic properties and occupancy of energy levels or bands, pyrite, just like many other sulphide minerals, is a semi-conductor (Osseo-Asare, 1992). Refer to Appendix A.2 for a more detailed discussion on the band structure of pyrite, as well as principles of dissolution of semiconductor minerals. Crundwell (1988) explains that, even though sulphide minerals are semiconductors, due to the high density of surface states, metal-like behaviour is observed. This allows one to apply the mixed potential theory, based on the corrosion of metals, to describe the dissolution behaviour.

2.6.1.2. Application of the mixed potential theory

Wadsworth (1979: 163-170) and Crundwell (2013) provide an overview of the mixed potential theory as applied to leaching reactions. According to the theory, the pyrite dissolution process constitutes independent anodic and cathodic half-reactions coupled through charge transfer, such that no net accumulation of charge occurs. The electrochemical kinetics is controlled by the potential and the species concentration at the solution-mineral interface, and may be described in terms of the Butler-Volmer equations of the respective half-cells. The value of the mixed potential is located somewhere between the half-cell potentials of the half-cells, and is defined by the kinetics of all the half-cells involved. In the case of the aqueous oxidation of pyrite with oxygen, the relevant half-reactions

include the anodic oxidation of the S_2^{2-} moiety associated with pyrite and the cathodic reduction of iron(III) and dissolved oxygen, as described below:

Anodic oxidation reactions:

$$FeS_2 + 8H_2O \longrightarrow Fe^{2+} + 2SO_4^{2-} + 16H^+ + 14e^- \quad (E^o = -0.366\ V) \quad 2.10$$

$$FeS_2 \rightarrow Fe^{2+} + 2S^o + 2e^- \quad (E^o = -0.443\ V) \quad 2.11$$

Cathodic reduction reactions:

$$O_2 + 4H^+ + 4e^- \rightarrow 2H_2O \quad (E^o = 1.229\ V) \quad 2.12$$

$$Fe^{3+} + e^- \leftrightarrow Fe^{2+} \quad (E^o = 0.771\ V) \quad 2.13$$

From the standard half-cell potentials, it is, thus, thermodynamically possible for both iron(III) and molecular oxygen to oxidise pyrite, as their equilibrium potentials are higher than the equilibrium potential of the anodic oxidation of pyrite, i.e., the coupling of the half-cell reactions would result in a positive cell potential. In addition, molecular oxygen can oxidise produced iron(II) back to iron(III). The reported mixed potentials for pyrite, cited by Lowson (1982), generally range between 0.62 (in air) and 0.75 V (SHE) (in O_2 at 12 atm) in solutions with varying acid media and strengths. The fact that the measured potentials were approximately midway between the equilibrium potentials (i.e., 0.34 and 1.23 V) of the two relevant half-cell reactions (Equations 2.10 and 2.12), provides further evidence of an electrochemically controlled reaction that may be described by the mixed potential theory of pyrite oxidation with molecular oxygen (Bailey & Peters, 1976; Lowson, 1982).

The polarisation behaviour (or current potential curves) of each of the half-reactions listed above may be studied independently via electrochemical techniques, and is characterised in terms of Tafel slopes and the exchange current density. In turn, these two parameters may be used to estimate how many electrons are involved in the rate-limiting step, considering the value of the transfer coefficient, as well as the order of the rate of the half-reaction in reagent concentration (Miller, 1979: 203-208, Nicol, Needes & Finkelstein, 1975).

Holmes and Crundwell (2000) applied the mixed potential theory to arrive at a rate equation for pyrite oxidation. The cathodic reduction of oxygen and of iron(III) was studied on a pyrite electrode and the anodic polarisation curve for pyrite was obtained by applying an anodic current. Holmes and Crundwell (2000) used the following methodology to derive the rate equation:

According to the Butler-Volmer equation, the rate of the anodic dissolution current may be related to the applied potential, according to Equation 2.14 (assuming that the only one electron is associated with the rate-determining step and, also, that the first electron transfer is rate-limiting):

$$i_{C:FeS_2} = k_{FeS_2}[H^+]^{-0.5}\exp(\frac{\beta_{FeS_2}FE}{R_gT}) \quad 2.14$$

Where k_{FeS_2} is the rate constant of the anodic reaction, β_{FeS_2} is the transfer coefficient, F is the Faraday constant (96485.33 C/mol), E is the potential, R_g the gas constant (8.314 J/mol.K) and T is temperature in K.

Similarly, for the iron(II)/iron(III) couple and the molecular oxygen reactions, the current density may be written as follows (Holmes & Crundwell, 2000):

$$i_{C:Fe} = k_{Fe^{2+}}[Fe^{2+}]\exp\left(\frac{\beta_{Fe}FE}{R_gT}\right) - k_{Fe^{3+}}[Fe^{3+}]\exp(\frac{-(1-\beta_{Fe})FE}{R_gT}) \quad 2.15$$

$$i_{C:O_2} = -k_{O_2}[O_2][H^+]^{0.14}\exp(\frac{-(1-\beta_{O_2})FE}{R_gT}) \quad 2.16$$

Where $[Fe^{2+}]$, $[Fe^{3+}]$ and $[O_2]$ represent the molal concentrations of the individual species, $k_{Fe^{2+}}$, $k_{Fe^{3+}}$ and k_{O_2} represent the rate constants of the individual half reactions, and β_{Fe} and β_{O_2} the transfer coefficients of the respective half reactions. Holmes and Crundwell (2000) experimentally confirmed that the order of each of these half reactions was approximately first order in iron(II), iron(III) and dissolved oxygen concentration, with a slightly negative dependence in proton concentration.

The Tafel slope $\left(\frac{2.303RT}{(1-\beta)F}\right)$ was measured as 133 mV/decade by Holmes and Crundwell (2000), while Biegler and Swift (1979) and Meyer (1979) report Tafel slopes ranging between 87 and 103 mV/decade, and 80 to 110 mV/decade, respectively, for the anodic polarisation of pyrite in acidic de-aerated solutions at ambient temperature. These Tafel slopes translate to transfer coefficients ranging between 0.44 and 0.74, assuming only one electron is transferred in the rate-determining step. More recently, Lin, Tsuchiya & Fan (2017) reported anodic Tafel slopes ranging between 210 and 270 mV/decade between 200 and 350°C, thereby corresponding to much lower transfer coefficients that range between 0.2 and 0.3. As regard to the reduction reactions, Biegler, Rand and Woods (1975) studied the kinetics of the oxygen reduction reaction on a pyrite electrode. At pH < 2 in oxygen-saturated conditions, the measured Tafel slope was ~127 mV/decade. The Tafel slope measured for the molecular oxygen reduction by Holmes and Crundwell (2000) was 115 mV/decade, and for the iron(II)/iron(III) couple, it ranged between 120 and 140 mV/decade.

From the above, the transfer coefficients were approximately 0.5 for each of the relevant half-reactions ($\beta_{FeS_2} \approx \beta_{Fe} \approx \beta_{O_2}$.) and, thus, enables simplification of the rate equations to arrive at an expression for the mixed potential (E_{oc}):

$$E_{oc} = \frac{R_g T}{F} \ln\left(\frac{k_{Fe^{3+}}[Fe^{3+}] + k_{O_2}[O_2][H^+]^{0.14}}{k_{FeS_2}[H^+]^{-0.5} + k_{Fe^{2+}}[Fe^{2+}]}\right) \quad 2.17$$

Which was derived from equating the anodic and cathodic currents as follows:

$$i_{C:FeS_2} = -i_{C:Fe} - i_{C:O_2} \quad 2.18$$

The mixed potential would, therefore, be a function of oxygen concentration, iron(II), iron(III) and acid concentration.

The observed rate of pyrite dissolution may be related to the current density, as follows:

$$r_{FeS_2} = \frac{i_{FeS_2}}{14F} \quad 2.19$$

And, therefore, the rate of pyrite oxidation, in the presence of iron(II), iron(III) and oxygen, may be represented by the following equation:

$$r_{FeS_2} = \frac{k_{FeS_2}[H^+]^{-0.5}}{14F}\left(\frac{k_{Fe^{3+}}[Fe^{3+}] + k_{O_2}[O_2][H^+]^{0.14}}{k_{FeS_2}[H^+]^{-0.5} + k_{Fe^{2+}}[Fe^{2+}]}\right)^{0.5} \quad 2.20$$

The reaction order in both the ferric and dissolved oxygen concentrations is half-order, and negative in iron(II) concentration. Application of the mixed potential theory, therefore, leads to a rate equation that is consistent with the results of many studies, listed in Table 2.3, as it accounts for the negative dependence on proton concentration and iron(II), as well as the half-order dependence in oxidant concentration (Long & Dixon, 2004; McKibben & Barnes, 1986; Warren, 195; 6; Williamson & Rimstidt, 1994; Zheng et al., 1986; Zhong, 2015). However, the rate equation derived by applying the mixed potential theory does not account for the first-order rate dependency in oxidant concentration, which was also observed in some instances (Bailey & Peters, 1976; Garrels & Thompson, 1960; McKay & Halpern, 1958; Papangelakis & Demopoulos, 1991; Williamson & Rimstidt, 1994).

In addition to the current-potential behaviour, which can be obtained from electrochemical studies (which are valuable for understanding the kinetics of the respective half-reactions), information on the reaction products and possible intermediate species may also be obtained.

2.6.1.2.1. Anodic oxidation of pyrite

In terms of the oxidation products, electrochemical studies in acidic aqueous electrolytes on pyrite electrodes have shown that the primary products of the anodic reaction are iron(III), sulphate and elemental sulphur (Bailey & Peters, 1976; Meyer, 1979; Peters & Majima, 1967). Bailey and Peters (1976) report a linear dependency between applied potential and sulphate yield, thus concluding, in agreement with Biegler and Swift (1979), that sulphur and sulphate is formed by competing independent pathways, and elemental sulphur is, once formed, stable and is not likely to be an

intermediate product. This finding implies that the reaction product, whether it is elemental sulphur or sulphate, will be very dependent on the type of oxidant used (which has varying equilibrium potentials, e.g., Fe^{2+}/Fe^{3+} = 0.77 V and O_2/H_2O = 1.23 V).

The oxidation of pyrite to sulphate involves the transfer of seven electrons. Steyl (2012: 289) assumed that the first electron transfer step in the reaction sequence (to form the HS· intermediate according to R.2.21), is rate-limiting, however, Steyl (2012: 289) does admit that there is no substantial experimental evidence to support this reaction.

$$S_2^{2-} + H^+ + h^+ \rightarrow S + HS\cdot \qquad 2.21$$

Crundwell (2013) makes a strong case against such an "acid attack" as the first step in the mechanism, as the anodic reaction rate has a very weak negative dependence on acid concentration (as was also observed from the reaction rate equations summarised in Table 2.3). This view is corroborated further by recent work by Bryson and Crundwell (2014), which found that the pyrite anodic polarisation curves were unaffected by acid concentrations ranging between 0.25 and 1 M HCl.

2.6.1.2.2. Cathodic reduction reactions

One of the most apparent differences between molecular oxygen and the iron(III) ion as reductant, is the interaction of these species with the surface of the pyrite. Electron transfer to the iron(III) ion will most likely occur from the mineral surface to the solvated iron(III) retained in the outer Helmholtz plane, i.e., the closest a solvated cation can approach the electrode surface.[d] On the other hand, oxygen is a neutral molecule with no hydration sphere, thus, direct adsorption (i.e., chemisorption) to the mineral surface is possible (Steyl, 2012: 357). To quantify the equilibrium coverage of the pyrite surface, adsorption of oxygen may be described by adsorption isotherms (Hamann, Hamnett & Vielstich, 2007: 208). Steyl (2012: 284) showed that, due to the associated hydration sphere of iron(III), direct interaction between pyrite's surface is unlikely, as a result of electrostatic interferences, whereas diatomic oxygen can approach pyrite's surface without any electrostatic hindrances and will, thus, be the more likely oxidant at POX conditions.

Even though molecular oxygen can approach the pyrite surface more closely, it is known that iron(III) is a more effective oxidant than molecular oxygen (Dutrizac & MacDonald, 1974; Moses, Nordstrom, Herman & Mills, 1987; Williamson & Rimstidt, 1994). Luther (1987) explains this phenomenon with

[d] The inner Helmholtz plane is comprised of oriented water dipoles (Hamann et al., 2007: 121). In other words, the ferric ion will be surrounded by a hydration shell/solvation sheath and electron transfer will occur via electron tunnelling through water dipoles (Steyl, 2012: 257).

reference to the fundamentals of the molecular orbital theory. According to the ligand field theory, the labile ferric aqueous d^5 molecular orbitals are split into partially occupied t_2g (π) and e_g^* (α^*) orbitals as a result of the orientation of water dipoles in its associated solvation sphere. The $e_g^*(\alpha^*)$ orbitals and the π^*-molecular orbital of S_2^{2-} overlap to form a strong α bond (Luther, 1987). Thus, the iron(III)/iron(II) redox couple can easily exchange electrons and it is a less strong, but kinetically more attractive oxidant. Conversely, slow molecular oxygen reduction kinetics at ambient temperatures may (at least partially) be attributed to limited wave function overlap and spin restrictions encountered during electron exchange between S_2^{2-} and molecular oxygen (Luther, 1987; Nicol, 2016). In other words, electron transfer from the π^*-molecular orbital of S_2^{2-} (i.e., the highest occupied molecular orbital) to the π^*-molecular orbital of O_2 (i.e., the lowest occupied molecular orbital) is unlikely (Luther, 1987).

Molecular oxygen reduction

The molecular oxygen (MO) reduction reaction is extremely well-researched as it is of great importance in the fuel-cell industry. A very useful review has been published by Appleby (1993) and, more recently, by Shi, Zhang, Kiu, Wang and Wilkinson (2006). The reduction reaction involves four electron transfers, has a standard electrode potential of 1.23 V (SHE) and is known to be highly irreversible (Appleby, 1993). Only a brief review of the main aspects, as applicable to pyrite mineral oxidation, will be given here.

The aqueous reduction of oxygen is likely to occur through a series of elementary one-electron transfer steps following many possible pathways. The so-called “peroxide path” is generally accepted, as shown below (Shi et al., 2006; Tributsch & Gerischer, 1976).

$$O_{2(aq)} + H^+ + e^- \leftrightarrow HO_2 \cdot \quad 2.22$$

$$HO_2 \cdot + H^+ + e^- \leftrightarrow H_2O_2 \quad 2.23$$

$$H_2O_2 + H^+ + e^- \leftrightarrow HO \cdot\cdot + H_2O \quad 2.24$$

$$HO \cdot\cdot + H^+ + e^- \leftrightarrow H_2O \quad 2.25$$

In most studies, the formation of the perhydroxyl radical (HO_2) is believed to be rate-limiting (Steyl, 2012: 252; Tributsch & Gerischer, 1976). Shi et al. (2006) cite various independent studies that concur that the first electron transfer step is most likely rate-limiting. It has been reported that pyrite acts as electrolytic catalyst for both oxygen reduction (Biegler, 1976) and for the decomposition of hydrogen peroxide (Tributsch & Gerischer, 1976); nevertheless, the kinetics of oxygen reduction on pyrite remains slow at room temperature.

Iron(III) reduction (and iron(II) oxidation) on the surface of pyrite

The iron(III) reduction reaction is characterised by a single electron transfer. Here, it should be mentioned that a distinction is made between the reduction of iron(III) on the surface of pyrite, and the reduction of iron(III) in the bulk of the solution, i.e., homogeneous iron(III) oxidation, which will be discussed in Section 2.6.2. Since it has been shown that the rate of oxidation of pyrite is much higher with iron(III) as the oxidising agent, than with dissolved oxygen, the role of dissolved oxygen, when sufficient iron(III) is present, is believed to be limited to the regeneration of iron(III) by oxygen on the surface of pyrite (Moses et al., 1987; Singer & Stumm, 1970). Iron(III) is, therefore, essentially the active oxidant of pyrite, but with iron(II) also serving as a catalyst for oxygen reduction, such that a higher overall reaction rate may be sustained. In other words, in a case where no iron is added externally, iron originates strictly from the surface of the pyrite and is cyclically oxidised by oxygen from iron(II) to iron(III) and reduced back to iron(II) by sulphide.

The proposed catalytic effect of the presence of iron(III) on the oxidation rate of pyrite may be illustrated using the schematic polarisation diagrams shown in Figure 2.6. A similar diagram has been shown by Li, Bergeron and Ghaareman (2017). Mediation via the iron(III)/iron(II) couple increases the oxidation kinetics, while molecular oxygen remains the principle oxidant or "electron sink". Therefore, with an increase in duration of the leaching experiment, the iron(III) concentration will gradually build up, causing an increase in the mixed potential and associated current density (i_o). Since one of the oxidation products acts as a catalyst for the oxidation reaction itself, autocatalytic behaviour during pyrite oxidation is expected, with the reaction rate curve characterised by a distinct lag period at the start (Levenspiel, 1999: 52-53).

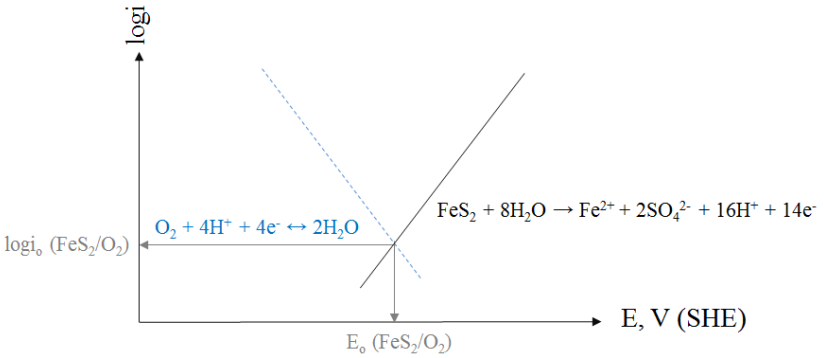

(a) FeS_2/O_2 system (at time 'zero')

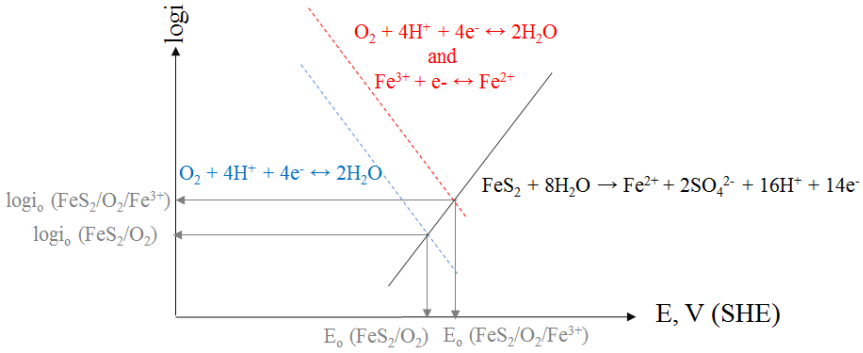

(b) $FeS_2/O_2/Fe^{3+}$ system (time > zero)

Figure 2.6: Schematic polarisation diagram of the mixed potential theory applied for pyrite oxidation in sulphuric acid solutions

However, the mechanism proposed above is mostly based on observations in systems where iron(III) was added externally, i.e., the fact that the oxidation rate is higher in the presence of iron(III) than for oxygen. It is, thus, doubtful whether a system where iron(III) or iron(II) is externally added to a pure O_2-pyrite system, to study its catalytic effect, would be representative of a real reacting pyrite surface. Since iron is intrinsically part of the mineral lattice, the workings of molecular oxygen cannot be isolated, as iron dissolution would occur simultaneously with the dissolution of pyrite. Some of the mechanistic proposals that consider the role of iron during pyrite oxidation are reviewed and included in Appendix A.3.

2.6.1.3. Role of iron(III) and oxygen as oxidants during POX

From the preceding discussion, which was mainly based on chemical leaching and electrochemical studies conducted at ambient conditions, it is evident that the exact mechanism by which pyrite is oxidised in the presence of oxygen is poorly understood – more so at conditions typical of POX, where the oxidation of pyrite with iron(III) alone (i.e., in the absence of oxygen) has not been studied before. Provided that these two reactions, namely pyrite oxidation with oxygen and pyrite oxidation

with iron(III), could have different activation energies, the relative contributions of the two reactions to the overall observed rate could be vastly different compared to their roles at lower temperatures.

Studies of pyrite oxidation kinetics at typical POX temperatures in the presence of oxygen, by Long and Dixon (2004), Papangelakis and Demopoulos (1991) and Warren (1956), did not explicitly consider the possible reaction of pyrite with iron(III), and only reported the observed reaction rate in terms of an apparent reaction order in either oxygen partial pressure or dissolved oxygen concentration. The data published by Long and Dixon (2004) was recently re-evaluated by Zhukov, Laari and Koiranen (2015) who developed a comprehensive kinetic model considering the contributions of both oxidants to the pyrite reaction rate. Their model adequately predicted the pyrite dissolution kinetics, as well as measured iron(II) and iron(III) concentrations in solution, thereby providing significant support for a dual-rate dependency in both oxidants at POX temperatures. A similar approach was followed in the current study.

2.6.1.4. Acid concentration

With regard to acid concentration, sulphuric acid is of importance, as pyrite is oxidised to form sulphate. In general, increased acid concentrations have shown to decrease the pyrite oxidation rate (as shown in Table 2.3) only slightly when oxidised by molecular oxygen and/or iron(III), meaning the rate-limiting step does not have a strong dependency on free acid.

In chemical oxidation studies, McKibben and Barnes (1986) found no dependency on acid concentration when pyrite was leached with oxygen; however, when iron(III) was employed in nitrogen-purged solutions, the rate was found to be negative in proton concentration with an order of 0.5. On the other hand, Zhong (2015) reports results showing that the oxidation of pyrite by the addition of iron(III), in the absence of dissolved oxygen, has no dependence on acid concentration over a relatively wide range of acid additions (6-47 g/L H_2SO_4).

In terms of electrochemical studies, varying acid concentrations have not shown to have any effect on the anodic dissolution of pyrite (Bryson & Crundwell, 2014) in 0.25-1 M HCl solutions (discussed in Section 2.6.1.1) when the potential was varied between 0.7 to 1.15 V (Ag/AgCl), indicating that the effect of acid on the rate of oxidation is most likely related to the mechanism by which iron(III) and oxygen interact with pyrite's surface.

There are a few proposed mechanisms by which increasing acid concentration could decrease the rate at which pyrite oxidation takes place. One or all of these could potentially contribute to this effect.

- High proton concentrations could prevent cations, such as the iron(III) ion and its associated water molecules in the solvation sphere, from approaching the pyrite surface, due to electrostatic repulsive forces, thus, leading to a decreased rate (Steyl, 2012: 284-285).

- Addition of sulphuric acid will unavoidably introduce more sulphate into the system, leading to re-speciation of iron(III) (and to a lesser extent iron(II)) and the formation of iron(III) species that could be less likely to interact with pyrite's surface. In support of this argument, Nicol, Miki, Zhang and Basson (2013) have shown that increasing sulphate concentrations (added in the form of sulphate salts) decrease the reduction rate of the iron(III) ion, as well as the oxygen reduction rate on pyrite surfaces, considerably.

No studies were found where the effect of acid concentration on the pyrite oxidation kinetics was investigated under pressure oxidation conditions. In other words, there is no experimental data available for the effect of acid addition on the oxidation kinetics of pyrite at temperatures between 180°C and 220°C. This area was addressed, specifically, by the current study.

2.6.1.5. Temperature

Firstly, it is known that the activation energy characteristic of diffusional processes is smaller than 21 kJ/mol (Wadsworth, 1979: 135). With reference to Table 2.3, a wide variation in activation energies has been reported, ranging anywhere between 33 and 110 kJ/mol. Based on the magnitude of the reported activation energy values, all of the studies were seemingly conducted under conditions where mass transfer processes did not dominate. The wide variation in reported data may suggest that different pyrite samples have different reactivity towards oxygen and/or iron(III) .

As mentioned in Section 2.6.1.3, studies that have been conducted at conditions relevant to POX were reported by Long and Dixon (2004), Papangelakis and Demopoulos (1991) and Warren (1956). Warren (1956) reports an activation energy of 80 kJ/mol between 130 and 190°C, while Papangelakis and Demopoulos (1991) report an activation energy of 110 kJ/mol between 160 and 180°C. On the other hand, Long and Dixon (2004) report a much lower activation energy, of 33 kJ/mol, between 170 and 230°C.

2.6.2. Iron(II) to iron(III) homogeneous oxidation

Due to the importance of iron(III) as an oxidant in the pyrite dissolution kinetics, the rate at which iron(II) is oxidised to iron(III) in the bulk of the solution, after it has diffused from pyrite's surface, requires consideration.

Dreisinger and Peters (1989), Lowson (1982) and Steyl (2012: 97-109) provide thorough overviews of the mechanistic and fundamental aspects of the aqueous oxidation of iron(II) by oxygen, as well as comprehensive lists of publications on the subject. In general, the reaction rate has been found to be first order in molecular oxygen concentration, and second order in iron(II) concentration. An increase in acidity decreases the rate of oxidation; however, this decrease is thought to be caused by solution

speciation changes. With the addition of sulphuric acid, the added associated protons form complexes with sulphate, previously bound to metal sulphate species, to form bisulphate. This increases the activity of the free iron(III) ions, which ultimately have a negative effect on the reaction kinetics, due to higher electro-repulsive forces between the iron(II) ions (Dreisinger & Peters, 1989). It is also known that this oxidation reaction is catalysed by the presence of metals, such as copper (Ruiz, Jerez & Padilla, 2016; Steyl, 2012: 212).

The studies of Cheng (2002), Ruiz et al. (2016) and Vraĉar and Cerović (1996) have the highest relevance, as they investigated the iron(II) to iron(III) oxidation rate in aqueous sulphate solutions at temperatures typical of POX. The conditions and listed reaction rate equations are summarised in Table 2.4. The activation energy was typically found to be ~80 kJ/mol. The study conducted by Vraĉar and Cerović (1996) was done under gas-liquid diffusional limitations, which may have lowered the observed activation energy considerably, to approximately 50 kJ/mol.

Table 2.4: Iron(II) oxidation studies

Experimental conditions				**Rate equation**	**Acti-vation energy, kJ/mol**	**Reference**
Temperature, °C	**Fe(II), g/L**	**pO_2, kPa**	**H_2SO_4, g/L**			
50-200	2-50	203-1014	0-50	$r = kpO_2[Fe^{(II)}]^2$	51	a
120-220	0.5	690	59	$r = kpO_2[Fe^{(II)}]^2$	78	b
140-200	11	101	49	$r = kpO_2[Fe^{(II)}]^2[SO4^{2-}][H_2SO_4]^{-0.5}$	80	c

a - (Vraĉar & Cerović, 1997); b - (Ruiz et al., 2016); c - (Cheng, 2002)

The exact "location of iron(II) oxidation", i.e., whether it is oxidised on the surface of pyrite or in the bulk phase, could also have important consequences for the observed leach kinetics of the iron(II) oxidation reaction. Littlejohn (2006) found that the iron(II) oxidation reaction is first order in iron(II) concentration, as opposed to second order, when catalysed by pyrite (i.e., when pyrite itself does not undergo oxidation due to a galvanic effect). Thus, in the presence of pyrite, iron(II) oxidation may take place at two distinct rates, which may be described by two different rate equations.

2.6.3. Mass transfer of species from the bulk of the solution to the pyrite surface

For hydrometallurgical mineral leaching systems, the reaction rate may also be dependent on the rate of mass transfer of species across the boundary layer, or the so-called "film resistance" at the surface of the solid. The magnitude of the mass transfer coefficient is, in turn, dependent on the hydrodynamic conditions within the reactor, as well as particle size (Harriott, 1962). In mechanically stirred vessels, an agitation speed targeting complete suspension of all solid particles is usually employed in leaching applications. Increasing the impeller speed or changing of the agitator arrangement beyond this point increases the value of the mass transfer coefficient only marginally

(Zwietering, 1958). This is evident by the discontinuity in the increase of the mass transfer coefficient as a function of the agitation speed identified by Harriott (1962). Elimination of mass transfer from the bulk of the solution to the particle surface as a rate limiting factor may be achieved by increasing the impeller speed to a point where no further increase in the rate of leaching is observed (see, e.g., Long & Dixon, 2004). However, Wadsworth (1979: 138-139) recommends that a more accurate method to determine whether a leaching reaction is limited by boundary layer diffusion is measuring the activation energy of the reaction.

2.6.4. Product layer diffusion

2.6.4.1. Surface passivation effects by sulphur

The formation of reaction products, such as elemental sulphur or polysulphides, could potentially hinder the movement of species from the bulk of the solution to the pyrite surface, and also limit the rate of transfer of other reaction products from the surface to the bulk of the solution. It is known that elemental sulphur starts to melt between 110 and 120°C (Thackray, 1970), and in reference to Figure 2.1, will convert to sulphate at temperatures above ~180°C (Mackiw et al., 1966). Therefore, at temperatures lower than 180°C, molten sulphur may coat particles, leading to impaired leaching kinetics. This phenomenon is characteristic of medium-temperature (~120-160°C) sulphide oxidation processes, and molten sulphur dispersants, such as lignosulphonates, are usually added to ensure mineral surfaces are adequately exposed to the oxidant (Owusu, Dreisinger & Peters, 1995). At temperatures exceeding 180°C, where conversion of elemental sulphur to sulphate is usually complete, coating by molten elemental sulphur is less likely. However, even at temperatures up to 230°C, Long and Dixon (2004) concluded that passivation of the pyrite surface as a result of the formation of an elemental sulphur film, had occurred. This observation was mostly based on deviations between the measured reaction kinetics towards the end of each kinetic test and an ideal shrinking particle model. This result suggests that elemental sulphur could possibly still be an important intermediate to consider at autoclave conditions.

2.6.4.2. Iron precipitation

Posnjak and Merwin (1922), Umetsu et al. (1977) and, more recently, Fleuriault et al. (2016), conducted studies to characterise the different iron(III)-containing precipitates at temperatures ranging up to ~200°C. It is generally known that iron(III) could precipitate as either hematite, jarosite or basic iron sulphate (Fleuriault et al., 2016). The exact composition of the product is dependent on the initial acid concentration, iron(III) solution concentration, operating temperature, the presence of other metal ions in solutions, the kinetics of precipitation, as well as the “apparent” solubility of the various products, which could also be metastable (Dutrizac & Sunyer, 2012; Fleuriault et al., 2016;).

Furthermore, the formation of iron precipitates on existing pyrite surfaces could have a passivating effect on the observed pyrite oxidation reaction kinetics (Tabelin, Veerawattananun, Ito & Igarashi, 2017), with the extent thereof dependent on the porosity of the surface layers. Provided these potential secondary effects, as well as the fact that iron in solution was used as the primary reaction progress variable (RPV), the majority of the batch POX test work was performed at conditions where precipitation was completely avoided (refer to Section 3.2.4.5 for support for this claim).

2.6.5. Gas-liquid interfacial mass transfer

The observed rate of pyrite leaching may also be governed by mass transfer of gaseous oxygen from the gas to the liquid phase. In these types of operations, especially in batch pressure reactors, gas-liquid transfer is often the rate limiting step of the overall process, due to the high intrinsic rate of chemical reactions at the temperatures of POX. Since the gas-liquid rate of transfer is a diffusional process, a reaction order of "1" in oxygen concentration would be observed if the overall rate of the process is limited by transfer of oxygen from the gas to the liquid phase. In addition, the reported activation energy will generally be less than 30 kJ/mol, should this diffusional process become rate-controlling.

A large portion of the test work conducted as part of this study was devoted to determining the oxygen gas-liquid mass transfer coefficient in the Parr batch pressure reactor used for the experimental work. This coefficient was required to enable prediction of the dissolved oxygen concentration during the POX batch tests. Therefore, methods to quantify the oxygen absorption rate and process parameters, which could have a significant impact on the transfer rate in agitated pressure reactors, are discussed in Sections 2.6.5.2 to 2.6.5.4. An extensive review of the subject has been published by Filippou, Cheng and Demopoulos (2000), which the reader is also referred to.

2.6.5.1. Oxygen solubility

Oxygen is sparingly soluble in water, and its solubility is reduced further in aqueous electrolyte solutions (compared to its solubility in pure water) owing to the salting-out effect. The aqueous oxygen solubility is also highly temperature dependent – an effect which must be accounted for at the conditions typical of pressure oxidation (Tromans, 2000). The fundamental background and equations used to predict oxygen solubility as a function of aqueous solution concentration, oxygen partial pressure and temperature, are provided in Appendix C.2.

2.6.5.2. Mass transfer in agitated liquids

In agitated systems, two distinct modes of transport, diffusion and convective mass transfer contribute to mass transfer. Convective mass transport is responsible for transporting the diffused gas from the

mobile gas-liquid interface to the interior of the moving fluid after it has diffused into the liquid (Danckwerts, 1970). Several models exist to describe the absorption process in agitated systems, of which the film model is the most widely applied, due to its simplicity (Danckwerts, 1970: 98-99). According to this theory, two thin, stagnant films of fluid exist in the vicinity of the interface between the gas and liquid phase in which transfer is effected solely by molecular diffusion, with the driving force being the chemical potential difference between the two phases. It has been found that the gas-side mass transfer resistance is usually negligible and, therefore, the rate of gas transfer is typically limited by the resistance in the film on the liquid side (Yoshida & Arakawa, 1968).

It has been found experimentally that the rate of absorption of a gas into an agitated liquid is described by Eq. 2.26 (Danckwerts, 1970: 97):

$$\frac{dm_A}{dt} = k_L a(m_A^* - m_A) \qquad 2.26$$

where m_A* (mol/kg) is the equilibrium concentration or solubility of the dissolved gas corresponding to the partial pressure of the gas at the interface between the gas and the liquid, k_L is the mass-transfer coefficient (1/m^2.min) and a is the interfacial area (m^2) between the gas and the liquid[e]. dm_A/dt is the average rate of transfer of gas per unit area (mol/kg.min) and m_A (mol/kg) is the average concentration of the dissolved gas in the bulk of the liquid.

A chemical reaction occurring in the liquid film could increase the rate of gas absorption, and the effect of a chemical reaction is often expressed in terms of the enhancement factor, E_L (Danckwerts, 1970: 34, 105). E_L provides a measure of the increased rate of absorption in a process, due to chemical reaction, relative to a process which is governed by physical absorption alone (Danckwerts, 1970: 34, 105). A detailed review on the effects of chemical reaction on gas absorption is provided in Appendix B.2. The "chemical enhancement" concept is important in relation to the chemical methods applied to determine the oxygen mass transfer coefficient (see Section 2.6.5.3).

2.6.5.3. Methods of determining the overall gas-liquid mass transfer coefficient

In general, methods of measuring oxygen mass transfer rates can be classified as either physical or chemical. In physical methods, oxygen content in the aqueous phase or oxygen partial pressure is measured directly. In chemical methods (also known as indirect methods), the rate of oxygen consumption is measured indirectly, by allowing some substance to react with oxygen in the aqueous

[e] It is common practice to group k_L and a together as a lumped parameter, k_La, which is well-known as the liquid-side mass transfer coefficient or the volumetric mass transfer coefficient (Danckwerts, 1970: 98). This parameter is commonly used as quantitative measure of the mass-transfer capability of a given reactor, and was also measured and used in this study.

phase and measuring the rate at which it reacts (Filippou et al., 2000). Both direct and indirect methods were employed during the current study.

Indirect/chemical method

The theoretical background for the utilisation of the chemical method as a tool for determining the mass transfer characteristics is given by the theory of absorption accompanied by a reaction, which is provided in Appendices B.1 and B.3. The sulphite oxidation method is generally used to quantify the overall oxygen gas-liquid mass transfer coefficient in stirred tank reactors (Linek & Vacek, 1981). In an aqueous solution of sodium sulphite, sulphite anions are oxidised to sulphate by dissolved oxygen according to the following reaction:

$$SO_3^{2-} + \frac{1}{2}O_2 \rightarrow SO_4^{2-} \qquad 2.27$$

Reaction 2.27 is normally slow, but it is accelerated appreciably in the presence of metal ions, such as Co(II) and Cu(II). The addition of cobalt sulphate as catalyst is usually preferred (Linek & Vacek, 1981).

The sulphite oxidation method makes use of conditions prevailing in the "slow reaction" regime, as discussed in Appendix B.2, to enable physical measurement of the k_La value. The reaction should be fast enough to reduce the bulk concentration of dissolved oxygen to zero, but not so fast that it causes chemical enhancement of oxygen absorption into the liquid. If these conditions are fulfilled, then the k_La value can be found using the calculated oxygen solubility and measurement of the absorption rate according to Eq. 2.28:

$$\frac{dm_A}{dt} = k_L a m_A^* \qquad 2.28$$

In order to meet the above-mentioned criteria, an empirical approach has to be followed, whereby the increase in absorption rate with increasing catalyst addition should be measured. The problem, thus, becomes one of determining the appropriate reaction conditions, so that the reaction proceeds at the desired rate. A typical profile of the absorption rate as a function of catalyst concentration is shown in Figure 2.7.

Region A (Figure 2.7) corresponds to the slow reaction regime, where the rate of reaction is not fast enough to reduce the bulk concentration to zero.

In Region B (Figure 2.7), the oxygen absorption rate is independent of catalyst concentration and the enhancement factor is close to unity. The reaction rate is fast enough to reduce the bulk concentration to zero. It is within this region that the k_La measurement should be made.

In Region C (Figure 2.7), the effects of reaction become visible, and in Region D, the influence of hydrodynamics on the rate of oxygen absorption becomes completely suppressed. Region C and Region D corresponds to the "fast reaction regime", where the enhancement factor is larger than unity. One other characteristic of the fast reaction regime is that the slope of the absorption rate vs. cobalt concentration on the logarithmic scale is equal to ½.

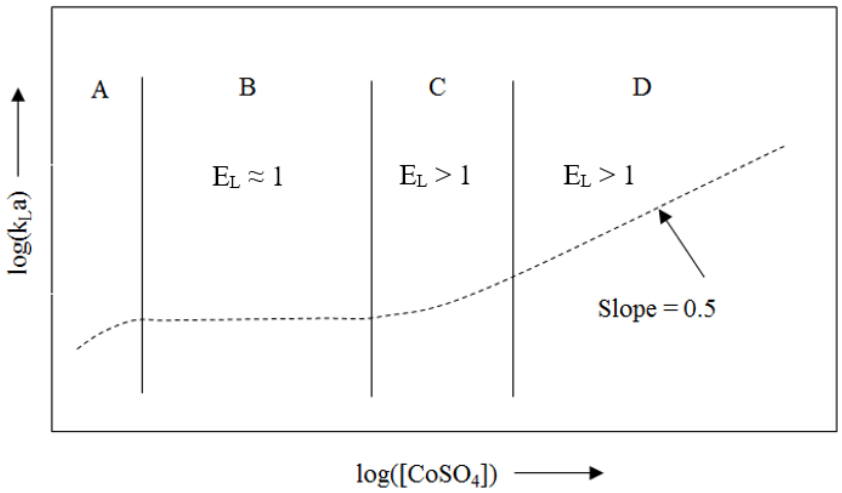

Figure 2.7: Oxygen absorption rate of oxygen as function of cobalt catalyst concentration (reproduced from Linek & Vacek, 1981)

The indirect/chemical method, thus, entails generation of a log-log plot of oxygen transfer rate *versus* catalyst concentration, which subsequently allows quantification of the k_La value in the correct reaction regime.

Physical/direct methods

Physical/direct methods are usually based on direct measurement of the change in gas concentration, either in the gas or liquid phase, as a function of time. This technique has one distinct limitation; the reciprocal of the k_La should be significantly larger than the response time of the gas sensor used.

A direct method based on measurement of the decrease in partial pressure in pure water, used by Albal, Shah, Schumpe and Carr (1983), was employed during this study (refer to Section 3.1.4). The method is particularly suited to batch pressure reactors where surface aeration is the dominant mode of transfer and the equipment is designed for high pressure applications. The method involves pressurisation of the reactor with a predetermined amount of oxygen and sealing the reactor from any

incoming oxygen, then initiating agitation and measuring the partial pressure decrease over time until equilibrium conditions are reached.

2.6.5.4. Effect of process variables

Numerous factors could have an effect on the rate of oxygen mass transfer from the gas to the liquid. From Equation 2.1, the following parameters define the rate of absorption:

- equilibrium concentration or solubility of oxygen in the liquid phase;
- interfacial area between the gas and the liquid; and
- physical mass transfer coefficient.

Different process variables may affect one or all of the abovementioned parameters.

Temperature

The effect of temperature on k_L and a are rarely investigated separately; instead, the effect of temperature on as a lumped parameter is studied and, therefore, the various effects temperature has on the parameters are also "lumped" together.

In general, it has been found that temperature increases the rate of gas absorption (Stenstrom & Gilbert, 1981). Temperature will increase the magnitude of the physical mass transfer coefficient due to an increase in diffusivity. However, increasing temperature may favour bubble coalescence to lower the effective interfacial area (Lin et al., 1998), therefore, the exact effect of temperature should be studied independently for each system of concern.

The increase in the k_La value with temperature may be predicted with an Arrhenius-type relationship (Filippou et al., 2000). It is known that the activation energy for solution diffusion is usually less than 20 kJ/mol (Wadsworth, 1979). However, measured activation energies of 33 kJ/mol (25-75°C) and 20 kJ/mol (80-150°C), respectively, are reported by Cheng (1994) and Steyl (2012: 93) in batch autoclave stirred reactors. The following empirical equation has been widely used to extrapolate the volumetric mass transfer coefficient to higher temperatures in stirred reactors (Stenstrom & Gilbert, 1981):

$$k_La(T) = k_La(T_R)\varepsilon^{(T-T_R)} \qquad 2.29$$

where $k_La(T)$ is the k_La value at the temperature (T) of interest and $k_La(T_R)$ is the k_La value at the reference temperature (T_R). Typical values of ε have been reported to range between 1.016 and 1.024 for stirred tank reactors (Stenstrom & Gilbert, 1981). These reported values correspond to activation energies ranging between ~19 and ~28 kJ/mol.

Solids concentration

It is important to know how the presence of solid particles affects gas-liquid mass transfer. Very few studies have been conducted to determine the effect of solids loading on mass transfer in typical hydrometallurgical leaching applications. Published work was mostly conducted on hydrogenation processes in bubble columns, where the solid particles acted as catalyst. Results generated during these studies are not necessarily representative of hydrometallurgical slurry reactors. Nevertheless, the type of solid particles (e.g., graphite, quartz, kieselguhr), particle size, solids loading and mode of reactor operation appear to be the major factors affecting the k_La value in slurry reactors.

In general, it was found that solids content up to 7~10% wt% increased the k_La value. However, when more solids were added, the k_La value decreased significantly. It was explained that a small quantity of solids may enhance the surface renewal rate without affecting the viscosity of the liquid, while a high solids loading would increase liquid viscosity and consequently lower the surface renewal rate (Lee & Foster, 1990). A decrease in the k_La value with higher solids content might also be attributed to the decrease in k_L due to a diffusion blocking effect at the gas-liquid surface (Derksen, Buist, Van Weert & Reuter, 2000). Above findings were in agreement with the outcomes of the study conducted by Van Weert, Van der Werff and Derksen (1995), in which mass transfer test work on sand (<50 μm)-water slurries in a sparged agitated tank reactor, was carried out. The results confirmed a decrease in oxygen transfer with high slurry densities. A decrease of roughly 40% in the k_La value was observed when the slurry density was increased from 10 to 40 vol.%. The behaviour of sulphide and silica mineral slurries in terms of oxygen mass transfer is of specific relevance to this study. Oxygen mass transfer coefficients in silica-water slurries were found to decrease with increasing slurry density, however, in pyrite-water slurries the effect was the opposite (Derksen et al., 2000). For the pyrite slurry, the k_La values increased by roughly 50% when the slurry density was increased to 12.7 vol.% solids, while in the silica slurry the k_La value decreased by 40% when the slurry density was increased to 15 vol.% solids. These results suggest that the k_La value measured in pyrite-containing slurries were most likely influenced by chemical enhancement (i.e., oxygen reacted with the pyrite), highlighting the difficulty of measuring the k_La value in systems where it could, potentially, be enhanced.

In general, most studies have shown that, at slurry densities less than 2 wt% solids, which are typical of what was used for the current study, the presence of solid particles has negligible effects on the magnitude of the k_La value (see, e.g., Lee & Foster, 1990). No correction for slurry density was, therefore, required in the current work.

Aqueous electrolyte solution

Zuidervaart, Reuter, Heerema, Van der Lans and Derksen (2000) provide an overview of published work about the influence of electrolytes on the rate of gas mass transfer. It has been proven that the addition of an electrolyte has an effect on the bubble coalescence frequency (Craig, Ninham & Pashley, 1993). It is understood that dissolved ions would initially decrease the rate of the bubble coalescence (which would result in smaller bubble formation and consequently increase the gas-liquid interfacial area) up to a critical concentration, above which the addition of electrolyte no longer has an effect on the k_La value (Line, Vacek & Benes, 1987). Craig et al. (1993) found this critical concentration to range between 0.006 mol/L and 0.3 mol/L for various 1-1, 1-2 and 2-2 electrolytes. However, the addition of some electrolytes, e.g., sulphuric acid, has no effect on the bubble coalescence frequency (Craig et al., 1993). The effect of electrolytes on the mass transfer rate should, thus, be investigated on a case-by-case basis.

Pressure

The effect of gas partial pressure on its solubility is well understood and was discussed in Section 2.6.5.1. Regarding the effects of gas pressure on the volumetric mass transfer coefficient, information from literature is not consistent. Various sources report a decrease in the k_La value ranging between 10 and 33% with increasing pressure (~3 to 22 bar) (Phillips, 1973; Yoshida & Arakawa, 1968). In support of this finding, Yoshida and Arakawa (1968) argued that pressure could have increased rate of surface renewal or interfacial turbulence, due to a change in surface tension caused by the increase in gas pressure.

On the other hand, an increase in k_La with increasing pressure (1 to 4 MPa) has also been recorded (Lee & Foster, 1990). They explain that increasing pressure would lower surface tension and, therefore, promote the formation of smaller bubbles, which would, ultimately, increase the gas-liquid interfacial area. A slight increase in the k_La *(*by approximately 10%) with an increase in pressure (1-3 MPa) in bubble columns has also been reported (Jin, Liu, Yang, He, Guo & Tong, 2004).

Albal et al. (1983) report that k_La was independent of pressure over oxygen pressures ranging from 1.38 to 9.65 MPa. Teramoto, Tai, Nishii and Teranishi (1974) found that the volumetric mass transfer coefficient was independent of gas pressure in the range of 10 to 50 atm. To explain this observation, they argued that, since pressure does not have an effect on the bulk physical or interfacial properties of water (i.e., the liquid phase diffusivities of water), it would not have an effect on the volumetric mass transfer coefficient (Teramoto et al., 1974). As this view is theoretically supported, it was also adopted for the current study.

Since many process variables will influence the gas-liquid mass transfer coefficient, and the fact that measurement of the actual value may be challenging, it is apparent that measured k_La values can, at most, serve as an approximation of the true value, with the associated error dependent on the measuring technique employed.

3. EXPERIMENTAL PROCEDURES

3.1. Oxygen mass transfer test work

3.1.1. Mode of aeration

It is important to consider the mode of oxygen addition (see Appendix B.3) when a closed-end laboratory pressure reactor is utilised for POX kinetic studies. Since the oxygen is not continuously vented from the reactor (which would have caused unacceptably high water loss due to evaporation) and the oxygen partial pressure had to be maintained constant during each batch POX test, the oxygen flow rate into the reactor decreased as each kinetic test proceeded. Therefore, if the oxygen had to be sparged into the reactor via a tube which is submerged in the slurry, the k_La value would have changed during the batch POX test.

To ensure that the k_La value was consistent throughout the batch pyrite POX campaign, as well as throughout the duration of each batch pressure oxidation test, oxygen gas was introduced directly into the head space of the reactor. In this way the gas-liquid interfacial area, which is created by the vortex of the slurry/solution during agitation, can be maintained constant for a selected impeller speed and configuration. All oxygen mass transfer test work was, thus, also performed with this mode of oxygen addition, to enable measurement of the k_La value under the exact same conditions as that used during the batch POX test work.

3.1.2. Geometry of reactor and reactor internals

During the course of the gas-liquid mass transfer work, the exact impeller spacing was changed and an additional inductor impeller was added to the impeller shaft. Altogether, three different arrangements were investigated. The exact positioning of the impellers in the 2 gallon Parr reactor and the liquid level that was employed (~5000 mL), is shown in Figure 3.1. The associated impeller dimensions and measured spacing between the impellers are included in Table 3.1.

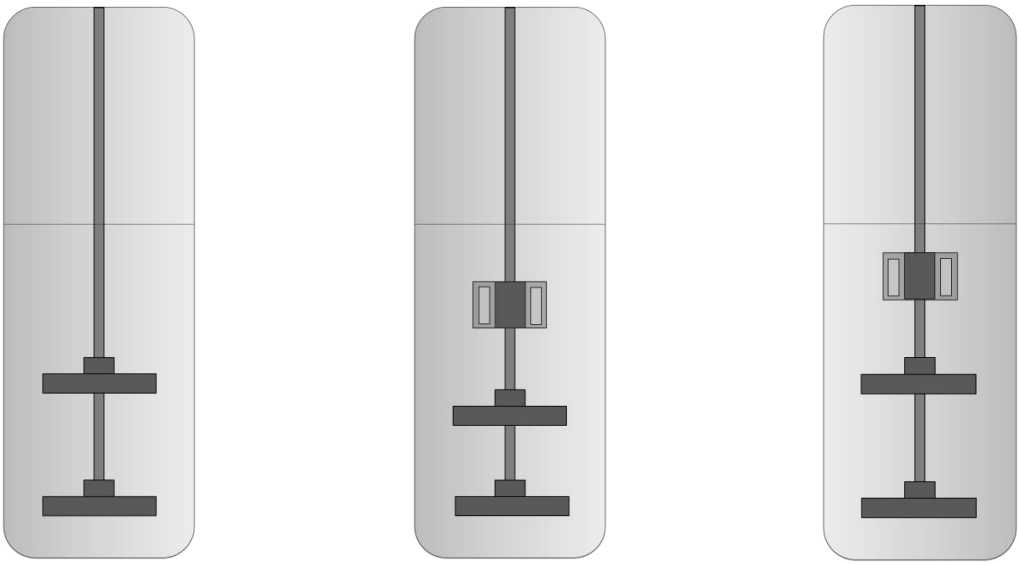

Arrangement A *Arrangement B* *Arrangement C*

Figure 3.1: Impeller and inductor arrangements assessed during this study

Table 3.1. Reactor geometry and impeller spacing

General		
Reactor diameter	152	mm
Reactor height	449	mm
45° pitch blade impeller diameter	93	mm
45° pitch blade impeller height	23	mm
Inductor diameter	60	mm
Inductor height	37	mm
Impeller spacing Arrangement A		
Distance between bottom and top impeller	128	mm
Impeller spacing Arrangement B		
Distance between bottom and top impeller	117	mm
Distance between top impeller and inductor	103	mm
Impeller spacing Arrangement C		
Distance between bottom and top impeller, mm	130	mm
Distance between top impeller and inductor, mm	110	mm

The addition of the third impeller to the system was intended to enhance the gas-liquid mass transfer rate by promoting gas induction at the gas-liquid surface. The results and motivation for taking this approach are provided in Section 4.1.

3.1.3. Indirect sulphite oxidation method

3.1.3.1. Experimental procedure

The theoretical basis for using the indirect sulphite oxidation method was provided in Section 2.6.5.3. To identify the region where the rate of the reaction with oxygen had been equal to the rate of physical absorption, an empirical approach was followed, i.e., the increase in absorption rate with increasing cobalt catalyst concentration was measured. Recall from Section 2.6.5.3 that a log-log plot of the measured k_La value *vs.* cobalt catalyst concentration should yield a distinct inflection point that is indicative of the physical oxygen absorption rate being identical to the sulphite oxidation reaction rate. The sulphite depletion rate measured in this physical absorption kinetic region may be regarded as a reflection of the 'true' gas-liquid mass transfer coefficient.

The method, thus, involved measuring the rate at which a sodium sulphite solution is oxidised to sodium sulphate. Doing so yielded the rate at which oxygen is absorbed into the solution, which, if measured in the physical absorption kinetic region, was used to determine the k_La value.

The following steps were followed during execution of this method; it is, to a large extent, based on the procedure developed by Steyl (2012: 598-599):

- A sodium sulphite solution containing 1.2 mol/kg Na_2SO_3 was prepared. The solution was poured into the reactor and contents heated to the required temperature.
- During the heating period, the reactor was stirred slowly at 100 rev/min.
- Once the operating temperature was reached, the impeller speed was increased and the required amount of cobalt catalyst injected into the solution. The catalyst-containing stock solution was prepared by dissolving cobalt sulphate heptahydrate ($CoSO_4.7H_2O$) in a predetermined amount of deionised water (see Appendix B.4). The cobalt concentrations in the sulphite solution were prepared to range between 0.05 and 10 mg/L.
- After the catalyst-containing solution had been injected, the solution was agitated for approximately five minutes to ensure homogeneity.
- Oxygen (>99.5%) was then introduced into the reactor by, either,

  A - continuously adding the gas into the reactor vapour space and venting (i.e., purging) from the reactor at a flow rate high enough to ensure complete displacement of air in the vapour phase; or

  B - by adding the required oxygen over pressure into the sealed autoclave reactor and maintaining the required oxygen pressure for the duration of the test. No venting was conducted.

- The test was then started and samples (~15 mL) were withdrawn from the reactor at dedicated time intervals. When the reactor was sealed (in Case B above), the samples were removed via the dip/sampling tube. Each sample was preceded by a "dead" sample to remove any stagnant solution remaining in the tube. The amount of sample taken at each sampling interval was kept at minimum to avoid liquid volume decrease during execution of the tests.
- The samples removed were immediately placed in an ice bath to cool the solution to room temperature and, thereafter, titrated for residual sulphate content by the iodometric back-titration method described in Appendix B.4.

The solution volume and mass were strictly controlled in each experiment to ensure experimental repeatability. Care was also taken to ensure that the concentration and volume of the solution added initially compensated for the fact that additional water was injected into the reactor with the catalyst.

An operating temperature of 50°C was selected for the sulphite oxidation tests, as operation at a slightly elevated temperature ensured that tests could be performed in a reasonable period (< 4 hours), without risking excessive evaporation of solution during the tests.

It is known that the indirect sulphite oxidation method may give rise to large errors, due to the employment of less accurate titration techniques and the possibility of having a catalyst induction period (see Ruchti, Dunn, Bourne & Stockar, 1985). In addition, a slight overestimation of the k_La value could occur due to the "chemical enhancement effect", as well as high ionic strength of the solution (see Zuidervaart et al., 2000). Therefore, values measured via this technique served only as an approximation of the order of magnitude of the volumetric mass transfer coefficient, and should be interpreted as such.

3.1.3.2. Data processing

To obtain the k_La value from the sulphite oxidation method, the oxygen consumption rate was plotted against time and a linear relationship regressed to the data points. From Equation 3.1, the slope of this linear correlation yielded the product of the k_La value and the oxygen solubility m_A^*.

$$\frac{dm_A}{dt} = k_L a m_A^* \qquad 3.1$$

The k_La value was then calculated by dividing the slope of the linear correlation by the calculated oxygen solubility. Calculation of the oxygen solubility in the sulphite/sulphate solution and the solution density, which was also required to process the data, was done according to the methods presented in Appendix C.2 and Appendix B.5, respectively.

3.1.4. Direct oxidation method

3.1.4.1. Experimental procedure

A direct method, based on measurement of the decrease in gas phase partial pressure, as previously used by Albal et al. (1983), was employed during this study. This technique involved using the relationship between the rate of oxygen gas absorption and the rate of change in oxygen partial pressure in pure water to calculate the k_La value.

The operating procedure entailed the following steps:

- The reactor was filled with the pre-determined volume of water and sealed.
- The reactor was subsequently pressurised to the required oxygen pressure and the oxygen feed valve closed.
- Agitation was then started, followed by immediate recording of the decrease in partial pressure as a function of time (at one-second intervals), until equilibrium conditions were attained, i.e., when no further decrease in partial pressure was observed.

It should, however, be noted that the direct measurement tests were performed at 20-30°C, as opposed to 50°C, which was employed during the indirect measurement tests. This was done to decrease the rate of absorption and, consequently, to allow for a longer period in which pressure measurements could be made.

The main benefit of the direct measurement is that enhancement cannot take place, as no reaction is occurring. With the pressure transducer used[f], rapid measurement was possible (response time less than 1 milli-second) and, therefore, continuous measurement could take place over a very short period of time.

In addition to the tests performed in pure water, a single test was performed in a solution representative of a typical batch pyrite pressure oxidation filtrate. The composition of the solution is provided in Table 3.2.

Table 3.2: Typical batch pyrite pressure oxidation filtrate composition

Al, mg/L	Fe(III), mg/L	Si, mg/L	H_2SO_4, mg/L
~20	~3400	~100	~38 000

[f] Ashcroft Model: G27M0105HM1000G

3.1.4.2. Data processing

The data, namely, recorded pressure vs. time measurements, was processed by assuming an ideal gas phase and conducting a total oxygen mass balance. The reasoning presented by Albal et al. (1983) was followed.

The drop in the gas phase partial pressure (p_{O_2}), after the reactor had been pressured, may be attributed solely to gas absorption into the liquid phase. Since the rate at which oxygen was transferred into the solution phase must have been equal to the rate at which it left the gas phase, the following relationship applied:

$$\frac{V_g}{R_g T}\frac{dp_{O_2}}{dt_s} = V_L k_L a(M_{O_2} - M^*_{O_2}) \tag{3.2}$$

where V_g and V_L is the volume of the gas phase and liquid phase (in m^3), respectively, R_g is the ideal gas constant (L.atm/mol.K), t_s the time in seconds and M_{O_2} the dissolved oxygen concentration (in mol/L). The equilibrium oxygen concentration ($M^*_{O_2}$) in solution may be calculated using Henry's Law and the oxygen partial pressure, as follows (assuming an ideal gas phase and an activity coefficient approaching unity):

$$M^*_{O_2} = \frac{p_{O_2}}{\mathcal{H}_{MO_2}} \tag{3.3}$$

Upon integration of Equation 3.2 and rearranging after substitution with Equation 3.3, Equation 3.4 may be derived. The time at which the gas-liquid dispersion became homogeneous was denoted as t_s'. The integration limits were the initial pressure $p_{O_{2,i}}$ at $t_s = t_s'$ and the final pressure $p_{O_{2,f}}$ at $t_s = t_s$.

$$-\ln\left(\frac{p_{O_2}(1+\alpha) - p_{O_{2,i}}}{\alpha p_{O_{2,i}}}\right) = k_L a(\alpha+1)(t_s - t_s') \tag{3.4}$$

Where $\alpha = \frac{V_L R_g T}{\mathcal{H}_{O_2} V_g}$

Also, when the system had reached equilibrium, the pressure corresponded to the final pressure ($p_{O_{2,f}}$) and the concentration of oxygen in the solution to the oxygen solubility, therefore α was defined as described by Equation 3.6 (Albal et al., 1983):

$$M^*_{O_2} = \frac{V_g}{V_L RT}\left(p'_{O_2} - p_{O_{2,f}}\right) = \frac{p_{O_{2,f}}}{\mathcal{H}_{MO_2}} \tag{3.5}$$

$$\alpha = \frac{p_{O_{2,i}} - p_{O_{2,f}}}{p_{O_{2,f}}} \tag{3.6}$$

Substitution of Equation 3.6 into Equation 3.4 then yielded the following relationship for obtaining the k_La value (Albal et al., 1983):

$$-\frac{p_{O_{2,f}}}{p_{O_{2,i}}}\ln\left(\frac{p_{O_2}-p_{O_{2,f}}}{p_{O_{2,i}}-p_{O_{2,f}}}\right)=k_La(t_s-t_s') \qquad 3.7$$

A plot of the left side of Equation 3.7 against (t_s-t_s') should yield a straight line with the slope equal to the overall volumetric mass liquid transfer coefficient. The value of t_s' was obtained by plotting the left-hand side of Equation 3.7 vs. (t_s-t_s') for several values of t' until the slope (i.e., the k_La value) did not change with (t_s-t_s').

3.2. Pyrite oxidation kinetics

3.2.1. Chemicals

All solutions were prepared by using deionised (DI) water, 98% analytical grade H_2SO_4 from ACE, $Fe_2(SO_4)_3.xH_2O$ from LABCHEM and 99.5% MgO from Axis House. The oxygen used for the study had a minimum purity of 99.5% (technical grade) and was supplied by Afrox.

The lignosulphonate-based biopolymer (L-800), used as sulphur dispersant, was supplied by Pionera.

3.2.2. Chemical and mineralogical analysis

All chemical analyses, except the iron(II) and sulphuric acid titrations (see Appendix D.1), were performed by MINTEK's Analytical Services Division. The procedures and methods are included in Appendix E. Base metals in solution were analysed via Inductively Coupled Plasma Optical Emission Spectroscopy (ICP-OES). Iron(III) in solution was calculated by subtracting the iron(II) in solution (determined by a potentiometric titration) from the total iron solution (determined via ICP-OES). Base metals in solids were also analysed by ICP-OES after fusion and acid digestion. Total sulphur and sulphide sulphur were analysed via combustion techniques. Elemental sulphur and sulphate sulphur were determined by selective dissolution with trichloroethylene and sodium carbonate, respectively.

All mineralogical analyses, X-ray diffraction (XRD) and scanning electron microscopy (SEM) followed by energy dispersive X-ray microanalysis (EDS), was conducted by MINTEK's Mineralogy Division. The corresponding procedures are included in Appendix E.

3.2.3. Experimental setup

3.2.3.1. Pressure reactor

All experiments were executed in a 2-gallon titanium grade 2 Parr reactor. The reactor internals are presented schematically in Figure 3.2. The slurry temperature was measured with a thermocouple placed in a titanium thermowell. The thermowell, which extended into the slurry, was also used as support for the stirrer shaft bracket. Heat was supplied by an external electrical heating mantle and cooling was enabled by passing cooling water through the internal cooling coils. A PID controller was used to control temperature to ±1.5°C of the target set point. The duration of the slurry heating period was ± 80 minutes. The total reactor pressure was controlled mechanically with a pressure regulator (0-60 barg) supplied by WIKA instruments. Temperature and total pressure, as well as agitation speed, was recorded online every 60 seconds using the SpecView software package. Samples were taken from the reactor via the sampling dip tube.

The reactor contents was stirred with a dual 4-pitched-blade impeller and one inductor-type impeller. Details of the exact impeller configuration investigated during the study are provided in Section 3.1.2. Agitation was controlled by the Parr controller unit to the set point ± 10 rev/min and the accuracy of the control system periodically validated by a SANAS certified tachometer. The maximum impeller speed of the system was 700 rev/min, however, the majority of the batch POX test work was conducted at 600 rev/min, as increasing the impeller speed beyond this point was not recommended by the suppliers of the motor and reactor.

All reactor internals were constructed from titanium grade 2, except for the acid injection lance. The acid injection lance was constructed from stainless steel 316 to minimise risks associated with oxygen flowing at high velocities coming into contact with titanium surfaces. The acid feed lance was located in the vapour space of the reactor and directed the acid directly towards the slurry surface.

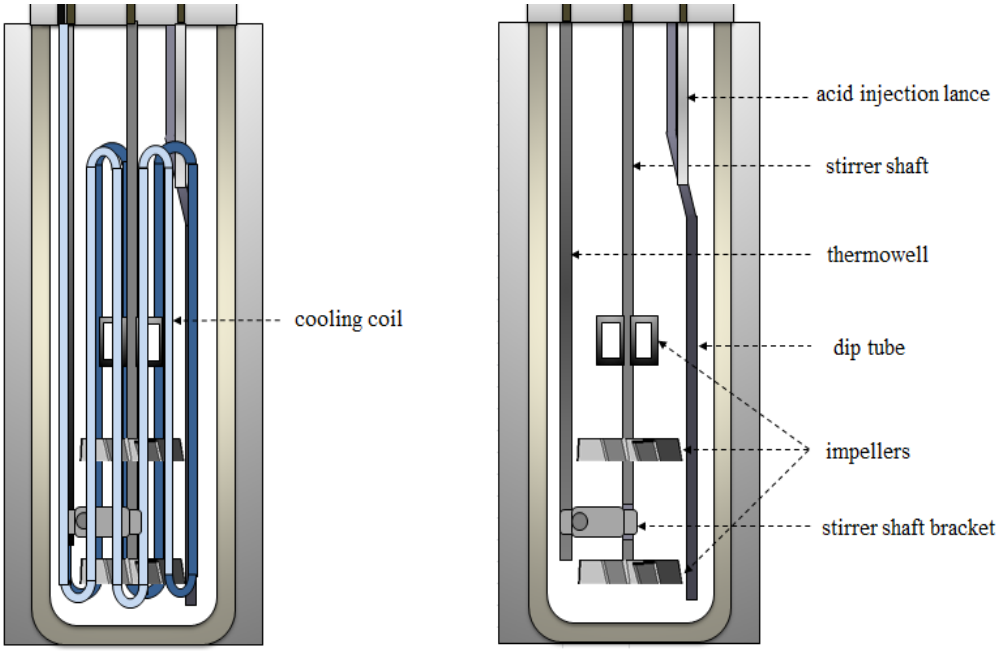

(a) with cooling coil *(b) without cooling coil*

Figure 3.2: Pressure reactor internals

3.2.3.2. Peripheral equipment

The experimental setup was equipped with a 500 mL polytetrafluoroethylene (PTFE) lined stainless steel acid injection bomb to enable acid injection into the reactor at high temperatures (> 180°C). The acid addition valve and the flexible hose, used to connect the acid bomb to the acid injection lance, were both also lined with PTFE. An 8-litre flash drum (stainless steel 316) was connected to the sample removal valve to facilitate instantaneous depressurisation of the slurry sample. An impingement plate was mounted in the flash drum to direct incoming slurry to the bottom of the drum, in this way minimising potential loss of slurry through the gas and steam vent. A schematic drawing of the experimental setup is shown in Figure 3.3.

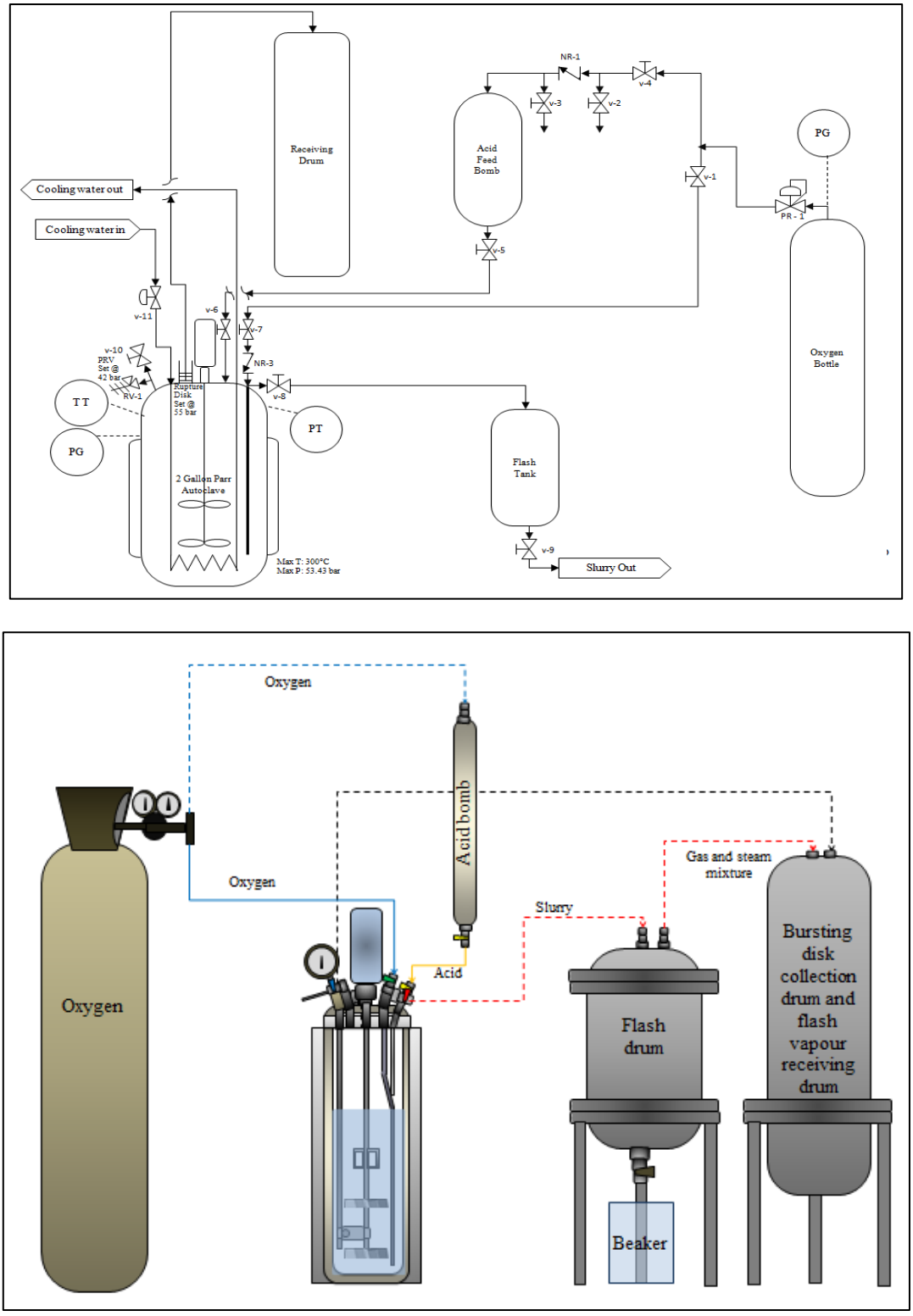

Figure 3.3: (a) Schematic drawing and (b) physical layout of experimental setup

3.2.4. Procedures and methods

3.2.4.1. Execution of tests in dilute solids suspensions

All tests were conducted at very low solids concentrations or dilute solids suspensions (< 1.5 wt%), to keep bulk acid and oxygen concentrations constant. By doing so, step changes in the oxygen and acid addition could be employed without causing secondary effects due to large changes in reagent concentrations.

3.2.4.2. Minimisation of heating and cooling effects

As a result of the long heating period (~80 minutes) of the reactor, no reagents were added to the reactor upfront. The reagents, namely, sulphuric acid and oxygen, were only added after the reactor temperature set point had been reached and was injected into the system via the acid feed bomb. In addition, the impeller speed was kept low, at 100 rev/min, during the heating period to minimise oxygen mass transfer into the slurry phase and potential pre-oxidation.

To ensure that slurry samples were truly representative of the system at the test temperature, extended cooling periods in which further oxidation could possibly occur, had to be minimised. Therefore, samples removed from the reactor were flashed into the stainless steel flash drum where the vapour-gas mixture and slurry phase were separated immediately. The flash drum was open to atmospheric pressure and, thus, the temperature instantly dropped to the solution boiling point. The slurry, which was collected from the flash drum, was subsequently pressure filtered to enable rapid solid-liquid separation.

3.2.4.3. Titanium reactor corrosion prevention

During development of the test procedure, the titanium reactor was seriously corroded several times. In one of the initial trial tests, the impeller speed was only increased to the set point impeller speed of 600 rev/min after acid and oxygen had been added, however during this test a steady increase in pressure was observed approximately 10 minutes after the time of acid addition. Only after the test was it discovered that the vessel walls had seriously corroded during the test.

It was reasoned that corrosive conditions must already have been present during the heating period to have resulted in rapid corrosion and gas formation with the onset of acid addition. During the heating period, trace amounts of oxygen in solution could have caused minor pyrite oxidation followed by iron(III) precipitation, both processes causing sulphuric acid production. In the presence of trace amounts of sulphuric acid and in the absence of any oxidising agent, pyrite could have dissolved via a non-oxidative mechanism to produce hydrogen sulphide gas. The presence of hydrogen sulphide gas

would have enhanced the reductive conditions in the system significantly and would also explain the observed rise in gas pressure. In the presence of hydrogen sulphide gas, the further addition of high concentrations of sulphuric acid most likely resulted in the observed titanium corrosion.

Even though the above arguments remained speculative, it was used as basis for altering the experimental procedure in the following manner:

- 0.1-1 g magnesium oxide, amounting to ~15-150 mg/L of magnesium in solution, was added, along with the pyrite, at the start of each test. Supported by above arguments, the objective of the magnesium addition was to neutralise any acid that may have formed during the heating period, to prevent non-oxidative pyrite dissolution. The magnesium oxide addition was reduced from 1 g to 0.05 g during the course of the campaign, to prevent possible passivating effects.
- The impeller speed was increased to the required set point value prior to the injection of acid and oxygen to the system. This was done as means of ensuring that high oxygen concentrations in the slurry are effected immediately when acid is added.

The precautionary measures listed above were effective to prevent corrosion for most of the experimental programme. Corrosion was, however, observed again in tests that were conducted subsequent to tests with pure acid solutions (~30 g/L).

Tests with pure acid solutions were incorporated in the test work programme to evaluate the possibility of iron contamination due to the corrosion of stainless steel parts and equipment in the experimental setup (see Section 3.2.4.4 for a discussion of the tests). In these tests, which followed the runs that evaluated possible iron corrosion, a distinct white titanium oxide powder was detected in the residues. The composition of the white powder was confirmed with X-ray fluorescence (XRF) and ICP-OES analysis. It was realised that the protective titanium dioxide layer was most probably damaged during the tests with pure acid solutions, causing titanium dissolution and precipitation as titanium dioxide. In an effort to promote the formation of the protective titanium dioxide layer on the reactor walls, the reactor was left in 1 wt% nitric acid solution for a period of 72 hours at room temperature. This strategy was, however, found to be ineffective, and titanium corrosion and precipitation was again evident in the tests that followed. Against this background, it was decided to add a small quantity of dissolved iron(III) (added as ferric sulphate salt) to the acid prior to injection. The amount of iron(III) added to the acid was limited to less than 25 mg/L and was accounted for in the calculation of sulphide oxidation extents. The addition of trace amounts of iron(III) salt prevented titanium corrosion for the entire duration of the remaining test work campaign.

Numerous tests were conducted to assess whether the chemicals added to prevent titanium corrosion, namely, magnesium oxide and ferric sulphate, had any influence on the reaction kinetics. The results of tests on Sample C at two residence times (5 and 10 minutes) are shown in Table 3.3. The high

degree of correlation between pyrite oxidation extents of 45 to 46% at 5 minutes and 77 to 82% at 10 minutes, despite varying magnesium oxide and ferric sulphate additions, indicated that the addition of these trace amount of salts did not have any effect on oxidation extent. Small variations between oxidation extents fell between the experimental error limits of this study and were, instead, the result of minor discrepancies in operating temperatures, operating pressures and chemical assays.

Table 3.3: Influence of MgO and $Fe_2(SO_4)_3$ addition on pyrite oxidation reaction kinetics (Sample C, 0.056 mol/kg FeS_2, 0.35 mol/kg H_2SO_4)

	Test #	MgO addition g	$Fe_2(SO_4)_3$ addition g	Impeller speed rev/min	Average temperature °C	Average pO_2 kPa	Residence time min	Fe extracted g/L	FeS_2 oxidation[a] %
Set 1	C26	0.5	0	600	199.63	709	5	1.49	46
	C34	0.5	0.445	600	201.69	661	5	1.56	46
	C38	0.1	0.445	600	201.13	676	5	1.50	45
Set 2	C1	0	0	700	202.03	600	10	2.68	80
	C25	0.5	0	600	201.60	646	10	2.70	82
	C35	0.5	0.445	600	201.65	646	10	2.66	79
	C39	0.1	0.445	600	200.96	677	10	2.59	77

[a] Calculation of pyrite oxidation based on Method 2, discussed in Section 3.2.5.

In Section 3.2.4.2 the general approach followed to minimise oxidation during the heating period was discussed. In addition to maintaining the impeller speed at a low 100 rev/min and injecting reagents at the operating temperature, magnesium oxide was added upfront, to neutralise small amounts of liberated acid (as discussed above). The degree of pre-oxidation was assessed by heating the pyrite slurry, in the presence of 0.5 g magnesium oxide, up to 200°C, followed by immediate cooling to ambient temperature again. The slurry was filtered and the solution was analysed for sulphur and iron. Any dissolved sulphur was not expected to precipitate at the measured pH value of 3.2, therefore, oxidation extent was based on sulphur in solution. As seen in Table 3.4, the solution contained 77 mg/L of sulphur, which corresponded to approximately 1.4% sulphide dissolution. This amount was considered insignificant and further strategies to mitigate oxidation during the heating period were not investigated. The fact that no iron was present in solution indicated that any dissolved iron precipitated again.

Table 3.4: Assessment of whether pyrite oxidation had occurred during the typical heating period to 200°C (0.056 mol/kg FeS_2, 100 rev/min, 0.05 g MgO addition)

	Solution chemical composition					Solution pH at 25°C	FeS_2 oxidation
	Al	Fe	Si	S	Mg		
	mg/L					(-)	%
Solution after heating to 200°C	<2	<2	<2	77	20	3.2	1.4

3.2.4.4. Evaluation of possible iron contamination and sulphuric acid evaporation

Additional tests were carried out to investigate whether any iron had been introduced into the reactor or to the final sample due to corrosion of the acid injection system or corrosion of the stainless steel flash drum. As iron in solution was the main RPV, contamination of the process slurry by iron was to be avoided as far as possible.

Two separate tests were conducted with only water and acid (no pyrite concentrate was introduced) at concentrations similar to what had been used in the batch kinetic tests.

- In the first test, acid was injected via the acid feed bomb, oxygen was introduced into the autoclave, and the test conducted for 10 minutes, followed by cooling of the entire reactor contents via the cooling coils. Thus, no flashing took place.
- In the second test, acid and oxygen were introduced as before, but the contents were flashed from the reactor at 10 minutes.

These separate tests were conducted to ensure that one would be able to identify the exact point of iron corrosion, if it had occurred. Solutions of both tests were analysed and the results are included in Table 3.5.

Table 3.5: Assessmment of whether iron was introduced into the slurry due to corrosion of stainless steel parts (0.349-0.352 mol/kg H_2SO_4, 200°C, 10 minutes)

	Solution composition			
	Al	Fe	Si	S
	mg/L			
Solution without flashing	<2	12.5	<2	13 500
Solution with flashing	<2	12.0	<2	15 600

From the test results it was evident that a small amount (<13 mg/L) of iron had been introduced into the system via the acid injection system. This amount, of 12 mg/L, was considered negligible and would not have affected the calculation of pyrite oxidation extents by more than 0.5%. Changes to the injection system to mitigate iron contamination were, thus, not considered further.

As no pyrite sample was introduced into the reactor during above tests, the quality of the mass balance around sulphuric acid could be evaluated. Sulphuric acid losses may have occurred during the tests due to the following reasons:

- During acid injection, small amounts of sulphuric acid may have remained behind in the acid feed bomb.

- Some sulphuric acid may have evaporated during the flashing process. This was, however, unlikely to be due to the low vapour pressure of sulphuric acid at the conditions employed during the test.

Results, included in Table 3.6, showed that an accountability of approximately 98% for sulphuric acid was obtained during both the tests, which was acceptable for monitoring acid concentrations as well as determining acid production by the oxidising pyrite. Since the quality of the mass balances was similar, in spite of the solution cooling method, acid losses most probably occurred during the acid injection process. At that stage, wash water had already been used to flush out the acid injection bomb after acid injection and, therefore, no further improvements could be made to increase the accountability of the acid balance. This apparent "acid loss" was accounted for in the interpretation of results.

Table 3.6: Asessment of quality of acid mass balance (0.349-0.352 mol/kg H_2SO_4, 10 minutes, 200°C, 600 rev/min)

	Acid in	Acid out	Accountability
	g		%
Test with flashing	146.3	143.2	97.9
Test without flashing	147.6	143.9	97.5

3.2.4.5. Iron precipitation

Since iron in solution served as the primary RPV, precipitation was preferably avoided during the batch POX tests. However, it should again be highlighted that, since sulphide analysis was also conducted on the POX residues, allowance was made to determine the pyrite oxidation extent, irrespective of whether precipitation occurred or not.

The data published by Umetsu et al. (1977), shown in Table 3.7, was initially utilised to provide an estimate of the allowable pyrite addition, i.e., to avoid precipitation. Provided that significantly shorter residence times (< 30 min) were employed during the batch oxidation tests at 200°C, compared to the residence times investigated by Umetsu et al. (1977) during their study of iron(III) hydrolysis, the pyrite addition was selected to ensure that the total iron in solution would not exceed 7 g/L. After the first few tests, it was confirmed by both mineralogical and chemical analysis (see Section 6.3) that no iron precipitation had occurred at the standard conditions employed during the majority of the test work campaign. At a later stage, data of Fleuriault et al. (2016) also became available, which agreed with the findings of the current study, in that it showed that an iron(III) concentration of at least 7 g/L is sustainable in solutions containing > 19 g/L free sulphuric acid at 195°C (which is close to 200°C) after 3 hours.

Table 3.7: Kinetics of $Fe_2(SO_4)_3$ hydrolysis

200°C, 30 g/L H_2SO_4 addition (Umetsu et al., 1977)	
Time, min	Iron(III) in solution, g/L
0	20
~60	~9.5-12
120	~4.5
195°C, 3 hours (Fleuriault et al., 2016)	
H_2SO_4 addition, g/L	Iron(III) in solution, g/L
5	~5
19.5	~7
40	~12

When the effect of low acid concentrations (i.e., 0.115 mol/kg or ~10 g/L) on the pyrite dissolution kinetics was evaluated, hematite and hydronium jarosite precipitation did occur; however, the pyrite oxidation was then based on the sulphide analysis in the solids (refer to Section 6.4). The different methods that were employed to calculate the oxidation extents are described in Section 3.2.5.

3.2.4.6. Final test procedures

Two methods of sample removal were employed during the test work campaign, namely, "start-and-stop" and "kinetic sampling" tests. Detailed aspects of both of these techniques will be discussed in the following sections.

3.2.4.6.1. "Start-and-stop" kinetic tests

During these tests a separate test was conducted for each kinetic data point. This method was employed for the majority of the test work campaign and was followed to achieve the following objectives:

- To eliminate sampling effects, which included changes in solution volume level and changes to solute concentrations as the test proceeded. Large variation in solution volume levels could have changed the k_La value during the course of the experiment.
- To ensure sufficient residue was generated during each test to conduct chemical assays on the solids. This allowed utilisation of solid sulphur speciation (in particular, sulphide) analysis to validate the extent of pyrite oxidation, thereby not relying solely on dissolved iron analysis as RPV. This approach also enabled tests to be conducted at low acid concentrations and high slurry densities without having to avoid iron precipitation, which would interfere with the interpretation of kinetic data.
- To ensure that sufficient residue was available for subsequent mineralogical analysis, namely, XRD and SEM at each kinetic data point.

Each “start-and-stop” test was conducted according to the following detailed procedure:

- The initial slurry was prepared by mixing the pre-weighed amount of pyrite concentrate and DI water in the reactor. The required amount of magnesium oxide was also added to the slurry.
- The reactor was sealed and heated to the desired set point temperature while the impeller was stirring slowly at 100 rev/min.
- During the heating period, a small amount of ferric sulphate salt (0.446 g) was dissolved into 20 mL of DI water and added to the pre-weighed required quantity of 98 wt% sulphuric acid. The acid solution was then transferred to the acid feed bomb.
- Once the reactor had reached temperature, the impeller speed was adjusted to the set point speed and the acid injected into the reactor with 300 kPa of oxygen.
- Immediately after the acid had been injected, a predetermined amount of wash water (80 mL) was added to the acid bomb and injected into the reactor with oxygen, bringing the autoclave to the final set point total pressure. Wash water was added to flush the acid feed bomb.
- Once the reactor had reached the total operating pressure, the test was officially started.
- On average, the period from when the agitation speed was increased until the total pressure was reached ranged between 1 and 2 minutes.
- During the actual test, temperature was controlled and the oxygen pressure maintained by feeding gas to the vessel continuously with the oxygen regulator.
- When the test was completed, a portion of the slurry (approximately half the sample) was flashed from the reactor by opening the sample removal valve, and collected into the flash drum. The sudden decrease to atmospheric pressure resulted in vapour-gas mixture separation from the slurry and a slurry temperature drop to the solution boiling point.
- Upon opening of the sample removal valve, oxygen feed to the system was stopped and the reactor immediately cooled to prevent further oxidation of the sample during the flashing process.
- The sample was subsequently removed from the flash drum and immediately filtered in a pressure filter, to separate the residue and solution.
- The filtrate was collected and rapidly cooled to 25°C in an ice bath, after which the iron(II) and free sulphuric acid titration were conducted (refer to Appendix D.1 for the procedure and comments on the accuracy of the titrations).
- The residue was thoroughly washed with pH 2 adjusted water by repulping, followed by a displacement wash with DI water.
- The residue was air-dried overnight and submitted for total sulphur, sulphide sulphur, sulphate sulphur, elemental sulphur and ICP base metal analysis.
- The filtrate was submitted for ICP base metal analysis.

- The slurry remaining in the autoclave was cooled to 30°C, removed and vacuum filtered. The residue was washed with pH 2 adjusted water by repulping and once with DI water in a displacement wash. The filtrate and residue of this sample was only occasionally submitted for chemical analysis to validate the mass balance.
- The amount of water, required acid and concentrate were calculated to ensure that a constant liquid volume was maintained during all tests (taking into account the effect of electrolyte composition and temperature). This was done in light of the fact that liquid volume had proven to have a major influence on the k_La value of the autoclave, as will be discussed in Chapter 4.

It should be emphasised, from the above procedure, that only half of the sample was removed from the reactor at the end of each test. The reason for doing so was that the reactor required a cooling medium (contact with the cooling coils) to decrease the temperature. In other words, a portion of the slurry had to remain behind to ensure that the reactor could be cooled and vented safely. Two residues and solution samples were, therefore, generated during each test.

3.2.4.6.2. Kinetic sampling tests

Towards the end of the test work campaign, a number of tests were conducted where kinetic samples were taken instead of the more accurate "start-and-stop" kinetic tests. This was done to maximise the use of the remaining sample mass. During these tests, 30 mL slurry samples were removed from the reactor at dedicated time intervals. Except for the fact that samples were intermittently removed from the reactor, the procedure employed for these tests was identical to the "start-and-stop" test procedure (which was described in Section 3.2.4.6.1). A small "dead" sample (~10 mL) was also taken prior to taking each kinetic sample, to remove any stagnant solution from the dip tube and sampling line.

This method was inherently associated with undesired large pressure fluctuations and a large decrease in solution volume over the duration of the test.

3.2.4.6.3. Comparison between "start-and-stop" and kinetic sampling tests

The similarity of batch kinetic test results conducted by employing the different test methods are illustrated in Figure 3.4. Here, fractional pyrite conversion as a function of time was plotted with the detail on the calculations used to process the results provided in Section 3.2.5.

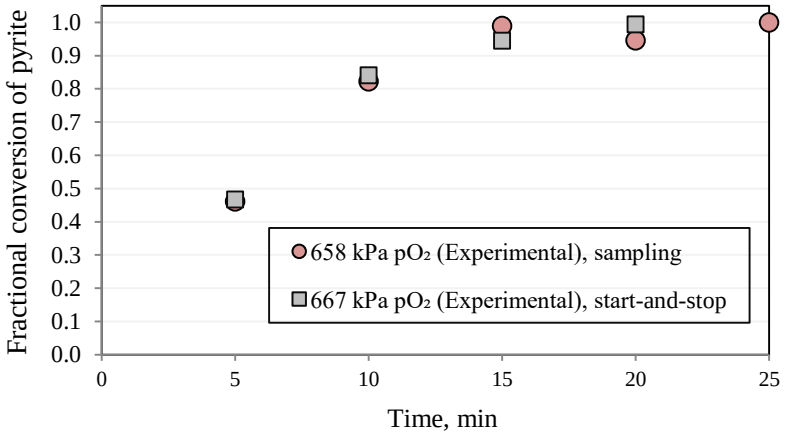

Figure 3.4: Comparison of results of start-and-stop and kinetic sampling tests using Sample D (-75+53 µm) (Experimental conditions: 0.35 mol/kg H_2SO_4, 201.6°C, 0.054 mol/kg FeS_2, 600 rev/min)

From the results it was clear that the test methods corresponded to within 5% of each other, which fell within the experimental error of this study. This meant that both sampling techniques could be used during the test work campaign. However, higher confidence was still associated with the start-and-stop tests, especially when more than five samples (>150 mL) were removed from the reactor during kinetic sampling, as this would significantly change the slurry volume.

3.2.4.7. Repeatability of batch kinetic tests

The repeatability of start-and-stop batch kinetic tests was evaluated by duplication of tests. The results of three data sets, each involving two duplicates, are included in Table 3.8.

Table 3.8: Repeatability of test work (201.5-202°C)

	Repeat	Test #	Time	pO_2	Total Fe	Fe(II)	H_2SO_4	Fe residue	FeS_2 conversion based on Fe in solution	
									Method 2[a]	Method 1[b]
			min	kPa	g/L	g/L	g/L	wt%	%	%
Set 1	1	C43	2	664	1.08	0.8	37.0	27.3	30	33
	2	C44	2	704	1.01	0.9	37.2	27.5	32	31
Set 2	1	D3	5	673	1.47	1.2	43.6	29.9	44	44
	2	D8	5	673	1.62	1.4	44.5	30.0	45	49
Set 3	1	D22	15	644	3.05	2.1	39.7	4.4	93	92
	2	D20	15	627	3.26	1.8	39.7	6.2	94	98

[a & b] *Method 1 and 2 calculations discussed in Section 3.2.5.*

Reasonable agreement between total iron, iron(II) and sulphuric acid concentration in solution was observed for all duplicate tests. In addition, iron content in the residues was comparable.

Pyrite oxidation extents agreed within 6% to one another, irrespective of the calculation methodology employed. The repeatability was, therefore, found to be acceptable for the purpose of the batch oxidation work.

3.2.5. Data processing

Since the "start-and-stop" test method allowed residue as well as solution samples to be collected from the reactor at each kinetic data point, the reaction progress could be based on either iron and sulphur concentration in solution or iron and sulphide content remaining in the residue as RPV. The experimental procedure also allowed conduction of a mass balance around the major elements in the concentrate, namely, silica, aluminium, iron and sulphur.

3.2.5.1. Oxidation extent

For calculation of oxidation extent, it was assumed that the slurry sample, which was taken by flashing approximately half the reactor contents, was fully representative of the reactor contents at the time of removal. Since only a portion of the slurry was removed, the total residue mass (remaining in reactor as well as that flashed out) and total filtrate volume (remaining in reactor as well as that flashed out) at the time of removal, assuming that the total reactor content was finally removed from the reactor, had to be calculated. The calculation of the total filtrate volume and residue mass after flashing for a single batch kinetic test, therefore, proceeded by assuming an elemental accountability (EAC) of 100% on both iron and sulphur and solving the two unknown variables, namely, filtrate

volume and dry residue mass. It should be noted that one had a fairly good estimate of these unknown variables, as the actual flashed filtrate volumes and residue masses were recorded.

The calculated values were then double-checked by evaluating both silica and aluminium EAC. The EAC was calculated as follows:

$$EAC\ (\%) = \frac{w_{i:conc} + w_{i:acid}}{w_{i:fil} + w_{i:res}} \times 100\% \qquad 3.8$$

where $w_{i:conc}$ is the mass of element *i* in the pyrite concentration, $w_{i:acid}$ is the mass of element *i* in the concentrated sulphuric acid added, $w_{i:fil}$ is the mass of element *i* in the filtrate and $w_{i:res}$ the mass of element *i* in the flashed residue.

After the total flashed volume and residue masses had been established, calculation of the fractional conversion of pyrite by the four different methods was enabled. The different methods are listed below.

Method 1: Based on iron content in pyrite concentrate and iron extracted into filtrate

$$FC\ (\%) = \frac{w_{Fe:fil}}{w_{Fe:conc}} \times 100\% \qquad 3.9$$

Method 2: Based on iron concentration ($m_{Fe:fil}$) in filtrate at time t and iron concentration in solution after complete pyrite conversion was obtained ($m_{Fefinal:fil}$)

$$FC\ (\%) = \frac{m_{Fe:fil}}{m_{Fe_{final}:fil}} \times 100\% \qquad 3.10$$

Method 3: Based on iron content in pyrite concentrate and residue

$$FC\ (\%) = \frac{w_{Fe:conc} - w_{Fe:res}}{w_{Fe:conc}} \times 100\% \qquad 3.11$$

Method 4: Based on sulphur content in pyrite concentrate and residue

$$FC\ (\%) = \frac{w_{S_2^{2-}:conc} - w_{S_2^{2-}:res}}{w_{S_2^{2-}:conc}} \times 100\% \qquad 3.12$$

Based on the results of the different calculation methodologies, it was found that Method 1 and Method 2 exhibited the highest degree of correlation between the methods, as well as the highest degree of repeatability between two tests. Both of these methods rely on the iron content in solution, with Method 1 based on the iron content in the pyrite feed concentrate and in the filtrate, and Method 2 based on the concentration of iron in solution expressed as a portion of the total iron concentration in solution after complete oxidation had been attained.

Even though methods based on solids analyses, namely Methods 3 and 4, served as a valuable cross-check, they were less reliable. This observation is thought to be related to segregation effects in the reactor, which caused heavier pyrite particles to be preferentially extracted from the reactor. Lighter quartz and pyrophyllite particles were probably located in the top portion of the slurry and, since the dip tube extended to the bottom of the reactor, the extraction of heavier particles were favoured. This notion was supported by the fact that samples containing less quartz and pyrophyllite exhibited a higher degree of correlation when oxidation extents were based on the different methods (as discussed above).

It should be noted that only Methods 1 and 2 were used to calculate fractional conversion when the kinetic sampling technique, discussed in Section 3.2.4.6.2, were employed for the batch kinetic tests. This was done because solids analysis was not conducted on the kinetic residues because of insufficient solids collected.

In summary, the oxidation extent of each test and each data point was scrutinised by taking all calculated results into account. The fractional conversion of each test, based on the four calculation methods, is included in Appendix D. Outliers were easily identified and were not considered in the reporting of the final results.

3.2.6. Calculation of oxygen partial pressure and other physical constants

The water vapour pressure (in gauge) was calculated by subtracting the atmospheric pressure[g] (p_{atm}) from the absolute water vapour pressure ($p_{w(abs)}$). The water vapour pressure is a function of temperature and was calculated by the procedures provided in Appendix C.7. The oxygen over pressure (p_{ovp}) was taken as the total pressure ($P_{total(g)}$) (recorded by the electronic pressure transducer in gauge pressure) minus the corresponding water vapour pressure in gauge. The calculation is shown in Equation 3.13:

$$p_{ovp} = P_{total(g)} - (p_{w(abs)} - p_{atm}) \qquad 3.13$$

The true oxygen partial pressure (p_{O_1})was taken as the over pressure plus the oxygen pressure present in atmospheric gas (approximated as 21 vol%). This fraction of oxygen (17 kPa) had to be accounted for, as the reactor was not vented with nitrogen prior to heating and, thus, the oxygen associated with atmospheric gas remained in the reactor vapour space.

$$p_{O_2} = p_{ovp} + (0.21 \times p_{atm}) \qquad 3.14$$

[g] The atmospheric pressure in Randburg, South Africa, is 83 kPa at 1753 m above sea level.

The use of the pure water vapour pressure (calculated by equations presented in Appendix C.7), as opposed to the solution vapour pressure, is supported by the fact that solutions up to 3 mol/kg H_2SO_4 still have activities exceeding 0.98 (Holmes & Mesmer, 1992).

The solution density was also required during experimental planning, to provide an estimate of solution volume at the operating temperatures employed (namely, 180 to 210°C). This was, in turn, required to ensure that all tests were conducted at identical starting liquid volumes. To enable prediction of the solution density, both temperature and solution composition were accounted for. In addition, the solution density was required to convert between the molarity and molality species concentration units. The correlations and underlying assumptions to predict solution volume and vapour pressure are provided in Appendices C.6 and C.7.

3.2.7. Test work matrix

The effects of temperature, oxygen over pressure, acid concentration, slurry density and particle size were tested on the pyrite concentrate after it had been screened into narrow size fractions. The characterisation of the individual size fractions is included in Chapter 5. The temperatures (180 to 210°C), oxygen over pressures (480-1130 kPa) and acid concentrations (10-50 g/L corresponding to 0.115-0.59 mol/kg H_2SO_4) are typical of industrial operation. The different test series are outlined in Table 3.9 and Table 3.10 where the shaded blocks indicate the variables tested in the specific series of tests. The 'baseline' test condition was 200°C, 30 g/L (or 0.35 mol/kg) H_2SO_4 and ~670 kPa pO_2. Log sheets for all tests are included in Appendix D.

Notable from the test work matrix is the varying partial pressures which were measured in test series where oxygen partial pressure should have been kept constant. This is the direct result of the insensitivity of the pressure regulator used to control pressure very accurately within the very short time intervals at pressures typically employed during this study (ranging between 16 and 27 barg total pressure) as well as the fact that each kinetic point was done as a separate test (refer to Section 3.2.4.6.1). The approach that was followed was to minimise venting which could in turn cause solution volume and species concentrations changes. Thus, if during the oxygen addition period the pressure was slightly overshot, no venting was done and the test left to continue at the initial pressure. The pressure was recorded throughout the test and during data interpretation converted to the dissolved oxygen concentration via Tromans' relationship (see Appendix C.2) and corrected with the measured dependence in oxygen concentration. Each batch kinetic curve, with the corresponding measured average pressure, was included as an individual data series during the model regression - in this way accounting for the pressure fluctuations when the rate dependencies were investigated.

Table 3.9: Test work matrix (effect of temperature, partial pressure, sulphuric acid addition and slurry density)

Test series number	Batch curve number	Particle size fraction used	Temperature	pO_2	H_2SO_4 addition	FeS_2 addition	Test type
		µm	°C	kPa	mol/kg	mol/kg	
1	PO1, PO2 PO3 PO4, PO6, PO7, PO8 PO5	+38-53	181 191 202 211	695[h] 796 662[i] 622	0.35	0.054	Start-and-stop Kinetic sampling Start-and-stop Kinetic sampling
2	PO9 PO4, PO6, PO7, PO8 PO10, PO13	+38-53	201	516 662[j] 1109, 1031	0.35	0.054	Start-and-stop Start-and-stop Start-and-stop & Kinetic sampling
3	PO11 PO4, PO6, PO7, PO8 PO12	+38-53	201	495 662[k] 558	0.115 0.35 0.59	0.054	Start-and-stop Start-and-stop Start-and-stop
4	PO16 PO14, P020, PO21 PO15	+53-75	201	483 667, 657, 659 1027	0.35	0.057	Start-and-stop Start-and-stop & Kinetic sampling Start-and-stop
5	PO18 PO14 PO17	+53-75	201	630 667 659	0.115 0.35 0.59	0.057	Start-and-stop Start-and-stop Start-and-stop
6	P014 PO19	+53-75	201	667 678	0.35	0.0568 0.1149	Start-and-stop Start-and-stop
7	PO24 PO22, PO23	+75-106	182 201	668 656[l]	0.35	0.089	Start-and-stop Start-and-stop

[h] Average pressure between PO1 and PO2 batch kinetic curves

[i] Average pressure between PO4, PO6, PO7, PO8 batch kinetic curves

[j] Average pressure between PO4, PO6, PO7, PO8 batch kinetic curves

[k] Average pressure between PO4, PO6, PO7, PO8 batch kinetic curves

[l] Average pressure between PO22 and PO23 batch kinetic curves

Test series number	Batch curve number	Particle size fraction used µm	Temperature °C	pO_2 kPa	H_2SO_4 addition mol/kg	FeS_2 addition mol/kg	Test type
8	PO25 PO22, PO23 PO26	+75-106	201	484 656[m] 841	0.35	0.091	Start-and-stop Start-and-stop Start-and-stop
9	PO27 PO28 PO29	+106-150	201	476 669 1127	0.35	0.050	Kinetic sampling Kinetic sampling Kinetic sampling

Table 3.10: Test work matrix (effect of particle size)

Test series number	Particle size µm	Temperature °C	pO_2 kPa	H_2SO_4 addition mol/kg	FeS_2 addition mol/kg	Test type
10	+38-53 +53-75 +106-150	201	1127, 1027, 1109 669, 667, 662 476, 483, 516	0.35	0.054 0.057 0.050	Start-and-stop Start-and-stop Kinetic sampling

[m] Average pressure between PO22 and PO23 batch kinetic curves

4. GAS-LIQUID MASS TRANSFER

In the context of the current fundamental study on pyrite oxidation kinetics it is important to have a quantitative description of the aqueous oxygen concentration, which is very difficult to measure at POX conditions, throughout the duration of the pyrite oxidation batch tests. The aim of the gas-liquid mass transfer work was thus to determine the oxygen gas-liquid mass transfer coefficient in the 2 gallon Parr reactor which was used to simulate the aqueous oxygen concentration during batch data regression (Chapter 7).

4.1. Indirect sulphite oxidation method

4.1.1. Identification of the correct kinetic regime for gas-liquid mass transfer tests

To enable identification of the 'physical absorption regime' during employment of the indirect sulphite oxidation method, the catalyst concentration was varied between 0.1 and 10 mg/L. During these tests the reactor was kept sealed, an oxygen pressure (209-223 kPag) was applied and the impellers configured according to Arrangement A. The conditions of these tests and the associated test results are included in Table 4.1 and presented graphically in Figure 4.1. The characteristic log-log plot (see Figure 4.1b), which is usually shown when the sulphite oxidation method is used, is also included in Figure 4.1.

Table 4.1: Influence of catalyst concentration on rate of O_2 absorption to identify correct kinetic regime for gas-liquid mass transfer (O_2 introduced under pressure, sealed reactor)

Agitator Speed	500	rev/min
Temperature	50	°C
Initial volume	5028	mL
Impeller arrangement	Twin impellers (A)	
Oxygen gas purity	99.5	wt%

Test #	**k_La, 1/min**	**[Co], mg/L**	**Pressure, kPag**	**O_2 solubility, mg/kg**	**Slope, mg/kg.min**
MT10	1.4	0.1	229	31.1	43
MT9	1.3	0.1	229	31.1	41
MT11	2.2	1.0	209	28.4	61
MT13	2.2	5.0	223	30.2	65
MT12	5.6	10.0	223	30.2	167

From the results shown in Table 4.1 and Figure 4.1, the k_La value was largely independent of catalyst concentration between 1 and 5 mg/L [Co] with measured oxygen absorption rates ranging between 61 and 65 mg/kg.min. The corresponding inflection point was also evident between 1 and 5 mg/L [Co] as shown in Figure 4.1b. Within this range, the k_La value was approximately 2.2 min^{-1} at 50°C.

The drastic increase in the measured rate when the catalyst concentration was increased to 10 mg/L was unmistakeably due to chemical enhancement.

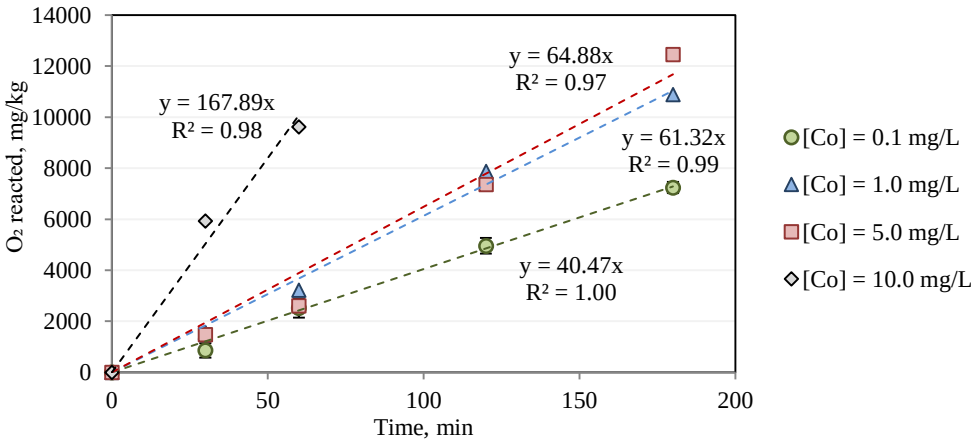

(a)

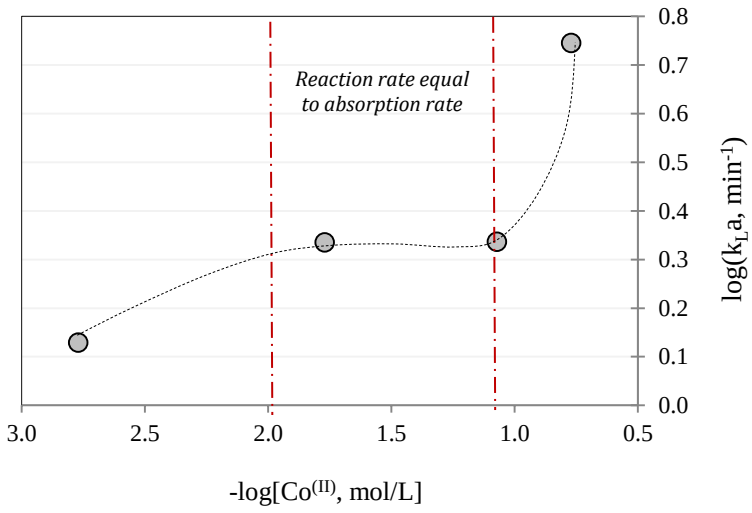

(b)

Figure 4.1: Identification of correct kinetic regime for gas-liquid mass transfer (a) Influence of $Co^{(II)}$ concentration on oxygen reacted over time (b) Log-log plot for identification of correct kinetic regime ([Na_2SO_3] initial = 1.2 mol/kg, 2 gallon Parr reactor, Impeller arrangement A, 500 rev/min, Initial volume 5028 mL, 50°C, 1 bar(g) pO_2)

To obtain confidence in the range of catalyst concentrations identified for accurate determination of the k_La value and to evaluate the potential of improving the k_La value by introduction of an inductor impeller, a second set of tests were conducted. The catalyst concentrations were varied between 0.06 and 8.13 mg/L and the impeller speed increased to 600 rev/min. In addition, the reactor was continuously purged and vented with oxygen as opposed to previous test work where the reactor was pressurised. This decision was mainly supported by challenges experienced in accurate pressure

measurement and control at such low pressures. Detailed test results are included in Table 4.2 and Figure 4.2.

Table 4.2: Influence of catalyst concentration on rate of O_2 absorption to identify correct kinetic regime for gas-liquid mass transfer (atmospheric pressure, continuous venting of O_2, open reactor)

Agitator Speed	600	rev/min
Temperature	50	°C
Initial volume	5 000	mL
Impeller arrangement	Twin Impellers and Inductor B	
Oxygen gas purity	99.5	wt%

	k_La, 1/min	[Co], mg/L	O_2 solubility, mg/kg	Slope, mg/kg.min
MT19/20	1.76	0.06	9.49	16.67
MT21	2.692	0.54	9.49	25.56
MT22	3.275	2.70	9.49	31.09
MT23	3.426	5.44	9.49	32.52
MT28	3.851	8.13	9.49	36.56

As seen from the rate of oxygen reacted plots (Figure 4.2a), the results suggested that the inflection point most likely ranged between 0.5 and 5 mg/L as the measured oxygen absorption rates in this regime did not vary appreciably i.e., from 26 to 33 mg/kg.min. Within this range the k_La value ranged between 2.7 and 3.4 min^{-1} (at 50°C). This result agrees with the previous identified reaction regime when the tests were conducted under oxygen pressure. In view of the above findings and to eliminate overestimation of the k_La value, all further mass transfer experiments were conducted with the addition of 0.54 mg/L cobalt catalyst.

The addition of the inductor impeller and the increase in agitation speed appeared to have only slightly increased the k_La value from ~2.2 min^{-1} to ~2.7-3.4 min^{-1}. This result meant that the inductor impeller was still submerged too far beneath the liquid surface to produce significantly higher surface renewal rates and/or to allow gas induction and subsequent dispersion for improved gas-liquid mass transfer. Subsequent optimisation studies were thus conducted.

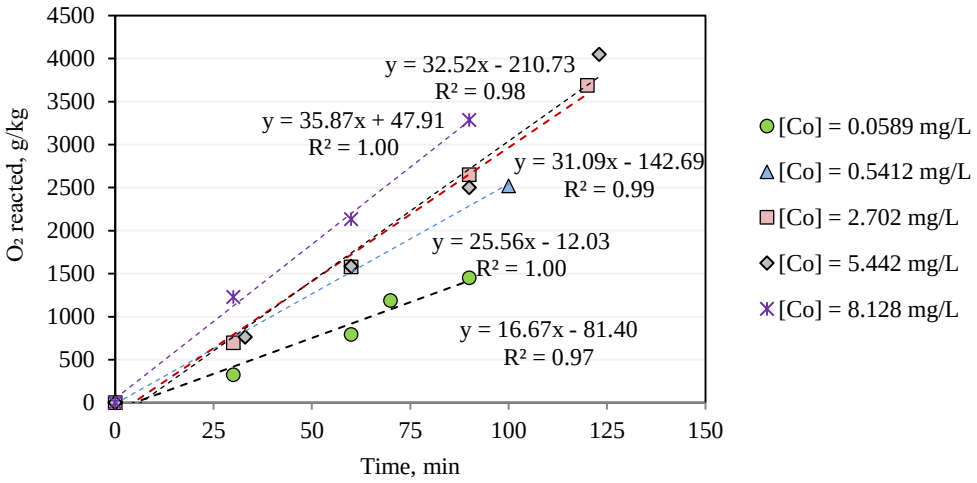

(a)

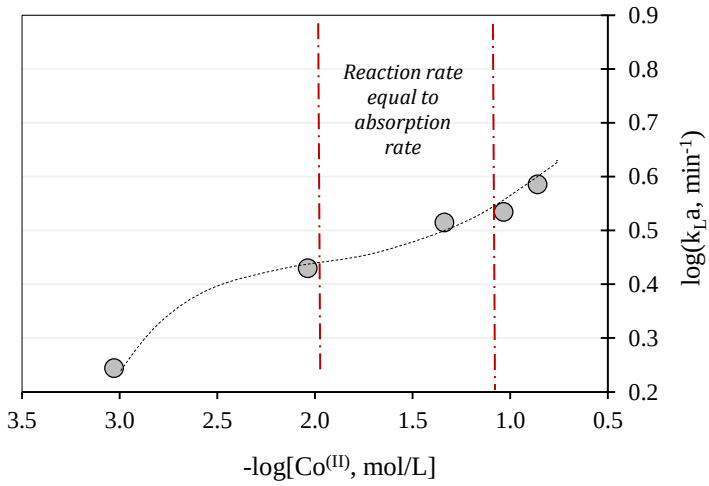

(b)

Figure 4.2: Identification of correct kinetic regime for gas-liquid mass transfer (a) Influence of $Co^{(II)}$ concentration on oxygen reacted over time (b) Log-log plot for identification of correct kinetic regime ([Na_2SO_3] initial = 1.2 mol/kg, 2 gallon Parr reactor, Impeller arrangement B, 600 rev/min, Initial volume 5000 mL, 50°C, continuous venting, atmospheric pressure)

4.1.2. Optimisation of gas-liquid mass transfer rate

Different starting liquid volumes, impeller speeds and impeller arrangements were tested during the optimisation work. The results of these tests are included in Table 4.3 with the measured rate of oxygen reacted over time and a graphical depiction of the measured k_La values included in Figure 4.3.

Table 4.3: Measured oxygen absorption rate at various impeller configurations, impeller speeds and initial starting volumes to optimise gas-liquid transfer in the 2 Gallon Parr reactor

[Co]	0.5	mg/L
Temperature	50	°C
Oxygen gas purity	99.5	wt%

Test Number	Initial volume	Agitator speed	Impeller arrangement	k_La	[Co]	O_2 solubility	Slope
	mL	rev/min	-	1/min	mg/L	mg/kg	mg/kg.min
MT 10, 9, 11	5045	500	A	2.2 a	0.1-1 a	23.4 b	51.5
MT16	5068	600	B	1.8	0.54	9.49	17.1
MT21	5000	600	B	2.7	0.54	9.49	25.6
MT 17, 18	4873	600	B	3.7 b	0.56	9.49	34.9
MT 14, 15	5068	700	B	6.8 c	0.54	9.49	67.7
MT29	5000	600	C	8.7	0.54	9.49	82.4

[a]Average of tests conducted at [Co] concentrations ranging between 0.1 and 1 mg/L. Measured k_La value ranged between 1.74 and 2.71 min^{-1}. Tests conducted under 1 bar(g) oxygen pressure [b]Average between 3.64 and 3.74 min^{-1} [c] Average between 6.7 and 7.2 min^{-1}

The most significant finding from these results was that the initial liquid volume had a considerable effect on absorption rates. This is evident when comparing the results of tests MT 16, MT 21 and MT 17&18. By decreasing the starting volume from 5068 mL to 4873 mL, the gas-liquid mass transfer rate was increased from 1.8 to 3.7 min^{-1}. This finding confirmed that a large distance between the liquid surface and the top impeller during reactor operation would impact the absorption rates negatively. In addition, the importance of strict initial solution volume control during the actual execution of batch pyrite pressure oxidation tests to eliminate variation in k_La values, was highlighted.

The absorption rate was increased further by increasing the impeller speed to 700 rev/min (see tests MT 14&15) and an improved k_La value was obtained (6.8 min^{-1}), however operation at agitator speeds exceeding 600 rev/min is not recommended by the suppliers of the motor and reactor.

Mass transfer tests with impeller Arrangement C, where the inductor and second impeller were moved up further on the stirrer shaft by 10 mm, resulted in the highest oxygen absorption rate with an associated k_La value of 8.7 min^{-1} at 50°C. Therefore, the k_La value was increased by a factor of three compared to the initial measured k_La value during the optimisation work. Arrangement C with an impeller speed of 600 rev/min was thus adopted for the pyrite batch oxidation test work.

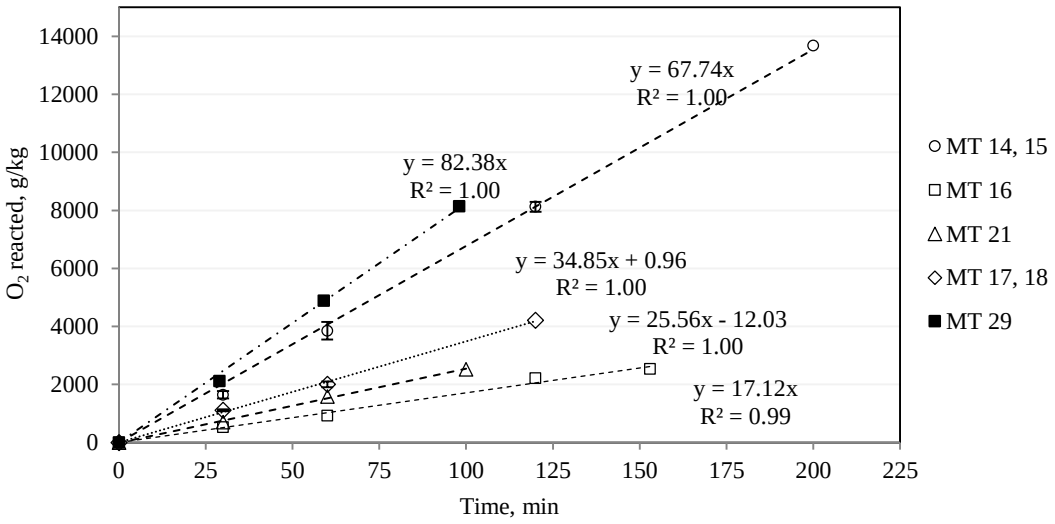

Figure 4.3: Optimisation of gas-liquid mass transfer rates by varying impeller configurations, impeller speeds and initial starting volumes: Oxygen reacted over time ([Na_2SO_3] initial = 1.2 mol/kg, 2 gallon Parr reactor, 50°C, 0.55 mg/L Co^{2+})

4.2. Direct method

Due to the importance of the k_La value in calculating the dissolved oxygen concentration, validation of the previous results by employing a direct method was required. The technique of Albal et al. (1983), described in Section 3.1.2, was used. The main benefits of the direct method are elimination of k_La value enhancement by chemical reaction as well as the fact that a constant liquid volume can be maintained for the duration of the test as no sampling is required.

The effect of initial volume and temperature on the k_La value in pure water was tested. In addition, the k_La value in the filtrate of a typical batch pyrite oxidation test was measured. The results are summarised in Table 4.4.

Table 4.4: Oxygen mass transfer measurements with the direct method

Agitator Speed	600	rev/min
Impeller arrangement	Twin Impellers and Inductor (C)	
Oxygen gas purity	99.5	wt%
t_s' [a]	3	s

Test #	Initial volume	Temperature	Initial pressure	Final pressure	k_La	k_La
	mL	°C	barg	barg	s^{-1}	min^{-1}
MT30	4804	20	19.88	18.62	0.077	4.6
MT31	4804	20	20.05	18.58	0.067	4.0
MT32	4904	20	21.76	19.97	0.062	3.7
MT33	4904	20	20.97	19.46	0.059	3.5
MT34	5004	20	20.16	18.35	0.047	2.8
MT35	5000	30	19.51	18.27	0.060	3.6
MT36	5104	20	19.95	18.23	0.033	2.0
MT37	5204	20	19.83	18.06	0.019	1.1
MT38b	5000	20	19.31	18.06	0.100	6.0
MT39	5000	45	20.28	19.34	0.068	4.1
MT40	5000	65	20.44	19.00	0.093	5.6

a – t_s' is the time at which the gas-liquid dispersion becomes homogeneous (see Equation 3.4)

b – conducted in typical batch pyrite pressure oxidation solution (see Table 3.2 for chemical composition)

In all tests performed an almost linear correlation (*R-squared* values close to unity) was observed when the left-hand side and right-hand side of Equation 3.7 was plotted against one another by using the recorded pressure measurements (see Appendix B.8 for raw data). It was found that t_s', the time at which the gas-liquid dispersion became homogeneous, was close to three seconds in all cases.

$$-\frac{p_{O_2,f}}{p_{O_2,i}}\ln\left(\frac{p_{O_2}-p_{O_2,f}}{p_{O_2,i}-p_{O_2,f}}\right)=k_La(t_s-t_s') \qquad \text{3.7 - repeat}$$

The k_La values evaluated by this technique were in the same order of magnitude compared to the k_La values measured with the indirect method.

4.2.1. Effect of initial liquid volume and presence of aqueous electrolyte

The effect of initial solution volume on the k_La value is shown in Figure 4.4 and Figure 4.5, respectively. The data indicated clearly that the oxygen mass transfer coefficient in the reactor decreased considerably with an increase in solution volume i.e., from 4.4 to 1.1 min^{-1} when solution volume was increased from 4800 mL to 5200 mL. This result confirmed previous observations made during employment of the sulphite oxidation method in the optimisation studies. Irrespective of higher

k_La values at solution volumes lower than 5000 mL, all batch pyrite oxidation tests were conducted strictly at 5000 mL to ensure sufficient residue samples for chemical analysis was collected at the low slurry densities (< 2 wt% solids) employed.

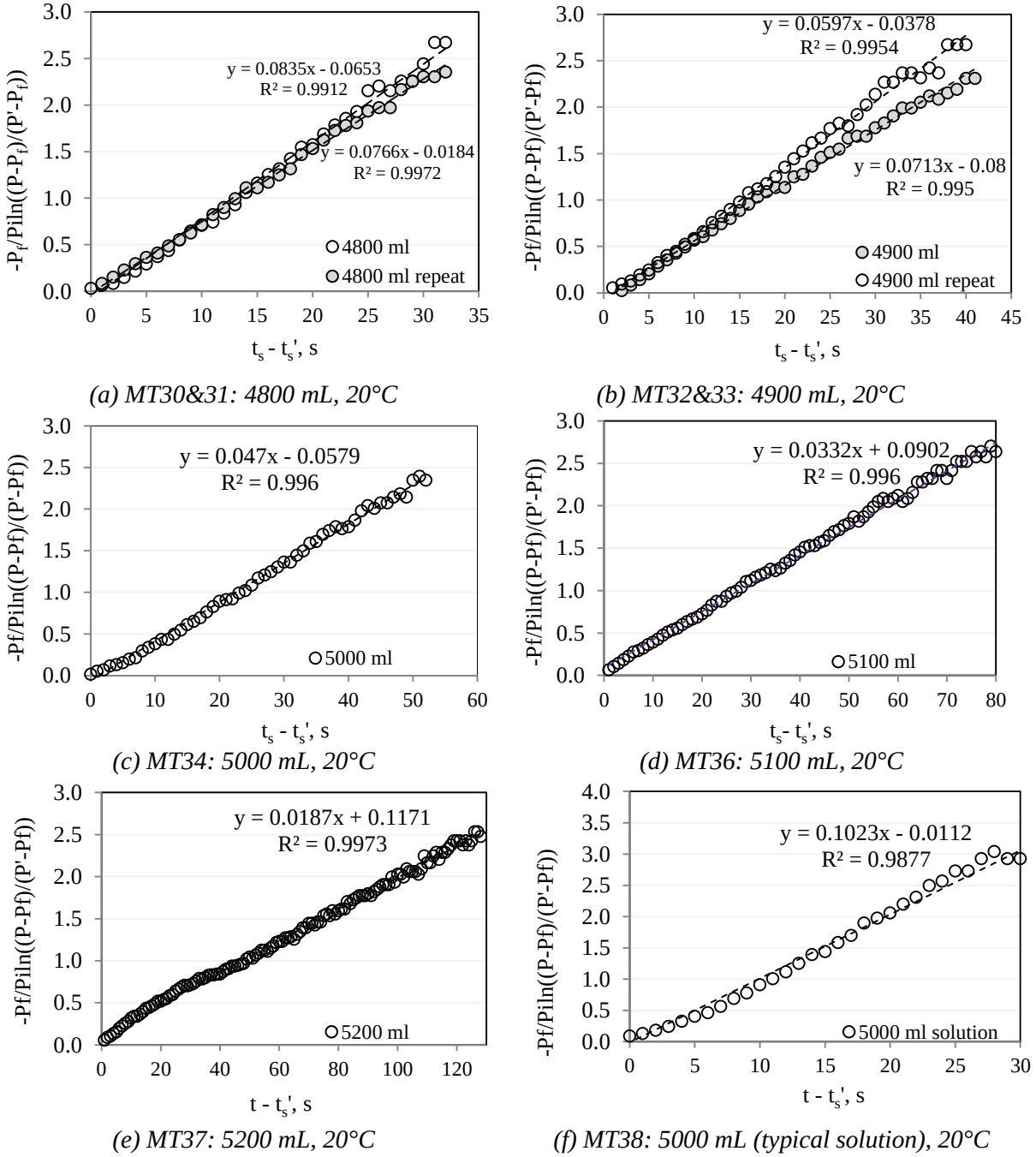

(a) MT30&31: 4800 mL, 20°C

(b) MT32&33: 4900 mL, 20°C

(c) MT34: 5000 mL, 20°C

(d) MT36: 5100 mL, 20°C

(e) MT37: 5200 mL, 20°C

(f) MT38: 5000 mL (typical solution), 20°C

Figure 4.4: Direct oxygen mass transfer measurements: Evaluation of k_La value by employing Equation 21 (600 rev/min, impeller Arrangement C) at different starting solution volumes

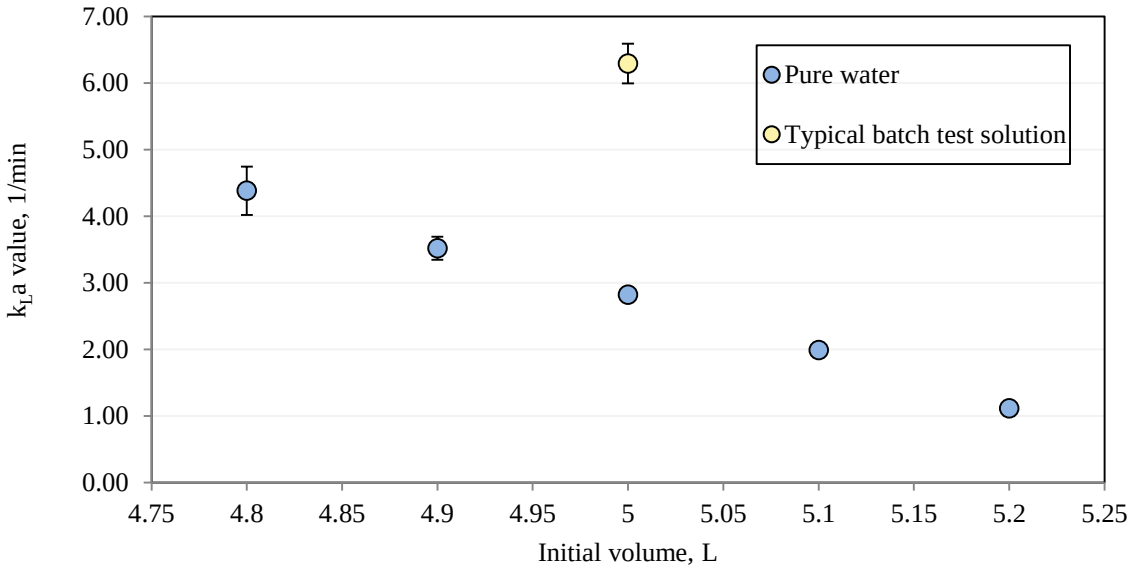

Figure 4.5: Effect of initial liquid volume on the k_La value in the 2 Gallon Parr reactor (impeller Arrangement C, 600 rev/min, 20°C)

Compared to pure water, the magnitude of the oxygen mass transfer coefficient was more than two times larger in a typical batch pyrite oxidation filtrate (6.3 vs. 2.8 min^{-1}), as also observed from data presented in Figure 4.5. This result confirms that the addition of iron and sulphuric acid to pure water has a positive influence on the rate of mass transfer. Previously, it has been found that dissolved ions either hinder or promote the rate of bubble coalescence and, therefore, it alters the gas-liquid surface area (Craig et al., 1993); however, understanding the exact mechanism by which ions influence bubble coalescence is beyond the scope of this study.

4.2.2. Effect of temperature

The effect of temperature on the k_La value is shown in Figure 4.6 and Figure 4.7. As expected, as temperature increased, the k_La value also increased. The associated activation energy was calculated as ~12 kJ/mol. The current measured activation energy value is much lower than the results of other researchers, who obtained activation energies of 21 and 33, 40 kJ/mol when the k_La value had been correlated to temperature in stirred reactors (Biley, 2015: 133; Cheng, 1994: 77; Steyl, 2012: 93). However, in these studies, the indirect method was used to determine the temperature dependence of the k_La value and, therefore, chemical enhancement could have taken place, especially at higher temperatures. For current modelling and simulation purposes, an activation energy of 12 kJ/mol will, thus, be used to correct the k_La value for temperature.

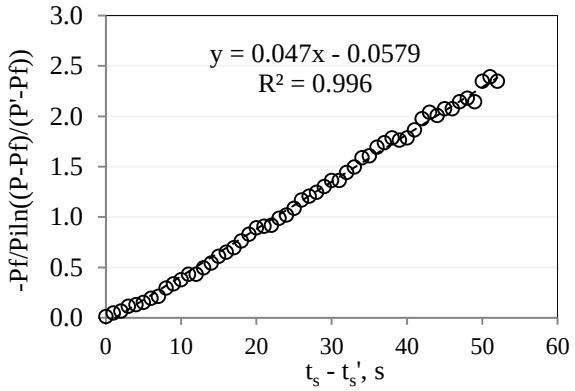

(a) MT34: 5000 mL, 20°C

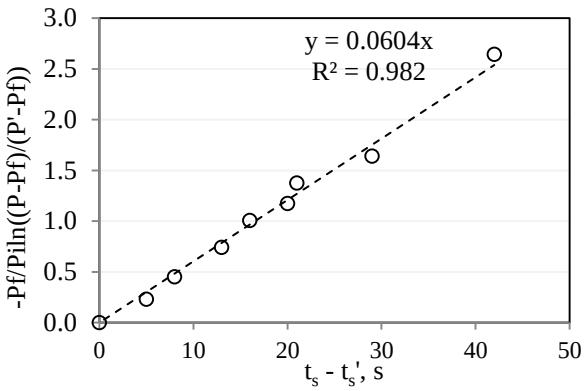

(b) MT35: 5000 mL, 30°C

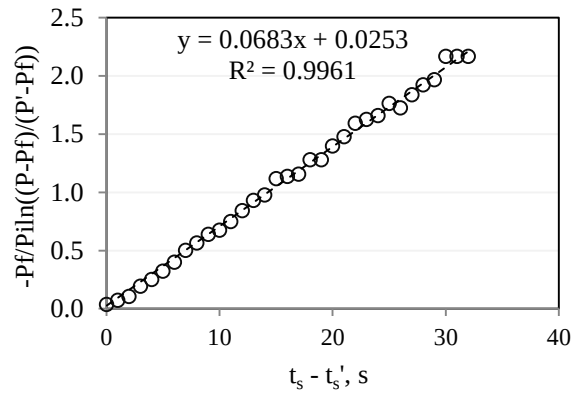

(c)MT39: 5000 mL, 45°C

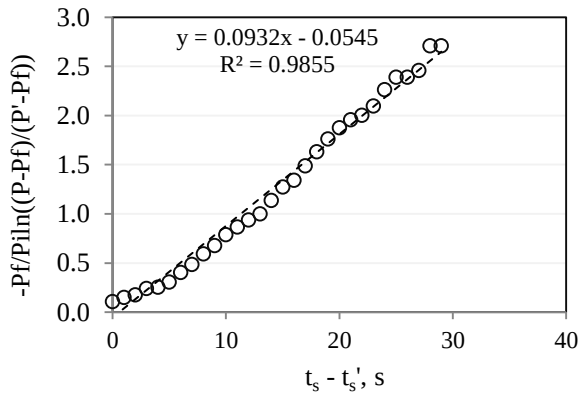

(d)MT40: 5000 mL, 65°C

Figure 4.6: Direct oxygen mass transfer measurements: Evaluation of k_La value by employing Equation 21 (600 rev/min, impeller Arrangement C) at different temperatures

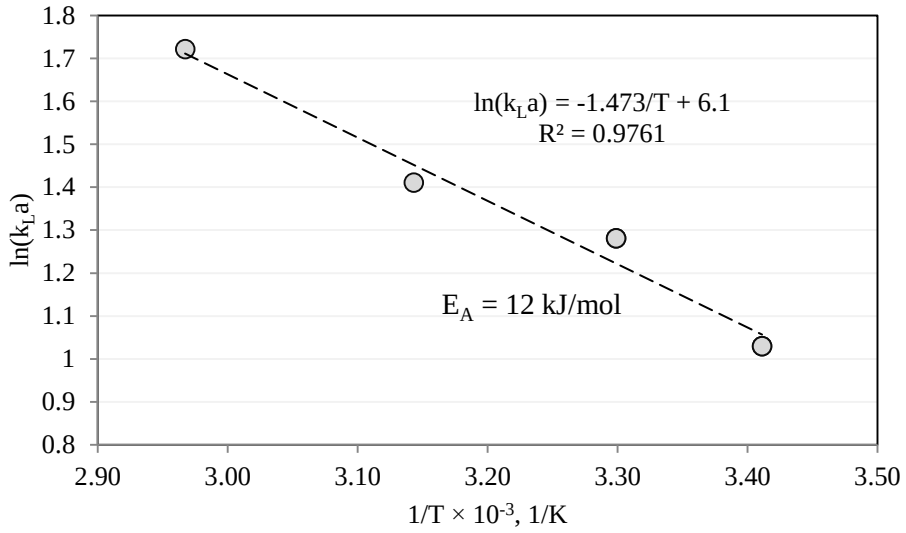

Figure 4.7: Effect of temperature on the k_La value in the 2 Gallon Parr reactor (Direct measurement, impeller Arrangement C, 600 rev/min)

4.3. Summary

Considering the results obtained, one may conclude that the magnitude of the k_La value was ~2.8 min^{-1} at 20°C, with an initial solution volume of 5000 mL and by employing impeller Arrangement C at 600 rev/min agitation speed in the Parr reactor. The order of magnitude of the k_La value was confirmed by both techniques. For modelling and simulation purposes, an activation energy of 12 kJ/mol may be used to correct the k_La value for temperature.

To ensure that a conservative value for the k_La value is used, no corrections to the k_La value will be made for the beneficial effect of aqueous electrolyte composition on the interfacial mass transfer rate. In addition, the effect of solid particles on the k_La value will not be taken into account, as it is known that, by employing slurry densities lower than 2 wt% solids, the presence of solid particles usually has negligible effect on the magnitude of the k_La value (see, e.g, Lee & Foster, 1990).

The study was successful in establishing the gas-liquid mass transfer coefficient in the 2-gallon Parr reactor.

5. SAMPLE PREPARATION AND CHARACTERISATION

5.1. Bulk concentrate preparation via sulphide flotation

A South African gold operation in the West Rand of the Witwatersrand area provided 15 tons of crushed ore (top size of 2.5 mm). Continued exploration activities have indicated that there exists large potential for further exploitation of gold and uranium resources at the specific operation where the sample originated from (Kenan & Chirenje, 2016).

A continuous mill-sulphide flotation pilot plant was operated at MINTEK to produce a sulphide concentrate. Pilot plant operational parameters were based on bench-scale batch milling and flotation test work. Details of the operational parameters, reagent selection and dosages, as well as the circuit, can be found in Tsotetsi and Pillay (2013). The gold, sulphide and uranium grade of the milled ore, as well as the performance of the flotation circuit, are provided in Table 5.1.

Table 5.1: Bulk sulphide concentrate analysis (Tsotetsi & Pillay, 2013)

	Mass pull	Au		U_3O_8		Sulphide	
		Grade	Recovery	Grade	Recovery	Grade	Recovery
	wt%	g/t	%	g/t	%	%	%
Feed	100	9	100	524	100	2	100
Bulk concentrate	3.5	138	65	1098	8	34	54
Tails	96.5	6	35	524	92	1	46

The ore was upgraded to a yield a flotation concentrate with a sulphide grade of 33.9 wt% in a mass pull of 3.3 wt%. The bulk of the uranium (i.e., 92 %) reported to the flotation tails, meaning that this Witwatersrand ore would most likely be amenable to the proposed flow sheet shown in Figure 2.2a. Gold recovery to the concentrate was approximately 64.6 %, to yield a final gold grade of 138 g/t. Even though uranium leaching and gold recovery are central to the context of this study, the current research focussed on the pyrite pressure oxidation kinetics which would dictate the autoclave size. The generated sulphide concentrate was subsequently used to study the high-temperature pyrite pressure oxidation rate.

5.2. Sample preparation for batch pressure oxidation tests

The bulk concentrate was subsequently screened to the following sizes: -150+106, -106+75, -75+53, -53+38, -38+25 µm (i.e., the root 2 sieve series) and -25 µm. Screening was conducted in small batches with a laboratory vibrating sieve shaker and, since the samples were wet-screened, all fines adhering to the surface of the particles were removed. The samples were subsequently dried at 40°C for 24 hours.

The particle size distribution (PSD) of the bulk sample is provided in Table 5.2. Approximately 60 wt% of the bulk sample had a particle size smaller than 25 µm, however, this portion of the sample was not considered for use in the subsequent oxidation kinetic study, as it would undergo oxidation at a high rate, which would make oxidation kinetics difficult to measure.

Table 5.2: Particle size distribution of the bulk pyrite concentrate

Sample	Screen size, µm	Mass % on screen
A	-25	57.9
B	25	9.8
C	38	11.3
D	53	9.4
E	75	6.8
F	106	2.8
G	150	1.5
H	212	0.2
I	300	0.2

Samples B, C, D, E and F were selected for this study and were characterised further. The particle size distributions, as determined by a Saturn Digisizer, of the five screened samples are presented in Figure 5.1. Key parameters that were used to characterise the particle size distribution of each size fraction are included in Table 5.3.

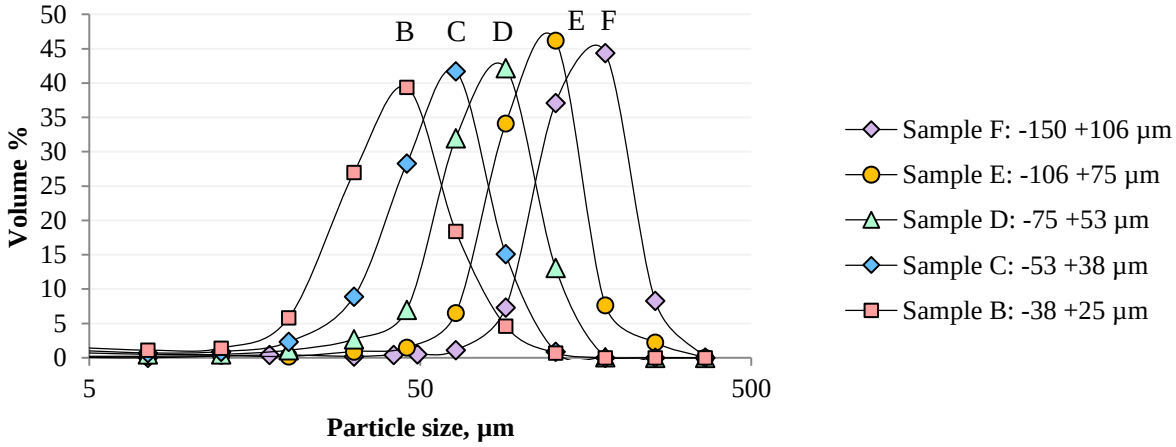

Figure 5.1: Particle size distribution of size fractions used during kinetic batch test work

Table 5.3: Arithmetic mean, median, span and CV of the volume particle size distributions

Sample	Arithmetic mean	M [n]	d_{50}	d_{10}	d_{90}	Span [o]	Variance (σ^2) [p]	CV [q] (σ/μ)
	µm	um	µm	µm	µm	%	-	-
B	31.5	44.7	43	25	65	94	354	0.421
C	45.5	57.8	57	35	81	81	431	0.359
D	64.0	80.0	79	50	110	75	723	0.336
E	90.5	114.8	112	75	150	67	1465	0.333
F	128.0	157	153	105	209	68	2068	0.290

The mean size (µ) and the width or spread may be used to characterise the size distributions of the different size fractions produced (Herbst, 1979). The particle size distributions were essentially symmetrical, as the distribution median (i.e., d_{50}) and mean closely corresponded. A large discrepancy between the calculated arithmetic mean (i.e., the average of two adjacent screen sizes) and true mean was observed. This was most probably due to the irregular shape of the pyrophyllite particles, which blocked screen apertures and generated a large proportion of near-size material. The distribution mean sizes increased by a factor of 1.41 ($\sqrt{2}$), which indicates that adequate size variation between samples was obtained. The variation was, thus, large enough to allow investigation of the influence of particle size during subsequent leaching experiments.

Both the span and coefficient of variation (CV) may be used to characterise the relative spread of the distributions around the mean. The relatively narrow spans and the small CV values (close to zero) indicates that narrow-sized fractions were successfully produced during screening of the samples, and that the leaching kinetics should approach the leaching kinetics of a monosize PSD (Herbst, 1979: 55-59). The span and CV values decreased with increasing mean particle size of the samples, which indicated that separation was more efficient for the larger particle size fractions and, therefore, experimental work on the larger sized fractions should yield more accurate results.

5.3. Characterisation of samples for batch POX tests

The quantitative XRD analyses of the differently sized samples are included in Table 5.4. It is evident from the analyses that the pyrite content increased as particle size increased (Sample E > Sample D > Sample C > Sample B). Sample E (-106+75 µm) had the highest pyrite content i.e., 80 wt%, while

[n] Mean of distribution, $\mu = \sum_{i=1}^{n} d_i^* f_i$

[o] Distribution span: $100\times(d_{90}-d_{10})/d_{50}$

[p] Variance of sizes around the mean, $\sigma^2 = \sum_{i=1}^{n}(d_i^* - \mu)^2 f_i$

[q] Coefficient of variation (relative spread around of sizes around mean), CV= σ/µ

Sample B (-53+38 µm) had the lowest pyrite content (57 wt%). This distribution is most probably a result of pyrite having more resistance (i.e., a higher breakage index) to milling, compared to the silicate minerals, pyrophyllite and quartz.

What is also notable from the XRD analysis results is that no marcasite (with chemical composition FeS_2 and orthorhombic structure) was detected in the samples. The presence of marcasite could have potentially interfered with the interpretation of pyrite leach kinetic data.

Table 5.4: Mineralogical composition of size fractions used during kinetic batch test work

Mineral	Mineral ideal formula	Sample B wt %	Sample C wt %	Sample D wt %	Sample E wt %	Sample F wt %
Pyrite	FeS_2	57	62	73	79	85
Quartz	SiO_2	7	8	11	10	8
Pyrophyllite	$Al_2Si_4O_{10}(OH)_2$	36	30	16	11	7

The densities of the samples are presented in Table 5.5. The density increased with increasing particle size, or increased with the pyrite content. This is expected as the mineral pyrite is denser compared to quartz and pyrophyllite.

Table 5.5: Density of size fractions used in kinetic batch test work

Sample	Density, g/cm^3
B	3.1784
C	3.4144
D	3.8224
E	4.1213
F	4.5544

SEM images of the samples are included in Figure 5.2 and confirm the mineralogical composition according to the XRD analysis. In all size fractions, most of the pyrite particles were well liberated. The SEM images, furthermore, confirmed that the smaller size fractions contained more quartz and pyrophyllite than the larger size fractions. Some quartz inclusions in pyrite grains were especially noted in Sample D, however these particles were in the minority and were expected to have an insignificant effect on the overall available pyrite surface area.

In addition, there was no distinct change in pyrite particle geometries with increasing particle size, i.e., “shapes of pyrite particles”. Therefore, it was not necessary to use different shape factors for different size fractions during modelling of the pyrite leach kinetics as a function of particle size (see McKibben and Barnes, 1986).

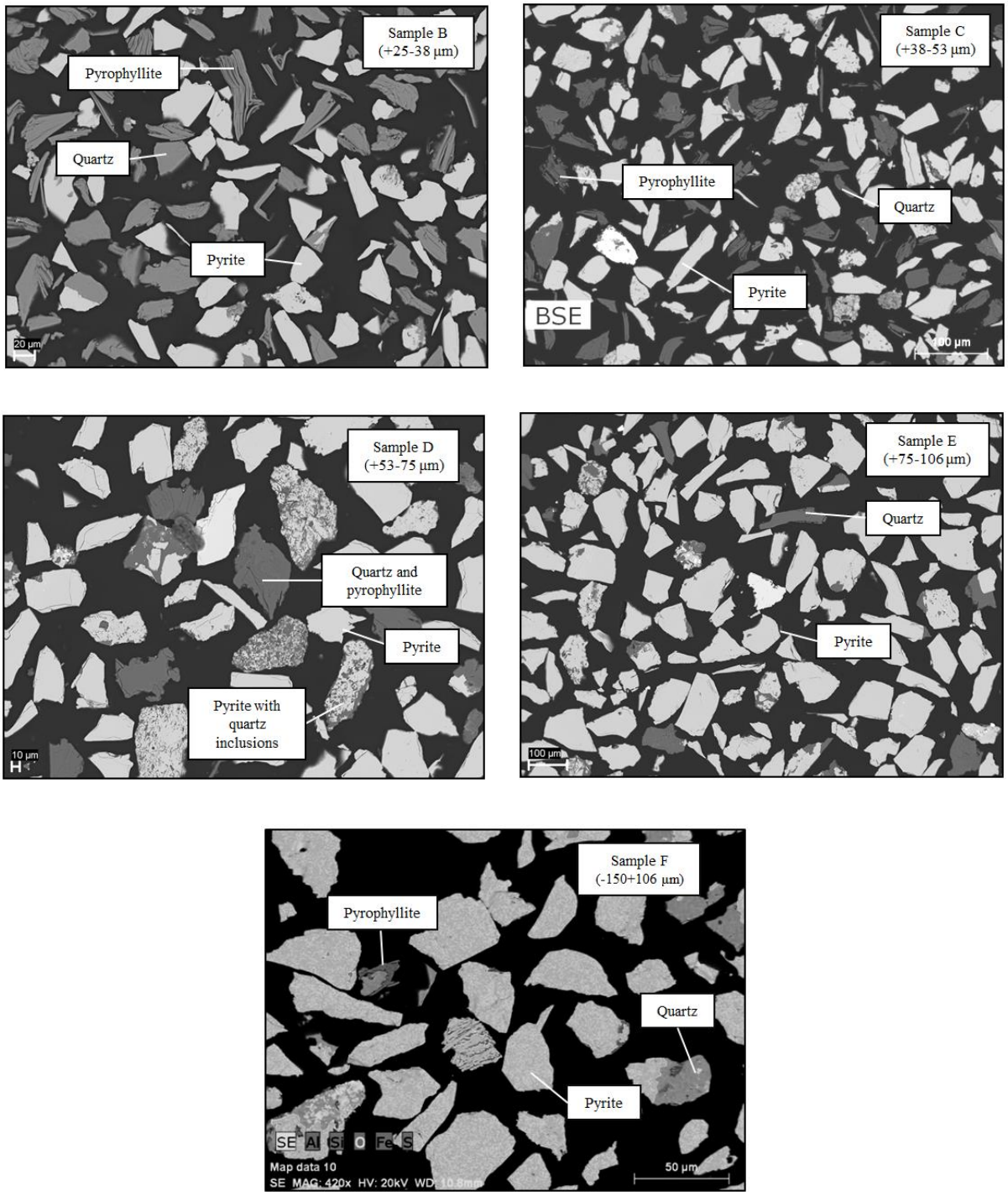

Figure 5.2: SEM images of the samples (Sample B, Sample C, Sample D, Sample E and Sample F) used in the kinetic batch test work

The chemical assays of the different size fractions are included in Table 5.6. Aluminium, silicon, iron and sulphide content correlated well with the reported quantitative XRD results for quartz, pyrophyllite and pyrite.

The corresponding sulphide to iron ratios are included in Table 5.6, and ranged between 1.88 and 1.98. Ideally, the stoichiometric S to Fe molar ratio should be 2 for pyrite, however, some sulphur deficiency in natural pyrite mineral samples have been reported as a result of sulphur vacancies in the cubic structure of pyrite (Birkholz, Fiechter, Hartmann & Tributch, 1991). Lowson (1982) cites S to Fe molar ratios ranging between 1.94 and 2.00, whereas Long and Dixon (2004) used pyrite samples with a mole ratio (S/Fe) of 1.92 in their investigation. In the current study, there was the possibility that some iron could be present as solid solution in the pyrophyllite crystal structure; however, Jiang, Essene & Peacor (1990) report that these concentrations (based on pyrophyllite mass) are usually low, ranging between 0.01 to 0.08 wt%. It was, therefore, assumed that all analysed Fe was associated with pyrite, and that the Fe to S ratio, currently reported for pyrite, is accurate. This assumption is reviewed and discussed in more depth in Section 6.7. To maintain consistency in data processing, it was decided to base the pyrite dissolution extent on iron content in the residues and in the solution throughout the experimental campaign, irrespective of the size fraction used (as discussed in Section 3.2.5).

Table 5.6: Sulphur speciation and chemical analysis of major elements in samples used in the kinetic batch test work

Sample	Al	Fe	Si	Total Sulphur	Sulphide	S/Fe
	wt %	wt %	wt %	wt %	wt %	mole/mole
B	5.34	27.40	15.35	30.90	29.56	1.88
C	4.17	29.62	12.46	32.02	32.18	1.89
D	2.40	35.55	8.95	39.57	40.13	1.94
E	1.00	39.90	5.70	44.70	44.30	1.93
F	0.44	39.70	3.90	45.70	45.21	1.98

Full chemical analyses of all the samples are included in Table 5.7. The chemical analysis indicated that arsenic was the most abundant minor element, with concentrations of approximately 0.1 wt%. It is known that the trace or minor metal content in pyrite natural mineral samples could have a significant effect on the reactivity of pyrite (Lehner & Savage, 2008). However, the trace metal content was comparable between all samples (size fractions), therefore, a major change in pyrite's reactivity with increasing particle size due to a variation in minor metal content, was unlikely.

Table 5.7: Chemical composition of minor elements in samples used for kinetic batch test work

Sample	As	Ca	Co	Cr	Cu	Mg	Mn	Ni	Pb	Ti	V	Zn	U
							mg/kg						
B	1210	244	640	306	243	300	248	437	170	228	43	150	166
C	1227	305	730	240	259	354	298	503	150	409	37	160	128
D	1225	275	950	163	287	348	359	592	160	294	32	160	147
E	1188	285	1000	115	306	312	417	642	135	328	29	120	188
F	979	339	967	351	292	311	425	541	110	489	18	135	200

6. BATCH PYRITE OXIDATION: RESULTS AND DISCUSSION

In this chapter, the main results of the pyrite batch oxidation tests are presented. All batch kinetic tests were done at low slurry densities (i.e., < 2 wt%) to ensure that the overall intrinsic rate constants and orders of reactions may be measured in solutions that have approximately constant concentrations during the course of a batch test. The main parameters that were studied during the test work campaign included temperature, oxygen partial pressure, acid concentration, particle size and solids loading.

6.1. Phenomenological rate model: Unreacted shrinking particle model

The unreacted shrinking particle (USP) model was applied to relate the macroscopic observed variables to the micro-scale reactions occurring on the pyrite particle surface. It was assumed *a priori* that the pyrite oxidation rate was controlled by a chemical reaction on the surface. This assumption was re-evaluated by studying the magnitude of the activation energy as presented in Section 6.2. The equations used to describe the observed pyrite oxidation based on the USP model, are discussed below. The detailed derivations of these equations are included in Appendix C.4.

The fractional conversion, X, of the mineral particle may be expressed in terms of the unreacted particle radius R_p (in m) to the initial particle radius R_{po} (in m), according to Equation 6.1.

$$X = 1 - (\frac{R_p}{R_{po}})^3 \qquad 6.1$$

Since it was assumed that the rate of reaction is limited by the reaction on the surface of the mineral particle, the conversion of the mineral may be described, as a function of time (t in minutes), by the following equation:

$$X = 1 - (1 - k_s t)^3 \quad or \quad 1 - (1 - X)^{\frac{1}{3}} = k_s t \qquad 6.2$$

The observed rate constant (k_s in 1/min) is a function of the intrinsic pyrite oxidation rate (r_{FeS2}, mol/min.m^2) and the initial particle size, R_{po}, per Equation 6.3:

$$k_s = \frac{MW_s r_{Fes_2}}{\rho_s R_{po}} \qquad 6.3$$

where MW_s is the mineral molar mass in kg/mol and ρ_s is the mineral density in kg/m^3. From Equation 6.2 it is clear that, provided the relationship $1 - (1 - X)^{\frac{1}{3}}$ vs. time is a linear (i.e., chemical reaction

controlled), the slope will yield the observed rate constant (k_s). In addition, the degree of linearity will remain subject to the requirement that reagent concentrations are constant for the duration of the test.

6.2. Influence of temperature

The rate of pyrite dissolution was investigated over the temperature range 180 to 210°C by using Sample C (-53 +38 µm) and from 180 to 200°C by utilising Sample E (-106 +75 µm). The results show that the oxidation rate is strongly temperature dependent (refer to Figure 6.1a and Figure 6.2a).

The results were modelled using the USP model, as discussed in Section 6.1. The observed rate constants were calculated by fitting the results in the form of plots of the left-hand side of Equation 6.2, i.e., $1-(1-X)^{1/3}$ vs. time. These plots are shown in Figure 6.1b and Figure 6.2b and indicate that the oxidation reactions were, indeed, chemical reaction controlled, as the corresponding R^2-squared values are close to unity in all tests.

To correct for the effect of temperature on the dissolved oxygen concentration, it was assumed that the rate of pyrite oxidation was first order in aqueous oxygen concentration and an "apparent" intrinsic rate constant (*k''*) calculated per the equations below (following from Equation 6.3):

$$k_s = \frac{MW_s r_{Fes_2}}{\rho_s R_o} = k''[O_2] \qquad 6.4$$

Where $k'' = \frac{MW_s k_{ins}}{\rho_s R_{po}}$ assuming $r_{Fes_2} = k_{ins}[O_2]$ 6.5

The dissolved oxygen concentration was approximated by the equilibrium oxygen concentration calculated, using the relationship published by Tromans (2000) – see Appendix C.2. The apparent intrinsic rate constant (*k''*) was related to temperature by the Arrhenius temperature dependency:

$$k'' = \bar{A}\exp(\frac{-E_A}{R_g T}) \qquad 6.6$$

where $\bar{A}$ is the pre-exponential factor, E_A the activation energy in J/mol, R_g the ideal gas constant (J/mol.K) and T the absolute temperature in K. The well-known Arrhenius plot may be generated by plotting lnk'' vs. 1/T. A linear relationship between lnk'' and 1/T should prevail, with the slope being equal to $-E_A/R_g$, thus, allowing calculation of the activation energy.

A plot of the apparent rate constants vs. temperature allowed generation of an Arrhenius activation energy plot as shown in Figure 6.1c and Figure 6.2c for Sample C and Sample E, respectively.

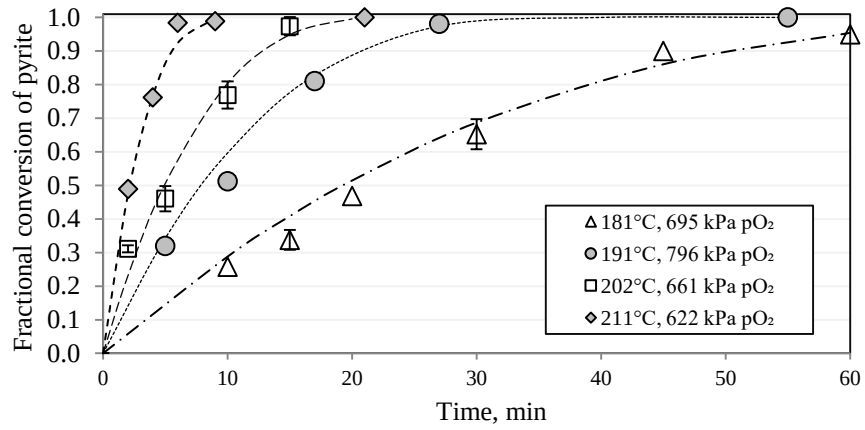

(a)

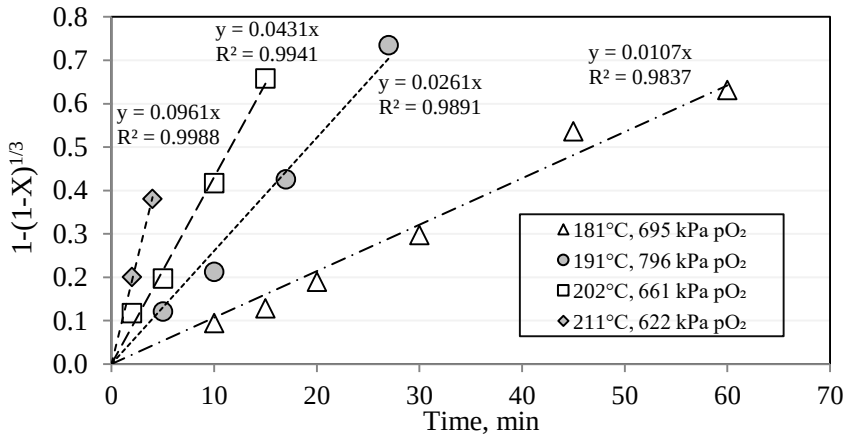

(b)

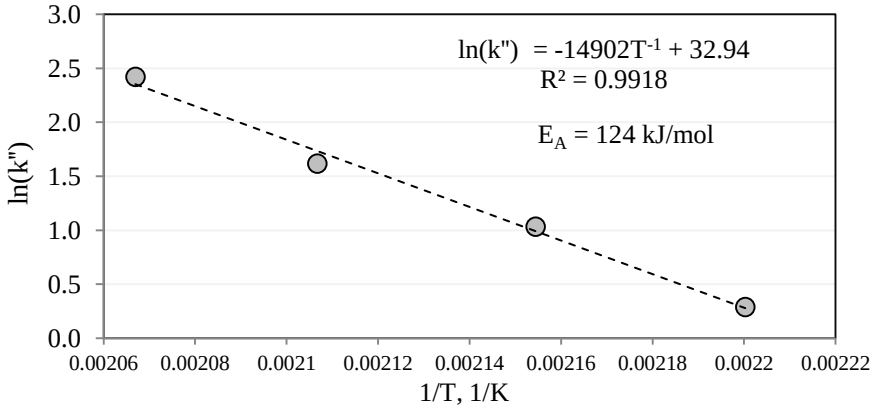

(c)

Figure 6.1: (a) Influence of temperature on pyrite oxidation kinetics (180-210°C) (b) Shrinking particle model plot (c) Arrhenius activation energy plot (observed rate constant calculated assuming first order dependency on oxygen partial pressure) (Experimental conditions: -53+38 µm - Sample C, 600 rev/min, starting volume 5000 mL, 0.054±0.001 mol/kg FeS_2, 0.35 mol/kg H_2SO_4)

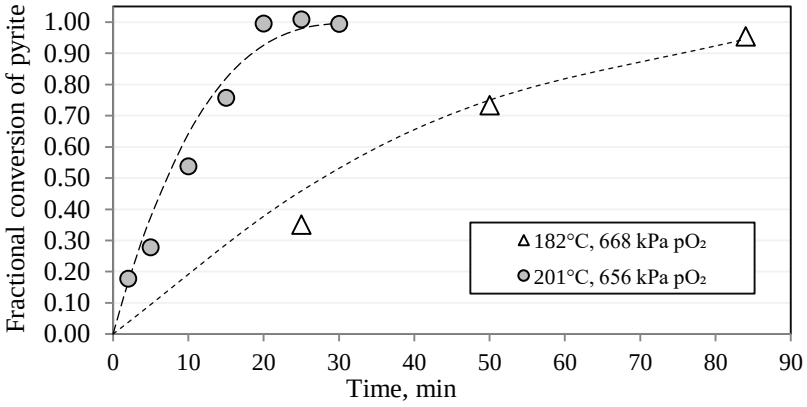

(a)

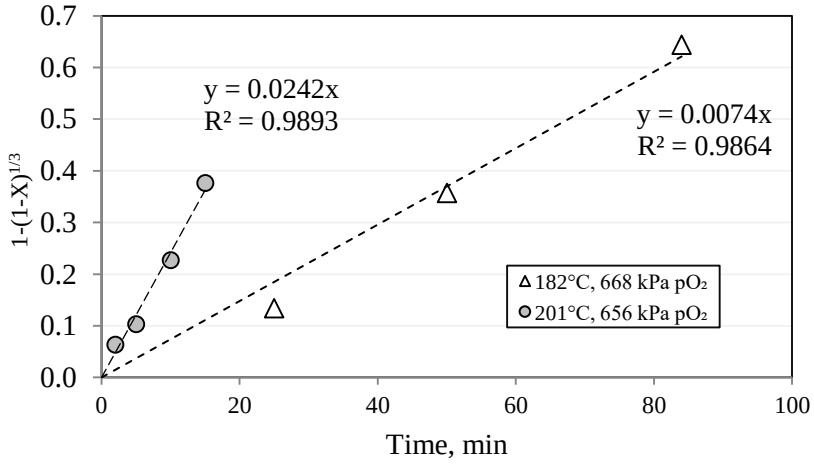

(b)

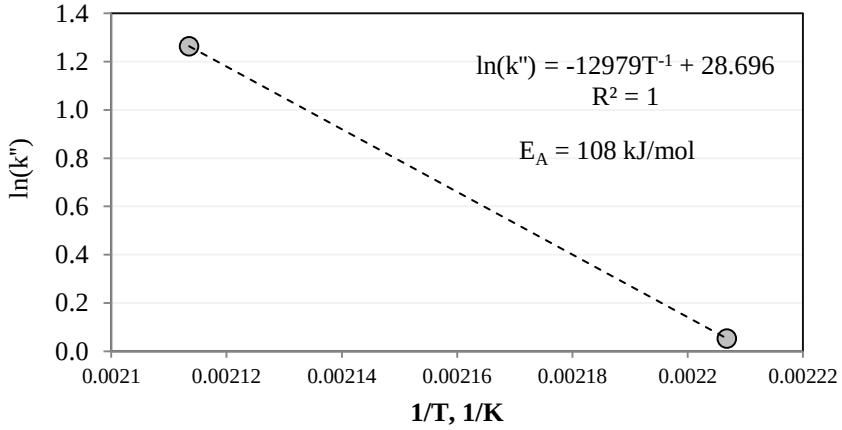

(c)

Figure 6.2: (a) Influence of temperature on pyrite oxidation kinetics (180-200°C) (b) Shrinking particle model plot (c) Arrhenius activation energy plot (observed rate constant calculated assuming first order dependency on oxygen partial pressure) (Experimental conditions: -105+75 µm - Sample E, 600-700 rev/min, starting volume 5000 mL, 0.0894±0.0028 mol/kg FeS_2, 0.35 mol/kg H_2SO_4)

The strong influence of temperature on the oxidation rate of pyrite was reflected by the high activation energies of 124 kJ/mol (R^2 = 0.99) and 108 kJ/mol calculated for Samples C and E, respectively. The fact that the activation energies calculated for the two samples ranged within 15% of one another instilled some confidence in the relative magnitude of the reported values.

This activation energy was considerably higher than the 33 kJ/mol (170-230°C) reported by Long and Dixon (2004). Papangelakis (1990:83) reports two activation energies for the oxidation of pyrite: an activation energy of 46 kJ/mol between 140 and 160°C, and an an activation energy of 110 kJ/mol between 160 and 180°C. The author proposes that this discrepancy may have been related to different reaction products forming at different temperatures, which changed the intrinsic reaction rates (Papangelakis, 1990: 85). Below 160°C, the formation of elemental sulphur is expected, whereas partial conversion to sulphate is believed to start occurring at 150°C (see Figure 2.1). This last-mentioned activation energy corresponds more closely to the current measured value. The low activation energy reported by Long and Dixon (2004) might have been associated with passivation of the surface, as the authors claim occurred towards the end of their batch tests; however, the exact reason remains unclear.

The activation energy characteristic of diffusion in solution is usually 21 kJ/mol or less (Wadsworth, 1979: 135); therefore, the calculated activation energies, ranging between 108 and 124 kJ/mol, suggest that the test work was not conducted under any diffusional limitations (i.e. neither oxygen diffusion from the gas phase to the liquid phase, nor oxygen diffusion from the bulk solution phase through the laminar layer to the particle surface), which supports the previous assumption that the oxidation reaction rate was limited by the chemical reaction on the surface of the particles. This indicated that the oxidation of this pyrite will benefit significantly from the higher temperatures typically used in pressure oxidation, as it is likely to be highly resistant to oxidation at ambient temperatures.

6.3. Influence of oxygen partial pressure

The effect of oxygen partial pressure (450-1 130 kPa) on the rate of pyrite kinetics was evaluated, using Samples C and D, with the results shown in Figure 6.3 indicating that the rate of pyrite oxidation increased with oxygen partial pressure.

The pyrite oxidation rates were very high, as indicated by the complete oxidation of the pyrite within 20 minutes at oxygen partial pressures typical of industrial operation, compared to the 30 to 60 minutes reported by Long and Dixon (2004) under similar experimental conditions (210°C, 0.5 M H_2SO_4, +44-149 µm, 690 kPa, 1 g/L pyrite). As noted previously, these authors also report a much lower activation energy. The high reactivity of the pyrite could be related to the presence of impurities, such as arsenic, nickel or cobalt present in the samples. These elements could have changed the semi-conducting properties and the intrinsic pyrite oxidation kinetics, as reported by Lehner and Savage (2008). Therefore, the rate equation and associated parameters are likely to be very ore-specific.

The dissolution curves (see Figure 6.3a and c) were modelled again, by using the USP model (shown by the dotted lines) with the assumption that the reactions are surface chemical reaction controlled. The logarithms of the apparent rate constants were then plotted against the logarithm of the dissolved oxygen concentration, to evaluate the order in aqueous oxygen concentration (see Figure 6.3b and d). In general, high correlation coefficients (R^2 values) were obtained. However, the order in aqueous oxygen concentration decreased with an increase in mean particle size. The observed order in oxygen concentration was 1.4 during leaching of Sample C, and decreased to 1.1 when Sample D was oxidised. Re-evaluation of the activation energy (Section 6.2) by using an order of 1.4 in oxygen concentration (see Equation 6.1) for Sample C, led to a small decrease in the calculated activation energy, of 124 kJ/mol to 121 kJ/mol. Since the partial pressure was kept roughly constant during the tests where temperature was investigated, the reaction rate was corrected by the same factor, ultimately having almost no effect on the calculated the activation energy.

A fractional order in the oxidant concentration (more specifically, “0.5”) is commonly used in support of an electrochemical controlling mechanism during mineral oxidation (Crundwell, 2013). An order of “1”, on the other hand, is congruent with a diffusion-controlled mechanism. Since the high activation energies (>100 kJ/mol) found during this study do not support a diffusion-controlled mechanism, the observed reaction orders, ranging between 1.1 and 1.4, are likely to be associated with the intrinsic rate equation. It is suggested that, in the case of highly reactive pyrite, a parallel non-oxidative mechanism may apply, as was noted for highly reactive pyrrhotite samples, which showed a reaction order of 1.2 in oxygen partial pressure at 180°C, as reported previously by Filippou, Konduru and Demopoulos (1997). In the case of pyrite, this would require a

disproportionation process during which the S_2^{2-} released by the pyrite should disproportionate to S^o and H_2S (refer to Reaction 2.3).

The measured oxidation extents were also validated by conducting mineralogical analysis on selected residues. The results of XRD and SEM characterisation of the residues generated during the oxidation of Sample C at an average partial pressure of 516 kPa O_2 are included in Table 6.1 and Figure 6.4, respectively. The reconciliation of the chemical analysis and the XRD analysis is presented in Table 6.2. Both sets of results confirm that pyrophyllite and quartz remain effectively inert during the leaching experiments, as their contents are both upgraded with increasing residence time. On average, the aluminium and silica concentrations in solution after each test corresponded to 20-25 and 40-50 mg/L, respectively. This amount corresponded to 4 wt% aluminium and 2 wt% silica dissolution, respectively.

The chemical and XRD analyses of the residues corresponded very well. The SEM images indicate no visible rims/coatings on the pyrite particle residues, confirming that particle shrinkage had not been limited by product layers and that the USP model is an appropriate choice to describe the leaching rate of this pyrite.

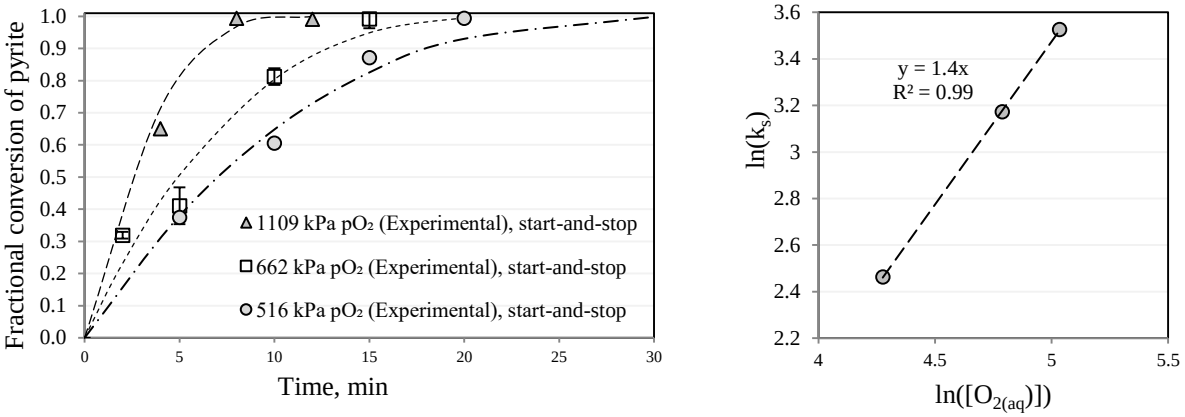

Sample C (-53 +38 µm), 0.054 mol/kg FeS_2, 0.35 mol/kg H_2SO_4

(a) *(b)*

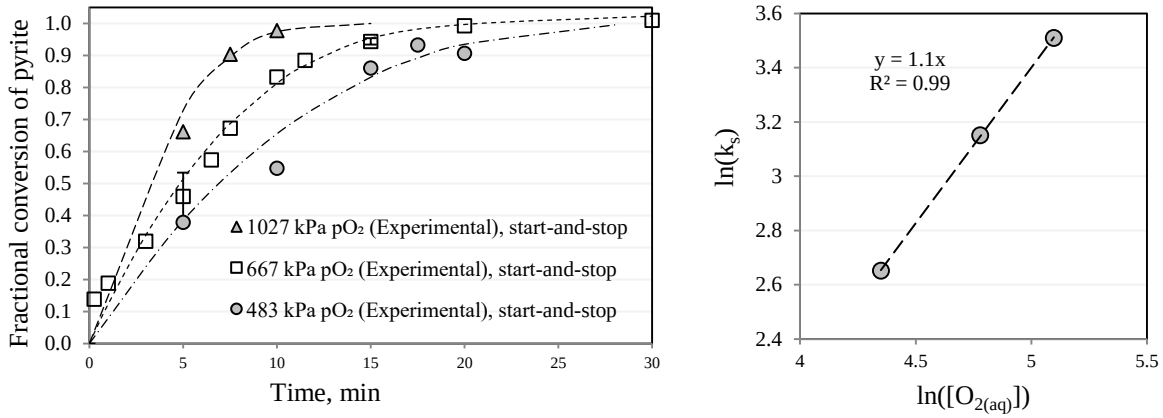

Sample D (-75 +53 µm), 0.057 mol/kg FeS_2, 0.35 mol/kg H_2SO_4

(c) *(d)*

Figure 6.3: Influence of oxygen partial pressure on the rate of pyrite dissolution: (a), (c) and (e) dissolution plots, (b), (d) and (f) logarithm of apparent rate constant vs. dissolved oxygen concentration (201°C, 600 rev/min, 5000 mL starting volume)

Table 6.1: XRD analysis of residues after oxidation of Sample C (-53+38 µm) (0.054 mol/kg FeS_2, 201°C, 516 kPa pO_2, 0.35 mol/kg H_2SO_4)

Minerals	Ideal Mineral Formula	5 min	10 min	15 min
			wt%	
Pyrite	FeS_2	51	42	21
Quartz	SiO_2	11	13	17
Pyrophyllite	$Al_2Si_4O_{10}(OH)_2$	38	45	61

Table 6.2: Reconciliation between XRD and ICP-OES analysis of residues generated during oxidation of Sample C (0.054 mol/kg FeS_2, 201°C, 516 kPa pO_2, 0.35 mol/kg H_2SO_4)

	Fe		Si		Al		Total S	
	XRD	ICP-OES	XRD	ICP-OES	XRD	ICP-OES	XRD	Combustion
	wt%							
5 min residue	23.7	25.0	17.0	15.2	5.7	5.1	27.3	26.8
10 min residue	19.6	19.6	20.1	20.4	6.7	5.8	22.5	23.4
15 min residue	9.8	10.4	27.0	26.0	9.1	9.4	11.2	13.8

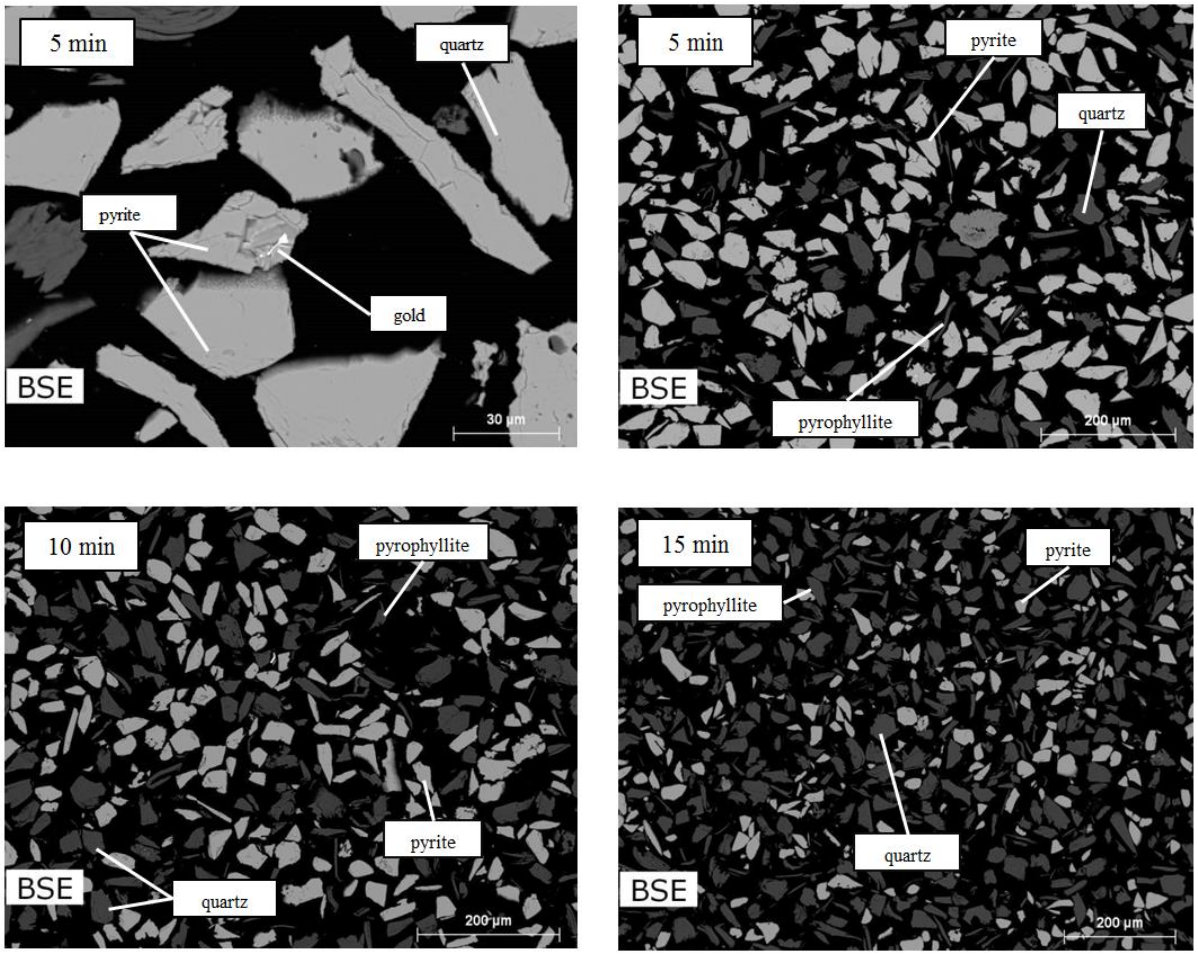

Figure 6.4: SEM images of residues after oxidation of Sample C for 5 minutes, 10 mintes and 15 minutes (516 kPa pO_2, 0.054±0.001 mol/kg FeS_2, 0.35 mol/kg H_2SO_4)

6.4. Influence of acid concentration

The effect of acid addition was also investigated on two particle size fractions (i.e., Sample C and Sample D), as shown in Figure 6.5. In both cases, the rate of pyrite oxidation was affected negatively by an increase in the initial acid concentration. This observation is consistent with previous findings from literature (Holmes & Crundwell, 2000; McKibben & Barnes, 1986; Williamson & Rimstidt, 1994).

Based on preliminary modelling of the data, i.e., not considering the effect of minor change in acid concentration over time, the order of the rate of pyrite oxidation in proton concentration ranged between -0.32 to -0.16. These correlations are based on a fit of the logarithmic relationship between the observed rate of reaction and the sulphuric acid concentration (shown in Figure 6.5b and d). The effect of oxygen partial pressure was corrected for by assuming a reaction rate order of 1.4 and 1 in dissolved oxygen concentration during processing of the data pertaining to Sample C and D, respectively. These orders were based on the results presented in Section 6.3.

Since the pyrite dissolution was affected negatively by acid addition (like the behaviour of other pyrite samples reported in literature), a direct acid/non-oxidative decomposition route is not proposed for governing the dissolution rate of this specific sample. In general, the weak negative dependence of the rate of pyrite oxidation in proton concentration has not been clarified to an acceptable extent. This effect is more pronounced when only iron(III) is present as oxidant (i.e., under nitrogen), compared to when both dissolved oxygen and iron(III) are present (Williamson & Rimstidt, 1994); supporting the notion that a highly protonated pyrite surface hinders iron(III), which could act as catalyst during the oxidation of pyrite, from coming into close proximity with the surface of pyrite. An alternative explanation was proposed by Crundwell (2013), who attributes the negative order in proton concentration to the positive influence of the adsorption of hydroxide ions on the pyrite on the rate-determining step. There is also the possibility that the negative order may be ascribed to more complexation between iron(III) and sulphate with higher sulphuric acid additions. The complexation ultimately lowers the free iron(III) available to act as catalyst or surrogated oxidant during the oxidation process (Nicol et al., 2013).

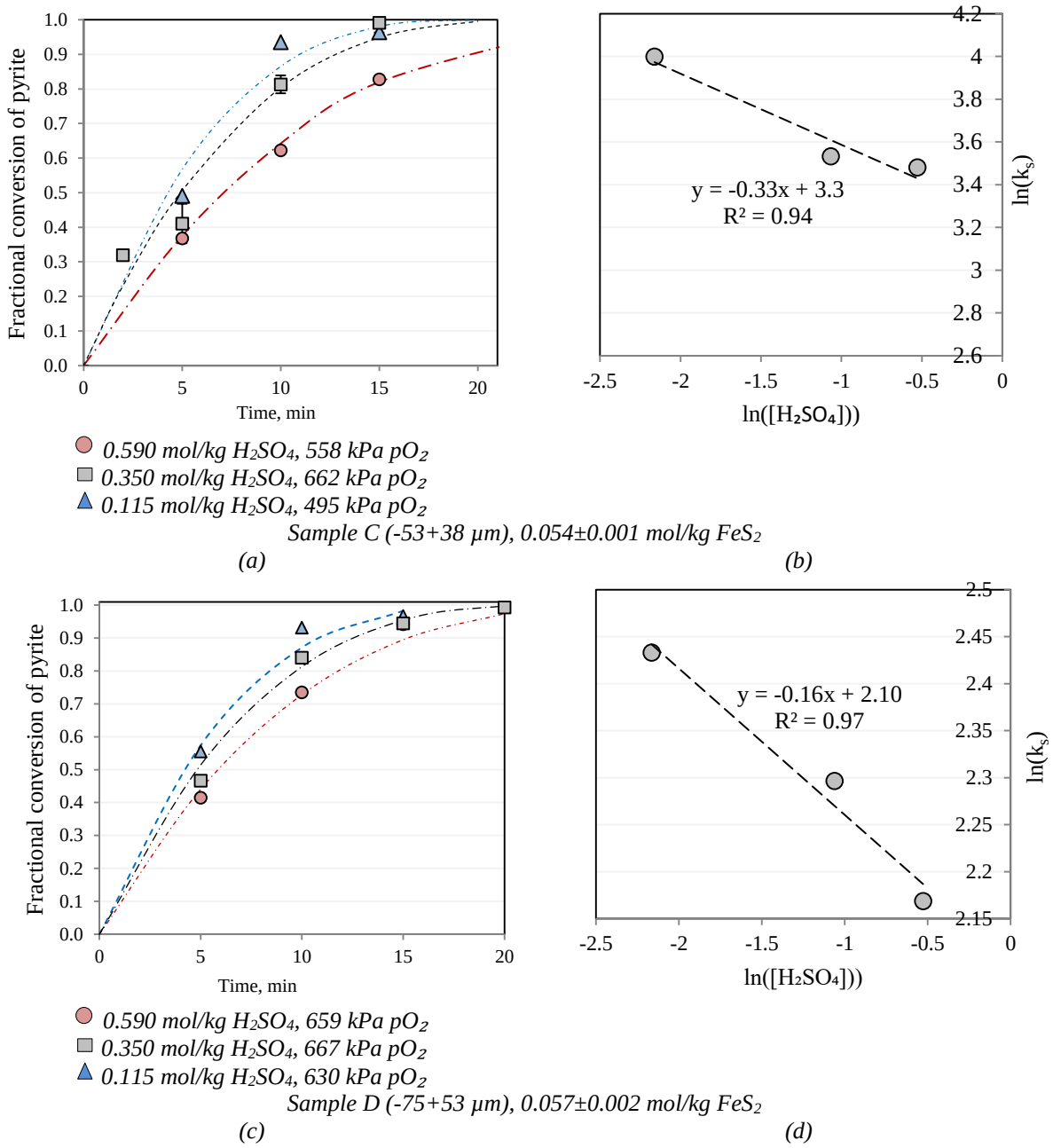

Figure 6.5: Influence of acid addition on the rate of pyrite oxidation (a) and (c) dissolution plots, (b) and (d) logarithm of apparent rate constant vs sulphuric acid concentration (201°C, 600 rev/min, 5000 mL starting solution volume)

XRD analysis was performed on the residues of the tests with low acid additions (i.e., 0.115 mol/kg H_2SO_4) to validate the chemical analysis. This is in lieu of the fact that dissolved iron could not be used as RPV during these tests; instead sulphide and total sulphur, with the difference being sulphate, were used to calculate extent of oxidation; the results are reported in Table 6.3. The mineralogical analyses indicate that iron-containing precipitates only formed at longer residence times, with significant hematite and hydronium jarosite reported after 15 minutes, i.e., prior to 10 minutes, no iron

precipitates were detected. This meant that the dissolved iron concentration could still be used as RPV during these tests (< 15 minutes). Based on solution analysis, the precipitation, thus, only occurred when the iron concentration in solution started to exceed 1.2 g/L. The XRD analyses were congruent with the chemical analysis for all three tests (see Table 6.4).

Table 6.3: XRD analysis of residues after oxidation of Sample C (-53 +38 µm) (0.115 mol/kg H_2SO_4, 600 rev/min, 495 kPa pO_2)

Minerals	Ideal mineral formula	5 min	10 min	15 min
			wt%	
Pyrite	FeS_2	51	16	2
Quartz	SiO_2	17	24	20
Pyrophyllite	$Al_2Si_4O_{10}(OH)_2$	30	59	52
Hematite	Fe_2O_3	1	<1	9
Arsenopyrite	FeAsS	1	-	-
Hydronium jarosite	$(H_3O)Fe_3(SO_4)_2(OH)_6$	-	-	17

Table 6.4: Reconciliation between XRD and ICP-OES analysis of residues generated during oxidation of Sample C (-53 +38 µm) (0.115 mol/kg H_2SO_4, 600 rev/min, 495 kPa pO_2)

	Fe		Si		Al		Total S	
	XRD	ICP-OES	XRD	ICP-OES	XRD	ICP-OES	XRD	Combustion
				wt%				
5 min residue	24.8	22.2	17.3	17.6	4.5	5.6	27.5	26.5
10 min residue	8.1	5.7	29.6	29.7	8.8	9.6	8.6	6.7
15 min residue	8.5	9.7	25.6	25.7	7.8	8.4	3.4	2.7

SEM imaging, using back-scattered electron imaging supported by EDS analyses of the residues, as shown in Figure 6.6, was used to follow the steps by which iron(III) precipitated during the oxidation period. No iron(III)-containing phases could be identified after 5 minutes' oxidation, but hematite nuclei were identified after 10 minutes' oxidation. The fact that hematite coatings/rims were not observed on existing pyrite particles is an important observation, in that it showed that the mineral kinetics were probably not inhibited by the formation of hematite, as the precipitation of hematite particles appeared to have occurred via primary nucleation. On the other hand, hydronium jarosite particles, identifiable as brighter white, fine grains in the images, were visible in the proximity of almost all the other mineral grains after 15 minutes' oxidation. The hydronium jarosite phases appeared to form solely because of secondary nucleation on all other existing surfaces. In addition, these phases appeared to be highly porous and were, therefore, not expected to limit oxidation at any point in time.

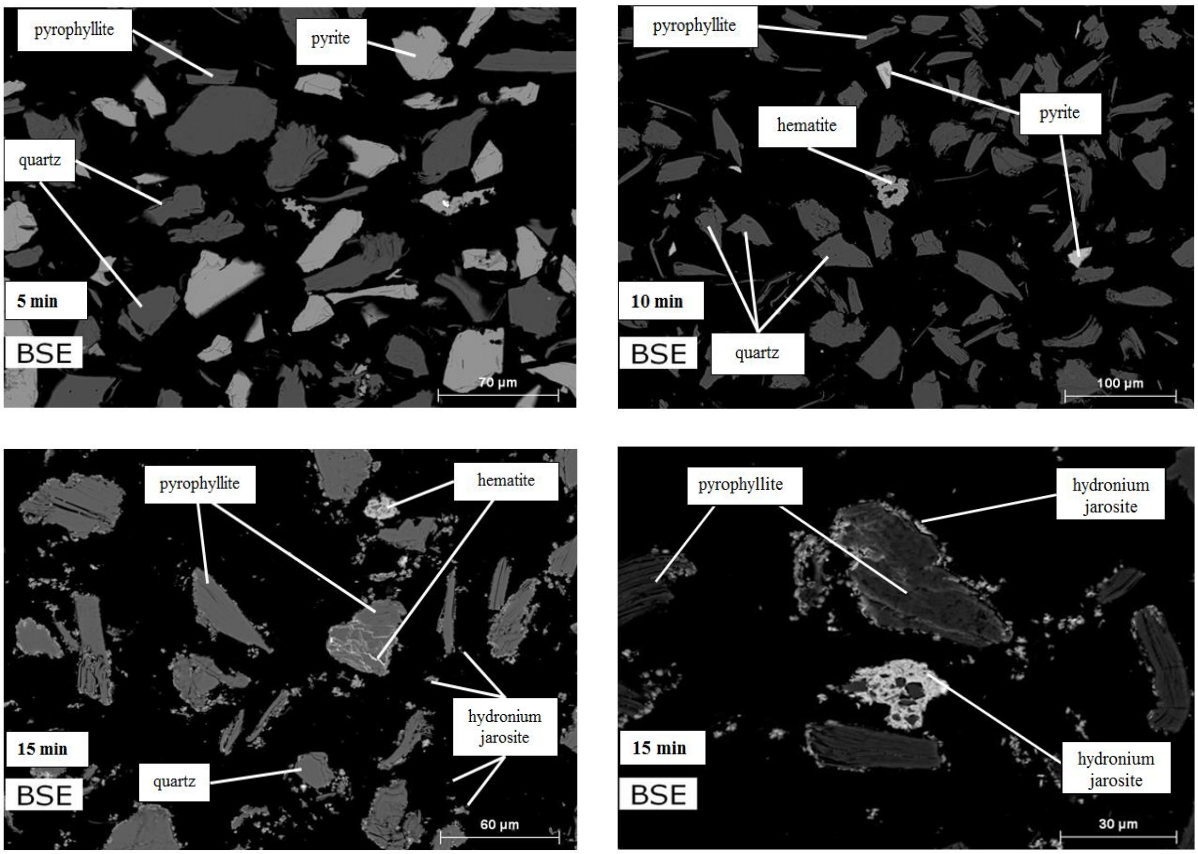

Figure 6.6: SEM back scattered electron images of the residues after oxidation of Sample C for 5 minutes, 10 minutes and 15 minutes (558 kPa pO_2, 0.054 mol/kg FeS_2, 201°C, 600 rev/min, 5000 mL starting solution volume)

6.5. Influence of particle size

The effect of particle size was investigated on Samples C, D and F and mean oxygen partial pressures of 1087, 665 and 492 kPa. The results are presented in Figure 6.7.

Apart from the tests conducted at an average partial pressure of 1087 kPa, the particle size appeared to have an insignificant influence on the rate of oxidation. According to Equation 6.3, the observed rate constant (k_s) should be directly dependent on the inverse of initial particle diameter (R_{po}), provided that the reaction rate (r_{FeS_2}) remain constant during the duration of the kinetic test.

$$k_s \propto \frac{1}{R_{po}} \qquad 6.7$$

Thus a $\log k_s$ vs. $\log R_{po}$ plot should yield a slope of -1. The log-log plots of all three particle size fractions are also included in Figure 1 and indicated that apart from the test conducted at 1087 kPa where the slope was -0.7, an increase in the average mean particle size did not affect the reaction rate significantly with slopes ranging between -0.10 and -0.15.

It is important to recall that, even though the CV values for the different size fractions associated with the different samples were not identical (Section 5.2), the variation between them (ranging between 0.29 and 0.36 for the size fractions currently under investigation), was considered small enough (< 0.5) to enable description of the reaction kinetics by assuming an uniform PSD and use of the mean particle size[r] (Cho & Sohn, 2016). It is known that the higher surface area per unit mass, associated with a smaller particle size, should yield faster dissolution kinetics, and since the variation in the mean particle size between the different size fractions was considered large, and the particle shapes similar between size fractions (see Section 5.2), these observed results were unexpected.

The fact that impurities are present in the pyrite, and that these may occur as a reactive rim on pyrite particles (Reich, Kesler, Utsunomiya, Palenik, Chryssoulis & Ewing, 2005), could explain the unexpected response of the ore to particle size reduction. Further mineralogical analysis is recommended to investigate the exact deportment of arsenic and other impurities in these samples.

As an alternative to the above explanation, there might also have been a shift in the primary oxidant with increasing particle size which would cause r_{FeS_2} to vary as the batch test proceeded, or some influence of secondary minerals on the reaction kinetics (which will be evaluated in Section 6.8)

[r] This criterion will only hold if particles are spherical. The reaction kinetics of particles with a PSD having a CV value larger than > 0.2 will already start to deviate from the reaction kinetics of particles having a uniform PSD, if the particles are flat plates (Cho & Sohn, 2016).

which could, similar to having impurities in the pyrite sample, cause the intrinsic reaction rate constant (k_{ins}) to be different for different size fractions investigated.

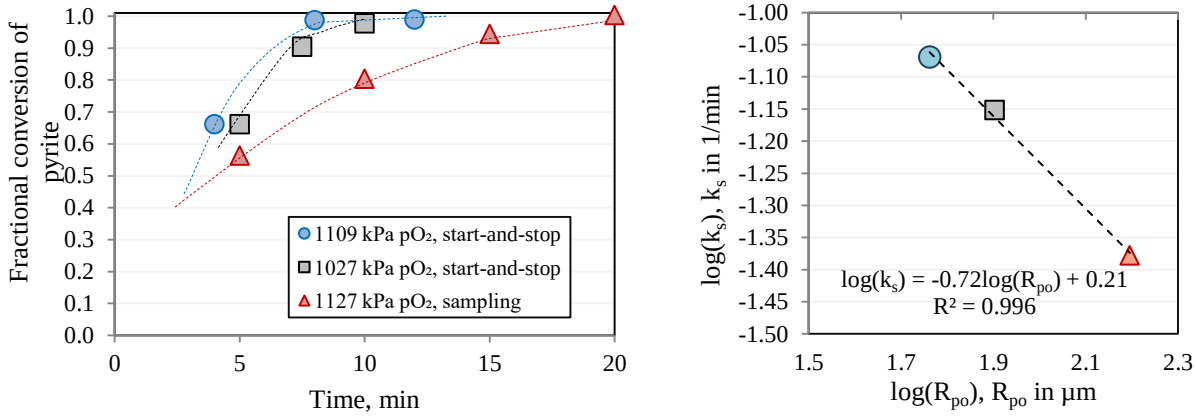

(a) 1027-1127 kPa pO2

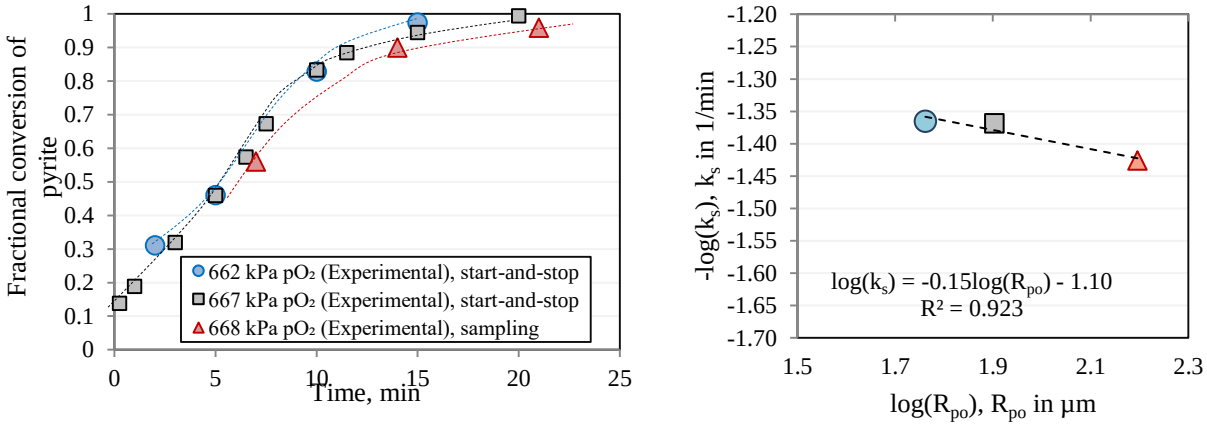

(b) 662-668 kPa pO2

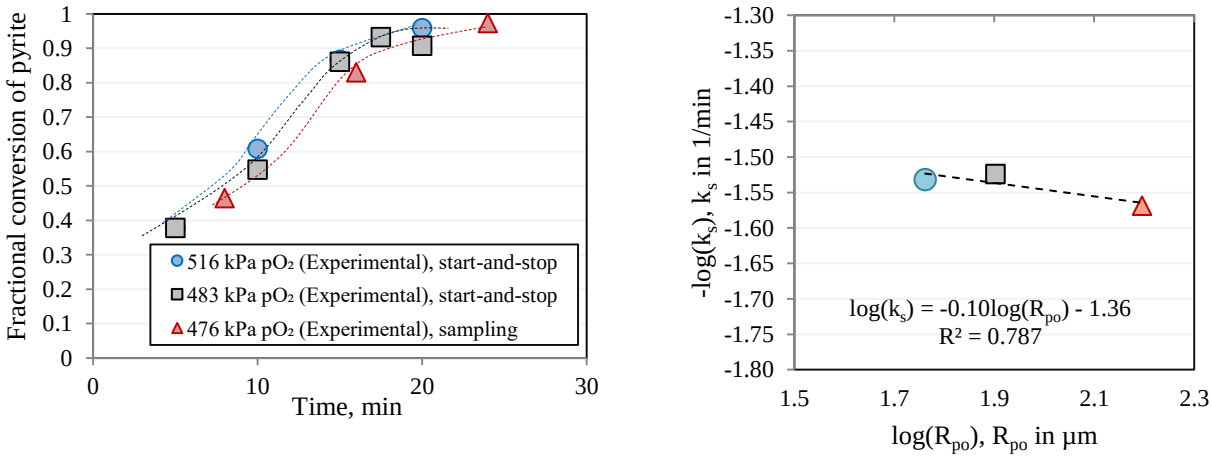

(c) 476-516 kPa pO2

-Sample C (-53+38 µm) -Sample D (-75+53 µm) -Sample F (-150+106 µm)

Figure 6.7: Influence of particle size on pyrite dissolution kinetics (600 rev/min, starting solution volume 5000 mL, 201.5°C, 0.35 mol/kg H_2SO_4, 0.050-0.057 mol/kg FeS_2)

6.6. Influence of slurry density on reaction kinetics

An increase in slurry density, from 0.057 to 0.115 mol/kg FeS_2, which corresponds to a total solids concentration increase from 0.85 wt% to 1.70 wt%, had a considerable impact on the dissolution kinetics (see Figure 6.8), with the extent of oxidation decreasing by almost 20% at the oxidation times recorded.

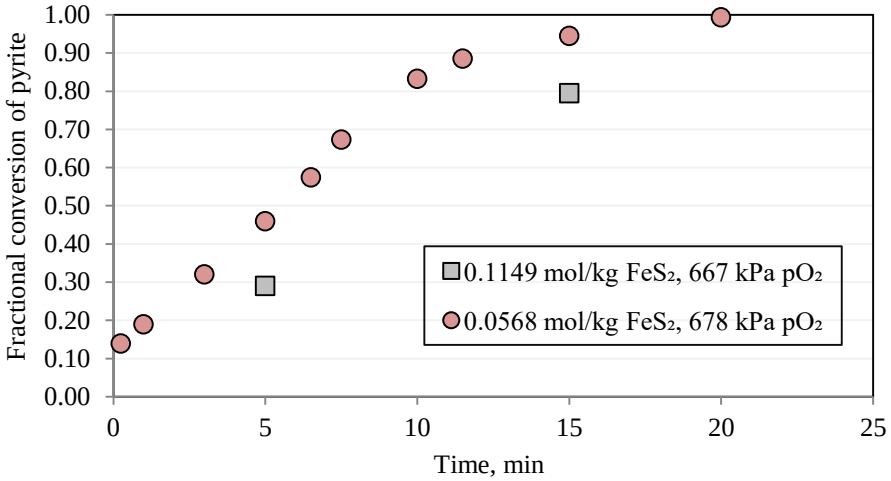

Figure 6.8: Influence of slurry density on pyrite oxidation kinetics (600 rev/min, starting solution volume 5000 mL, 201.5°C, 0.35 mol/kg H_2SO_4)

Since it is known that an excess of dissolved oxygen would be present for these conditions (as will be shown in Section 7.8), a reduction in the reaction rate due to oxygen "starvation" was unlikely. As mentioned before, the measured activation energy (124 kJ/mol) did not support a diffusion-controlled step, such as gas-liquid mass transfer, to be rate-controlling. Therefore, secondary effects were likely the cause of the phenomenon.

A pyrite oxidation rate dependency on the iron(II)/iron(III) concentration ratio (i.e., iron(III)/iron(II) couple) could serve as a plausible explanation. Initial iron(II) concentrations were doubled, with an increase in solids concentration, and could thus potentially have slowed down the kinetics considerably.

It is also worthwhile to consider the fact that, as solids density increases, the pyrophyllite and quartz addition also increased. In view of the fact that the surface area (i.e., particle size) had an almost negligible effect on reaction rate (see Section 6.5), a phenomenon that may also be related to secondary mineral content, an investigation into the potential role of secondary minerals was initiated.

6.7. Effect of secondary minerals

To evaluate whether the presence of pyrophyllite and quartz could have had any impact on the rate of pyrite oxidation, Sample D was upgraded further by flotation. The upgraded flotation concentrate

from Sample D was denoted as “Sample DD” and the associated chemical analysis of Sample D and Sample DD is included in Table 6.5. The mineralogical analysis is reported in Table 6.6.

Table 6.5: Chemical analysis of major elements in Samples D and DD

Sample	Al	Fe	Si	Total sulphur	S/Fe
		wt%			mole/mole
D	2.40	35.55	8.95	39.57	1.94
DD (upgraded)	1.46	40.30	5.44	46.70	2.02

Table 6.6: XRD mineralogical composition of Samples D and DD

Mineral	Mineral ideal formula	Sample D	Sample DD (upgraded)
		wt %	wt %
Pyrite	FeS_2	73	86
Quartz	SiO_2	11	10
Pyrophyllite	$Al_2Si_4O_{10}(OH)_2$	16	4

Both chemical and mineralogical analysis confirms that the pyrite concentrate had been upgraded from an initial pyrite content of 73 wt% to a final content of 86 wt%. The pyrophyllite content decreased, from 16 wt% to 4 wt%. Notable in the chemical analysis is also the change in the S/Fe ratio, from 1.94 to 2.02 when the sample was upgraded, suggesting that some iron (~1 wt%) may have been associated with pyrophyllite, thus, resulting in an iron-to-sulphur ratio closer to the ideal ratio of pyrite upon removal of pyrophyllite. Alternatively, this could have indicated that smaller pyrite particles had iron-to-sulphur ratios further removed from the ideal pyrite iron-to-sulphur ratio (possibly associated with other minerals, such as arsenopyrite, FeAsS). However, until further mineralogical analysis is conducted on the pyrophyllite particles, these arguments remain speculative. In any case, irrespective of whether this might have been true, the effect on the calculated sulphide oxidation extent would have been, at most, 3%, which is within the experimental error of this study.

The particle size distribution (measured by a Saturn Digisizer) was analysed again and compared to the original PSD of Sample D. The associated characteristic parameters of the PSDs are included in Table 6.7. The PSDs of the samples compared very well with each other. The upgraded concentrate (Sample DD) had a slightly larger PSD mean, of 83.9 µm (compared to the original mean of 80 µm). This indicates that a large portion of the finer particles (mainly pyrophyllite particles smaller than 53 µm) had been removed from the sample during flotation. The upgraded concentrate also had a smaller span, of 70%, compared to the initial span of 75%. From the PSD it was therefore expected that the upgraded concentrate would oxidise at a marginally slower rate than the original sample.

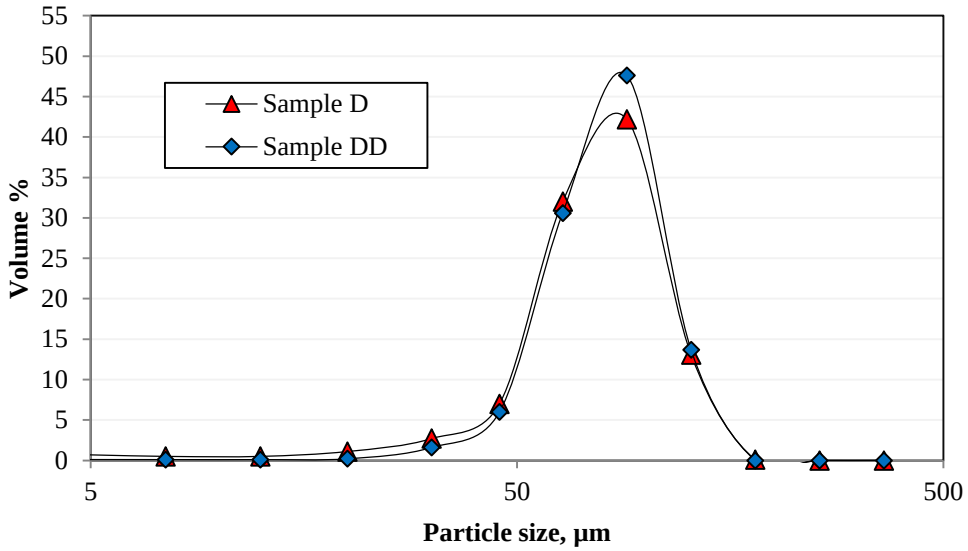

Figure 6.9: Particle size distribution of Sample D and Sample DD

Table 6.7: Arithmetic mean, median, span and CV of the volume particle size distributions

Sample	Arithmetic mean	μ^s	d_{50}	d_{10}	d_{90}	Span[t]	Variance (σ^2)[u]	CV[v] (σ/μ)
	µm	um	µm	µm	µm	%	-	-
D	64	80.0	79	50	110	75	723	0.336
DD	64	83.9	82	55	112.5	70	532	0.275

Two kinetic tests were subsequently performed on the two flotation concentrates. The pyrite addition was kept approximately constant, between 0.054 and 0.057 mol/kg. This meant that the total solids loading was slightly higher during oxidation of Sample D, with higher pyrophyllite and quartz content, compared to oxidation of Sample DD. The results of the oxidation tests conducted on Sample DD, as well as Sample D, are included in Table 6.8.

[s] Mean of distribution, $\mu = \sum_{i=1}^{n} d_i^* f_i$

[t] Distribution span: $100\times(d_{90}-d_{10})/d_{50}$

[u] Variance of sizes around the mean, $\sigma^2 = \sum_{i=1}^{n}(d_i^* - \mu)^2 f_i$

[v] Coefficient of variation (relative spread around of sizes around mean), CV= σ/µ

Table 6.8: Batch oxidation test results on Sample DD and Sample D (201°C)

Repeat	Test #	pO_2	Pyrite added	Time	Fe_{total}	Fe(II)	H_2SO_4	Fe residue	Total S residue	Fractional FeS_2 conversion (%)			
		bar	mol/kg	min	g/L	g/L	g/L	Wt%	Wt%	Based on Fe total in solution	Based on Fe in residue	Based on S in residue	Average
1	D35	6.45	0.0559	3	1.15	1.0	37	32.20	37.50	33.2	31.99	27.84	31
2	DD41	6.48	0.0543	3	1.25	1.2	38	39.80	43.00	37.0	31.16	35.82	35
1	D36	6.83	0.0571	7.5	2.24	1.9	39	25.70	30.00	64.2	61.93	62.25	63
2	DD40	6.71	0.0544	7.5	2.23	2.0	37	33.10	36.10	68.0	66.80	68.87	68

The kinetic data points at 3 minutes and 7.5 minutes both suggested that Sample DD had oxidised faster than Sample D, with the fractional pyrite conversion, based on all indicators, higher. At 3 minutes the oxidation extent was 35% for Sample DD and only 31% for Sample D. Similarly, at 7.5 minutes the oxidation extent was 5% higher for Sample DD than Sample D, i.e., 68% vs. 63%. The pyrite addition during utilisation of Sample DD was 2.8-4.8% lower than Sample D. The data reported above provides some support for the suggestion that a higher gangue content might have inhibited the oxidation of the pyrite, possibly by direct screening of the surface of the pyrite, by releasing iron(II) iron into solution or, indirectly, the dissolution of silica and the precipitation of a polymeric silica layer on the pyrite – as has been shown by Espiari, Rashchi and Sadrnezhaad (2006) to be the case in the treatment of zinc tailings. From these findings, further mineralogical analysis of the pyrophyllite particles is strongly recommended.

6.8. Existence of an induction period and pre-oxidation

An induction period was noted in most of the batch oxidation plots. Oxidation curves where the effect was most noticeable are included in Figure 6.10 – red S-shapes drawn on the plots illustrate this effect clearly. The effect was also studied further by including more data points on a single batch oxidation curve, especially during the 0 to 5 minutes operating window, as shown in Figure 6.11.

Experimental data points at 0.25 and 1 minute, in Figure 6.11, clearly show that pre-oxidation had occurred. Approximately 15% of the pyrite had already oxidised prior to the start of the test. Since it was known that pre-oxidation did not occur during the heating period (Section 3.2.4.2), the oxidation that occurred prior to time "zero" was certainly associated with the injection period. On average, it took approximately 1 to 1.5 minutes to adjust impeller speed, inject the required acid, inject the wash water and to adjust the oxygen partial pressure of the system. This period, thus, allowed for oxidation to occur, especially in this highly reactive system. The effect may be accounted for in the batch simulation, by including the injection period and introducing a step change in the oxygen partial pressure (shown in Section 7.2).

The plots of $1-(1-X)^{1/3}$ against time were included in Figure 6.10 and Figure 6.11, to evaluate whether the macroscopic behaviour of the system can be satisfactory modelled with the USP model. If the system is surface reaction controlled, these plots should yield straight lines. In general, high correlation coefficients ($R^2 > 0.93$) were obtained, however, the S shapes around the ideal USP-surface chemical reaction plots indicate that the initial oxidation rate was slower than the oxidation rate towards the end of the batch tests. Similar effects have not been observed on the batch POX kinetic curves in the previously published work of Long and Dixon (2004) and Papangelakis and Demopoulos (1991).

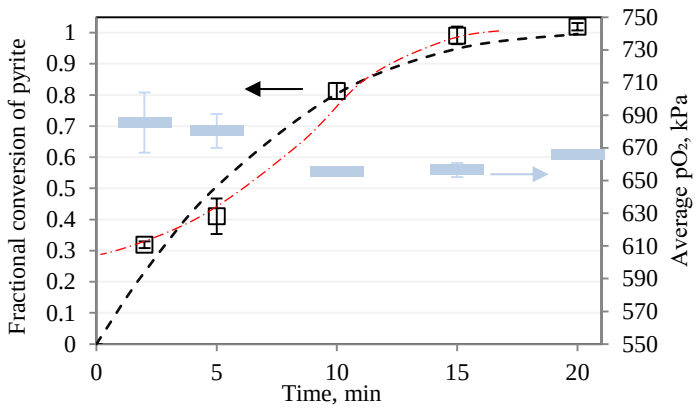

□- *Pyrite conversion,* ▬ *- Partial pressure*

Sample C (-53+38 µm), 0.054 mol/kg FeS_2, start-and-stop

(a)

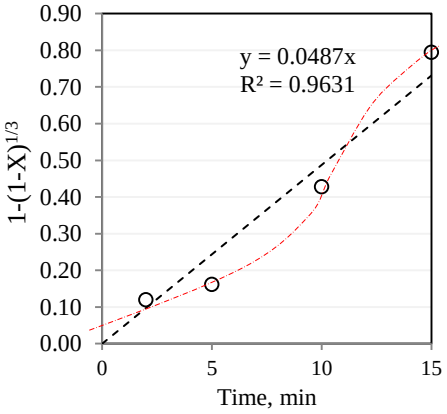

(b)

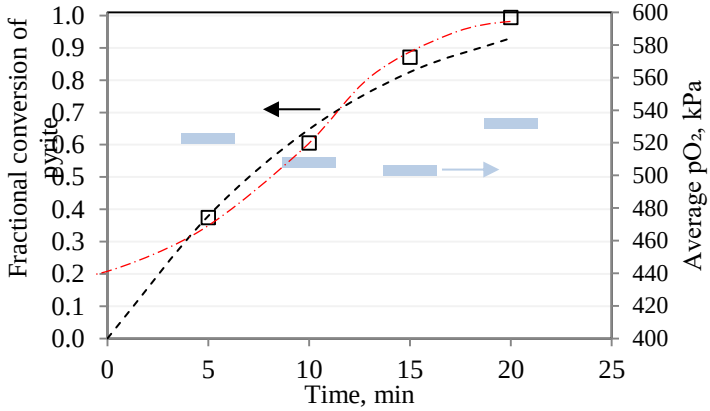

□- *Pyrite conversion,* ▬ *- Partial pressure*

Sample C (-53+38 µm), 0.053 mol/kg FeS_2, start-and-stop

(c)

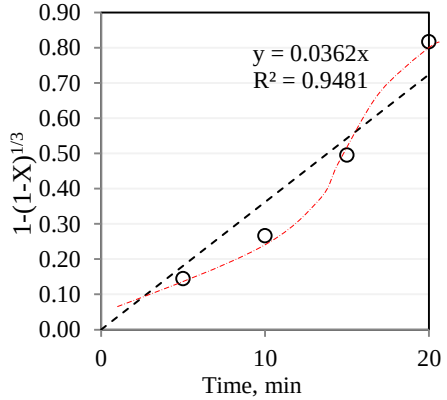

(d)

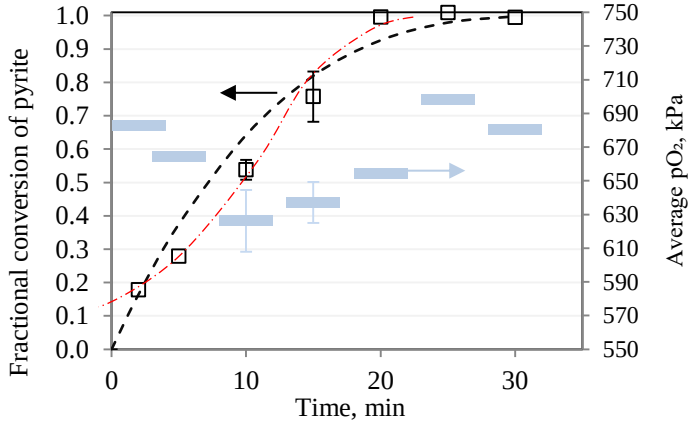

□- *Pyrite conversion,* ▬ *- Partial pressure*

Sample E (-106+75 µm), 0.092 mol/kg FeS_2, start-and-stop

(e)

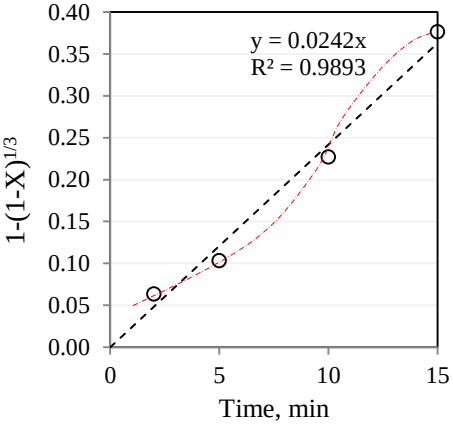

(f)

Figure 6.10: Curves showing typical S-shape around ideal USP-surface chemical reaction plots (Experimental conditions: 0.35 mol/kg H_2SO_4, 201.5°C, 600 rev/min, starting volume 5000 mL)

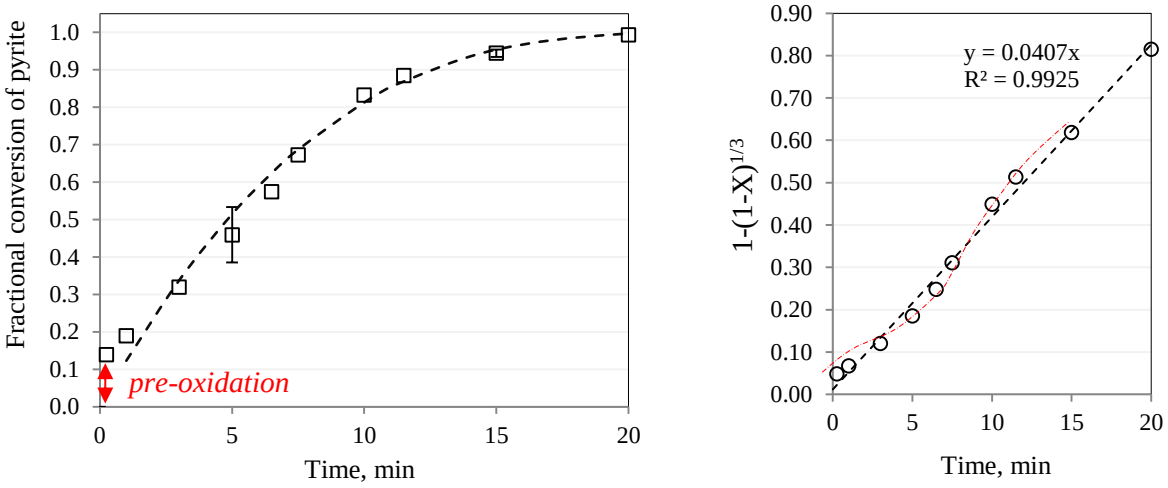

Sample D (-75+53 µm), 0.057 mol/kg FeS_2, start-and-stop

Figure 6.11: Batch oxidation curve showing pre-oxidation and typical S-shape around ideal USP-surface chemical reaction plots (Experimental Conditions: 0.35 mol/kg H_2SO_4, 201.5°C, 667 kPa pO_2, 600 rev/min, starting volume 5000 mL)

From the literature search (see Section 2.6.1), the role of iron(III) as an oxidant at typical POX conditions has not been studied in isolation. Steyl (2012: 357) proposes that iron(III) play a lesser role as an oxidant at POX conditions, because iron(III) has a large hydration sphere, whereas oxygen can approach the surface of pyrite more closely. However, Luther (1987) provides a detailed discussion as to why iron(III) is a superior oxidant compared to oxygen, based on molecular orbital theory considerations (see Section 2.6.1.2 for full discussion). The induction period noticed on the batch oxidation curves shown in Figure 6.10 suggest that iron(III) may have to be considered as an oxidant at POX conditions, which is in agreement with the proposal by Zhukov et al. (2015), who modelled the experimental data published by Long and Dixon (2004) based on this assumption. Since the dissolved oxygen was in excess and was kept constant at the conditions the test work was conducted at (see Section 7.2 for predicted dissolved oxygen concentrations), and iron(III) had to be generated in situ by pyrite dissolution, a rate dependency on iron(III) concentration served as a plausible explanation for the observed "lag" period. This possibility will be revisited in Section 7.2.

Aside from the possible role of iron(III) in contributing to these observed S-shaped curves around the ideal USP plots, other factors that may also have played a role will be considered in Sections 6.8.1 to 6.8.3 to follow.

6.8.1. Experimental artefacts

6.8.1.1. Pressure fluctuations

To investigate experimental artefacts associated with pressure control as a possible cause for the observed induction period, the average oxygen partial pressure for each test was also included in Figure 6.10. As shown, increased partial pressures were almost always observed at the start of each test. Upon oxygen addition, the sample initially consumed oxygen very rapidly; however, for the regulator to introduce fresh oxygen into the system, a certain pressure difference between the system and the regulator had to be attained. Low sensitivity of the regulator, thus, delayed the recovery of oxygen pressure to the set point value slightly. At first, it was thought that this behaviour could have been the cause of the observed S-shaped curves, however, as indicated by the experimental errors on the initial data points (see Figure 6.10a), the initial pyrite oxidation rate was relatively insensitive to variation in oxygen partial pressure. Therefore, pressure fluctuations were not considered to be the cause of the observed induction period.

6.8.1.2. Temperature fluctuations

Since cold acid was injected at the start of each test, an initial temperature upset could have impacted the rate of the reaction – this could have had a marked impact on the oxidation rate, especially in such a highly reactive system. Evaluation of the recorded temperature measurements indicate that a 0.5-2°C temperature drop did occur during the reagent addition period, however due to the exothermic nature of the sulphide oxidation reaction, the temperature was restored to the set-point value less than 1 minute after the oxygen partial pressure was adjusted. As observed from Figure 6.2, the observed lag periods only occurred after 3 minutes into the tests, therefore, a temperature drop at the start of the test was not likely to be the cause of the induction period.

6.8.2. Elemental sulphur formation

The induction period could have been due to the formation of dense microscopic elemental sulphur layers on the surface of particles, which consequently inhibited the transfer of dissolved oxygen to the surface of pyrite particles. Trace amounts of elemental sulphur (< 1 wt%) had been detected in some of the residues. To assess whether elemental sulphur was causing this phenomenon, separate kinetic batch tests were done with the addition of ~0.5 g/L lignosulphonate (LS). The lignosulphonate was injected via the acid feed bomb at the start of the test.

LS is commonly used as sulphur dispersant in industrial zinc sulphide oxidation operations. The strong adsorption of LS on sulphide mineral surfaces reduces the attraction between elemental sulphur

and the mineral surface, thus, preventing it from reducing the leach kinetics (Owusu et al., 1995). The results of current test work are included in Figure 6.12.

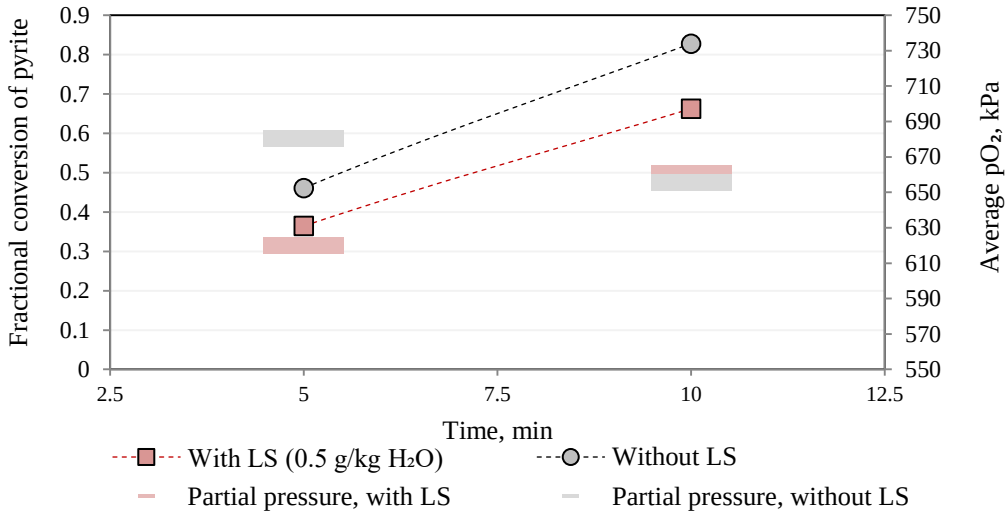

Figure 6.12: Batch oxidation curve showing the effect of lignosulphonate addition on the rate of pyrite oxidation (Experimental conditions: 0.054 FeS_2 mol/kg, 0.35 mol/kg H_2SO_4, 201.5°C, 600 rev/min, starting volume 5000 mL)

The results, 5- and 10-minute data points, clearly indicate that the addition of LS decreased the rate of pyrite oxidation and that the surfactant remained active for the duration of the experiments, i.e., degradation was not a factor at these short reaction times. Even though a large variation in the oxygen partial pressure existed at the 5-minute data point, the difference in fractional conversion (36% vs 46%) could not be related solely to the effect of oxygen partial pressure on leach kinetics. At 10 minutes, the addition of LS clearly reduced the leach kinetics. Since the addition of LS had the opposite effect than what it would have had in the presence of elemental sulphur, coating by elemental sulphur was unlikely to be responsible for the observed induction period.

6.8.3. Fe-oxide precipitation during the heating period

Alternatively, the induction period could have been caused by minor amounts of dissolved iron precipitating as an iron hydroxide/oxide on the surface of the pyrite particles during the heating period. It is known that the electrical conductivity of iron oxide phases, such as hematite, are lower than that of pyrite (Telford, Geldart & Sheriff, 1990: 385), which could, therefore, slow down the rate of electron transfer to the surface (Tabelin et al., 2017). Once the acid is injected, it may take a few minutes for the hydroxide layer to be dissolved before the observed pyrite oxidation kinetics is restored to its true rate.

SEM imaging and EDS analyses were used to characterise the residues generated at 15 seconds and 1 minute, to establish whether such iron oxide coatings were visible. EDS-generated elemental colour

images are shown in Figure 6.13. As seen, no visible iron oxide layers were detected on any of the pyrite particles. This was also confirmed by further magnification (not shown here). It is, however, acknowledged that SEM imaging may not be considered as a conclusive technique for studying very thin surface coatings, therefore, further analysis, beyond the scope of the current investigation, may have to be done to ascertain whether iron(III) oxide coatings may have limited the reaction rate at the start of the oxidation process.

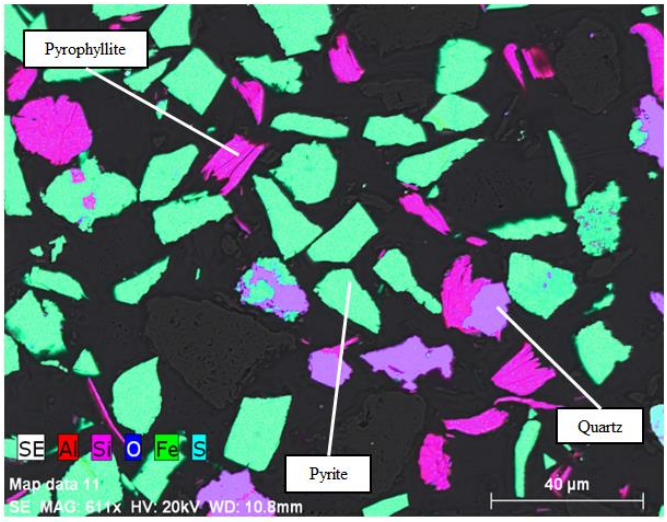

(a) 15 seconds, 14% pyrite oxidation

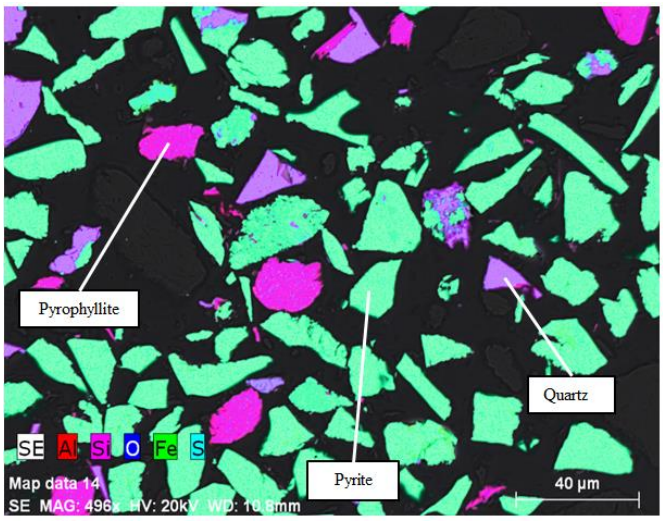

(b) 1 minute, 19% pyrite oxidation

Figure 6.13: SEM images with EDS-generated elemental colouringon pyrite batch oxidation residues to investigate whether Fe-oxide layers were present on pyrite particles (Experimental conditions: Sample D, 0.057 mol/kg FeS_2, 587 kPa pO_2, 0.35 mol/kg H_2SO_4, 201.5°C, 600 rev/min, starting volume 5000 mL)

6.9. Summary

The above sections provided preliminary data processing that indicated that the rate of pyrite oxidation could be expressed by the following rate equation:

$$r_{Fes_2} = k_1[O_2]^{1.1\ to\ 1.4}[H^+]^{-0.2\ to -0.3} \quad 6.8$$

However, S-shapes around the ideal USP-surface chemical reaction plots, and/or distinct lag periods on the kinetic curves, suggest some dependence on the iron(III) concentration with increasing oxidation time. Due to the high reactivity of the sample, some degree of pre-oxidation occurred during the reagent addition period. This may have affected the derived reaction orders.

The activation energy of pyrite was calculated as ~108-121 kJ/mol (180 to 210°C), which indicates that chemical reaction on the surface was rate controlling, and that no diffusional limitations had taken place (neither by diffusion from the gas to the liquid phase, nor by diffusion of the reagent species through the boundary layer to the surface of pyrite).

Other observations include a very weak dependency of the oxidation rate on particle surface area (or particle size), a lower rate of oxidation at higher slurry density, and a possible decreased rate of oxidation caused by the presence of secondary minerals.

To obtain more confidence in the derived reaction orders, a batch oxidation model was developed in Matlab, wherein the changes in iron(III) and iron(II) concentrations, as well as some of the experimental artefacts, such as pre-oxidation during the reagent addition period, were considered. The modelling framework and results are presented in Chapter 7.

7. MODELLING OF THE BATCH PYRITE OXIDATION SYSTEM

This chapter will describe the key aspects of the model that was used for kinetic parameter estimation by regression of the simulation to the batch kinetic experimental data, as well as the associated results.

7.1. Modelling framework

7.1.1. Reactions

The following reactions were taken into consideration during modelling of the pyrite oxidation process:

On the surface of pyrite particles: Pyrite oxidation

$$FeS_2 + 0.5O_2 + 2H^+ \rightarrow Fe^{2+} + 2S^\circ + H_2O \quad 7.1$$

$$FeS_2 + 2Fe^{3+} \rightarrow 3Fe^{2+} + 2S^\circ \quad 7.2$$

$$2S^\circ + 2H_2O + 3O_2 \rightarrow 2SO_4^{2-} + 4H^+ \quad 7.3$$

In the bulk solution phase: Homogeneous iron(II) oxidation

$$Fe^{2+} + 0.25O_2 + H^+ \leftrightarrow Fe^{3+} + 0.5H_2O \quad 7.4$$

It was assumed that both iron(III) and oxygen could act as oxidants and that all sulphate is produced via an elemental sulphur intermediate. Reaction 7.3 was incorporated to provide larger flexibility in terms of predicting elemental sulphur yields and sulphuric acid concentrations.[w] It was also assumed that all generated iron(III) originated from the homogeneous oxidation of iron(II).

Reaction 7.4 represents the homogenous oxidation of iron(II) to iron(III) in the bulk solution phase. This reaction was presumed to be completely independent of reactions occurring on the pyrite surface. In other words, it was assumed that this reaction was not catalysed by the presence of pyrite, since very low solids densities were employed during the study. This assumption may have to be reviewed in the future, when high pulp density results are available.

Iron(III) precipitation was not accounted for, as sulphuric acid addition was carefully chosen to avoid iron(III) precipitation in most of the tests that were used for the regression. When the effect of low

[w] However, as already mentioned in Section 6.8.2, this was later found not to be required, as only trace amounts of elemental sulphur were detected in the residues.

acid concentrations (i.e., at sulphuric acid additions of 10 g/L) was tested, and hematite precipitation occurred, the pyrite oxidation extent had been based solely on sulphide sulphur analysis of the residues and not on iron (neither in solution nor in the residues).

Regarding other minerals, it was assumed that pyrophyllite, as well as silica, remain inert during the process. The amount of MgO added (which was less than 230 mg/L in all cases) were also considered negligible in terms of its effect on the sulphur balance, due to possible kieserite precipitation.

7.1.2. Rate equations

7.1.2.1. Pyrite oxidation

From literature discussed in Chapter 2, the concentrations of aqueous oxygen, iron(III) and iron(II) should be considered in the intrinsic rate equation of pyrite oxidation. Preliminary modelling of the data (presented in Chapter 6) indicates a reaction order in oxygen concentration, ranging between 1.1 and 1.4; however, no correction was made for the possible direct reaction between pyrite and iron(III), which may have slightly increased this value. In the simulation, provision was made for the oxidation of pyrite, with both of these reagents occurring at separate rates, where r_1 and r_2 represent the rate of oxidation of pyrite with oxygen and iron(III) via Reactions 7.1 and 7.2, respectively.

$$r_{FeS_2} = r_1 + r_2 \quad 7.5$$

$$r_1 = k_1[H^+]^{n_1}[O_2]^{n_2} \quad 7.6$$

$$r_2 = k_2[Fe^{(III)}]^{n_3} \quad 7.7$$

where k_1 and k_2 represent the reaction rate constants with units of $mol^{(1-(n_1+n_2))}.kg^{(n_1+n_2)}/m^2.min$ and $mol^{(1-n_3)}.kg^{n_3}/m^2.min$ respectively, and with all reagent concentrations expressed in mol/kg H_2O, i.e., molality. All reaction rates (r_{FeS_2}, r_1, and r_2) are expressed in $mol/m^2.min$.

In terms of sulphur conversion to sulphate, a first order reaction in both elemental sulphur and dissolved oxygen concentration was assumed. Since only trace amounts of elemental sulphur was observed in some residues, an arbitrary, large rate constant was assumed for this reaction, to ensure full conversion to sulphate. Since the formation of elemental sulphur was observed to have no impact on the oxidation rate of pyrite, according to the findings presented in Section 6.8.2, it was also assumed to occur at a rate independent of the pyrite surface area, i.e., not on the pyrite surface itself.

$$r_3 = k_3[S^o][O_2] \quad 7.8$$

where r_3 and k_3 is expressed in mol/m^2.min and in kg^2/mol.m^2.min, respectively. The above assumption might have to be reviewed in future, when higher slurry density test work data become available.

To adjust the rate constants for an increase in temperature, a modified form of the Arrhenius activation energy relationship, presented in Section 6.2, was used.

$$k_1=k_{R1}\exp\left(\frac{-E_{A1}}{R_g}\left(\frac{1}{T}-\frac{1}{T_{R1}}\right)\right) \quad 7.9$$

$$k_2=k_{R2}\exp\left(\frac{-E_{A2}}{R_g}\left(\frac{1}{T}-\frac{1}{T_{R2}}\right)\right) \quad 7.10$$

$$k_3=k_{R3}\exp\left(\frac{-E_{A3}}{R_g}\left(\frac{1}{T}-\frac{1}{T_{R3}}\right)\right) \quad 7.11$$

Where k_{Ri} refers to the measured intrinsic reaction rate constant at the reference temperature (T_{Ri} in K) for each i^{th} reaction listed above.

7.1.2.2. Iron(II) to iron(III) homogeneous oxidation rate

The iron(II) to iron(III) homogenous oxidation rate was not studied in isolation during the test work campaign. Such a kinetic study with synthetic iron(II) sulphate in sulphuric acid solutions between 180 and 230°C was conducted by Ruiz et al. (2016). Therefore, the published experimental data of Ruiz et al. (2016) was reinterpreted in terms of the rate equation and the corresponding activation energy calculated. The raw data, as well as the details of the procedure employed to arrive at a rate equation, are included in Appendix C.4.

The oxidation rate of iron(II) was modelled by the following equations:

$$r_4 = k_4[H^+]^{-0.25}[Fe^{(II)}]^2[O_{2(aq)}]\,, mol/kg.min \quad 7.12$$

$$k_4 = k_{R4}\exp\left(\frac{-E_{A4}}{R}\left(\frac{1}{T}-\frac{1}{T_{R4}}\right)\right),\ kg^{1.75}/mol^{1.75}.min \quad 7.13$$

where r_4 and k_4 have the units mol/kg.min and kg$^{1.75}$/mol$^{1.75}$.min, respectively.

The second-order (or bimolecular) dependency in iron(II) concentration and first-order dependency in oxygen concentration is widely accepted (Ruiz et al., 2016; Steyl, 2012: 98-101). It has also been shown that increasing hydrogen ion molality decreases the rate of oxidation. Other metal concentrations were considered too low (Cu < 5 mg/L, Zn < 20 mg/L and Al < 25 mg/L) to catalyse the iron(II) homogenous oxidation rate.

7.1.3. Equilibrium aqueous oxygen concentration

An empirical equation provided by Tromans (1998a) to predict the oxygen solubility in aqueous solutions based on thermodynamic analysis, was used during simulation of the current system. The relationship proved to be accurate at temperatures up to 200°C and sulphuric acid concentrations ranging to 1.59 mol/kg (Tromans, 1998b), which is well beyond the range of sulphuric acid concentrations employed during this study. The complete set of equations used to predict the oxygen solubility is included in Appendix C.2.

7.1.4. Rate of particle shrinkage

Following from the preceding equations provided in Chapter 6, Equations 6.1 to 6.3, the particle radius shrinkage as a function of time, i.e., a dynamic description of the change in particle radius, may be expressed as follows:

$$\frac{dR_p}{dt} = \frac{-r_{FeS_2} MW_s}{\rho_s}, m/s \qquad 7.14$$

The rate of the fractional conversion of a pyrite particle during a batch oxidation test may be described according to Equation 7.15.

$$\frac{dX}{dt} = \frac{3r_{FeS_2} MW_s (1-X)^{2/3}}{\rho_s R_{po}}, 1/min \qquad 7.15$$

The above equations are valid strictly for a single particle size or monosized feed. Since the particle size fractions were screened into narrow-sized fractions, as shown in Chapter 5, and the CV values of all size fractions were shown to range between 0.29 and 0.42, integration over all particle sizes to obtain a mean conversion was not required. This assumption is supported by the analysis conducted by Cho and Sohn (2015), who showed that, for spherical particles, the PSD may be approximated by a uniform size distribution as long as the CV values are smaller than 0.50 (Cho & Sohn, 2016).

7.1.5. Speciation

The speciation and complexation of the major species (Fe^{2+}, Fe^{3+}, H^+, HSO_4^{2-} and SO_4^{2-}) were not considered in this study and, therefore, only apparent reaction orders were obtained from the simulation results and regressions. Sulphuric acid was, however, modelled as a monoprotic acid (see discussion to follow) in all simulations, to enable prediction of the hydrogen ion concentration.

It is known that sulphuric acid is a strong acid and dissociates fully into the bisulphate anion and hydrogen cation. The dissociation of the bisulphate anion is, however, incomplete at lower pH values,

which usually complicates the prediction of the hydrogen ion activity, especially at temperatures lower than 100°C. The dissociation of the bisulphate ion decreases with an increase in temperature, such that its dissociation may be ignored at 200°C, even in highly acidic conditions (discussed in more detail in Appendix C.1).

7.1.6. Oxygen gas-liquid mass transfer

In the batch model, the rate of oxygen gas absorption into the aqueous solution was described by Equation 7.16, as proposed by Danckwerts (1970), assuming that the rate controlling step is the mass transfer through the boundary layer on the liquid side of the gas-liquid interface, and extrapolated to the temperatures employed during this study according to Equation 7.17:

$$\frac{d[O_2]}{dt} = k_L a([O_2]^* - [O_2]) \qquad 7.16$$

$$k_L a = k_L a_{ref} \left(\frac{-E_{A5}}{R_g} (\frac{1}{T} - \frac{1}{T_{R5}}) \right) \qquad 7.17$$

The $k_L a$ value and the associated activation energy (E_{A5}) were independently measured (refer to Chapter 4).

7.1.7. Differential equations

Characterisation of the dynamic behaviour of the high-temperature oxidation of pyrite in a batch stirred reactor requires the description of the component processes in terms of differential equations. For this purpose, it was assumed that the reactor was perfectly mixed, had a constant volume and operated at constant temperature and pressure in both position and time within the reactor. Furthermore, since the experimental work was conducted in a closed-end reactor, oxygen was continuously fed into the reactor to maintain the required oxygen partial pressure. This, in essence, infers semi-batch mode of operation.

The differential equations were based on material balances for each species and the kinetics of the processes involved for each species. The material balance around pyrite was done in terms of the reactions occurring on the surface of the mineral based on the shrinking particle model, whereas the rates of iron(II) oxidation and iron(III) precipitation were dependent on bulk solution concentrations. The stoichiometric coefficients used and the relevant reaction rates were presented in Section 7.1.1 and 7.1.2, respectively.

Assuming a monosize particle distribution, the mean conversion rate of the pyrite feed sample may be described by Equation 7.18:

$$\frac{dX_{mean}}{dt} = \frac{3r_1 MW_s(1-X)^{2/3}}{\rho_s R_{po}} + \frac{3r_2 MW_s(1-X)^{2/3}}{\rho_s R_{po}}, 1/min \quad 7.18$$

To describe the dissolved oxygen content, both the rate at which it absorbs into the solution phase and the rate at which it reacts with pyrite, iron(II) and elemental sulphur were taken into account:

$$\frac{d[O_2]}{dt} = k_L a([O_2]^* - [O_2]) - 0.5\, N_{FeS_2:0} \frac{3r_1 MW_s(1-X)^{\frac{2}{3}}}{\rho_s R_{po}} - 0.25r_4 - 1.5r_3 \quad 7.19$$

The rates of change of the other species in the bulk solution were described by:

$$\frac{d[Fe(II)]}{dt} = N_{FeS_2:0} \frac{3r_1 MW_s(1-X)^{2/3}}{\rho_s R_{po}} + 3N_{FeS_2:0} \frac{3r_2 MW_s(1-X)^{2/3}}{\rho_s R_{po}} - r_4 \quad 7.20$$

$$\frac{d[H_2SO_4]}{dt} = -N_{FeS_2:0} \frac{3r_1 MW_s(1-X)^{2/3}}{\rho_s R_{po}} - 0.5r_4 + r_3 \quad 7.21$$

$$\frac{d[Fe(III)]}{dt} = r_4 - 2N_{FeS_2:0} \frac{3r_2 MW_s(1-X)^{2/3}}{\rho_s R_{po}} \quad 7.22$$

$$\frac{d[S^o]}{dt} = 2N_{FeS_2:0} \frac{3r_1 MW_s(1-X)^{2/3}}{\rho_s R_{po}} + 2N_{FeS_2:0} \frac{3r_2 MW_s(1-X)^{2/3}}{\rho_s R_{po}} - r_3 \quad 7.23$$

For the current simulation, it was assumed that the mass of the solvent, namely, water, remained constant for the duration of the test. The assumption is reasonable, considering the low slurry densities (~1 wt% solids) employed during the tests. In addition, all species concentrations were expressed in molal concentration units, that is mol/kg solvent. This convention was followed as the unit is independent of the solution volume, which changes significantly with temperature. Appendix C.5 provides details regarding the conversion from the molarity to molality concentration unit.

The differential equations were numerically solved in Matlab with an ordinary differential equation (ODE) solver, namely ODE45, which is one of the library functions available in the software. The ODE45 solver is based on the Runge-Kutta-Fehlberg integration algorithm with variable step size.

For each test, the set of initial conditions and the interval of integration were supplied. The Matlab code employed to model pyrite oxidation in the batch reactor is provided in Appendix F.

7.1.8. Kinetic parameter estimation

7.1.8.1. Objective functions and model performance

Two model cases were compared during regression of the experimental data:

- Case Study 1 – pyrite oxidation with only oxygen (i.e., $r_1 > 0$, $r_2 = 0$), first order in dissolved oxygen concentration and the order in proton concentration fixed at -0.3 (as per the outcomes of the data analysis presented in Section 6.4).
- Case Study 2 – pyrite oxidation with both oxygen and iron(III), 0.5 order in iron(III) concentration and with variable order in the oxygen concentration. The order of 0.5 in iron(III) concentration was chosen based on the outcomes of the mixed potential theory analysis, as presented in Section 2.6.1.2. This assumption was made since the rate of pyrite was not independently tested by varying iron(III) concentration. The possible negative influence of iron(II) on the reaction rate was neglected, to keep the number of constants to be regressed to a minimum. A similar assumption with regard to exclusion of the possible role of iron(II), was previously made by Steyl (2012: 447).

During each of the case studies, the regressions were done by minimising the sum of the squared errors between experimentally measured and simulated data points for the tests considered. All the data points pertaining to a single batch oxidation curve were regressed under the assumption that the oxygen partial pressure and temperature remained constant. The partial pressure and temperature were calculated by using the average recorded pressure and temperature readings pertaining to the separate kinetic batch kinetics, and averaging these values again for the tests pertaining to a single batch oxidation curve.

The absolute average relative deviation (AARD) was used to quantify the deviation between experimental and model predicted values. "AARDConv" denotes the relative deviation associated with the difference between the model predicted fractional pyrite conversion and the experimentally measured fractional pyrite conversion, and "AARDFe(II)" the relative deviation between the model predicted iron(II) concentration and the experimentally measured iron(II) concentration. AARDConv and AARDFe(II) were calculated as follows:

$$AARDConv\ (\%) = 100 \times \frac{1}{B_i} \sum \frac{\left| z_{i:conv}^{model} - z_{i:conv}^{exp} \right|}{x_{i:conv}^{exp}} \tag{7.24}$$

$$AARDFe(II)\ (\%) = 100 \times \frac{1}{B_i} \sum \frac{\left| z_{i:Fe(II)}^{model} - z_{i:Fe(II)}^{exp} \right|}{z_{i:Fe(II)}^{exp}} \tag{7.25}$$

Where z_i^{model} denotes the predicted value and z_i^{exp} the experimental value of all B_i data points evaluated during the analysis. The subscripts "conv" and "Fe(II)" denote the fractional pyrite conversion and the molal concentration of iron(II), respectively. Therefore, since the AARD is a direct measure of the normalised deviation between the model predicted value and the experimental data point, the model performance was evaluated and quantified using these values. An AARD value approaching zero indicates better correlation between predicted and real experimental values.[x]

The Matlab library function *fminsearch* was used to minimise the defined objective function (E_F), which was either AARDConv or AARDConv plus AARDFe(II) (see Equation 7.26 and 7.27), depending on which case study was investigated. The *fminsearch* function is based on the Nelder-Mead simplex algorithm (Lagarias, Reeds, Wright & Wright, 1998).

Case study 1:

$$E_F = AARDConv\ (\%) \tag{7.26}$$

Case study 2:

$$E_F = AARDConv\ (\%) + AARDFe(II)\ (\%) \tag{7.27}$$

The reason for a differentiation between "AARDConv" and "AARDFe(II)" was made and the reason why they were used differently in the objective function will become more apparent from the results presented in Section 7.2. In short, this was done to evaluate whether an improved prediction of the iron(II) concentrations could be obtained by incorporating a direct reaction between pyrite and iron(III) without compromising the model performance in terms of its ability to predict the pyrite conversion.

The experimental iron(III) concentration data was not used during the regression analysis, as the iron(III) concentration was calculated by subtracting the iron(II) concentration from the total iron concentration during data processing. Since the pyrite fractional conversion already provides a direct measure of the total iron in solution during the regression, incorporation of the relative deviation between the calculated "measured" iron(III) concentration and the model predicted iron(III) concentration as part of the objective function serves no purpose and means that one is essentially double-accounting for the relative deviation associated with conversion values. The relative deviation between the measured and predicted free acid concentrations was not considered either, as the measured free acid concentrations remained relatively constant throughout all tests.

[x]As an example, say the predicted fractional conversional is 0.2 and the measured fractional conversion is 0.15, the absolute difference would be 0.05, which gives rise to 33% AARD.

7.1.8.2. Initial conditions

For the case study where a rate dependency on iron(III) concentration was incorporated (Equation 7.7), it was evident that the rate of pyrite oxidation with iron(III) is to some extent dependent on the initial values that were assumed. In addition, the model robustness decreased when a "zero" value was assumed as a starting concentration, as this concentration level is not possible in physical reality. Therefore, a default initial value of 1×10^{-5} mol/kg (corresponding to ~0.5 mg/L) was set for batch kinetic "runs", where no ferric was added to the system initially. Where ferric was injected, as per the procedure provided in Section 3.2.4.3, the actual ferric concentration (3.7×10^{-4} mol/kg ≈ 20 mg/L) was used.

7.2. Results and discussion

The experimental results of Sample C, Sample D and Sample E were regressed separately, since the results could not be predicted by a single set of model parameters. The fact that this would not be possible was already reflected by the results presented in Sections 6.5 to 6.7, i.e., the pyrite oxidation rate was found to be relatively independent of surface area (see Section 6.5) and the presence of secondary minerals appeared to have played some role in inhibiting the oxidation rate (Sections 6.6 and 6.7). Recall that the size fractions that were used contained variable amounts of pyrophyllite and quartz and contained various impurities (arsenic, nickel, cobalt), thus, providing justification for the approach followed. The kinetic parameters that were varied during the regression analysis included the order in dissolved oxygen concentration, n_2, and the reaction rate constants k_{R1} and k_{R2}. The activation energies E_{A1} and E_{A2} were regressed by considering the tests that were conducted at temperatures higher (210°C) and lower than 200°C (180°C and 190°C), after the reaction order n_2 and the rate constants k_{R1} and k_{R2} were fixed at 200°C. The number of adjustable parameters was kept to a minimum, as inclusion of more parameters could not be justified, given the available experimental data. The model constants and values that were fixed are included in Table 7.1.

Table 7.1: Model constants and values fixed during the regression

Parameter	Unit	Status	Value	Comments
k_{R3}	$kg^2/mol.m^2.min$	Fixed	1000	Arbitrary large constant chosen
k_{R4}	$kg^{1.75}/mol^{1.75}.min$	Fixed	782.5	(data from Ruiz et al., 2016)
E_{A3}	kJ/mol	Fixed	80	Arbitrary value
E_{A4}	kJ/mol	Fixed	69	(data from Ruiz, et al., 2016)
$k_L a_{ref}$	1/min	Fixed	2.8	See Chapter 4
E_{A5}	kJ/mol	Fixed	12	See Chapter 4
MWs	kg/mol	Constant	119.98×10^{-3}	
ρ_s	kg/m^3	Constant	5000	
T_{R1}	K	Constant	474.75	
T_{R2}	K	Constant	474.75	
T_{R3}	K	Constant	474.75	
T_{R4}	K	Constant	474.75	
T_{R5}	K	Constant	293.15	See Chapter 4

In terms of the fixed values, an arbitrary, large rate constant of 1 000 $kg^2/mol.m^2.min$, with an associated activation energy of 80 kJ/mol, was selected for the oxidation of elemental sulphur to sulphate, based on the previous discussion presented in Section 7.1.2.1. The rate constant (782.5 $kg^{1.75}/mol^{1.75}.min$) and activation energy (69 kJ/mol) of the homogenous oxidation of iron(II) to iron(III) was regressed independently, based on the experimental results published by Ruiz et al. (2016) – refer to Section 7.1.2.2. The k_La value of 2.8 min^{-1} and the associated activation energy of 12 kJ/mol were measured independently during the current investigation (see Chapter 4).

In all the simulation runs, provision was made for a reagent injection period (typically 2 minutes prior to the official start of test) wherein the oxygen partial pressure was increased in a step-wise manner, first for injecting the acid, and then, thereafter, for injection of the wash water and adjusting the final pressure to the required set point value. The injection pressure was taken as the average recorded (or logged) pressure, two minutes prior to the official start of the test. This was done to account for pyrite pre-oxidation that may have taken place during this period. Experimental data close to the formal starting time of the experiment i.e., time "zero", suggested that pre-oxidation had indeed taken place (see Section 6.8).

During regression of Case Study 1, i.e., when only oxygen was considered to react directly with pyrite, only AARDConv was used as the objective function. During regression of Case Study 2, the objective function was set to include both AARDConv and AARDFe(II). The regression was then performed until the AARDConv obtained for both case studies roughly corresponded. This was done to evaluate whether an improved prediction of the iron(II) concentration could be obtained by

inclusion of a direct reaction of pyrite with iron(III), but without compromising the ability of the model to predict the fractional pyrite conversion. The regressed values are provided in Table 7.2 for Samples C, D and E. The value of the AARD for both the fractional conversion and iron(II) concentrations are also included in these tables.

Table 7.2: Model and regressed parameters for Sample C, D and E

Parameter	Unit	Status	Sample C Value	Sample D Value	Sample E Value
R_o	µm	Fixed	57.8	80.0	114.8
Data points evaluated			49	26	15
		Case Study 1			
k_{R1}	$\frac{mol^{(1-(n_1+n_2))}.kg^{(n_1+n_2)}}{m^2.min}$	Regressed	7.45	10.01	10.43
k_{R2}	$\frac{mol^{(1-n_3)}.kg^{n_3}}{m^2.min}$	Regressed	n/a	n/a	n/a
n_1	(-)	Fixed	-0.3	-0.3	-0.3
n_2	(-)	Fixed	1	1	1
n_3	(-)	n/a	n/a	n/a	n/a
E_{A1}	kJ/mol	Regressed	118	n/a	118[y]
AARDConv	%	Calculated	5.9	6.7	10.2
AARDFe(II)	%	Calculated	32.3	36.6	37.6
		Case Study 2			
k_{R1}	$\frac{mol^{(1-(n_1+n_2))}.kg^{(n_1+n_2)}}{m^2.min}$	Regressed	1.09	7.77	0.79
k_{R2}	$\frac{mol^{(1-n_3)}.kg^{n_3}}{m^2.min}$	Regressed	1.47	0.91	1.05
k_{R1}: k_{R2}	(-)	Regressed	1 : 1.34	1 : 0.12	1 : 1.32
n_1	(-)	Regressed	-0.30	-0.29	-0.30[z]
n_2	(-)	Regressed	0.72	1.01	0.61
n_3	(-)	Fixed	0.5	0.5	0.5
E_{A1}	kJ/mol	Regressed	121	n/a	142
E_{A2}	kJ/mol	Regressed	134	n/a	94
AARDConv	%	Calculated	7.0	7.1	9.0
AARDFe(II)	%	Calculated	19.7	23.3	17.9

In both cases, for all three samples, the experimental and predicted fractional conversion data points corresponded within ~11% of one another, as reflected by the calculated AARDConv values. This indicated that both case studies, irrespective of whether only oxygen was considered as oxidant, or

[y] Fixed according to outcomes of Case Study 1 on Sample C.

[z] Fixed according to outcomes of Case Study 1 on Sample C.

whether both oxygen and iron(III) were considered as oxidants, were able to predict pyrite conversion to a reasonable degree. However, the addition of a rate-dependency on the iron(III) concentration ($r_2 > 0$) lowered the AARDFe(II) significantly from 32% to 20%, 37% to 23% and 38% to 18% for Samples C, D and E, respectively. Therefore, the outcome of this analysis provided some evidence of a dual rate dependency on both oxygen and iron(III) as oxidants at conditions typical of POX. In general, the AARDFe(II) remained high (~20%) for the Case Study 2 model, which may, at least in part, be ascribed to the experimental error associated with the titrations conducted at low iron(II) concentrations (< 2 g/L) (refer to Appendix D.1 for comments on the accuracy of the iron(II) titrations). A high deviation from the experimental iron(II) titrated measurements has also been reported by Zhukov et al. (2015) in a similar modelling study on pyrite oxidation at high temperatures.

The variable reaction orders in dissolved oxygen concentration, ranging from 0.6 to 1.0, which were regressed during the evaluation of the Case Study 2 model, indicates that the current model equations cannot be used to obtain a conclusive order in oxygen concentration. This is believed to be due to the rate-dependency on the iron(III) concentration, as well as a very high interdependency between the rate constant k_1 and the reaction order n_2. Further details on the model performance and possible reasons for discrepancies are provided in Section 7.2.1 to 7.2.4.

7.2.1. Modelling of the influence of oxygen partial pressure

The model performance was compared to the test work data in terms of oxygen partial pressure for Sample C and D, as shown in Figure 7.1 and Figure 7.2, respectively.

In both cases (Case 1 and 2), high correlation between simulated and experimental data for the pyrite oxidation extent was observed. The simulation confirmed an observed first-order dependency of pyrite oxidation in dissolved oxygen concentration, which had previously been thought to be higher at “1.4” and “1.1”. This is a direct consequence of the ability of the simulation to incorporate effects, such as possible pre-oxidation during the reagent addition period, as well as to account for changing iron(III) concentrations as the batch test proceeded (in Case 2). Comparison of the simulation results of Case 1 and Case 2 showed that Case 1 (i.e., only accounting for oxygen as oxidant) was superior in simulating the pyrite oxidation behaviour, as well as the high degree of pyrite oxidation (30%) at 2 minutes into the batch test at an average oxygen partial pressure of 662 kPa.

With regard to the induction period, which is shown and discussed in Section 6.8, incorporation of a pyrite oxidation rate dependency in iron(III) concentration could not completely “capture” this behaviour, as is evident by the results shown in Figure 7.1c and Figure 7.2c. An improved prediction of the pyrite fractional conversion by employing the Case 2 model on results pertaining to Sample D

at 667 kPa pO_2 (Figure 7.2c) suggests that an oxidation rate dependency in the iron(III) concentration could potentially account for the "lag period" shown between 0 and 8 minutes. However, this result will remain speculative until passivation of the pyrite surface by iron-oxides, per the recommendations provided in Section 6.8.3, is completely ruled out. In addition, a rate dependency in iron(II) ion concentration should be considered in future.

More complex forms of the rate equations, discussed in Chapter 2, could also have been evaluated; however, provided that the iron(II) to iron(III) homogenous oxidation rate, as well as the oxidation of pyrite with iron(III), were not studied in isolation as part of the current experimental programme, use of more complex equations could not be justified, given the current, available experimental data.

The predicted dissolved oxygen concentration pertaining to both cases is also shown in Figure 7.1b&d and Figure 7.2b&d. Due to the high rate of oxidation at 1109 kPa pO_2, the dissolved oxygen concentration was lower than the oxygen solubility between 0 and 10 minutes; more so, in Case 2, where the rate of oxygen consumption was slightly higher. Provided that a conservative estimate of the k_La value was used (see Section 4.3), the dissolved oxygen concentration was probably always equal to the equilibrium solubility during the batch POX tests.

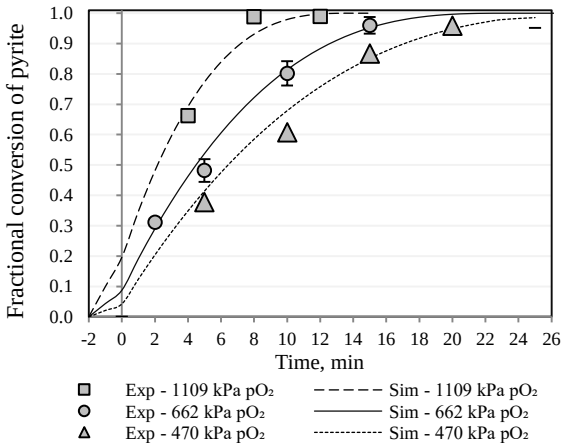

(a) Fractional pyrite conversion

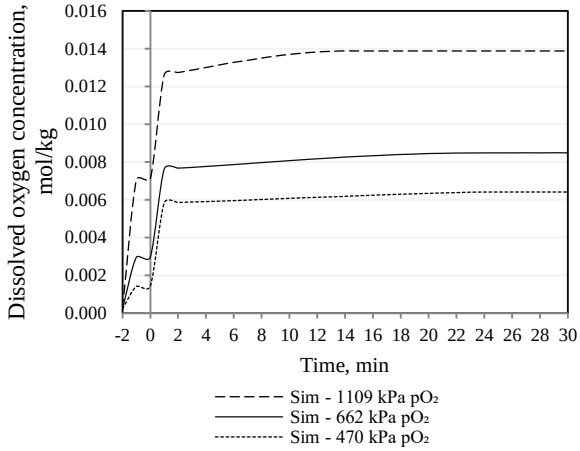

(b) Simulated dissolved oxygen concentration

Sample C - Case study 1

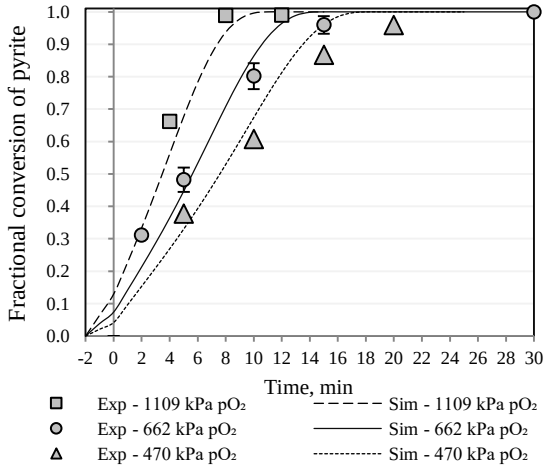

(c) Fractional pyrite conversion

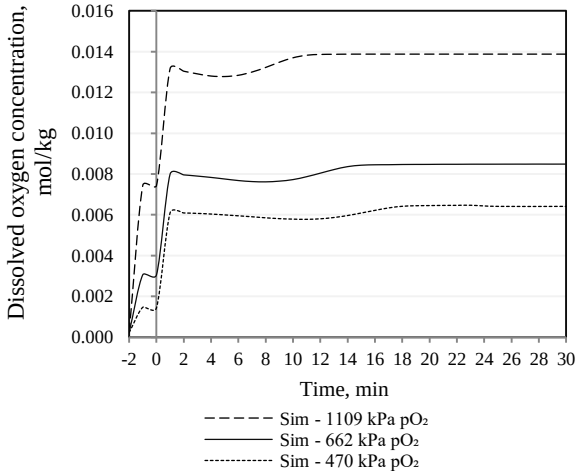

(d) Simulated dissolved oxygen concentration

Sample C – Case study 2

Figure 7.1: Simulated batch pyrite oxidation process vs. experimental data – Fractional pyrite conversion and dissolved oxygen concentration (Sample C (-53 +38 µm), 0.054 mol/kg FeS_2, 0.35 mol/kg H_2SO_4)

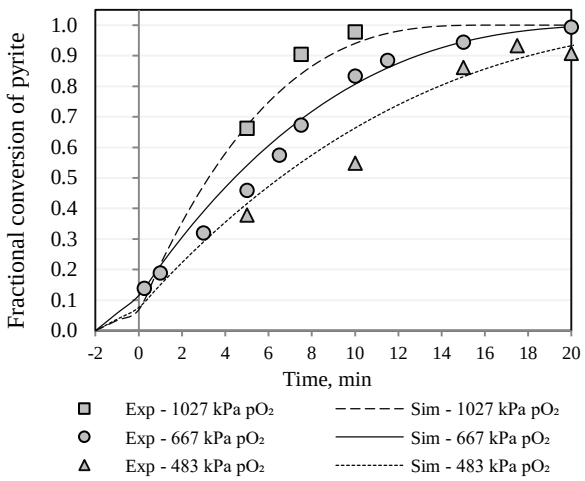

(a) Fractional pyrite conversion

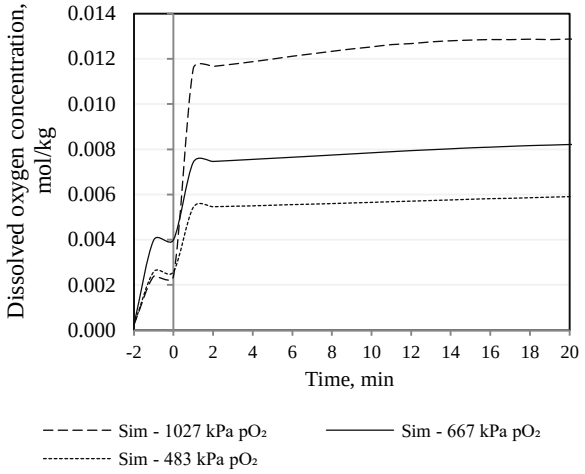

(b) Simulated dissolved oxygen concentration

Sample D - Case 1

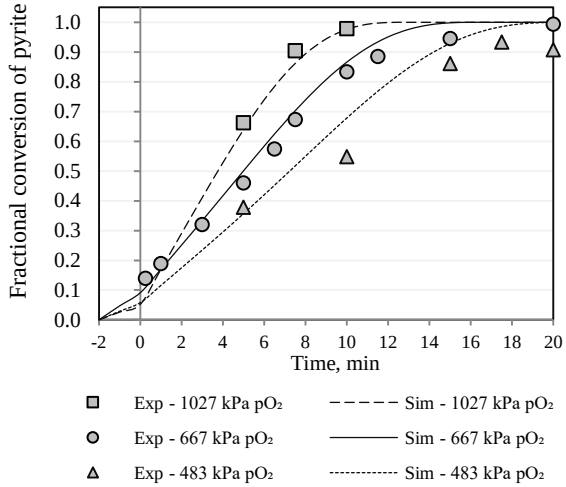

(c) Fractional pyrite conversion

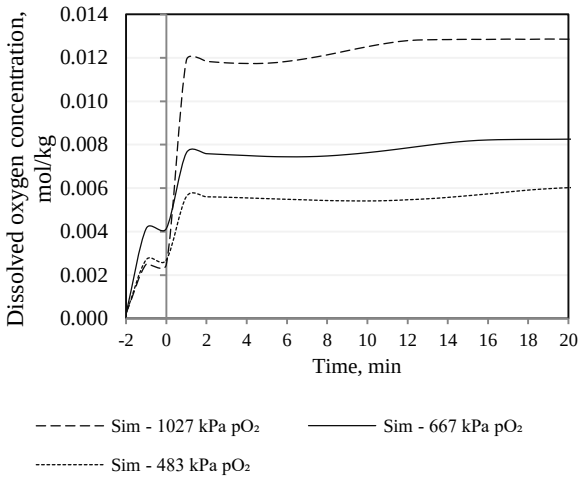

(d) Simulated dissolved oxygen concentration

Sample D – Case 2

Figure 7.2: Simulated batch pyrite oxidation process vs. experimental data – Fractional pyrite conversion and dissolved oxygen concentration (Sample D (-75 +53 µm), 0.057 mol/kg FeS_2, 0.35 mol/kg H_2SO_4)

The performance of the model to predict the change in iron(II) and iron(III) concentration is displayed in Figure 7.3. The test conducted at 667 kPa pO_2 (Sample D) was selected for presentation (the kinetic sampling test at 695 kPa pO_2 was included to illustrate the trend), however, similar results were obtained for all simulations.

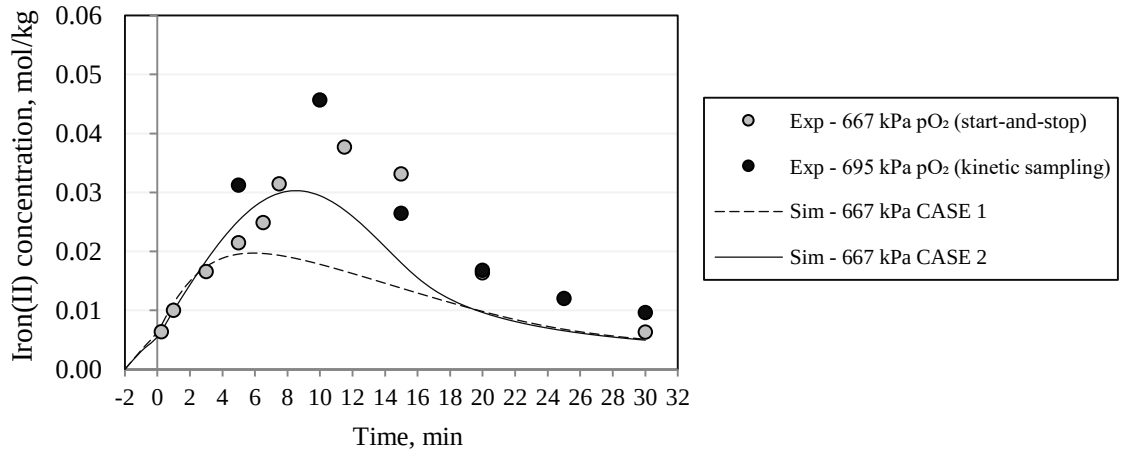

(a) Iron(II) concentration

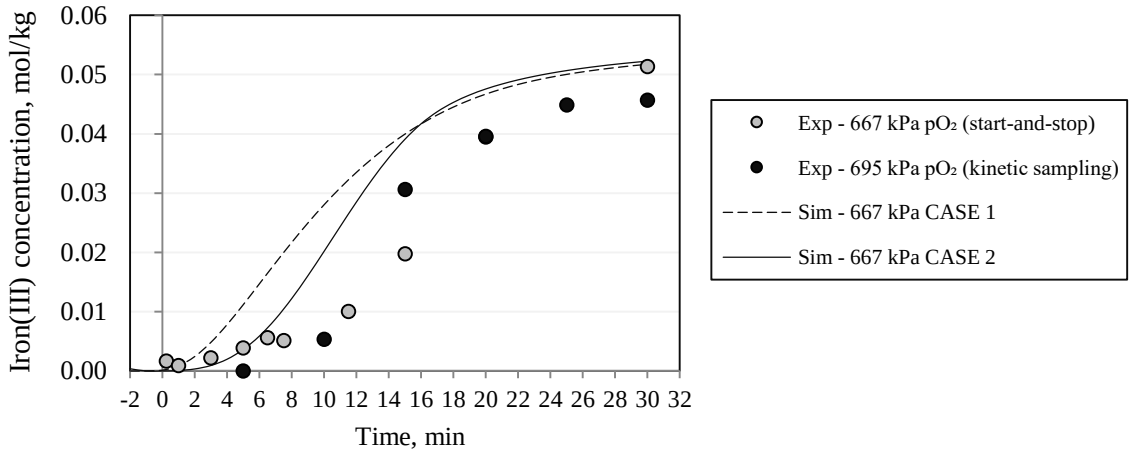

(b) Iron(III) concentration

Figure 7.3: Simulated batch pyrite oxidation process vs. experimental data: Iron(II) and iron(III) concentrations (Sample D (-75 +53 µm), 0.057 mol/kg FeS_2, 0.35 mol/kg H_2SO_4)

From the experimental results, notably low iron(III) and high iron(II) concentrations were observed during the period in which pyrite was oxidised, which strongly suggest that the produced iron(III) was consumed by pyrite again, to generate iron(II). As already discussed, simulation results confirm this observation and indicate that direct reaction between pyrite and iron(III) had taken place. This is evident from the superior performance of the Case 2 model (Figure 7.3) compared to the Case 1 model, in predicting the iron(II) and iron(III) concentrations. Within the first 10 minutes of the experiment, iron(III) essentially short-circuits at the surface of pyrite and is not detected in the bulk of the solution until the rate at which iron(III) is generated starts to exceed the rate at which the remaining pyrite can react with it. This, in essence, suggests that the rate of pyrite oxidation with iron(III) is higher than molecular oxygen, which is in agreement with proposals in the literature (Luther, 1987; Moses et al., 1987; Singer & Stumm, 1970). A reaction rate that is solely dependent on

iron(III) concentration would have been characterised by extended lag periods at the start of each test, which was not observed. The fact that high oxidation rates were observed at the start of each of the tests may suggest that both oxygen and iron(III) react in parallel with pyrite. This conclusion is synonymous with the conclusions drawn by Zhukov et al. (2015) in a similar study (refer to the discussion presented as part of the Literature Study in Section 2.6.1.3).

A similar discrepancy between the simulated and the experimental results at the highest iron(II) concentration of ~0.045 mol/kg (at 10 minutes) was also observed by Zhukov et al. (2015). This observation and the fact that the true pyrite oxidation rate seems to be described by a combination of the Case 1 and Case 2 models infer that there are complexities that are not adequately addressed by the current, simplified rate equations.

In summary, the true pyrite oxidation rate seems to be described by a combination of the Case 1 and Case 2 models, the former being superior in predicting pyrite oxidation extent and the latter superior in predicting iron(II) and iron(III) concentrations. Three possibilities, which may serve as an explanation for these effects, are provided below:

- A catalytic dependence of k_1 on the iron(III) to iron(II) ratio at the surface of pyrite particles, where [Fe(III)]* and [Fe(II)]* denote surface species:

$$k_1 \propto \frac{[Fe(III)]^*}{[Fe(II)]^*}$$

- The ability of pyrite to catalyse the iron(II) to iron(III) homogeneous reaction rate (r_3) without undergoing oxidation itself.
- And lastly, a possible rate dependency of r_2 in iron(II) concentration, which was not considered in the current model.

When comparing the regression results of the Case 2 studies with one another (Sample C compared to Sample D), as listed in Table 7.2, the ratio of the regressed rate constants k_1 to k_2 changed from 1.36 to 0.12, implying that the relative importance of the two rate equations (r_1 and r_2) may have changed with increasing particle size. This might have been influenced by secondary minerals/impurities in the samples, which altered the kinetics of the oxidation of this specific pyrite (refer to Section 6.7).

The simulation results pertaining to Sample E cannot be compared directly to the results obtained when modelling the POX behaviour of Sample C and Sample D, as the test work was performed at a slightly higher slurry density of 0.089 mol/kg FeS_2. The simulation results, however, suggest reasonable correlation between the experimental data and model prediction, as shown in Figure 7.4.

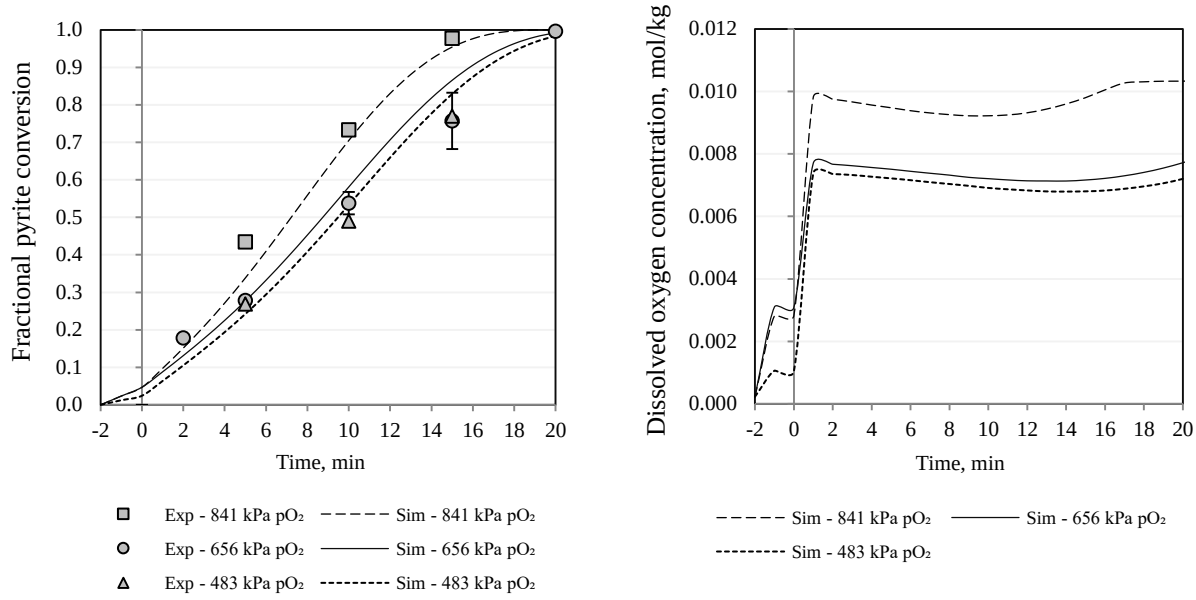

(c) Fractional pyrite conversion *(d) Simulated dissolved oxygen concentration*

Sample E – Case 2

Figure 7.4: Simulated batch pyrite oxidation process vs. experimental data – Fractional pyrite conversion and dissolved oxygen concentration (Sample E, -105+75 µm - Sample E, 600-700 rev/min, starting volume 5000 mL, 0.0894±0.0028 mol/kg FeS_2, 0.35 mol/kg H_2SO_4)

7.2.2. Modelling of the influence of acid concentration

The order that was assumed for the effect of acid concentration on the reaction kinetics was chosen as -0.3, based on the data presented in Section 6.4. According to the results presented in Figure 7.5, the simulations that had been conducted to simulate the effect of acid concentration on the oxidation kinetics of Sample C, gave reasonable estimates of the pyrite oxidation extent. Nearly similar results were obtained for Sample D (not shown here), however, due to the weak dependency of the oxidation rate on acid concentration, a wider range should be investigated in future studies to prevent the overlapping of batch test curves.

As a result of the very low solids densities employed during the test work, the sulphuric acid concentrations remained approximately constant for the duration of the tests, as indicated in Figure 7.5c.

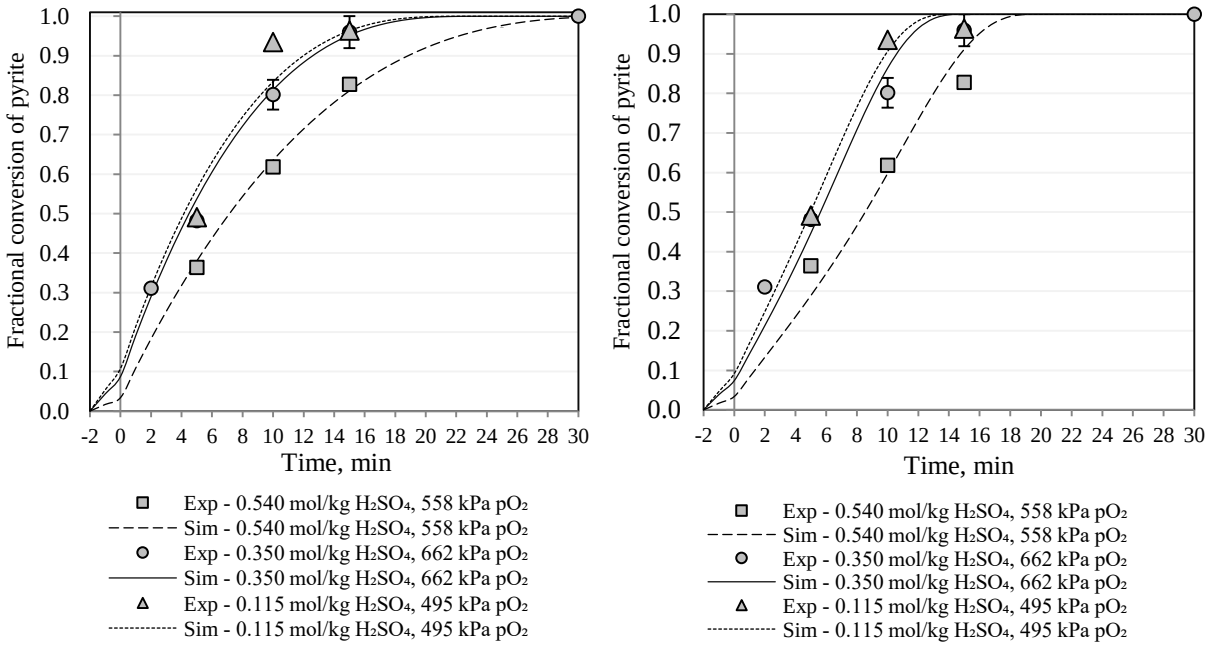

(a) Fractional pyrite conversion
Case 1

(b) Fractional pyrite conversion
Case 2

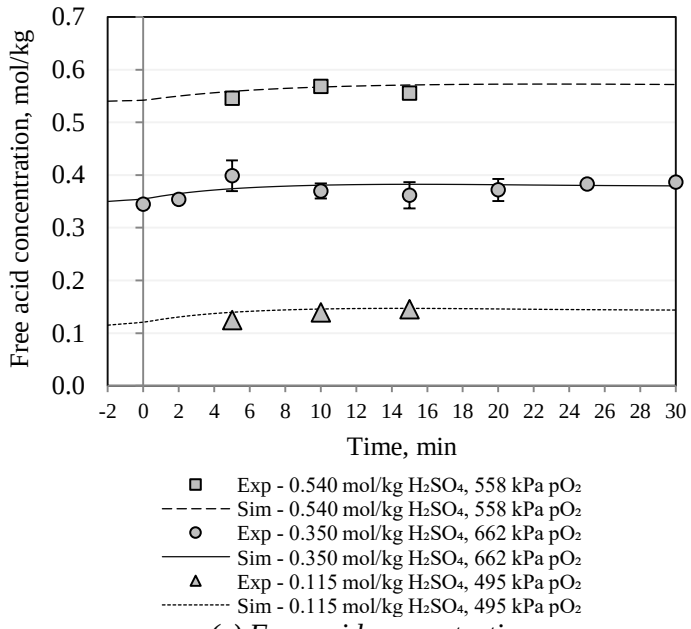

(c) Free acid concentrations
Case 1 or Case 2

Figure 7.5: Simulated batch pyrite oxidation process vs. experimental data (Sample C (-53 +38 µm), 0.054 mol/kg FeS_2)

7.2.3. Modelling of the influence of temperature

Based on the model that considered only molecular oxygen as an oxidant (Case 1), the activation energy was calculated as 118 kJ/mol (listed in Table 7.2), which corresponded to the value calculated (i.e., 124 kJ/mol) in Chapter 6. The dynamic model, therefore, confirms that the pyrite oxidation kinetics were measured under conditions that were free from diffusional-limitations. The activation energies for the two rate equations (E_{A1} and E_{2A}) were calculated as 121 and 134 kJ/mol. This relative magnitude of the activation energies were not as expected, in that kinetically faster reactions (i.e., oxidation with iron(III)) should have lower activation energies, however Zhukov et al. (2015) also report a slightly higher activation energy for the pyrite oxidation reaction with iron(III) as opposed to oxygen (50 vs. 46 kJ/mol). The opposite was true for the regression analysis carried out on Sample E, where E_{A1} and E_{2A} were found to be 124 and 94 kJ/mol; however, this result is probably less reliable, as only two temperatures were used in the regression.

Referring to Figure 7.6, the effect of temperature on the Sample C pyrite reaction kinetics as well as on the iron(II) and iron(III) concentrations was modelled with the regressed constants related to the "Case 2" scenario. The simulation exhibited a relatively high degree of correspondence to the experimental values for all temperatures investigated in terms of the ability to predict the pyrite oxidation extent.

However, the model, again, failed to account for the observed peak in the iron(II) concentration at approximately 80% pyrite oxidation (0.047 mol/kg vs. 0.035 mol/kg) – this was especially true at the highest temperature that was investigated (i.e., 211°C). Possible reasons for this phenomenon have already been discussed.

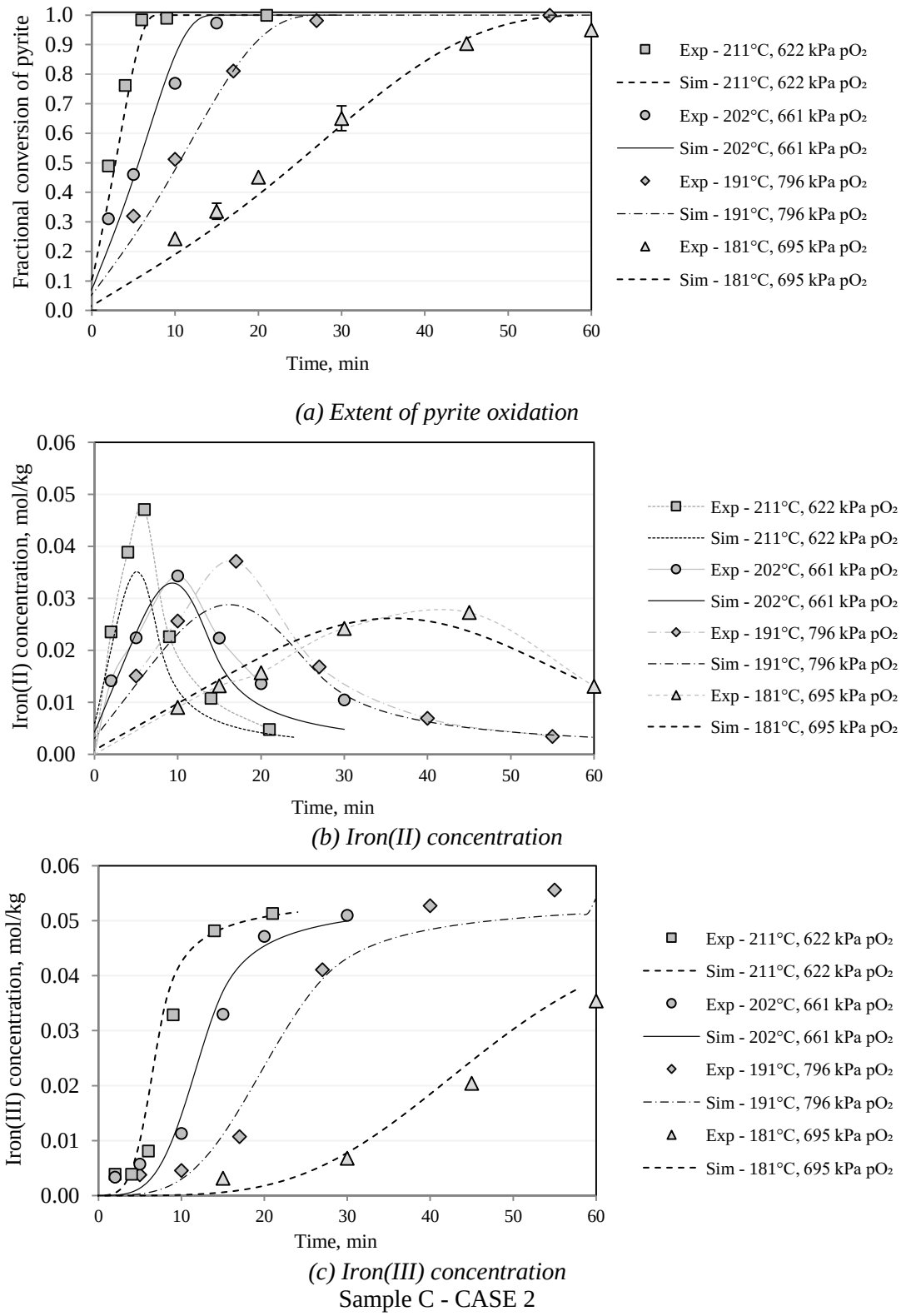

Figure 7.6: Simulated batch pyrite oxidation process vs. experimental data – temperature and iron(II) and iron(III) concentrations (Sample C (-53 +38 µm), 0.054 mol/kg FeS_2)

7.2.4. Modelling of the influence of solids concentration

In Section 6.6 it was proposed that the decreased oxidation rate with increasing solids concentration could be the result (as proposed in Equation 7.6 or r_2) of "oxygen starvation". Modelling of the system (Figure 7.7), based on the two case studies, indicates that oxygen starvation was unlikely, as dissolved oxygen concentration was always at least 75% of the solubility (refer to Figure 7.7b and d). In addition, a conservative k_La value was used, as was mentioned in Section 4.3, meaning that the simulated dissolved oxygen concentration was likely lower than the actual dissolved oxygen concentration.

Studies at even higher solids concentrations would be required to ascertain the role of secondary minerals, as it is believed that the formation of polymerised silica layers may have contributed to this phenomenon. Moreover, Steyl (2012; 437, 448, 479) observed a decrease in the oxidation rate by approximately 10 times when the solids concentration was increased from ~2 wt% to 8.85 wt% during oxidation of a pyrite-containing concentrate at 155°C in sulphate media. Steyl (2012: 480) proposes that a change in the mechanism occurred, shifting from a reaction rate that is purely dependent on iron(III) as surrogate oxidant, to a reaction rate that is purely dependent on dissolved oxygen concentration. Therefore, the possibility exists of a change in the mechanism of oxidation with increasing solids concentration – this possibility most certainly warrants further investigation. A pyrite oxidation rate dependency on the iron(II) concentration, which is known to have a negative effect on the rate, should also be considered in future studies.

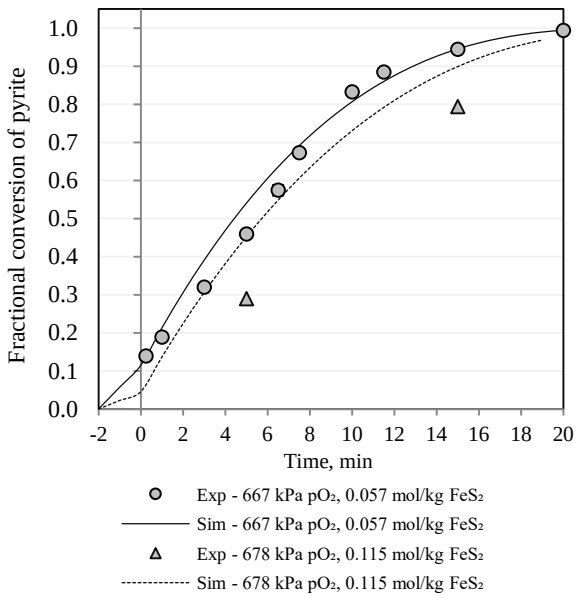

(a) Fractional pyrite conversion

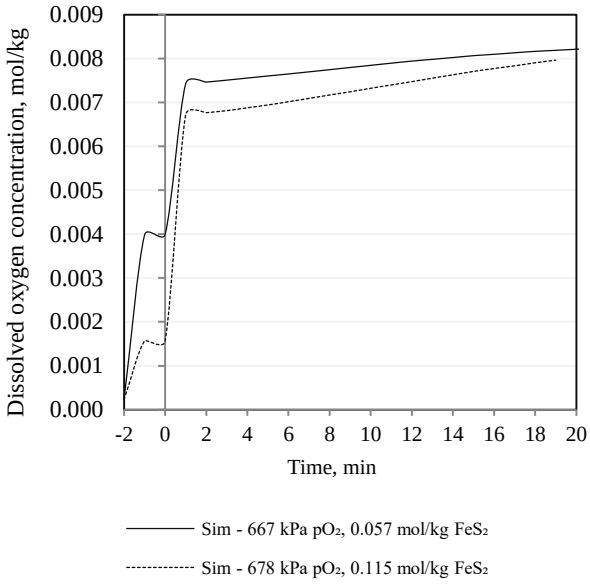

(b) Simulated dissolved oxygen concentration

Sample D – Case 1

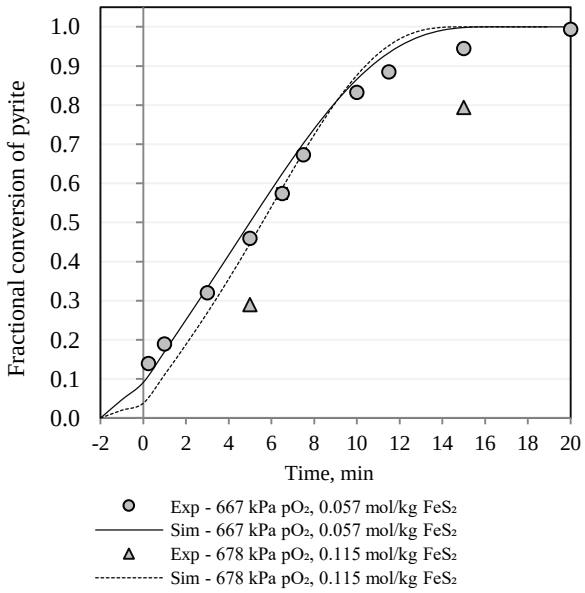

(c) Fractional pyrite conversion

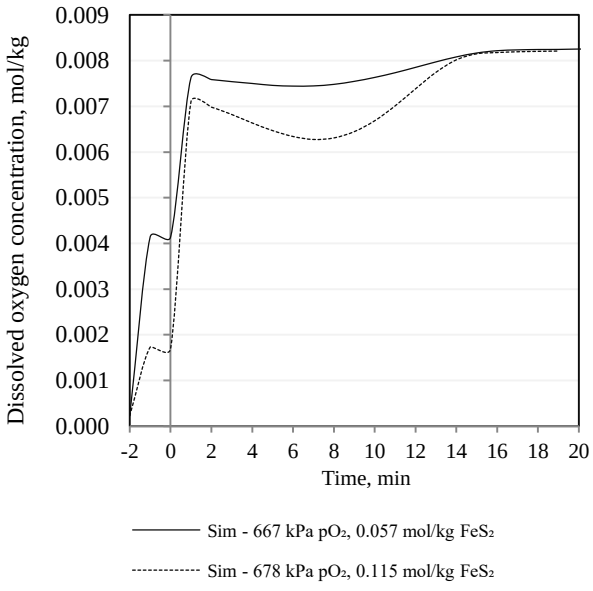

(d) Simulated dissolved oxygen concentration

Sample D – Case 2

Figure 7.7: Simulated batch pyrite oxidation process vs. experimental data: Fractional pyrite conversion and dissolved oxygen content (Sample D (-75 +53 µm), 0.057 mol/kg FeS_2, 0.35 mol/kg H_2SO_4)

8. CONCLUSIONS AND RECOMMENDATIONS

The aim of this study was to develop a rate equation to describe the pressure oxidation kinetics of a Witwatersrand pyrite concentrate. In order to achieve this, batch pressure oxidation tests were conducted on narrow size fractions to characterise the effect of temperature, oxygen partial pressure, acid concentration, particle size and slurry density on the rate of a specific pyrite sample. The batch oxidation tests were conducted at low slurry densities to maintain the reagent concentrations in excess.

8.1. Oxygen gas-liquid mass transfer

Preceding the pressure oxidation studies, the value of the oxygen gas-liquid mass transfer coefficient pertaining to the pressure reactor used in the current investigation, was measured and optimised. This was done to enable dynamic modelling of the dissolved oxygen concentration during the batch pressure oxidation process, which was, in turn, required to confirm the observed reaction orders and kinetic parameters. The study was successful in establishing the gas-liquid mass transfer coefficient in the 2-gallon Parr reactor and optimising the value for the setup used. Further studies, especially at temperatures exceeding 100°C, are recommended to confirm the measured activation energy.

8.2. Sample preparation and characterisation

The bulk flotation concentrate sample was screened into narrow size fractions to enable approximation of the size fractions by a monosize feed distribution to ultimately determine the effect of particle size or surface area on the rate of the pyrite oxidation reaction. Each size fraction was characterised separately. Chemical and mineralogical analysis confirmed that natural upgrading of the sample occurred during size classification, i.e., the size fraction with the largest mean particle size had the highest pyrite grade and vice versa. The primary secondary mineral present in all samples was the phyllosilicate mineral, pyrophyllite, followed by quartz. The samples were further characterised by high levels of impurities, more specifically arsenic, nickel and cobalt; however, further mineralogical studies would be required to establish to which mineral phases these impurities report to, e.g., whether arsenic exists as arsenopyrite particles or in solid-solution in the pyrite matrix as so-called “arsenian pyrite”. Mineralogical studies should also be conducted to evaluate whether pyrophyllite contains either iron(III) or iron(II), as liberation of these species into solutions, even at low concentrations, could have some impact on the observed dissolution behaviour.

8.3. Pyrite oxidation behaviour

Batch pressure oxidation studies revealed that the pyrite samples were highly reactive (the +37-53 μm fraction oxidised within 20 minutes at 200°C and ~670 kPa pO_2). Such high reactivity required

monitoring of the batch oxidation tests at very short time periods (e.g., 5 minutes), which proved to be challenging at high temperatures, due to temperature and pressure instabilities that occur during and after reagent injection (typically taking between 1 to 2 minutes).

Of the variables tested, temperature and oxygen partial pressure had the largest effect on the oxidation rate. The oxidation rate was only weakly dependent on acid concentration. The initial lag period observed in some of the tests pointed to a rate dependency on the iron(III)/iron(II) couple.

Secondary minerals and/or impurities appeared to play some role in inhibiting the oxidation rate, since an increase in particles size (or decrease in surface area), when comparing Sample C to Sample D, did not reduce the oxidation rate as one would expect. In addition, an increase in the solids concentration reduced the oxidation rate significantly.

8.4. Prediction of the rate of pyrite oxidation

Dynamic modelling of the system accounted for the effect of changing surface area and oxygen solubility, as well as experimental artefacts, such as pre-oxidation during the reagent addition period. This instilled confidence in the reaction orders and rate equations that would be required to describe the system.

The behaviour of the different pyrite samples proved to be too complex to be described by a single set of equations with fixed parameters, therefore, experimental data pertaining to each individual feed size fraction was regressed separately. Provision was made for a rate equation that only takes oxidation via molecular oxygen into consideration, as well as a rate equation that accounts for oxidation with both oxygen and iron(III). Parameter regression confirmed a high activation energy of approximately 118 kJ/mol based solely on oxygen as oxidant. Equally high activation energies, of 121 kJ/mol and 134 kJ/mol, were calculated for dual rate dependency on oxygen and the iron(III) in two additive rate determining equations. The calculated activation energies clearly indicate that no diffusional processes have limited the observed oxidation rate and that the rate was controlled by a chemical reaction on the surface of pyrite particles.

Inclusion of a reaction that accounted for direct oxidation with iron(III) gave superior performance in predicting the associated iron(II) to iron(III) concentrations, which were also monitored, indicating that both iron(III) and oxygen is responsible for oxidising pyrite at conditions typical of POX. Such a dual rate dependency and associated autocatalytic behaviour could also be responsible for the previously reported reaction orders, which varied between 0.5 and 1 in published literature sources. A negative order in proton concentration was confirmed; however, the exact order in oxygen concentration as well as in iron(III) concentration could not be obtained from the current regressions. This is the consequence of a high dependency between the reaction rate constants and the orders in

oxidant concentrations, as well as the initial iron(III) concentrations. Reasonable agreement with experimental data could be obtained by employing an order in oxygen concentration ranging between "0.6 and 1" at a fixed order in iron(III) concentration of 0.5. It is recommended that the rate of pyrite oxidation as a function of iron(III) and iron(II) concentration (in the absence of oxygen) should be studied at temperatures typical of POX, to determine the reaction orders in both of these species independently. Future experimental work should be done to independently measure the rate of iron(II) to iron(III) homogeneous oxidation (in the absence of pyrite) at conditions employed during this study, to provide more confidence in the literature-published values that were used in the current regression. Further optimisation can also be done during the model regression.

Current measurements do not adequately support the determination of an exact reaction mechanism. Some issues that remain unresolved include the relatively weak dependence on particle surface area, as well as the fact that an increase in slurry density (at a very low solids content) decreased the rate of reaction. Both of these effects are thought to be caused in some or other way by the presence of secondary minerals.

From the dynamic model and parameter estimation, the pyrite oxidation extent may be described by a rate equation that has the following functional form; however, the relative magnitude of k_1 and k_2, as well as the reaction orders appear to be sample dependent.

$$r_{FeS_2} = k_1[H^+]^{-0.3}\,[O_2]^{n_2}\exp\left(\frac{-E_{A1}}{R_g}\left(\frac{1}{T}-\frac{1}{T_{R1}}\right)\right) + k_2[Fe(III)]^{n_3}\exp\left(\frac{-E_{A2}}{R_g}\left(\frac{1}{T}-\frac{1}{T_{R2}}\right)\right) \qquad 8.1$$

8.5. Practical implications

Since the oxidation of pyrite was very rapid, the size of the industrial autoclave will most likely be dictated by the iron(II) to iron(III) homogenous oxidation rate (at all temperatures investigated). Complete conversion to iron(III) would be required to ensure maximum acid production, which would be dictated by the extent of iron precipitation. In addition, due to the high reactivity of the sample, a high risk is present of oxygen gas-liquid mass transfer to become rate-limiting. Special attention should, thus, be given to reactor impeller design and the mode of oxygen injection. Very rapid pyrite oxidation kinetics could also lead to reductive conditions in the autoclave.

Pyrophyllite rejection in the flotation step should be targeted, as the presence of this mineral appears to slow down the kinetics of the oxidation reaction, however, tests at higher slurry densities would be required to confirm this observation.

8.6. Other recommendations

In terms of execution of the actual tests, it is recommended that a gas trap or condenser be installed to capture and condense the water vapour, which was not accounted for in this study, as it reported to the bursting disk receiving drum, which was not weighed. This will serve as a confirmatory check when calculations are performed involving correction of the increase in species concentrations during the flashing process. In addition, it is recommended that an oxygen mass flow meter be installed in the setup, so that an online measurement of the quantity of oxygen reacted with pyrite may be obtained. This will also serve as an independent measurement of the pyrite oxidation kinetics.

In this study, the dynamic model regressions were performed using average pressure and temperature measurements obtained from multiple tests performed as part of a “single batch oxidation curve”. To obtain more accurate results, each measured point (i.e., temperature and pressure) and each batch POX test should be considered separately during the regression. This will call for a more robust optimisation function, as well as a more comprehensive regression routine compared to the routine that was employed in the current investigation.

REFERENCES

Abraitis, P., Pattrick, R. & Vaughan, D., 2004. Variations in the compositional, textural and electrical properties of natural pyrite: a review. *International Journal of Minerals Processing*, 74:41-59.

Albal, R., Shah, Y., Schumpe, A. & Carr, N., 1983. Mass transfer in multiphase agitated contactors. *Chemical Engineering Journal*, 27:61-80.

AngloGoldAshanti, 2017. *Mineral resource and ore reserve report 2017*. s.l.: AngloGoldAshanti. Available: www.aga-reports.com. [14 June 2018].

Antonijevic, M., Dimitrijevic, M. & Jankovic, Z., 1997. Leaching of pyrite with hydrogen peroxide in sulphuric acid. *Hydrometallurgy*, 46:71-83.

Appleby, A. 1993. Electrocatalysis of aqueous dioxygen reduction. *Journal of Electroanalytical Chemistry*, 357:117-179.

Bailey, L. & Peters, E, 1976. Decomposition of pyrite in acids by pressure leaching and anodization: the case for an electrochemical mechanism. *Canadian Metallurgical Quarterly*, 15(4):333-344.

Basolo, F. & Pearson, R. 1967. *Mechanisms of inorganic reactions.* 2nd ed. New York: John Wiley and Sons.

Berezowsky, R., Collins, M., Kerfoot, D. & Torres, N. 1991. The commercial status of pressure leaching technology. *JOM, The Journal of The Minerals, Metals & Materials Society (TMS)*, 43(2), February:9-15.

Biegler, T. 1976. Oxygen reduction on sulphide minerals. Part II. Relation between activity and semiconducting properties of pyrite electrodes. *Journal of Electroanalytical Chemistry*, 70:265-275.

Biegler, T., Rand, D. & Woods, R., 1975. Oxygen reduction on sulphide minerals. Part I. Kinetics and mechanism at rotated pyrite electrodes. *Electroanalytical Chemistry and Interfacial Electrochemistry*, 60:151-162.

Biegler, T. & Swift, D., 1979. Anodic behaviour of pyrite in acid solutions. *Electrochimica Acta*, 24:415-420.

Biley, C. 2015. Thermodynamic and kinetics modelling of iron(III) reduction with sulfur dioxide gas. Unpublished doctoral thesis. Stellenbosch: University of Stellenbosch.

Birkholz, M., Fiechter, S., Hartmann, A. & Tributsch, H. 1991. Sulfur deficiency in iron pyrite (FeS_{2-x}) and its consequences for band-structure models. Physical Review B, 43(14):11926-11936.

Bovey, H. & Stewart, L. 1979. Pressure leaching of uranium-bearing Witwatersrand ores. *Journal of the South African Institute of Mining and Metallurgy*, February:477-484.

Bradley, D. & Pitzer, K. 1979. Thermodynamics of Electrolytes 12. Dielectric properties of water and Debye-Huckel parameters to 350°C and 1 kbar. *Journal of Physical Chemistry*, 83(12):1599-1603.

Bryson, L. & Crundwell, F. 2014. The anodic dissolution of pyrite (FeS_2) in hydrochloric acid solutions. *Hydrometallurgy*, 143:42-53.

Chandra, A. & Gerson, A. 2010. The mechanisms of pyrite oxidation and leaching: A fundamental perspective. *Surface Science Reports*, 65:293-315.

Cheng, T.C-M. 1994. Measurement of oxygen mass transfer rates in a laboratory batch pressure reactor. Unpublished master's thesis. Montreal: McGill University.

Cheng, T. C-M. 2002. Production of hematite in acidic zinc sulphate media. Unpublished doctoral thesis Montreal: McGill University.124-126.

Cho, J. & Sohn, H. 2016. Effects of particle shape and size distribution on the overall fluid-solid reaction rates of particle assemblages. *The Canadian Journal of Chemical Engineering*, 94(August 2016):1516-1523.

Conway, M. & Gale, D. 1990. Sulfur's impact on the size of pressure oxidation autoclaves. *Journal of Metallurgy*, September:19-22.

Cornish, L., 2017. Massive new gold tailings retreatment venture established in South Africa. *Mining Review Africa*, 22 November. [Online] Available: https://www.miningreview.com/massive-new-surface-gold-retreatment-business-established-south-africa/. [13 June 2017]

Cotton, F., Wilkinson, G. & Gaus, P. 1976. Transition elements, in F.A. Cotton & G. Wilkinson (eds.). *Basic inorganic chemistry*. New York: John Wiley & Sons. 501-587.

Craig, V., Ninham, B. & Pashley, R. 1993. The effect of electrolytes on bubble coalescence in water. *Journal of Physical Chemistry*, 97:10192-10197.

Crundwell, F. 1988. The influence of the electronic structure of solids on the anodic dissolution and leaching of semiconducting sulphide minerals. *Hydrometallurgy*, 21:155-190.

Crundwell, F. 2013. The dissolution and leaching of minerals: Mechanisms, myths and misunderstandings. *Hydrometallurgy*, 139:132-148.

Danckwerts, P.V. 1970. *Gas-liquid reactions.* New York: McGraw-Hill.

Demopoulos, G. 1985. Acid pressure leaching of a sulphidic uranium ore with emphasis on radium extraction. *Hydrometallurgy*, 15:219-242.

Derksen, J., Buist, K., Van Weert, G. & Reuter, M. 2000. Oxygen transfer in agitated silica and pyrite slurries. *Minerals Engineering*, 13(1):25-36.

Descostes, M., Vitorge, P. & Beaucaire, C. 2004. Pyrite dissolution in acidic media. *Geochimica et Cosmochimica Acta*, 68(22):4559-4569.

Dreisinger, D. & Peters, E. 1989. The oxidation of ferrous sulphate by molecular oxygen under zinc pressure-leach conditions. *Hydrometallurgy*, 22:101-119.

Dutrizac, J. & MacDonald, R. 1974. Ferric ion as a leaching medium. *Minerals Science and Engineering*, 6(2):60-100.

Dutrizac, J. & Sunyer, A. 2012. Hematite formation from jarosite-type compounds by hydrothermal conversion. *Canadian Metallurgical Quarterly*, 51(1):11-23.

Espiari, S., Rashchi, F. & Sadrnezhaad, S. 2006. Hydrometallurgical treatment of tailings with high zinc content. *Hydrometallurgy*, 82:54-62.

Ewart, T. 2011. Acid mine drainage in the Gauteng province of South Africa - A phenomenological study on the degree of alignment between stakeholders concerning a sustainable solution to acid mine drainage. Unpublished master's thesis. Stellenbosch: Stellenbosch University.

Feather, C. & Snegg, J. 1978. The role of brannerite in the recovery of uranium from Witwatersrand Reefs. *Transactions of the Geological Society of South Africa*, 81(2):255-260.

Filippou, D., Cheng, T. & Demopoulos, G., 2000. Gas-liquid oxygen mass-transfer; from fundamentals to applications in hydrometallurgical systems. *Mineral Processing and Extractive Metallurgy Review*, 20:447-502.

Filippou, D., Konduru, R. & Demopoulos, G. 1997. A kinetic study on the acid pressure leaching of pyrrhotite. *Hydrometallurgy*, Volume 47:1-18.

Fivaz, C. 1988. Presidential address: How the MacArthur-Forrest cyanidation process ensured South Africa's golden future. *Journal of the South African Institute of Mining and Metallurgy*, 88(9):309-318.

Fleming, C., Brown, J. & Botha, M. 2010. *An economic and environmental case for re-processing gold tailings in South Africa*, SGS Minerals.

Fleuriault, C., Anderson, C. & Shuey, S., 2016. Iron phase control during pressure oxidation at elevated temperature. *Minerals Engineering*, 98:161-168.

Folmer, J., Jellinek, F. & Calis, G., 1988. The electronic structure of pyrites, particularly CuS_2 and $Fe_{1-X}Cu_xSe_2$: An XPS and Mossbauer Study. *Journal of Solid State Chemistry*, 72:137-144.

Ford, M. 1993. Uranium in South Africa. *Journal of the South African Institute of Mining and Metallurgy*, 93(2):37-58.

Forward, F. & Halpern, J. 1955. Acid pressure leaching of uranium ores. *Journal of Metals*, 7(3), March:463-467.

Fuchs, R., Ryu, D. & Humphrey, A. 1971. Effect of surface aeration on the scale-up procedures for fermentation processes. *Ind. Eng. Chem. Process Des. Develop.*, 10(2):190-196.

Garrels, R. & Thompson, M. 1960. Oxidation of pyrite by iron sulfate solutions. *Americal Journal of Science*, 258(A):57-67.

Gilligan, R. & Nikoloski, A. 2015. Leaching of brannerite in the ferric sulphate system - Part 1: Kinetic reaction mechanisms. *Hydrometallurgy*, 156:71-80.

Gold One International Limited. 2012. *Cooke Uranium Project.* s.l.:Gold One International Limited. Available: https://hotcopper.com.au/documentdownload?id=tuE7JrfFgm%2FOGe3nZXuPH2%2FzTUVfsgq6nA3%2F0YJdkqtzGuvSSYETCgphPh6nwwdLgmt7P9FMeoy9odnKCYszyeEjZA%3D%3D. [16 June 2018].

Gold Fields, 2017. *2017 Mineral resources and mineral reserves supplement.* s.l.: Gold Fields. Available: https://www.goldfields.com/reports/annual-report-2017/pdf/full-mr.pdf. [15 Jun 2018].

Goldwyer, N., 2007. First new primary SA uranium production in decades ramps up. *Creamer Media's Mining Weekly*, 29 June. Available: http://www.miningweekly.com/print-version/first-new-primary-sa-uranium-production-in-decades-ramps-up-2007-06-29. [15 June 2018]

Hamann, C., Hamnett, A. & Vielstich, W. 2007. *Electrochemistry.* 2nd ed. Weinheim: Wiley-VCH Verlag.

Harmony, 2018. *FY18 Interim results.* s.l.: Harmony. Available: http://www.harmony.co.za/downloads/send/132-q2-fy2018/2600-interim-results-for-the-six-months-ended-31-december-2017. [14 June2018]

Harriott, P. 1962. Mass transfer to particles. Part 1. Suspended in Agitated tanks. *A.I.Ch. E. Journal*, 8(1):93-102.

Herbst, J. 1979. Rate processes in multiparticle metallurgical systems, in H.Y. Sohn & M.E. Wadsworth (Eds.). *Rate processes of extractive metallurgy.* New York: Plenum Press. 55-59.

Holmes, H. & Mesmer, R. 1992. Isopiestic studies to H_2SO_4(aq) at elevated temperatures: thermodynamic properties. *Journal of Chemical Thermodynamics*, 24:317-328.

Holmes, P. & Crundwell, F. 2000. The kinetics of the oxidation of pyrite by ferric ions and dissolved oxygen: An electrochemical study. *Geochimica et Cosmochimica Acta*, 64(2):263-274.

Holmes, P. & Crundwell, F., 2013. Polysulfides do not cause passivation: Results from the dissolution of pyrite and implications for other sulfide minerals. *Hydrometallurgy,* Volume 139:101-110.

Hung, A., Muscat, J., Yarovsky, I. & Russo, S., 2002. Density-functional theory studies of pyrite FeS_2 (100) and (110) surfaces. *Surface Sciences,* 513(3), August:511-524.

Incropera, F., Dewitt, D., Bergman, T. & Lavine, A., 2007. *Fundamentals of Heat and Mass Transfer.* 6th ed. Hoboken: John Wiley & Sons.

IRW Press, 2017. Sibanye-Stillwater declares mineral resources and mineral reserves as at 31 December 2017. *IRW Press*. 19 February 2018. Available: https://www.irw-press.com/en/news/sibanye-stillwater-declares-mineral-resources-and-mineral-reserves-as-at-31-december-2017_42461.html?isin=ZAE000173951. [15 Jun 2018].

Janisch, P. 1986. Gold in South Africa. *Journal of the South African Institute of Mining and Metallurgy*, 86(8):273-316.

Janse van Rensburg, S. 2016. *Guidelines for retreatment of SA gold tailings: MINTEK's learnings,* in Proceedings of the 23rd WasteCon Conference. Johannesburg: Institute of Waste Management of South Africa: 367-376.

Jeffery, G., Bassett, J., Mendham, J. & Denney, R.. 1989. *Vogel's textbook of quantitative chemical analysis.* 5th ed. London: Longman Scientific & Technical (co-published with John Willey & Sons)

Jiang, W., Essene, E. & Peacor, D. 1990. Transmission electron microscopic study of coexisting pyrophyllite and muscovite: Direct evidence for the metastability of illite. *Clays and Clay Minerals,* 38(3):225-240.

Jin, H., Liu, D., Yang, S., He, G., Guo, Z. & Tong, Z. 2004. Experimental study of oxygen mass transfer coefficient in bubble column with high temperature and high pressure. *Chemical Engineering Technology*, 27(12):1267-1272.

Kelsall, G., Yin, Q., Vaughan, J.J., England, K.E.R. & Brandon, N.P. 1999. Electrochemical oxidation of pyrite (FeS_2) in aqueous electrolytes. *Journal of Electroanalytical Chemistry,* 471(2):116-125.

Kenan, A. & Chirenje, E. 2016. Uranium in South Africa: Exploration and supply capacity. *Natural Resources and Conservation,* 4(2):25-33.

Kinnaird, J. & Nex, P. 2016. Uranium in Africa. *Episodes*, 39(2):335-360.

Knopf, D., Luo, B., Krieger, U. & Koop, T. 2003. Thermodynamic dissociation constant of the bisulfate iron from Raman and ion interaction modelling studies in aqueous sulfuric acid at low temperatures. *Journal of Physical Chemistry,* Issue 107:4322-4332.

Koretsky, M. 2004. *Engineering and Chemical Thermodynamics.* Hoboken(NJ): John Wiley & Sons.

Lagarias, J., Reeds, J., Wright, M. & Wright, P. 1998. Convergence properties of the Nelder-Mead simplex method in low dimensions. *SIAM Journal of Optimisation*, 9(1):112-147.

Laliberté, M. & Cooper, W. E. 2004. Model for calculating the density of aqueous electrolyte solutions. *Journal of Chemical Engineering Data*, Volume 49:1141-1151.

Lee, J. & Foster, N. 1990. Measurement of gas-liquid mass transfer in multi-phase reactors. *Applied Catalysis*, 63:1-36.

Lehner, S. & Savage, K. 2008. The effect of As, Co and Ni impurities on pyrite oxidation kinetics: Batch and flow-through reactor experiments with synthetic pyrite. *Geochimica et Cosmochimica Acta,* 72:1788-1800.

Levenspiel, O. 1999. *Chemical reaction engineering.* 3rd ed. Hoboken, NJ: John Wiley & Sons.

Li, L., Bergeron, I. & Ghaareman, A., 2017. The effect of temperature on the kinetics of the ferric-ferrous redox couple on pyrite. *Electrochimica Acta,* Volume 245:814-828.

Liley, E., Thomson, G.H., Friend, D.G., Daubert, T.E. & Buck, E. 1997. Physical and Chemical Data. In: R. Perry, Green. D.W & Maloney. J.O, eds. *Perry's chemical engineers' handbook.* 7th ed. New York: McGraw-Hill.

Linek, V. & Vacek, V. 1981. Chemical engineering use of catalyzed sulfite oxidation kinetics for the determination of mass transfer characteristics of gas-liquid contactors. *Chemical Engineering Science*, 36(11):1747-1768.

Lin, T., Tsuchiya, K. & Fan, L. 1998. Bubble flow characteristics in bubble columns at elevated pressure and temperature. *AIChE Journal*, 44(3), March:545-560.

Littlejohn, P.O.L., 2006. The enhancing effect of pyrite on the kinetics of ferrous iron oxidation by dissolved oxygen. Unpublished master's thesis. Vancouver: The University of British Columbia.

Lloyd, P., 1981. The flotation of gold, uranium and pyrite from Witwatersrand ores. *Journal of the South African Institute of Mining and Metallurgy*, 81(2), February:41-47.

Long, H. & Dixon, D., 2004. Pressure oxidation of pyrite in sulfuric acid media: a kinetic study. *Hydrometallurgy*, 73:335-349.

Lottering, M.J., Lorenzen, L., Phala, N.S., Smit, J.T. & Schalkwyk, G.A.C. 2008. Mineralogy and uranium leaching response of low grade South African ores. *Minerals Engineering*, 21(1), January:16-22.

Lowson, R., 1982. Aqueous oxidation of pyrite by molecular oxygen. *Chemical Reviews,* 82(5):462-495.

Lundström, M., Liipo, J., Karonen, J. & Aromaa, J. 2009. Dissolution of six sulfide concentrates in the hydrocopper environment, in *The South African Institute of Mining and Metallurgy Base Metals Conference*: 127-138.

Lunt, D., Boshoff, P., Boylett, M. & El-Ansary, Z. 2007. Uranium extraction: the key process drivers. *The Journal of the Southern African Institute of Mining and Metallurgy*, 107:419-425.

Luther, G., 1987. Pyrite oxidation and reduction: Molecular orbital theory considerations. *Geochimica et Cosmochimica Acta*, 51(12):3193-3199.

Mackiw, V., Benz, T. & Evans, D. 1966. Recent developments in pressure hydrometallurgy. *Metallurgical Reviews*, 11(1):143-158.

McKay, D. & Halpern, J. 1958. A kinetic study of the oxidation of pyrite in aqueous suspension. *Transactions of the Metallurgical Society of AIME,* 212, June:301-308.

McKibben, M. & Barnes, H. 1986. Oxidation of pyrite in low temperature acidic solutions: Rate laws and surface textures. *Geochimica et Cosmochimica Acta*, 50:1509-1520.

Meyer, R. 1979. Electrochemistry of FeS_2. *Journal of Electroanalytical Chemistry*, 101:59-71.

Miller, J.D. 1979. Hydrometallurgical processes, in H. Sohn & M. Wadsworth (Eds.). *Rate processes of extractive metallurgy.* New York: Plenum Press. 203-208.

Mishra, K. & Osseo-Asare, K. 1988. Aspects of the interfacial electrochemistry of semiconductor pyrite (FeS). *Journal of the Electrochemistry Society: Electrochemical Science and Technology*, 135(10):2502-2509.

Moses, C. & Herman, J. 1991. Pyrite oxidation at circumneutral pH. *Geochimica et Cosmochimica Acta*, 55:471-481.

Moses, C., Nordstrom, D., Herman, J. & Mills, A. 1987. Aqueous pyrite oxidation by dissolved oxygen and by ferric iron. *Geochimica Cosmochimica Acta*, 51:1561-1571.

Nengovhela, A., Yibas, B. & Ogola, J. 2006. Characterisation of gold tailings dams of the Witwatersrand Basin with reference to their acid mine drainage potential, Johannesburg, South Africa. *Water SA*, 32(4):500-506.

Nicol, M. 2016. *Oxygen - Why is it ineffective as an oxidant in hydrometallurgical processes?* [Powerpoint Presentation] Cape Town: The Southern African Institute of Mining and Metallurgy.

Nicol, M., Miki, H., Zhang, S. & Basson, P. 2013. The effects of sulphate ions and temperature on the leaching of pyrite. 1. Electrochemistry. *Hydrometallurgy,* 133:188-196.

Nicol, M., Needes, C. & Finkelstein, N. 1975. Electrochemical model for the leaching of uranium dioxide, in A.R. Burkin (Ed.). *Leaching and reduction in hydrometallurgy*. London: Institution of Mining and Metallurgy. 1-11.

Nicol, M. & Scott, P. 1979. The kinetics and mechanism of the non-oxidative dissolution of some iron sulphides in aqueous acidic solution. *Journal of the South African Institute of Mining and Metallurgy,* 79(10), May:298-305.

Osseo-Asare, K. 1992. Semiconductor electrochemistry and hydrometallurgical processes. *Hydrometallurgy*, 29:61-90.

Owusu, G., Dreisinger, D. & Peters, E. 1995. Effect of surfactants on zinc and iron dissolution rates during oxidative leaching of sphalerite. *Hydrometallurgy* 38(3), August:315-324.

Pabalan, R. & Pitzer, K. 1988. Heat capacity and other thermodynamic properties of $Na_2(SO_4)_{aq}$ in hydrothermal solutions and the solubilities of sodium sulfate minerals in the system Na-Cl-SO_4-OH-H_2O to 30°C. *Geochimica et Cosmochimica Acta*, Volume 52:2393-2404.

Papangelakis, V. 1990. Mathematical modelling of an exothermic pressure leaching process. Unpublished doctoral thesis. Montreal: McGill University.

Papangelakis, V. & Demopoulos, G. 1991. Acid pressure oxidation of pyrite: reaction kinetics. *Hydrometallurgy,* 26(3):309-325.

Papangelakis, V. & Demopoulos, G. 1992. On the attainment of stable autothermal operation in continuous pressure leaching reactors. *Hydrometallurgy,* 29:297-318.

Peters, E. 1976. Direct leaching of sulfides: Chemistry and applications. *Metallurgical Transactions B,* 7B(December):505-517.

Peters, E. & Majima, H. 1967. Electrochemical reactions of pyrite in acid perchlorate solutions. *Canadian Metallurgical Quarterly,* 7(3):111-117.

Phillips, K. 1973. Proposed explanation for apparent dependence of liquid mass-transfer coefficients on pressure. *Canadian Journal of Chemical Engineering*, 51:371-374.

Pitzer, K., Roy, R. & Silvester, L. 1977. Thermodynamics of Electrolytes. 7. Sulfuric Acid. *Journal of the American Chemical Society,* 99(15):4930-4936.

Posnjak, E. & Merwin, H. 1922. The system, Fe_2O_3-SO_3-H2O. *Journal of the American Chemical Society*, 44(2):1965-1995.

Reich, M., Kesler, S.E., Utsunomiya, S., Palenik, C.S., Chryssoulis, S.L. and Ewing, R.C. 2005. Solubility of gold in arsenian pyrite. *Geochmica et Cosmochimica Acta*, 69(11):2781-2796.

Rimstidt, J. & Vaughan, D., 2003. Pyrite oxidation: A state-of-the-art assessment of the reaction mechanism. *Geochimica et Cosmochimica Acta*, 67(5):873-880.

Robinson, R.E, James, G.S., Van Zyl, P.C.N., Marsden, D.D. & Bosman, D.J. 1958. *Preliminary assessment of the important economic factors in the pressure leaching of low-grade South African uranium ores.* Geneva, s.n.:318-325.

Ruchti, G., Dunn, I., Bourne, J. & Stockar, U.V., 1985. Practical guidelines for the determination of oxygen transfer coefficients (k_La) with the sulfite oxidation method. *The Chemical Engineering Journal*, 30:29-38.

Ruiz, M., Jerez, O. & Padilla, R. 2016. Kinetics of the cupric catalyzed oxidation of Fe(II) by oxygen at high temperature and high pressure. *Mineral Processing and Extractive Metallurgy Review*, 37(3):160-167.

Schumpe, A. 1993. The estimation of gas solubilities in salt solutions. *Chemical Engineering Science*, 48(1):153-158.

Shatalov, V. & Pirkovskii, S. 2007. Oxidation of pyrite by oxygen and concurrent leaching of uranium from ore under the conditions of an autogenous autoclave process. *Atomic Energy*, 12(2):146-150.

Shi, Z., Zhang, J., Liu, J-S., Wang, H. and Wilkinson, D.P. 2006. Current status of ab initio quantum chemisty study for oxygen electroreduction on fuel cell catalysts. *Electrochimica Acta*, Volume 51:1905-1916.

Singer, P. & Stumm, W. 1970. Acidic mine drainage: The rate-determining step. *Science*, 167(3291):1121-1123.

Sippola, H., 2012. Thermodynamic modelling of concentrated sulfuric acid solutions. *CALPHAD: Computer coupling of Phase Diagrams and Thermochemistry*, Issue 38:168-176.

Skoog, D., West, D., Holler, F. & Crouch, S., 2004. *Fundamentals of analytical chemistry*. 8th ed. Belmont(CA): Brooks/Cole.

Smirnov, I. & Matveev, A. 2001. Scientific principles, technology and equipment for hydrometallurgical processing of uranium and complex ores. *Atomic Energy*, 92(4):815-823.

Söhnel, O. & Novotny, P., 1984. Densities of Aqueous Solutions of 18 Inorganic Substances. *Journal of Chemical Engineering Data*, Volume 29:379-382.

Stanley, G. (ed.) 1987. *The extractive metallurgy of gold in South Africa.* Volume 2. Monograph Series M7. Johannesburg: The South African Institute of Mining and Metallurgy.

Stenstrom, M. & Gilbert, R. 1981. Effects of alpha, beta and theta factor upon the design, specification and operation of aeration systems. *Water Research*, 15:643-654.

Steyl, J.dT. 2012. Simulating the medium temperature chalcopyrite oxidation system in batch and continuous autoclaves. Unpublished doctoral thesis. Stellenbosch: Stellenbosch University.

Tabelin, C., Veerawattananun, S., Ito, M. & Igarashi, T. 2017. Pyrite oxidation in the presence of hematite and alumina. II Effects on the cathodic and anodic half-cell reactions. *Science of the Total Environment*, 581-582, March:126-135.

Telford, W., Geldart, L. & Sheriff, R, 1990. *Applied geophysics.* 2nd ed. Cambridge: Cambridge University Press.

Teramoto, M., Tai, S., Nishii, K. & Teranishi, H., 1974. Effects of pressure on liquid-phase mass-transfer coefficients. *Chemical Engineering Journal*,:223-226.

Thackray, M. 1970. Melting point intervals of sulfur allotropes. *Journal of Chemical and Engineering Data*, 15(4):495-497.

Thomas, K. 2005. Pressure oxidation overview, in M.D. Adams & B.A. Wills (eds.). *Developments in minerals processing.* Volume 15. s.l.: Elsevier. 346-369.

Tributsch, H. & Gerischer, H. 1976. The oxidation and self-heating of metal sulphides as an electrochemical corrosion phenomenon. *Journal of Applied Chemical Biotechnology*, 26:747-761.

Tromans, D., 1998a. Temperature and pressure dependent solubility of oxygen in water: a thermodynamic analysis. *Hydrometallurgy*, 48(2), May:327-342

Tromans, D. 1998b. Oxygen solubility modelling in inorganic solutions: concentration, temperature and pressure effects. *Hydrometallurgy*, 50(3), November:279-286.

Tromans, D. 2000. Modelling oxygen solubility in water and electrolyte solutions. *Industrial Engineering Chemistry Research*, 39:802-812.

Tsotetsi, J. & Pillay, K. 2013. *Sulphide concentrate production by flotation on a gold sample*. s.l.: Mintek. Internal report 41383

Umetsu, Y., Tozawa, K. & Sasaki, K. 1977. The hydrolysis of ferric sulphate solution at elevated temperatures. *Canadian Metallurgical Quarterly*, 16(1):111-117.

Van Weert, G., Van der Werff, D. & Derksen, J.J. 1995. Transfer of O_2 from air to mineral slurries in a Rushton turbine agitated tank. *Minerals Engineering*, 8(10): 1109-1124.

Venter, R. & Boylett, M. 2009. The evaluation of various oxidants used in acid leaching of uranium, in *Hydrometallurgy Conference 2009* The South African Institute of Mining and Metallurgy:445-456.

Verster, R. & Pieterse, H. 2008. *The use of autoclaves in uranium leach flowsheets.* Perth: ALTA Metallurgical Services.

Vezina, J. & Gow, W. 1969. *Some design aspects of the pressure oxidation acid leaching of a Canadian uranium ore.* Ottawa: Queen's Publisher.

Von Rahden, H. 1970. *Mineralogical and geochemical studies of some Witwatersrand gold ores with special reference to the nature of the phyllosilicate.* Unpublished doctoral thesis. Johannesburg: University of the Witwatersrand.

Vraĉar, R. & Cerović, K. 1997. Kinetics of oxidation of Fe(II) ions by gaseous oxygen at high temperatures in an autoclave. *Hydrometallurgy,* 44:113-124.

Wadsworth, M. 1979. Hydrometallurgical processes, in H.Y. Sohn & M.E. Wadsworth (Eds.). *Rate processes of extractive metallurgy*. New York: Plenum Press. 135.

Warren, I. 1956. The generation of sulphuric acid from pyrite by pressure leaching. *Australian Journal of Applied Science,* 7:346-358.

Whitman, W. 1923. Two-film theory of absorption. *Chemical and Metallurgical Engineering*, 29:147.

Wiersma, C. & Rimstidt, J. 1984. Rates of reaction of pyrite and marcasite with ferric iron at pH 2. *Geochimica et Cosmochimica Acta,* 48:85-92.

Williamson, M. & Rimstidt, J. 1994. The kinetics and electrochemical rate-determining step of aqueous pyrite oxidation. *Geochimica et Cosmochimica Acta*, 58(24):5443-5454.

Winde, F., Brugge, D., Nidecker, A. & Ruegg, U. 2017. Uranium from Africa - An overview on past and current mining activities: Re-apprasing associated risks and chances in a global context. *Journal of African Earth Sciences,* 129:759-778.

World Nuclear Association. 2012. *Energy for the world - why uranium?* December. World Nuclear Association Information Library [Online]. Available: http://www.world-nuclear.org/information-library/nuclear-fuel-cycle/introduction/energy-for-the-world-why-uranium.aspx. [2018, July 9]

World Nuclear Association. 2018. *Plans for new reactors worldwide.* August. World Nuclear Association Information Library [Online]. Available: http://www.world-nuclear.org/information-library/current-and-future-generation/plans-for-new-reactors-worldwide.aspx. [2018, July 9]

Yoshida, F. & Arakawa, S., 1968. Pressure dependence of liquid mass transfer coefficients. *AIChE Journal*, 14:962-963.

Zheng, C., Allen, C. & Bautista, R. 1986. Kinetic study of the oxidation of pyrite in aqueous ferric sulfate. *Industrial & Engineering Chemistry Process Design and Development*. V25:308-317.

Zhong, S. 2015. Leaching kinetics of gold bearing pyrite in H_2SO_4-$Fe_2(SO_4)_3$ system. *Transactions of Nonferrous Metals Society of China*. 25(10):3461-3466.

Zhukov, V., Laari, A. & Koiranen, T. 2015. Kinetic modelling of high-pressure pyrite oxidation with parameter estimation and reliability of analysis using the Markov Chain Monte Carlo Method. *Industrial and Engineering Chemistry Research*, 54:9920-9930.

Zuidervaart, E., Reuter, M.A., Heerema, R.H., Van der Lans, R.G.J.M. & Derksen, J.J. 2000. Effect of dissolved metal sulphates on gas-liquid oxygen transfer in agitated quartz and pyrite slurries. *Minerals Engineering*, 13(14-15):1555-1564.

Zwietering, T. 1958. Suspending of solid particles in liquid by agitators. *Chemical Engineering Science*, 8:244-253.

SOFTWARE REFERENCES

HSC Chemistry (HSC, 2006) Chemical Reaction and Equilibrium Software with Thermochemical Database, Outokumpu Research, Pori, Finland, Release 6.0.

Matlab (2018). The MathWorks Inc. Release 2018a.

APPENDICES

APPENDIX A: Supporting information for literature study

Appendix A.1: Molecular orbitals of pyrite

Six electrons from the sulphur atom (3p4 and 3s2 electrons) and eight electrons from the iron atom (3d8 valence electrons) are involved in bonding in FeS_2 (Abraitis et al., 2004). The strong fields generated by the sulphur ligands and their orientation around the 3d orbitals of the iron results in extensive splitting of the 3d orbitals into the triply degenerate t_{2g} (d_{xy}, d_{yz} and d_{xz}) and doubly degenerate e_g^* orbitals (d_{z2} and d_{x2-y2}) (Abraitis et al., 2004; Chandra & Gerson, 2010; Cotton, et al., 1976: 511; Lowson, 1982). The six 3d electrons from Fe^{2+} cation are paired and occupy the t_{2g} orbital (low-spin state). The t_{2g} orbital remains non-bonding (Chandra & Gerson, 2010) and the higher energy e_g^* orbitals remain unoccupied (Abraitis, et al., 2004; Lowson, 1982). The remaining 14 electrons (from the $(S_2)^{2-}$ anion) fill the $3s_\sigma$, $3s_{\sigma*}$, $3p_\sigma$, $3p_\pi$ and $3p_{\pi*}$ orbitals (Lowson, 1982). The $3p_{\sigma*}$ remain unoccupied. The molecular orbital scheme of the $(S_2)^{2-}$ anion and Fe^{2+} is shown in Figure A.1.

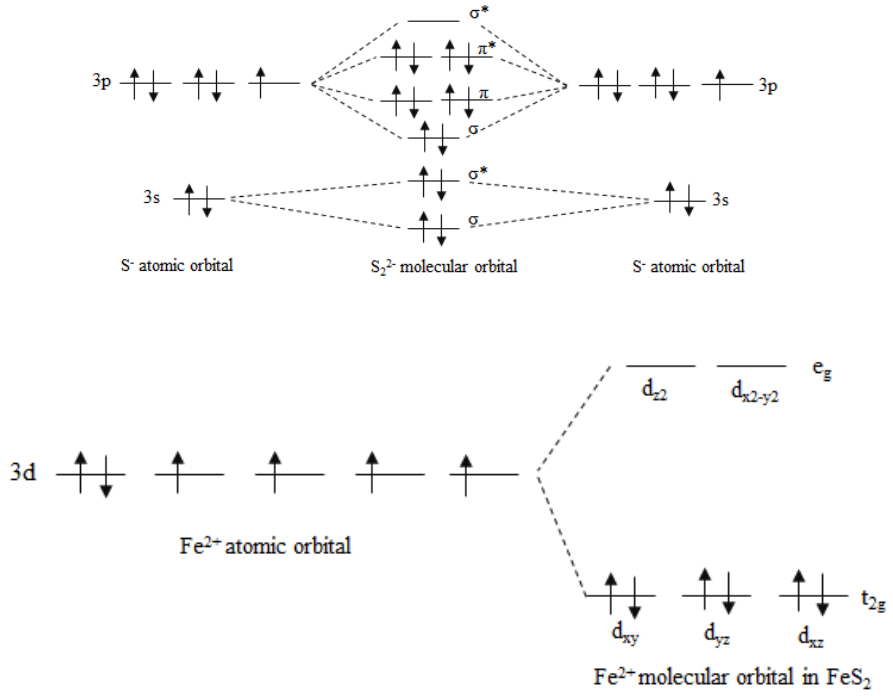

Figure A.1: Molecular orbitals of S^{2-} and Fe^{2+} in FeS_2 (Hung et al., 2002; Luther, 1987)

Appendix A.2: Valence band structure and electrochemical dissolution of pyrite

In pyrite the valence band is composed mainly of the t_{2g} states and the primary bonding band, located just below the t_{2g} band, is composed of the 3p (from S_2^{2-}) and Fe 3d (bonding e_g) orbitals. The lower part of the conduction band is a mixture of the $3_{p\sigma}$* and e_g* anti-bonding orbitals. The band gap is

located between the e_g^* and the t_{2g} non-bonding orbitals and have been measured as 0.96 ± 0.12 V[aa] (Lowson, 1982).

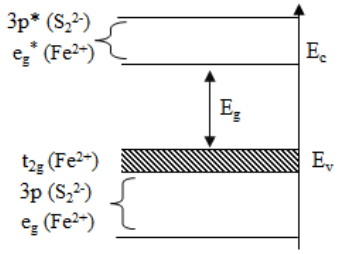

Figure A.2: Schematic band structure of FeS_2 (redrawn from Mishra & Osseo-Asare (1988))

Electrochemical dissolution in most semiconductor minerals proceeds via hole (h^+) formation. A hole is defined as the absence of one of the bonding electrons in the valence band of the solid. This leads to weakening of the bond with an adjacent atom and a remaining unpaired electron at the surface. The atom associated with the unpaired electron is then especially susceptible to attack by a nucleophilic agent resulting in bond breakage with the adjacent atom and a new bond being created between the surface atom and the nucleophilic species (Osseo-Asare, 1992).

A hole in the valence band of the mineral may either be injected by a redox couple (i.e., "capturing" of one the bonding electrons) or by applying an anodic electric current (Steyl, 2012: 234). Considering the role of the redox couple, the probability of electron transfer between a donor and an acceptor site is dictated by whether there is sufficient alignment between the energy level of the redox couple (E_{redox}) and the energy levels of the semiconductor mineral i.e., either the conduction band or the valence band (Crundwell, 1988; Osseo-Asare, 1992). Pyrite's resistance to dissolution is said to be partly due to its valence band consisting of the Fe^{2+} non-bonding orbitals and this means that hole injection into this band will result in the formation of Fe^{3+} sites and not in the breaking of bonds. The valence bands of other sulphide minerals such as ZnS consist of bonding orbitals which means hole injection leads to direct bond breaking between surface atoms and thus explains why these sulphide minerals are more easily leachable compared to pyrite (Crundwell, 1988; Osseo-Asare, 1992)

[aa] The band gap of semiconductors is typically less than 2 eV (Osseo-Asare, 1992)

Appendix A.3: Pyrite oxidation mechanisms

The most plausible and accepted mechanisms for the oxidation of pyrite have been provided by Kelsall, Yin, Vaughan, England and Brandon (1999), Moses and Herman (1991) and Rimstidt and Vaughan (2003). There is general agreement that thiosulphate is the key intermediate and that thiosulphate is oxidised to SO_4^{2-} and/or elemental sulphur, depending on the oxidation potential. The mechanism provided by Rimstidt and Vaughan (2003) is briefly reviewed.

The anodic site on the pyrite surface is the S_2^{2-} moiety whereas the cathodic site is the Fe^{2+} atom. The rate-limiting step in the reaction pathway is the first electron transfer from the cathodic site to the oxidant. On the other hand Kelsall, Yin, Vaughan, England and Brandon (1999) proposed that the first electron transfer is most likely to occur from S_2^- (the anodic site). Either way, all four electrons from the anodic site pass through the cathodic site to the oxidant. Electron removal from the anodic site results in the terminal sulphur becoming increasingly electropositive. This results in attachment of the water to the anodic site by a nucleophilic attack (accounting for the fact that the "O" atom in sulphate originates from H_2O and not from O_2) and electron transfer from H_2O to S^{2-}. The proton is liberated and balances the positive charge created at the cathodic site. This process of sequential H_2O addition and proton liberation repeats itself until Fe-S-SO_3 is formed. Depending on the strength of the Fe-S bond compared to the S-S bond in the surface, SO_4^{2-} or HSO_3^- breaks away either as thiosulphate ($S_2O_3^{2-}$) or FeS_2O_3 followed by solvation of the species. The thiosulphate ($S_2O_3^{2-}$) or FeS_2O_3 is decomposed to H_2SO_3, SO_4^{2-}, elemental sulphur and Fe^{2+} prior to diffusing to the bulk of the solution. The existence of other intermediates such as $S_2O_4^{2-}$, $S_2O_5^{2-}$ and $S_2O_6^{2-}$ are also possible. The ratio of the final products i.e. Fe^{2+}, SO_4^{2-}, S and H_2SO_3 will depend on the rates of the different reactions and the potential (Kelsall et al., 1999). Key in this proposed mechanism is that the $S^{(-1)}$ remains part of pyrite's crystal lattice until it has been completely oxidised to S^{4+}. Steyl (2012: 483) have emphasised the fact some intermediate radical species may be more mobile than others which would take part in further oxidation much more readily.

Several detailed 'hole' generation and consumption reaction mechanisms, in which various surface and aqueous radical intermediates were considered, were proposed by Steyl (2012: 258-273). Crundwell (1988) and Steyl (2012: 263) also pointed out that the intermediate OH· could play an important role in the oxidation mechanism. The "splitting of water" to form OH· radicals is said to occur as a result of hole consumption or electron transfer to the t_{2g} valence band of pyrite by the H_2O/OH· redox couple (according to Reaction A.3) (Steyl, 2012: 263).

$$H_2O + h^+ \leftrightarrow H^+ + OH\cdot \qquad (E^o = 2.6 - 2.8\ V) \qquad A.3$$

The holes in pyrite's t_{2g} valence band do not lead to mineral dissolution directly and is unique to pyrite as a result of its electron structure. The OH radical, after it has been produced, is a strong oxidising agent to effect sulphide oxidation to sulphate and/or sulphur and explains the "O" atom in the sulphate originating from water and not from molecular oxygen itself (Crundwell, 1988; Steyl, 2012). Steyl (2012) also suggested that the "splitting of water" could be the rate-limiting step in the anodic dissolution process. However, the original holes in the t_{2g} band, which enables subsequent "splitting of H_2O", is proposed to remain dependent on electron-exchange/or hole injection by iron(III).

The mechanism by which the iron(II)/iron(III) redox couple catalyses the oxidation kinetics have not been clarified to date. Steyl (2012: 446) suggested a mechanism by which dissolved oxygen is complexed with both lattice iron and aqueous iron, followed by electron exchange. A different mechanism has been proposed by (Moses & Herman, 1991), in which it was assumed that the reaction sequence characteristic of aqueous iron(II) to iron(III) homogeneous oxidation (refer to Section 2.6.2), is occurring at the pyrite surface. Both of the suggested mechanisms are shown Figure A.3.

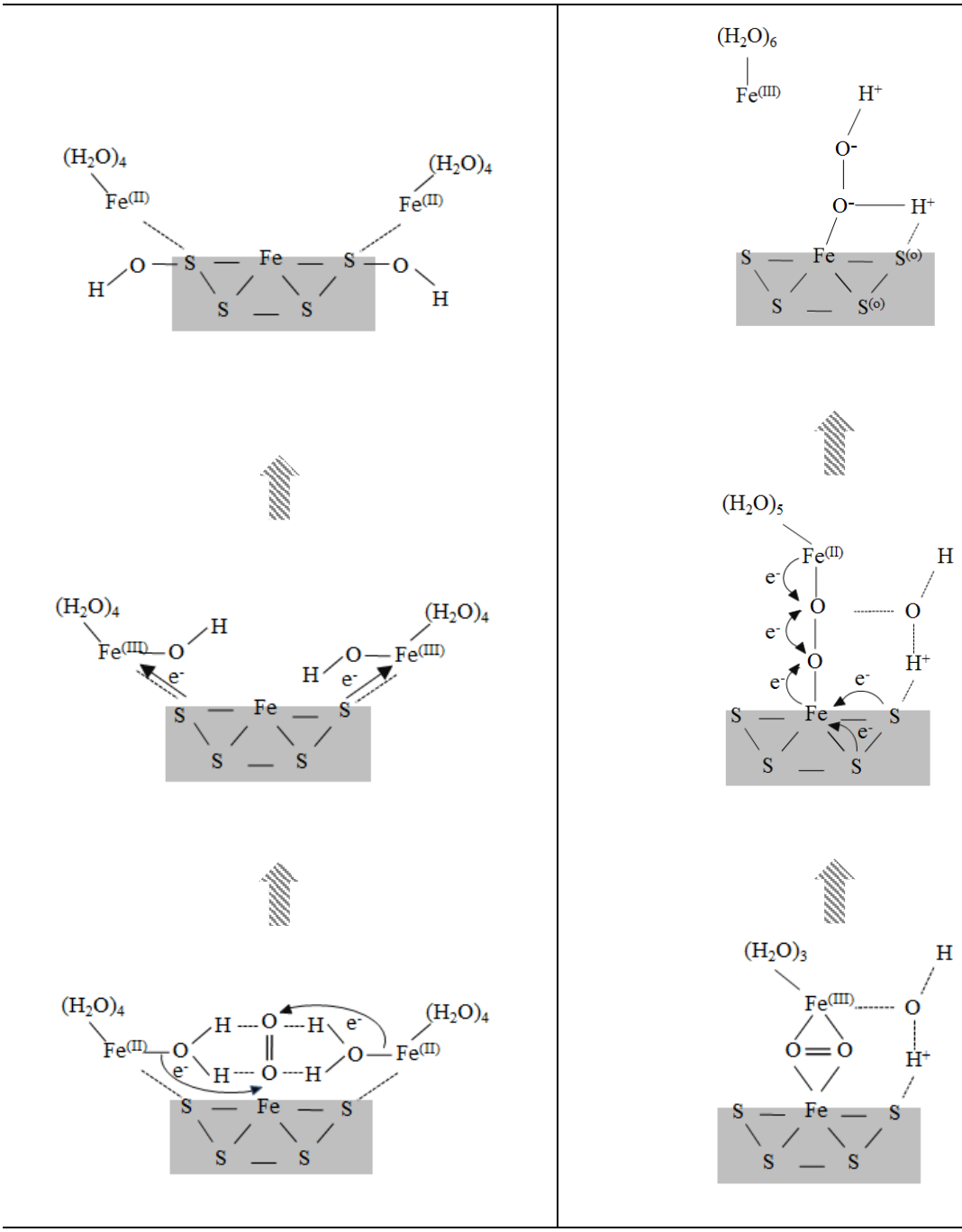

(a) *(b)*

Figure A.3: Proposed mechanisms for pyrite oxidation with oxygen catalysed by iron(III) (a) Reaction pathway suggested by (Moses & Herman, 1991) (b) Reaction sequence proposed by Steyl (2012: 446)

APPENDIX B: GAS-LIQUID MASS TRANSFER

Appendix B.1: Models to describe absorption into agitated liquids: Film model

Several simplified models exist to describe the absorption process in agitated systems. In this study the film model was employed. The film model is based on the two-film theory which was originally proposed by Whitman (1923). Since the gas-side resistance is usually negligible (Yoshida & Arakawa, 1968), focus will be turned to the liquid phase and corresponding mathematical considerations.

Following from Danckwerts (1970: 11), a film with thickness δ (in m) is assumed to exist at the gas-liquid interface i.e., $x = 0$ at the gas-liquid surface and $x = \delta$ at a distance δ below the surface. The concentration of solute A is c_A^* at $x = 0$ and c_A^0 where $x = \delta$. c_A^0 thus corresponds to the bulk concentration of the liquid. By assuming steady-state $(\partial c_A/\partial t = 0)$ and that no chemical reaction occurs with the diffusant ($r_A = 0$), the following expressions may be derived:

$$D_A \frac{d^2 m_A}{dx^2} = 0 \qquad \text{B.1}$$

$$D_A \frac{dm_A}{dx} = constant \qquad \text{B.2}$$

Since the concentration gradient (dm_A/dx) over the film is constant (Eq. B.6), the concentration linearly decreases from m_A^* at the interface to m_A^0 at the film's inner edge. The concentration gradient may therefore be written as:

$$\frac{dm_A}{dx} = -\frac{(m_A^* - m_A^0)}{\delta} \qquad \text{B.3}$$

The rate of absorption (J_A) in mol.m/min.kg of diffusant A, as a function of the concentration gradient, are defined as follows (Danckwerts, 1970: 11, 98):

$$J_A = D_A \frac{(m_A^* - m_A^0)}{\delta} \qquad \text{B.4}$$

The rate of absorption of a gas into an agitated liquid has been found experimentally to be described by Eq. B.5 (where k_m is the physical mass transfer coefficient with units m/min) (Danckwerts, 1970: 97):

$$J_A = k_m(m_A^* - m_A^0) \qquad \text{B.5}$$

It can be therefore be shown that, according to the film model (by equating Eq. B.8 and B.9), the physical mass transfer coefficient is linearly dependent on the diffusion coefficient and inversely proportional to the film thickness as shown in Eq. B.6 (Danckwerts, 1970: 98):

$$k_m = \frac{D_A}{\delta} \qquad \text{B.6}$$

Appendix B.2: Effect of reaction on absorption

A steady-state mass balance for a gas component A undergoing a pseudo-nth-order reaction with one of the liquid phase components may be written as follows (Linek & Vacek, 1981):

$$D_A \frac{\partial^2 m_A}{\partial x^2} = k_n m_A^n \qquad \text{B.7}$$

The effect of chemical reaction on the rate of gas absorption may also be described with the aid of the film model (Appendix B.1). A dimensionless quantity, the Hatta number (H_A), is often used to quantify the degree of chemical enhancement and to identify the kinetic regime in the film. The Hatta number is defined as follows (Linek & Vacek, 1981):

$$H_A = \left(\frac{2k_n {m_A^*}^{n-1} D_A}{(n+1)k_m^2}\right)^{\frac{1}{2}} \qquad \text{B.8}$$

The solute A concentration profiles in the "diffusion film" in different reaction rate regimes for a first order reaction are presented in Figure B.1 where "B" denotes the liquid phase component which reacts with A.

REGION A: Very slow reaction in the bulk of the liquid (H_A<0.02)

The bulk of the liquid becomes and remains saturated with gas and no reaction takes place in the liquid side diffusion film. k_La is thus sufficiently large enough to keep the liquid virtually saturated with gas in spite of its removal by reaction. Knowledge of the solubility of the gas thus gives its concentration in the liquid (Danckwerts, 1970). The concentration gradient over the diffusion film is very small as seen in Figure B.1a. It is within this regime that one may establish the kinetics of a chemical reaction (Danckwerts, 1970).

REGION B: Slow reaction in the bulk of the liquid *($0.02 < H_A < 0.3$)*

In this case, the concentration of the dissolved gas m_A^0 is substantially less than m_A*. The reaction is fast enough to maintain the bulk concentration virtually at zero, while not being fast enough for an appreciable amount of reaction to occur in the film (Ruchti, et al., 1985). In this region, the k_La

should be measured. The concentration gradient over the diffusion film is linear as shown in Figure B.1b (Cheng, 1994).

REGION C AND D: Fast reaction in the bulk of the liquid *(H_A > 0.3)*

In this regime, the reaction is so fast that the majority of the diffusant reacts in the film before reaching the bulk of the solution. The concentration-gradient at the gas-liquid surface is greater than at the inner boundary of the film giving rise to an enhancements factor that is greater than unity (Linek & Vacek, 1981). The concentration profiles for moderately fast and very fast reactions are shown in Figure B.1c and d.

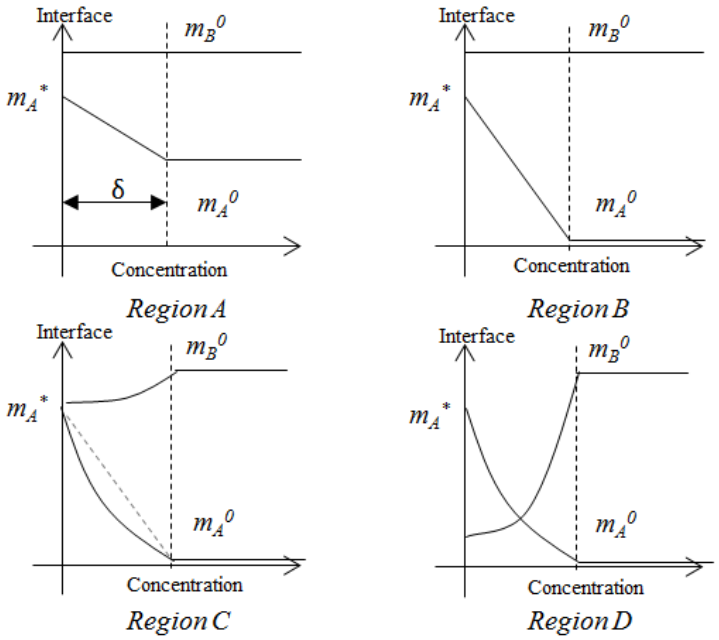

Figure B.1: Liquid-phase concentration profiles for mass transfer with chemical reaction: film theory (redrawn from Cheng (1994))

Appendix B.3: Methods of aeration

Sparging

In sparged systems the gas is usually introduced below the impeller to enable gas dispersion resulting from cavities formed at the impeller blades. The stirring speed and the gas throughput are two independent variables which could be adjusted to control gas holdup and interfacial area, therefore the k_La-values in these systems could vary over a wide range and are typically controlled at very high levels (Albal et al., 1983).

`Surface aeration

Surface aeration is defined as the aeration or oxygen transfer that takes place in the gas-liquid interface when the liquid is agitated, without the sparging of air/oxygen (Fuchs et al., 1971).

Depending on the stirring speed, there are three regimes of mass transfer from the gas in the vessel head space to the liquid phase during surface aeration. At low stirring speeds, the surface diffusion regime is dominant as mass transfer occurs mainly by diffusion (such as in quiescent liquids). As the stirring speed increases, the liquid surface will start to break up. The rate of surface renewal increases and convective forces become more prevalent. This regime is called the surface convection regime. The last regime is the surface entrainment regime. This regime is characterised by complete breakage of the liquid surface and a very high liquid surface renewal rate. Gas entrainment velocity into the liquid is consequently high. Surface entrainment can be achieved in agitated tank reactors without baffles by vortex aeration at high stirring speeds. In tanks with baffles, surface entrainment can be obtained with an agitator located just below the liquid surface at relatively low stirring speeds (Albal et al., 1983; Lee & Foster, 1990).

Major factors which have an effect on the entrained gas flow rate include (Lee & Foster, 1990):

- Agitator stirring speed
- Relative position of impeller/s to the liquid surface
- Impeller diameter
- Type of impeller used

Appendix B.4: Procedures and reagents for oxygen gas-liquid mass transfer test work

Iodimetric back-titration

To determine the residual sulphite concentration in the 2 gallon Parr batch reactor during the oxygen mass transfer tests, an iodimetric titration was conducted on each kinetic sample. The iodimetric titration is based on the following reaction (Jeffery et al., 1989: 398):

$$SO_3^{2-} + I_2 + H_3O \rightarrow SO_4^{2-} + 2H^+ + 2I^- \qquad \text{B.15}$$

Each kinetic sample which was removed from the reactor was rapidly cooled in an ice bath to room temperature. The titration followed immediately per the following procedure (provided by Jeffrey et al., 1989: 398):

Fifty (50) ml of the standard 0.1 M iodine solution, 10 ml 2 M hydrochloric acid (HCl) and 150 ml DI water was added to a 500 ml conical flask. The 4 ml sulphite-containing kinetic sample was added to the iodine solution and swirled gently until completely mixed. The excess iodine was then titrated with the 0.1 M sodium thiosulphate solution according to the following reaction:

$$2S_2O_3^{2-} + I_2 \rightarrow S_4O_6^{2-} + 2I^- \qquad \text{B.16}$$

The initial solution had a pale yellow colour and the end-point was characterised by a change from pale yellow to colourless. The detection of the end-point was made clearer with the addition of starch (~ 1 ml) just before reaching the end-point. The addition of starch to the iodide formed a blue-coloured complex. When starch was added, the end-point was characterised by the change in colour from a dark blue to a light-blue (almost colourless) solution. The volume thiosulphate added to reach the end-point was recorded and used to calculate the initial sulphite ion concentration in the kinetic sample.

The preparation methods for the titrants and indicators are included in Table B.1. In all cases analytical (AR) grade reagents were used.

Table B.1: Preparation methods of titrants and indicators

Preparation of 0.1M iodine solution		
Recipe	Method	Reference
▪ 40 g potassium iodide (KI) ▪ 25.5 g resublimed iodine (I_2)	Dissolve salts with water to 1 L. Store in cool dark place in amber-coloured glass-stoppered bottle.	Jeffery et al. (1989: 389)
Preparation of 0.1 M thiosulphate solution		
Recipe	Method	Reference
▪ 25 g sodium thiosulphate pentahydrate crystals ($Na_2S_2O_3.5H_2O$) ▪ 0.1 g sodium carbonate (Na_2CO_3)	Dissolve salts in previously boiled distilled water. Store in cool dark place in amber-coloured glass-stoppered bottle.	Jeffery et al. (1989: 390-391)
Preparation of starch indicator		
Recipe	Method	Reference
▪ 0.1 g soluble starch ▪ 2-3 g KI	Prepare paste of 0.1 g soluble starch with water, introduce paste into 100 ml boiling water. Boil for 1 minute and allow to cool.	Jeffery et al. (1989: 388)

	Add 2-3 g KI. Store in cool dark place in glass-stoppered bottle.

All solutions prepared were standardised per the procedures provided below:

- ***Iodine solution standardisation (Jeffery et al., 1989: 390)***

The 0.1 M iodine solution was standardised with the 0.1 M thiosulphate solution. The end-point was again indicated by the change in colour from dark-blue to almost colourless after the starch indicator had been added.

- ***Thiosulphate solution standardisation (Jeffery et al., 1989: 392)***

Potassium dichromate ($K_2Cr_2O_7$) was used for the standardisation of the thiosulphate solution. 0.1 g of $K_2Cr_2O_7$ was accurately weighted and dissolved in 50 ml of water. Three (3) g of KI was mixed with 100 ml water followed by the addition of 6 ml concentrated HCl and the $K_2Cr_2O_7$ solution. The solution swirled gently and left to stand for 5 minutes until the following reactions had gone to completion.

$$Cr_2O_7^{2-} + 6I^- + 14H^+ \rightarrow 2Cr^{3+} + 7H_2O + 3I_2 \quad \text{B.17}$$

$$3I_2 + 3I^- \leftrightarrow 3I_3^- \quad \text{B.18}$$

The liberated iodine was then titrated with the sodium thiosulphate solution. The reaction between the thiosulphate and tri-iodide ion has the following stoichiometry:

$$6S_2O_3^{2-} + 3I_3^- \rightarrow 3S_4O_6^{2-} + 9I^- \quad \text{B.19}$$

The endpoint, which was characterised by similar colour changes than previously described, was then used to calculate the thiosulphate concentration per the stoichiometry of the listed reactions.

Cobalt catalyst stock solution

A cobalt catalyst stock solution was prepared by the addition of 1.321 g $CoSO_4$.Heptahydrate (0.975 purity) in 1 L of deionised water to yield a concentration of 270 mg/L. The stock solution was subsequently analysed via ICP-OES and reported by MINTEK's Analytical Services Division as 263 mg/L.

Appendix B.5: Calculation of $Na_2SO_{3(aq)}$-$Na_2SO_{4(aq)}$ system solution density

It is important to predict the solution volume in the autoclave after it has been charged with the required amount of Na_2SO_3 solution. The increase in solution volume with temperature and the change in volume as Na_2SO_3 is converted to Na_2SO_4 have to be accounted for, as this will affect the distance between the liquid level and the top impeller. The density of the solution is also critical in conversion from molarity (M) to the molality (m) scale during data analyses. Therefore, a correlation for solution density as function of Na_2SO_3 concentration, Na_2SO_4 concentration and temperature is required.

Density data for aqueous electrolyte mixtures of Na_2SO_3 and Na_2SO_4 could not be found in literature. Data for the systems Na_2SO_3-H_2O and Na_2SO_4-H_2O at temperatures ranging to 80°C and compositions to 20 wt % were however located (Liley et al., 1997; Söhnel & Novotny, 1984). By evaluation of both the datasets, it was found that the ratio between the solution density and the density of water remains constant over the temperature ranges investigated. Two equations were regressed from the datasets, both having regression coefficients close to unity, as shown in Figure B.2 and Figure B.3.

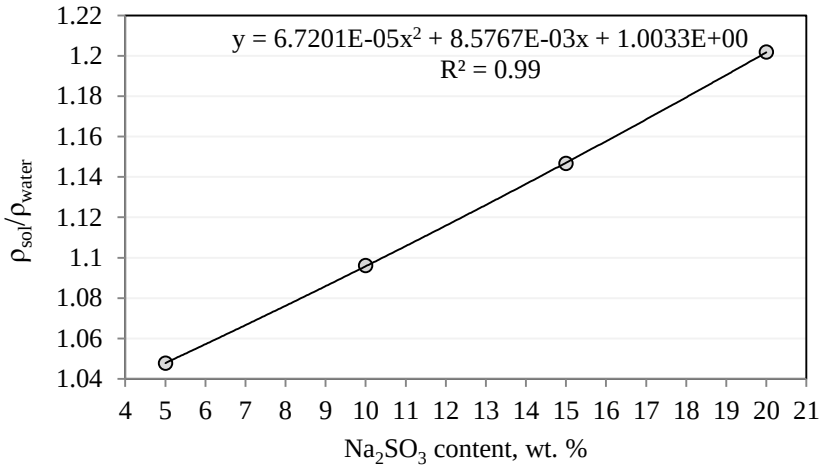

Figure B.2: Relative density of Na_2SO_3 solutions to the density of pure water as a function of Na_2SO_3 content (Söhnel & Novotny, 1984)

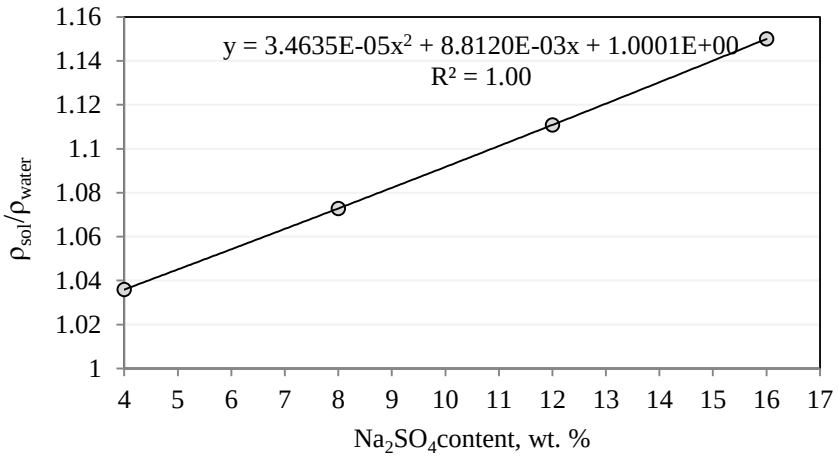

Figure B.3: Relative density of Na_2SO_4 solutions to the density of pure water as a function of Na_2SO_4 content (Liley, et al., 1997)

The density of water as a function of temperature can easily be obtained from standard steam tables found in standard thermodynamic text books (Koretsky, 2004).

To calculate the density of a solution containing both $Na_2SO_{3(aq)}$ and $Na_2SO_{4(aq)}$, a weighted average of the relative densities calculated by the suggested regression equations were used. Note that the total electrolyte concentration ($1-w_{H2O}$) instead of the concentration of just one electrolyte was used in the regression equations. A similar assumption has been made in previously published density models (Laliberté & Cooper, 2004).

Appendix B.6: Calculation of vapour pressure of $Na_2SO_{3(aq)}$-$Na_2SO_{4(aq)}$ system

Na_2SO_3-Na_2SO_4 system

To estimate the solution vapour pressure, data from Pabalan and Pitzer (1988) were regressed by Steyl (2012: 578-579) as a function of temperature and $Na_2SO_{4(aq)}$ concentration. Due to the unavailability of vapour pressure data for sodium sulphite solutions in the open literature, it was assumed that the solution vapour pressure is identical to that of sodium sulphate solutions at equal concentrations. The following relationships were found:

$$lnp_w = p_1 + p_2\left(\frac{T_c}{T_0}\right)^{0.5} + p_3[Na_2SO_4] \qquad T < 100°C \qquad \text{B.20}$$

$$lnp_w = p_1 + 2p_2\ln\left(\frac{T_c}{T_0}\right) + p_3[Na_2SO_4] \qquad T \geq 100°C \qquad \text{B.21}$$

Where p_w is the solution vapour pressure in kPa and T_c the solution temperature in °C. T_o refers to unit temperature i.e., 1°C.

Table B.2: Parameter values of Equations B.20 and B.21 (Steyl, 2012: 579)

	T_c < 100°C	***$T_c \geq$ 100°C***
p_1	-2.6031	-3.8878
p_2	7.221×10^{-1}	4.004×10^{-1}
p_3	-3.48×10^{-2}	-3.02×10^{-2}

Appendix B.7: Log sheets of mass transfer work

Indirect method: Sodium sulphite

Test number: MT9					
Agitation speed	500	rev/min	Vapour pressure of solution	11.718	kPa
Impeller arrangement	A		O_2 partial pressure	234	kPa(abs)
Pressure	229	kPa(g)	O_2 solubility	31.07	mg/kg
Temperature	50	°C	O_2 gas purity	99.5	%
$[Na_2SO_3]$ starting	1.172	mol/L	$[CoSO_4]$	0.10	mg/L
[Thiosulphate]	0.101	mol/L	Total mass in	5624	g
[Iodine]	0.102	mol/L	Starting volume	5000	ml

Time	Sample volume	Thiosulphate added	Estimated density	$[Na_2SO_3]$	O_2 reacted
min	ml	ml	kg/m^3	mol/L	mg/kg
0	4.0	7.6	1124	1.175	0
30	4.0	13.2	1125	1.105	1145
60	4.0	21.7	1125	0.998	2885
120	4.0	33.4	1127	0.851	5274
180	4.0	41.9	1127	0.744	7021

Test number: MT10					
Agitation speed	500	rev/min	Vapour pressure of solution	11.718	kPa
Impeller arrangement	A		O_2 partial pressure	234	kPa(abs)
Pressure	229	kPa(g)	O_2 solubility	31.07	mg/kg
Temperature	50	°C	O_2 gas purity	99.5	%

$[Na_2SO_3]$ starting	1.172	mol/L	$[CoSO_4]$	0.10	mg/L
[Thiosulphate]	0.101	mol/L	Total mass in	5624	g
[Iodine]	0.102	mol/L	Starting volume	5000	ml

Time	Sample volume	Thiosulphate added	Estimated density	$[Na_2SO_3]$	O_2 reacted
min	ml	ml	kg/m3	mol/L	mg/kg
0	4.1	8.5	1124	1.136	0
30	4.1	11.4	1125	1.100	579
60	4.1	19.3	1125	1.004	2146
120	4.1	31.8	1127	0.850	4647
180	4.1	45.8	1128	0.678	7466

Test number: MT11					
Agitation speed	500	rev/min	Vapour pressure of solution	11.718	kPa
Impeller arrangement	A		O_2 partial pressure	214	kPa(abs)
Pressure	208.63	kPa(g)	O_2 solubility	28.36	mg/kg
Temperature	50	°C	O_2 gas purity	99.5	%

$[Na_2SO_3]$ starting	1.172	mol/L	$[CoSO_4]$	1.00	mg/L
[Thiosulphate]	0.101	mol/L	Total mass in	5624	g
[Iodine]	0.102	mol/L	Starting volume	5000	ml

Time	Sample volume	Thiosulphate added	Estimated density	$[Na_2SO_3]$	O_2 reacted
min	ml	ml	kg/m^3	mol/L	mg/kg
0	4.0	13.0	1125	1.108	0
30	4.0	20.6	1125	1.012	1566
60	4.0	28.7	1126	0.910	3226
120	4.0	51.4	1128	0.625	7883
180	4.0	65.9	1129	0.442	10885

Test number: MT12					
Agitation speed	500	rev/min	Vapour pressure of solution	11.737	kPa
Impeller arrangement	A		O_2 partial pressure	223	kPa(abs)
Pressure	217.65	kPa(g)	O_2 solubility	30.19	mg/kg
Temperature	50	°C	O_2 gas purity	99.5	%

[Na_2SO_3] starting	1.172	mol/L	[$CoSO_4$]	9.99	mg/L
[Thiosulphate]	0.101	mol/L	Total mass in	5624	g
[Iodine]	0.102	mol/L	Starting volume	5000	ml

Time	Sample volume	Thiosulphate added	Estimated density	[Na_2SO_3]	O_2 reacted
min	ml	ml	kg/m_3	mol/L	mg/kg
0	4.0	20.9	1121	1.008	0
30	4.0	49.8	1123	0.644	5929
60	4.0	67.8	1125	0.418	9628
120	4.0	96.0	1127	0.063	15476
180	4.0	90.9	1127	0.127	14417

Test number: MT13					
Agitation speed	500	rev/min	Vapour pressure of solution	11.728	kPa
Impeller arrangement	A		O_2 partial pressure	223	kPa(abs)
Pressure	217.65	kPa(g)	O_2 solubility	29.87	mg/kg
Temperature	50	°C	O_2 gas purity	99.5	%

$[Na_2SO_3]$ starting	1.172	mol/L	$[CoSO_4]$	5.00	mg/L
[Thiosulphate]	0.101	mol/L	Total mass in	5624	g
[Iodine]	0.102	mol/L	Starting volume	5000	ml

Time	Sample volume	Thiosulphate added	Estimated density	$[Na_2SO3]$	O_2 reacted
min	ml	ml	kg/m3	mol/L	mg/kg
0	4.0	32.9	1125	0.857	0
30	4.0	38.9	1124	0.781	1480
60	4.0	45.0	1125	0.705	2607
120	4.0	68.1	1127	0.414	7368
180	4.0	92.7	1129	0.104	12463

Test number: MT19&20					
Agitation speed	600	rev/min	Vapour pressure of solution	11.718	kPa
Impeller arrangement	B	-	O_2 partial pressure	71.48	kPa(abs)
Pressure	0.00	kPa(g)	O_2 solubility	9.49	mg/kg
Temperature	50	°C	O_2 gas purity	99.5	%

$[Na_2SO_3]$ starting	1.172	mol/L	$[CoSO_4]$	0.06	mg/L
[Thiosulphate]	0.100	mol/L	Total mass in	5571	g
[Iodine]	0.100	mol/L	Starting volume	4953	ml

Time	Sample volume	Thiosulphate added	Estimated density	$[Na_2SO_3]$	O_2 reacted
min	ml	ml	kg/m3	mol/L	mg/kg
0	4.0	10.5	1125	1.119	0
30	4.0	12.1	1125	1.099	325
60	4.0	14.4	1125	1.070	792
70	4.0	16.4	1125	1.046	1189
90	4.0	17.7	1125	1.029	1453
110	4.0	21.9	1126	0.976	2318

Test number: MT21					
Agitation speed	600	rev/min	Vapour pressure of solution	11.718	kPa
Impeller arrangement	B		O_2 partial pressure	71.48	kPa(abs)
Pressure	0.00	kPa(g)	O_2 solubility	9.49	mg/kg
Temperature	50	°C	O_2 gas purity	99.5	%

$[Na_2SO_3]$ starting	1.172	mol/L	$[CoSO_4]$	0.54	mg/L
[Thiosulphate]	0.100	mol/L	Total mass in	5570	g
[Iodine]	0.100	mol/L	Starting volume at temperature	4952	ml

Time	Sample volume	Thiosulphate added	Estimated density	$[Na_2SO_3]$	O_2 reacted
min	ml	ml	kg/m^3	mol/L	mg/kg
0	4.0	9.6	1125	1.130	0
30	4.0	13.1	1125	1.087	701
60	4.0	17.4	1125	1.033	1585
100	4.0	22.0	1126	0.975	2521

Test number: MT22					
Agitation speed	600	rev/min	Vapour pressure of solution	11.718	kPa
Impeller arrangement	B		O_2 partial pressure	71.48	kPa(abs)
Pressure	0.00	kPa(g)	O_2 solubility	9.49	mg/kg
Temperature	50	°C	O_2 gas purity	99.5	%

$[Na_2SO_3]$ starting	1.172	mol/L	$[CoSO_4]$	2.70	mg/L
[Thiosulphate]	0.100	mol/L	Total mass in	5571	g
[Iodine]	0.100	mol/L	Starting volume	4953	ml

Time	Sample volume	Thiosulphate added	Estimated density	$[Na_2SO_3]$	O_2 reacted
min	ml	ml	kg/m^3	mol/L	mg/kg
0	4.0	9.6	1124	1.130	0
30	4.0	13.1	1125	1.087	698
60	4.0	17.4	1125	1.033	1579
90	4.0	22.6	1126	0.968	2649
120	4.0	27.8	1126	0.903	3688

Test number: MT23					
Agitation speed	600	rev/min	Vapour pressure of solution	11.718	kPa
Impeller arrangement	Twin Impellers and Inductor B		O_2 partial pressure	71.48	kPa(abs)
Pressure	0.00	kPa(g)	O_2 solubility	9.49	mg/kg
Temperature	50	°C	O_2 gas purity	99.5	%

$[Na_2SO_3]$ starting	1.172	mol/L	$[CoSO_4]$	5.44	mg/L
[Thiosulphate]	0.100	mol/L	Total mass in	5571	g
[Iodine]	0.100	mol/L	Starting volume	4953	ml

Time	Sample volume	Thiosulphate added	Estimated density	$[Na_2SO_3]$	O_2 reacted
min	ml	ml	kg/m3	mol/L	mg/kg
0	4.0	9.7	1125	1.129	0
33	4.0	13.5	1125	1.082	762
60	4.0	17.5	1125	1.031	1585
90	4.0	22.0	1126	0.975	2501
123	4.0	29.6	1126	0.880	4049

Test number: MT28					
Agitation speed	600	rev/min	Vapour pressure of solution	11.718	kPa
Impeller arrangement	B		O_2 partial pressure	71.48	kPa(abs)
Pressure	0.00	kPa(g)	O_2 solubility	9.49	mg/kg
Temperature	50	°C	O_2 gas purity	99.5	%

$[Na_2SO_3]$ starting	1.172	mol/L	$[CoSO_4]$	8.13	mg/L
[Thiosulphate]	0.100	mol/L	Total mass in	5571	g
[Iodine]	0.100	mol/L	Starting volume	4953	ml

Time	Sample volume	Thiosulphate added	Estimated density	$[Na_2SO_3]$	O_2 reacted
min	ml	ml	kg/m3	mol/L	mg/kg
0	4.0	10.3	1125	1.122	0
30	4.0	16.3	1125	1.046	1229
60	4.0	20.8	1126	0.991	2135
90	4.0	26.4	1126	0.920	3285

Test number: MT16					
Agitation speed	600	rev/min	Vapour pressure of solution	11.718	kPa
Impeller arrangement	B		O_2 partial pressure	71.48	kPa(abs)
Pressure	0.00	kPa(g)	O_2 solubility	9.49	mg/kg
Temperature	50	°C	O_2 gas purity	99.5	%

[Na_2SO_3] starting	1.172	mol/L	[$CoSO_4$]	0.54	mg/L
[Thiosulphate]	0.100	mol/L	Total mass in	5647	g
[Iodine]	0.100	mol/L	Starting volume at temperature	5020	ml

Time	Sample volume	Thiosulphate added	Estimated density	[Na_2SO_3]	O_2 reacted
min	ml	ml	kg/m3	mol/L	mg/kg
0	4.0	9.9	1125	1.127	0
30	4.0	12.5	1125	1.094	528
60	4.0	14.4	1125	1.070	925
120	4.0	20.2	1125	0.998	2214

Test number: MT17					
Agitation speed	600	rev/min	Vapour pressure of solution	11.718	kPa
Impeller arrangement	B		O_2 partial pressure	71.48	kPa(abs)
Pressure	0.00	kPa(g)	O_2 solubility	9.49	mg/kg
Temperature	50	°C	O_2 gas purity	99.5	%

$[Na_2SO_3]$ starting	1.172	mol/L	$[CoSO_4]$	0.56	mg/L
[Thiosulphate]	0.100	mol/L	Total mass in	5429	g
[Iodine]	0.100	mol/L	Starting volume	4827	ml

Time	Sample volume	Thiosulphate added	Estimated density	$[Na_2SO_3]$	O_2 reacted
min	ml	ml	kg/m^3	mol/L	mg/kg
0	4.0	10.1	1125	1.124	0
30	4.0	15.7	1125	1.054	1138
60	4.0	19.4	1125	1.008	1901
120	4.0	30.8	1126	0.866	4213

Test number: MT18					
Agitation speed	600	rev/min	Vapour pressure of solution	11.718	kPa
Impeller arrangement	B		O_2 partial pressure	71.48	kPa(abs)
Pressure	0.00	kPa(g)	O_2 solubility	9.49	mg/kg
Temperature	50	°C	O_2 gas purity	99.5	%

$[Na_2SO_3]$ starting	1.172	mol/L	$[CoSO_4]$	0.56	mg/L
[Thiosulphate]	0.100	mol/L	Total mass in	5429	g
[Iodine]	0.100	mol/L	Starting volume	4827	ml

Time	Sample volume	Thiosulphate added	Estimated density	$[Na_2SO_3]$	O_2 reacted
min	ml	ml	kg/m^3	mol/L	mg/kg
0	4.0	9.8	1125	1.128	0
30	4.0	15.1	1125	1.061	1077
60	4.0	20.2	1125	0.998	2104

Test number: MT14					
Agitation speed	700	rev/min	Vapour pressure of solution	11.718	kPa
Impeller arrangement	B		O_2 partial pressure	71.48	kPa(abs)
Pressure	0.00	kPa(g)	O_2 solubility	9.49	mg/kg
Temperature	50	°C	O_2 gas purity	99.5	%

$[Na_2SO_3]$ starting	1.172	mol/L	$[CoSO_4]$	0.53	mg/L
[Thiosulphate]	0.100	mol/L	Total mass in	5647	g
[Iodine]	0.100	mol/L	Starting volume at temperature	5020	ml

Time	Sample volume	Thiosulphate added	Estimated density	$[Na_2SO_3]$	O_2 reacted
min	ml	ml	kg/m^3	mol/L	mg/kg
0	4.0	9.6	1125	1.131	0
30	4.0	18.3	1125	1.022	1768
60	4.0	30.0	1126	0.876	4151
120	4.0	50.3	1128	0.622	8298

Test number: MT15					
Agitation speed	700	rev/min	Vapour pressure of solution	11.718	kPa
Impeller arrangement	B		O_2 partial pressure	71.48	kPa(abs)
Pressure	0.00	kPa(g)	O_2 solubility	9.49	mg/kg
Temperature	50	°C	O_2 gas purity	99.5	%

$[Na_2SO_3]$ starting	1.172	mol/L	$[CoSO_4]$	0.54	mg/L
[Thiosulphate]	0.100	mol/L	Total mass in	5646	g
[Iodine]	0.100	mol/L	Starting volume	5020	ml

Time	Sample volume	Thiosulphate added	Estimated density	$[Na_2SO_3]$	O_2 reacted
min	ml	ml	kg/m^3	mol/L	mg/kg
0	4.0	11.0	1125	1.113	0
30	4.0	18.7	1125	1.017	1522
60	4.0	28.8	1126	0.890	3550
120	4.0	50.2	1128	0.623	7947

Test number: MT29					
Agitation speed	600	rev/min	Vapour pressure of solution	11.718	kPa
Impeller arrangement	C		O_2 partial pressure	71.48	kPa(abs)
Pressure	0.00	kPa(g)	O_2 solubility	9.49	mg/kg
Temperature	50	°C	O_2 gas purity	99.5	%

$[Na_2SO_3]$ starting	1.172	mol/L	$[CoSO_4]$	0.54	mg/L
[Thiosulphate]	0.100	mol/L	Total mass in	5571	g
[Iodine]	0.100	mol/L	Starting volume at temperature	4953	ml

Time	Sample volume	Thiosulphate added	Estimated density	$[Na_2SO3]$	O_2 reacted
min	ml	ml	kg/m^3	mol/L	mg/kg
0	4.0	11.7	1125	1.104	0
29	4.0	22.1	1126	0.974	2115
59	4.0	35.7	1127	0.804	4887
98	4.0	51.6	1128	0.605	8138

Direct method: Oxygen partial pressure change

MT	**32**		Oxygen solubility (measured)	0.0274	mol/kg
Volume of liquid	4900	ml	Oxygen solubility (theoretical)	0.0258	mol/kg
Volume of gas phase	2671	ml	k_La	3.35	min^{-1}
Temperature	20	°C	t’	3	s

Time	**Pressure**	**$-P_f/P_i\ln((P-P_f)/(P'-P_f))$**	**Time**	**Pressure**	**$-P_f/P_i\ln((P-P_f)/(P'-P_f))$**	**Time**	**Pressure**	**$-P_f/P_i\ln((P-P_f)/(P'-P_f))$**
s	psig	(-)						
1	315.6	0.000	72	290.2	2.837	143	290.0	3.004
2	316	-0.014	73	290.2	2.837	144	290.1	2.917
3	316.2	-0.020	74	290.4	2.696	145	289.9	3.101
4	314.9	0.024	75	290.3	2.764	146	289.8	3.209
5	314.9	0.024	76	290.4	2.696	147	289.7	3.331
6	313.3	0.083	77	290.3	2.764	148	290.0	3.004
7	311.8	0.141	78	290.1	2.917	149	290.0	3.004
8	310.3	0.203	79	290.0	3.004	150	290.0	3.004
9	308.5	0.284	80	290.1	2.917	151	290.0	3.004
10	307.1	0.353	81	290.1	2.917	152	290.1	2.917
11	305.8	0.421	82	290.2	2.837	153	290.0	3.004
12	304.6	0.489	83	290.4	2.696	154	290.0	3.004
13	303.4	0.562	84	290.3	2.764	155	289.9	3.101
14	302.8	0.601	85	290.2	2.837	156	290.0	3.004
15	301.8	0.670	86	290.0	3.004	157	290.0	3.004
16	300.9	0.737	87	290.1	2.917	158	289.7	3.331
17	300.2	0.792	88	290.0	3.004	159	290.0	3.004
18	299.2	0.878	89	290.1	2.917	160	290.2	2.837
19	298.5	0.943	90	290.1	2.917	161	289.9	3.101

20	297.7	1.023	91	290.3	2.764	162	289.7	3.331
21	297.2	1.078	92	290.2	2.837	163	289.7	3.331
22	296.8	1.123	93	290.2	2.837	164	290.0	3.004
23	296.8	1.123	94	290.0	3.004	165	289.8	3.209
24	295.9	1.236	95	290.1	2.917	166	289.9	3.101
25	295.7	1.263	96	290.0	3.004	167	289.7	3.331
26	295.1	1.349	97	290.0	3.004	168	290.0	3.004
27	294.5	1.443	98	290.1	2.917	169	290.0	3.004
28	294.2	1.495	99	290.1	2.917	170	289.7	3.331
29	294	1.531	100	290.2	2.837	171	290.0	3.004
30	293.4	1.648	101	290.3	2.764	172	289.8	3.209
31	293.3	1.669	102	290.2	2.837	173	289.8	3.209
32	293.3	1.669	103	290.0	3.004	174	289.8	3.209
33	292.9	1.758	104	290.0	3.004	175	289.8	3.209
34	292.7	1.806	105	290.0	3.004	176	289.8	3.209
35	292.4	1.884	106	290.1	2.917	177	290.0	3.004
36	292.1	1.968	107	290.1	2.917	178	290.0	3.004
37	292.1	1.968	108	290.2	2.837	179	289.6	3.472
38	291.9	2.029	109	290.1	2.917	180	289.8	3.209
39	291.7	2.095	110	290.3	2.764	181	289.8	3.209
40	291.8	2.062	111	290.0	3.004	182	289.8	3.209
41	291.6	2.129	112	290.0	3.004	183	289.9	3.101
42	291.5	2.165	113	289.9	3.101	184	289.8	3.209
43	291.2	2.282	114	290.1	2.917	185	289.9	3.101
44	291.2	2.282	115	290.0	3.004	186	289.9	3.101
45	290.9	2.417	116	289.9	3.101	187	290.0	3.004
46	290.9	2.417	117	290.2	2.837	188	289.8	3.209
47	290.9	2.417	118	290.2	2.837	189	289.8	3.209

48	291.0	2.370	119	289.9	3.101	190	289.7	3.331
49	290.9	2.417	120	289.9	3.101	191	289.7	3.331
50	291.0	2.370	121	289.8	3.209	192	289.6	3.472
51	290.8	2.466	122	290.1	2.917	193	289.7	3.331
52	290.8	2.466	123	289.9	3.101	194	290.0	3.004
53	290.8	2.466	124	290.1	2.917	195	289.9	3.101
54	290.5	2.633	125	290.2	2.837	196	289.8	3.209
55	290.4	2.696	126	290.1	2.917	197	289.7	3.331
56	290.7	2.518	127	290.1	2.917	198	289.8	3.209
57	290.8	2.466	128	289.8	3.209	199	289.8	3.209
58	290.5	2.633	129	289.8	3.209	200	289.6	3.472
59	290.5	2.633	130	289.9	3.101	201	289.8	3.209
60	290.3	2.764	131	289.9	3.101	202	290.0	3.004
61	290.4	2.696	132	290.0	3.004	203	290.0	3.004
62	290.4	2.696	133	290.0	3.004	204	290.0	3.004
63	290.2	2.837	134	290.2	2.837	205	289.8	3.209
64	290.3	2.764	135	290.0	3.004	206	289.8	3.209
65	290.6	2.574	136	289.8	3.209	207	289.9	3.101
66	290.4	2.696	137	290.0	3.004	208	289.7	3.331
67	290.5	2.633	138	290.0	3.004			
68	290.2	2.837	139	289.9	3.101			
69	290.2	2.837	140	289.8	3.209			
70	290.1	2.917	141	289.8	3.209			
71	290.1	2.917	142	290.1	2.917			

MT	33		Oxygen solubility (measured)	0.0274	mol/kg
Volume of liquid	4900	ml	Oxygen solubility (theoretical)	0.0267	mol/kg
Volume of gas phase	2671	ml	k_La	3.69	min^{-1}
Temperature	20	°C	t'	3	s

Time	Pressure	$-P_f/P_i\ln((P-P_f)/(P'-P_f))$	Time	Pressure	$-P_f/P_i\ln((P-P_f)/(P'-P_f))$	Time	Pressure	$-P_f/P_i\ln((P-P_f)/(P'-P_f))$
s	psig	(-)						
1	304.1	0.000	72	282.4	3.210	143	282.3	3.353
2	303.8	0.012	73	282.5	3.210	144	282.1	3.729
3	303.2	0.038	74	282.5	3.087	145	282.3	3.353
4	302.8	0.055	75	282.5	3.087	146	282.3	3.353
5	301.9	0.096	76	282.2	3.087	147	282.2	3.522
6	301.2	0.128	77	282.3	3.522	148	282.2	3.522
7	299.9	0.192	78	282.1	3.353	149	282.4	3.210
8	298.9	0.245	79	282.5	3.729	150	282.2	3.522
9	297.5	0.323	80	282.4	3.087	151	282.2	3.522
10	296.3	0.397	81	282.3	3.210	152	282.3	3.353
11	295.6	0.442	82	282.4	3.353	153	282.1	3.729
12	294.5	0.518	83	282.4	3.210	154	282.2	3.522
13	293.7	0.578	84	282.3	3.210	155	282.4	3.210
14	292.8	0.650	85	282.3	3.353	156	282.2	3.522
15	291.7	0.747	86	282.4	3.353	157	282.4	3.210
16	291	0.814	87	282.5	3.210	158	282.2	3.522
17	290.3	0.887	88	282.4	3.087	159	282.1	3.729
18	289.6	0.965	89	282.5	3.210	160	282.2	3.522
19	288.8	1.064	90	282.5	3.087	161	282.1	3.729
20	288.5	1.104	91	282.4	3.087	162	282.3	3.353

21	288.1	1.160	92	282.4	3.210	163	282.1	3.729
22	287.6	1.236	93	282.2	3.210	164	282.1	3.729
23	287	1.335	94	282.4	3.522	165	282.2	3.522
24	286.5	1.427	95	282	3.210	166	282.4	3.210
25	286.1	1.508	96	282.2	3.995	167	282.4	3.210
26	285.7	1.596	97	282.3	3.522	168	282.2	3.522
27	285.5	1.643	98	282.5	3.353	169	282.2	3.522
28	285.1	1.746	99	282.6	3.087	170	282.1	3.729
29	284.9	1.803	100	282.3	2.978	171	282	3.995
30	285	1.774	101	282.3	3.353	172	282.2	3.522
31	284.6	1.894	102	282.4	3.353	173	282.2	3.522
32	284.3	1.995	103	282.4	3.210	174	282.3	3.353
33	284	2.108	104	282.3	3.210	175	282.2	3.522
34	283.7	2.238	105	282.7	3.353	176	282.3	3.353
35	283.7	2.238	106	282.4	2.880	177	282.2	3.522
36	283.5	2.336	107	282.5	3.210	178	282.1	3.729
37	283.5	2.336	108	282.2	3.087	179	282.2	3.522
38	283.6	2.285	109	282.2	3.522	180	282.2	3.522
39	283.4	2.389	110	282.3	3.522	181	282.2	3.522
40	283.5	2.336	111	282.2	3.353	182	282.3	3.353
41	283	2.637	112	282.4	3.522	183	282.3	3.353
42	283	2.637	113	282.2	3.210	184	282.2	3.522
43	283	2.637	114	282.4	3.522	185	282.3	3.353
44	282.9	2.711	115	282.4	3.210	186	282.2	3.522
45	282.8	2.792	116	282.4	3.210	187	282.1	3.729
46	282.8	2.792	117	282.1	3.210	188	282.2	3.522
47	283	2.637	118	282.2	3.729	189	282	3.995
48	282.9	2.711	119	282.4	3.522	190	282.1	3.729

49	282.7	2.880	120	282.3	3.210	191	282	3.995
50	282.7	2.880	121	282.3	3.353	192	282.2	3.522
51	282.6	2.978	122	282.5	3.353	193	282.3	3.353
52	282.7	2.880	123	282.5	3.087	194	282.1	3.729
53	282.7	2.880	124	282.4	3.087	195	282.2	3.522
54	282.4	3.210	125	282.3	3.210	196	282	3.995
55	282.7	2.880	126	282.1	3.353	197	282	3.995
56	282.6	2.978	127	282.3	3.729	198	282.2	3.522
57	282.6	2.978	128	282.3	3.353	199	282.4	3.210
58	282.6	2.978	129	282.2	3.353	200	282.2	3.522
59	282.5	3.087	130	282.2	3.522	201	282.3	3.353
60	282.5	3.087	131	282.5	3.522	202	282.2	3.522
61	282.5	3.087	132	282.4	3.087	203	282	3.995
62	282.4	3.210	133	282.2	3.210	204	281.9	4.371
63	282.6	2.978	134	282.3	3.522	205	282	3.995
64	282.7	2.880	135	282.2	3.353	206	282	3.995
65	282.5	3.087	136	282.2	3.522	207	281.8	5.013
66	282.3	3.353	137	282.1	3.522	208	282.2	3.522
67	282.4	3.210	138	282	3.729			
68	282.3	3.353	139	282.3	3.995			
69	282.3	3.353	140	282.4	3.353			
70	282.2	3.522	141	282.3	3.210			
71	282.2	3.522	142	282.4	3.353			

MT	**30**		Oxygen solubility (measured)	0.0274	mol/kg
Volume of liquid	4800	ml	Oxygen solubility (theoretical)	0.0256	mol/kg
Volume of gas phase	2771	ml	k_La	4.75	min^{-1}
Temperature	20	°C	t_s'	3	s

Time	**Pressure**	**$-P_f/P_i\ln((P-P_f)/(P'-P_f))$**	**Time**	**Pressure**	**$-P_f/P_i\ln((P-P_f)/(P'-P_f))$**	**Time**	**Pressure**	**$-P_f/P_i\ln((P-P_f)/(P'-P_f))$**
s	psig	(-)						
1	288.4	0.000	72	270.7	3.060	143	270.4	3.584
2	287.9	0.026	73	270.6	3.205	144	270.3	3.854
3	287.8	0.031	74	270.5	3.375	145	270.2	4.233
4	287.2	0.063	75	270.4	3.584	146	270.2	4.233
5	286.8	0.085	76	270.5	3.375	147	270.2	4.233
6	285.7	0.149	77	270.5	3.375	148	270.3	3.854
7	284.6	0.217	78	270.6	3.205	149	270.5	3.375
8	283.5	0.290	79	270.4	3.584	150	270.4	3.584
9	282.4	0.369	80	270.4	3.584	151	270.4	3.584
10	281.6	0.432	81	270.5	3.375	152	270.1	4.882
11	280.3	0.543	82	270.6	3.205	153	270.3	3.854
12	279.3	0.639	83	270.7	3.060	154	270.4	3.584
13	278.7	0.701	84	270.4	3.584	155	270.2	4.233
14	278.4	0.734	85	270.3	3.854	156	270.3	3.854
15	277.6	0.828	86	270.5	3.375	157	270.1	4.882
16	276.9	0.918	87	270.5	3.375	158	270.4	3.584
17	276	1.049	88	270.3	3.854	159	270.4	3.584
18	275.4	1.148	89	270.3	3.854	160	270.2	4.233
19	274.9	1.239	90	270.6	3.205	161	270.3	3.854
20	274.6	1.298	91	270.6	3.205	162	270.3	3.854

21	274.1	1.406	92	270.5	3.375	163	270.2	4.233
22	273.6	1.527	93	270.4	3.584	164	270.3	3.854
23	273.5	1.554	94	270.3	3.854	165	270.2	4.233
24	273.1	1.667	95	270.4	3.584	166	270.3	3.854
25	272.8	1.763	96	270.1	4.882	167	270.4	3.584
26	272.6	1.832	97	270.3	3.854	168	270.5	3.375
27	272.4	1.907	98	270.5	3.375	169	270.3	3.854
28	271.9	2.126	99	270.4	3.584	170	270.1	4.882
29	271.8	2.176	100	270.4	3.584	171	270.4	3.584
30	271.9	2.126	101	270.3	3.854	172	270.2	4.233
31	271.7	2.230	102	270.2	4.233	173	270.3	3.854
32	271.7	2.230	103	270.3	3.854	174	270.2	4.233
33	271.4	2.412	104	270.4	3.584	175	270.4	3.584
34	271.1	2.637	105	270.3	3.854	176	270.2	4.233
35	271.1	2.637	106	270.4	3.584	177	270.6	3.205
36	271	2.727	107	270.4	3.584	178	270.3	3.854
37	270.9	2.825	108	270.6	3.205	179	270.2	4.233
38	271	2.727	109	270.3	3.854	180	270.2	4.233
39	270.9	2.825	110	270.5	3.375	181	270.3	3.854
40	271	2.727	111	270.4	3.584	182	270.1	4.882
41	270.8	2.935	112	270.3	3.854	183	270.2	4.233
42	270.9	2.825	113	270.5	3.375	184	270.5	3.375
43	270.9	2.825	114	270.3	3.854	185	270.5	3.375
44	270.7	3.060	115	270.5	3.375	186	270.3	3.854
45	270.6	3.205	116	270.5	3.375	187	270.1	4.882
46	270.6	3.205	117	270.4	3.584	188	270.3	3.854
47	270.9	2.825	118	270.4	3.584	189	270.3	3.854
48	270.7	3.060	119	270.4	3.584	190	270.2	4.233

49	270.8	2.935	120	270.5	3.375	191	270.3	3.854
50	270.5	3.375	121	270.3	3.854	192	270.4	3.584
51	270.6	3.205	122	270.3	3.854	193	270.3	3.854
52	270.6	3.205	123	270.3	3.854	194	270.4	3.584
53	270.4	3.584	124	270.5	3.375	195	270.3	3.854
54	270.6	3.205	125	270.6	3.205	196	270.1	4.882
55	270.6	3.205	126	270.4	3.584	197	270.1	4.882
56	270.6	3.205	127	270.2	4.233	198	270.2	4.233
57	270.7	3.060	128	270.4	3.584	199	270.1	4.233
58	270.4	3.584	129	270.2	4.233	200	270.3	3.854
59	270.3	3.854	130	270.3	3.854	201	270.4	3.584
60	270.5	3.375	131	270.4	3.584	202	270.4	3.584
61	270.5	3.375	132	270.4	3.584	203	270.2	4.233
62	270.3	3.854	133	270.6	3.205	204	270.1	4.882
63	270.4	3.584	134	270.5	3.375	205	270.1	4.882
64	270.7	3.060	135	270.3	3.854	206	270.2	4.233
65	270.8	2.935	136	270.3	3.854	207	270.1	4.882
66	270.6	3.205	137	270.1	4.882	208	270.1	4.882
67	270.4	3.584	138	270.3	3.854			
68	270.4	3.584	139	270.3	3.854			
69	270.4	3.584	140	270.2	4.233			
70	270.4	3.584	141	270.6	3.205			
71	270.3	3.854	142	270.7	3.060			

MT	31		Oxygen solubility (measured)	0.0274	mol/kg
Volume of liquid	4800	ml	Oxygen solubility (theoretical)	0.0256	mol/kg
Volume of gas phase	2771	ml	k_La	4.02	min^{-1}
Temperature	20	°C	t_s'	3	s

Time	Pressure	$-P_f/P_i\ln((P-P_f)/(P'-P_f))$	Time	Pressure	$-P_f/P_i\ln((P-P_f)/(P'-P_f))$	Time	Pressure	$-P_f/P_i\ln((P-P_f)/(P'-P_f))$
s	psig	(-)						
1	290.8	0.000	72	270	2.851	143	269.6	3.323
2	290.5	0.013	73	269.9	2.948	144	269.6	3.323
3	290	0.035	74	269.8	3.057	145	269.8	3.057
4	288.9	0.084	75	269.8	3.057	146	269.9	2.948
5	287.5	0.152	76	269.8	3.057	147	269.7	3.181
6	286.1	0.225	77	269.8	3.057	148	269.7	3.181
7	284.9	0.292	78	269.9	2.948	149	269.6	3.323
8	283.8	0.358	79	269.9	2.948	150	269.7	3.181
9	283.1	0.403	80	269.9	2.948	151	269.5	3.492
10	282	0.478	81	269.8	3.057	152	269.7	3.181
11	281.1	0.545	82	269.8	3.057	153	269.5	3.492
12	280.2	0.616	83	269.9	2.948	154	269.7	3.181
13	279.2	0.703	84	269.8	3.057	155	269.8	3.057
14	278.1	0.808	85	269.7	3.181	156	269.8	3.057
15	277.4	0.882	86	269.9	2.948	157	269.8	3.057
16	276.6	0.975	87	269.8	3.057	158	269.5	3.492
17	275.7	1.091	88	269.8	3.057	159	269.7	3.181
18	275.7	1.091	89	269.9	2.948	160	269.5	3.492
19	275.3	1.148	90	269.8	3.057	161	269.5	3.492
20	274.8	1.225	91	269.8	3.057	162	269.4	3.698
21	274.4	1.291	92	269.9	2.948	163	269.5	3.492

22	273.6	1.439	93	269.8	3.057	164	269.8	3.057
23	273.3	1.502	94	269.7	3.181	165	269.9	2.948
24	272.9	1.592	95	269.9	2.948	166	269.8	3.057
25	272.5	1.692	96	269.8	3.057	167	269.7	3.181
26	272.3	1.746	97	269.9	2.948	168	269.6	3.323
27	272.2	1.775	98	269.8	3.057	169	269.6	3.323
28	271.8	1.898	99	269.5	3.492	170	269.5	3.492
29	271.7	1.932	100	269.7	3.181	171	269.5	3.492
30	271.7	1.932	101	269.8	3.057	172	269.7	3.181
31	271.2	2.122	102	269.6	3.323	173	269.7	3.181
32	271	2.210	103	269.6	3.323	174	269.6	3.323
33	270.9	2.257	104	270.1	2.763	175	269.6	3.323
34	270.9	2.257	105	269.9	2.948	176	269.6	3.323
35	270.8	2.307	106	270	2.851	177	269.6	3.323
36	270.7	2.360	107	269.8	3.057	178	269.6	3.323
37	270.9	2.257	108	269.7	3.181	179	269.5	3.492
38	270.6	2.416	109	269.7	3.181	180	269.5	3.492
39	270.5	2.476	110	269.8	3.057	181	269.7	3.181
40	270.3	2.608	111	269.9	2.948	182	269.6	3.323
41	270.3	2.608	112	269.9	2.948	183	269.7	3.181
42	270.1	2.763	113	270	2.851	184	269.6	3.323
43	270.1	2.763	114	269.9	2.948	185	269.7	3.181
44	270.3	2.608	115	269.8	3.057	186	269.6	3.323
45	270.3	2.608	116	269.7	3.181	187	269.7	3.181
46	270.3	2.608	117	269.7	3.181	188	269.5	3.492
47	270.1	2.763	118	269.8	3.057	189	269.8	3.057
48	270.2	2.682	119	269.5	3.492	190	269.6	3.323
49	270.1	2.763	120	269.6	3.323	191	269.8	3.057

50	270	2.851	121	269.9	2.948	192	269.5	3.492
51	270.1	2.763	122	269.7	3.181	193	269.6	3.323
52	269.9	2.948	123	269.9	2.948	194	269.6	3.323
53	270.4	2.540	124	269.8	3.057	195	269.4	3.698
54	270	2.851	125	269.8	3.057	196	269.5	3.492
55	270	2.851	126	269.8	3.057	197	269.5	3.492
56	269.8	3.057	127	269.6	3.323	198	269.8	3.057
57	269.9	2.948	128	269.6	3.323	199	269.8	3.057
58	269.9	2.948	129	269.9	2.948	200	269.5	3.492
59	269.7	3.181	130	269.9	2.948	201	269.5	3.492
60	269.9	2.948	131	269.9	2.948	202	269.5	3.492
61	270.1	2.763	132	269.5	3.492	203	269.6	3.323
62	269.9	2.948	133	269.6	3.323	204	269.6	3.323
63	270	2.851	134	269.8	3.057	205	269.6	3.323
64	269.9	2.948	135	269.6	3.323	206	269.8	3.057
65	269.7	3.181	136	269.7	3.181	207	269.7	3.181
66	269.7	3.181	137	269.6	3.323	208	269.8	3.057
67	270	2.851	138	269.8	3.057			
68	269.8	3.057	139	269.8	3.057			
69	269.9	2.948	140	270	2.851			
70	270.1	2.763	141	269.7	3.181			
71	269.9	2.948	142	269.6	3.323			

MT	**34**		Oxygen solubility (measured)	0.0252	mol/kg
Volume of liquid	5004	ml	Oxygen solubility (theoretical)	0.0264	mol/kg
Volume of gas phase	2571	ml	k_La	2.82	min^{-1}
Temperature	20	°C	t_s'	3	s

Time	**Pressure**	**$-P_f/P_i\ln((P-P_f)/(P'-P_f))$**	**Time**	**Pressure**	**$-P_f/P_i\ln((P-P_f)/(P'-P_f))$**	**Time**	**Pressure**	**$-P_f/P_i\ln((P-P_f)/(P'-P_f))$**
s	psig	(-)						
1	292.4	0.0000	72	267	2.9778	143	266.3	4.0731
2	292.8	-0.0137	73	266.9	3.0737	144	266.4	3.8114
3	292	0.0139	74	266.9	3.0737	145	266.4	3.8114
4	291	0.0496	75	267	2.9778	146	266.5	3.6084
5	290.5	0.0679	76	266.9	3.0737	147	266.3	4.0731
6	289.3	0.1136	77	266.9	3.0737	148	266.2	4.4419
7	288.9	0.1294	78	267	2.9778	149	266.2	4.4419
8	288.3	0.1535	79	266.7	3.3023	150	266.4	3.8114
9	287.3	0.1953	80	266.6	3.4425	151	266.3	4.0731
10	286.9	0.2125	81	266.8	3.1808	152	266.4	3.8114
11	285.1	0.2945	82	266.8	3.1808	153	266.5	3.6084
12	284.2	0.3384	83	266.7	3.3023	154	266.3	4.0731
13	283.4	0.3793	84	266.5	3.6084	155	266.3	4.0731
14	282.4	0.4331	85	266.8	3.1808	156	266.3	4.0731
15	282.4	0.4331	86	266.6	3.4425	157	266.3	4.0731
16	281.3	0.4963	87	266.6	3.4425	158	266.3	4.0731
17	280.5	0.5451	88	266.5	3.6084	159	266.2	4.4419
18	279.5	0.6101	89	266.5	3.6084	160	266.3	4.0731
19	278.9	0.6515	90	266.5	3.6084	161	266.5	3.6084
20	278.3	0.6948	91	266.4	3.8114	162	266.3	4.0731

21	277.4	0.7639	92	266.6	3.4425	163	266.4	3.8114
22	276.6	0.8301	93	266.7	3.3023	164	266.4	3.8114
23	275.9	0.8923	94	266.7	3.3023	165	266.2	4.4419
24	275.7	0.9108	95	266.6	3.4425	166	266.3	4.0731
25	275.6	0.9203	96	266.5	3.6084	167	266.2	4.4419
26	274.9	0.9891	97	266.6	3.4425	168	266.3	4.0731
27	274.6	1.0203	98	266.4	3.8114	169	266.2	4.4419
28	274	1.0861	99	266.6	3.4425	170	266.4	3.8114
29	273.3	1.1694	100	266.3	4.0731	171	266.3	4.0731
30	273	1.2076	101	266.3	4.0731	172	266.4	3.8114
31	272.7	1.2474	102	266.6	3.4425	173	266.3	4.0731
32	272.3	1.3034	103	266.5	3.6084	174	266.2	4.4419
33	271.9	1.3631	104	266.5	3.6084	175	266.1	5.0725
34	271.9	1.3631	105	266.6	3.4425			
35	271.4	1.4437	106	266.4	3.8114			
36	271.1	1.4957	107	266.4	3.8114			
37	270.6	1.5895	108	266.3	4.0731			
38	270.5	1.6095	109	266.5	3.6084			
39	270.1	1.6942	110	266.6	3.4425			
40	269.9	1.7397	111	266.5	3.6084			
41	269.7	1.7876	112	266.7	3.3023			
42	269.8	1.7634	113	266.5	3.6084			
43	269.7	1.7876	114	266.3	4.0731			
44	269.4	1.8645	115	266.3	4.0731			
45	269	1.9784	116	266.3	4.0731			
46	268.8	2.0412	117	266.4	3.8114			
47	268.9	2.0092	118	266.4	3.8114			
48	268.7	2.0742	119	266.6	3.4425			

49	268.7	2.0742	120	266.5	3.6084
50	268.5	2.1443	121	266.5	3.6084
51	268.4	2.1814	122	266.3	4.0731
52	268.5	2.1443	123	266.3	4.0731
53	268	2.3473	124	266.3	4.0731
54	267.9	2.3939	125	266.4	3.8114
55	268	2.3473	126	266.4	3.8114
56	267.8	2.4431	127	266.4	3.8114
57	267.4	2.6717	128	266.5	3.6084
58	267.5	2.6090	129	266.5	3.6084
59	267.7	2.4951	130	266.5	3.6084
60	267.6	2.5503	131	266.2	4.4419
61	267.7	2.4951	132	266.3	4.0731
62	267.3	2.7391	133	266.4	3.8114
63	267.3	2.7391	134	266.3	4.0731
64	267.2	2.8120	135	266.5	3.6084
65	267.1	2.8911	136	266.5	3.6084
66	267.2	2.8120	137	266.4	3.8114
67	267.3	2.7391	138	266.3	4.0731
68	267.3	2.7391	139	266.4	3.8114
69	267.2	2.8120	140	266.3	4.0731
70	267	2.9778	141	266.3	4.0731
71	266.9	3.0737	142	266.5	3.6084

MT	**35**		Oxygen solubility (measured)	0.0207	mol/kg
Volume of liquid	5004	ml	Oxygen solubility (theoretical)	0.0217	mol/kg
Volume of gas phase	2571	ml	k_La	3.6	min^{-1}
Temperature	30.5	°C	t_s'	3	s

Time	**Pressure**	**$-P_f/P_i\ln((P-P_f)/(P'-P_f))$**	**Time**	**Pressure**	**$-P_f/P_i\ln((P-P_f)/(P'-P_f))$**	**Time**	**Pressure**	**$-P_f/P_i\ln((P-P_f)/(P'-P_f))$**
s	psig	(-)						
0	283	0.000	18	270	0.714	31	263	1.640
3	280	0.122	23	267	1.005	39	262	1.903
7	279	0.167	26	265	1.269	52	260	2.909
10	277	0.263	30	264	1.436	85	259	0.000
15	273	0.493						

MT	**36**		Oxygen solubility (measured)	0.0250	mol/kg
Volume of liquid	5100	ml	Oxygen solubility (theoretical)	0.0258	mol/kg
Volume of gas phase	2471	ml	k_La	2.00	min^{-1}
Temperature	20	°C	t_s'	3	s

Time	**Pressure**	**$-P_f/P_i\ln((P-P_f)/(P'-P_f))$**	**Time**	**Pressure**	**$-P_f/P_i\ln((P-P_f)/(P'-P_f))$**	**Time**	**Pressure**	**$-P_f/P_i\ln((P-P_f)/(P'-P_f))$**
s	psig	(-)						
1	289.3	0.000	51	267.7	1.754	101	264.8	3.152
2	288.7	0.022	52	267.5	1.805	102	264.7	3.274
3	287.9	0.052	53	267.4	1.832	103	264.6	3.414
4	287.3	0.075	54	267.1	1.916	104	264.4	3.784
5	286.3	0.115	55	267.3	1.859	105	264.7	3.274
6	285.4	0.153	56	267.1	1.916	106	264.9	3.044
7	284.4	0.196	57	266.9	1.977	107	264.9	3.044
8	283.5	0.238	58	266.7	2.042	108	264.9	3.044
9	282.5	0.286	59	266.5	2.112	109	264.6	3.414
10	282.2	0.301	60	266.4	2.149	110	264.8	3.152
11	281.6	0.331	61	266.5	2.112	111	264.5	3.581
12	280.8	0.374	62	266.4	2.149	112	264.6	3.414
13	280.3	0.401	63	266.3	2.188	113	264.7	3.274
14	279.7	0.435	64	266.5	2.112	114	264.6	3.414
15	278.9	0.483	65	266.4	2.149	115	264.7	3.274
16	278.3	0.521	66	266.2	2.229	116	264.6	3.414
17	277.9	0.547	67	265.9	2.363	117	264.7	3.274
18	277.6	0.566	68	265.9	2.363	118	264.5	3.581
19	277	0.608	69	265.8	2.412	119	264.5	3.581
20	276.5	0.643	70	265.8	2.412	120	264.4	3.784

21	276.1	0.673	71	265.6	2.519	121	264.5	3.581
22	275.8	0.696	72	265.6	2.519	122	264.7	3.274
23	275.3	0.736	73	265.8	2.412	123	264.6	3.414
24	274.8	0.777	74	265.6	2.519	124	264.7	3.274
25	274.1	0.838	75	265.4	2.641	125	264.7	3.274
26	273.6	0.884	76	265.4	2.641	126	264.5	3.581
27	273.6	0.884	77	265.4	2.641	127	264.3	4.047
28	273	0.943	78	265.2	2.782	128	264.5	3.581
29	272.6	0.985	79	265.3	2.709	129	264.5	3.581
30	272.4	1.006	80	265.2	2.782	130	264.5	3.581
31	272	1.051	81	265.3	2.709	131	264.4	3.784
32	271.4	1.122	82	265.1	2.861	132	264.7	3.274
33	271.3	1.134	83	265.2	2.782	133	264.5	3.581
34	271	1.173	84	265.2	2.782	134	264.6	3.414
35	270.8	1.199	85	265.2	2.782	135	264.4	3.784
36	270.6	1.226	86	265.1	2.861	136	264.4	3.784
37	270.3	1.269	87	264.9	3.044	137	264.4	3.784
38	270.4	1.254	88	264.9	3.044	138	264.2	4.417
39	270.2	1.283	89	264.9	3.044	139	264.5	3.581
40	269.8	1.344	90	265.2	2.782	140	264.5	3.581
41	269.6	1.376	91	265	2.948	141	264.7	3.274
42	269.2	1.444	92	264.8	3.152	142	264.6	3.414
43	269	1.480	93	264.9	3.044	143	264.3	4.047
44	268.7	1.536	94	264.9	3.044	144	264.5	3.581
45	268.6	1.556	95	264.8	3.152	145	264.4	3.784
46	268.6	1.556	96	264.6	3.414	146	264.4	3.784
47	268.4	1.596	97	264.9	3.044	147	264.4	3.784
48	268.3	1.617	98	264.8	3.152	148	264.4	3.784

49	268	1.683	99	264.9	3.044	149
50	267.8	1.730	100	264.8	3.152	150

MT	**37**		Oxygen solubility (measured)	0.0248	mol/kg
Volume of liquid	5200	ml	Oxygen solubility (theoretical)	0.0258	mol/kg
Volume of gas phase	2371	ml	k_La	1.12	min^{-1}
Temperature	20	°C	t_s'	3	s

Time	**Pressure**	**$-P_f/P_i\ln((P-P_f)/(P'-P_f))$**	**Time**	**Pressure**	**$-P_f/P_i\ln((P-P_f)/(P'-P_f))$**	**Time**	**Pressure**	**$-P_f/P_i\ln((P-P_f)/(P'-P_f))$**
s	psig	(-)	s	psig	(-)	s	psig	(-)
1			86	265.5	1.39	171	262.3	3.15
2	286.8	0.01	87	265.6	1.39	172	262.3	3.15
3	286.1	0.03	88	265.4	1.45	173	262.5	2.95
4	285.4	0.06	89	265.3	1.45	174	262.5	2.95
5	284.6	0.09	90	265.2	1.43	175	262.3	3.15
6	284.2	0.11	91	265.2	1.46	176	262.5	2.95
7	283.5	0.14	92	265.2	1.46	177	262.6	2.87
8	283	0.16	93	265.1	1.54	178	262.6	2.87
9	282.1	0.20	94	265.2	1.56	179	262.5	2.95
10	281.4	0.23	95	265	1.54	180	262.4	3.05
11	280.8	0.26	96	264.9	1.60	181	262.2	3.26
12	280.3	0.28	97	264.8	1.56	182	262.4	3.05
13	279.5	0.32	98	264.7	1.60	183	262.3	3.15
14	279.1	0.34	99	264.7	1.62	184	262.3	3.15
15	279.1	0.34	100	264.7	1.62	185	262.4	3.05
16	278.6	0.37	101	264.4	1.70	186	262.5	2.95
17	278.1	0.40	102	264.6	1.68	187	262.5	2.95
18	277.4	0.44	103	264.3	1.73	188	262.3	3.15
19	277.2	0.45	104	264.3	1.75	189	262.3	3.15
20	276.9	0.46	105	264.4	1.77	190	262.3	3.15

21	276.5	0.49	106	264.1	1.77	191	262.3	3.15
22	276	0.52	107	264.2	1.77	192	262.2	3.26
23	276	0.52	108	264.2	1.80	193	262.2	3.26
24	275.7	0.54	109	264.2	1.77	194	262.6	2.87
25	275.5	0.55	110	264.3	1.82	195	262.5	2.95
26	275	0.59	111	264.1	1.85	196	262.5	2.95
27	274.8	0.60	112	263.7	1.88	197	262.4	3.05
28	274.2	0.64	113	263.9	1.91	198	262.3	3.15
29	273.9	0.66	114	263.9	1.91	199	262.3	3.15
30	273.6	0.69	115	263.7	1.91	200	262	3.55
31	273.3	0.71	116	263.6	2.00	201	262.3	3.15
32	273.4	0.70	117	263.8	1.94	202	261.9	3.74
33	273.2	0.72	118	263.6	2.03	203	262.3	3.15
34	273	0.73	119	263.6	2.03	204	262.5	2.95
35	272.7	0.76	120	263.5	2.00	205	262.3	3.15
36	272.3	0.79	121	263.4	2.10	206	262.2	3.26
37	272.4	0.78	122	263.3	2.06	207	262.2	3.26
38	272.2	0.80	123	263.3	2.06	208	262.2	3.26
39	271.9	0.83	124	263.3	2.06	209	262.2	3.26
40	271.8	0.84	125	263.4	2.03	210	262.1	3.40
41	271.8	0.84	126	263.3	2.10	211	262.3	3.15
42	271.7	0.84	127	263.4	2.25	212	262.3	3.15
43	271.7	0.84	128	263.3	2.17	213	262.5	2.95
44	271.4	0.87	129	263.1	2.17	214	262.1	3.40
45	271.1	0.90	130	263.1	2.25	215	262.1	3.40
46	271	0.91	131	263.2	2.29	216	262.1	3.40
47	270.7	0.94	132	263	2.21	217	262.3	3.15
48	270.7	0.94	133	263.1	2.29	218	262.2	3.26

49	270.6	0.95	134	263	2.29	219	262.1	3.40
50	270.5	0.96	135	263.4	2.33	220	262.4	3.05
51	270.4	0.97	136	263.2	2.38	221	262.3	3.15
52	269.9	1.02	137	263	2.43	222	262.4	3.05
53	269.7	1.04	138	262.8	2.43	223	262.1	3.40
54	269.8	1.03	139	262.9	2.43	224	262.4	3.05
55	269.5	1.07	140	262.9	2.38	225	262.2	3.26
56	269.3	1.09	141	263	2.43	226	262.3	3.15
57	269	1.13	142	262.8	2.38	227	262.2	3.26
58	269	1.13	143	262.9	2.43	228	262.2	3.26
59	269.1	1.11	144	263.1	2.53	229	262.3	3.15
60	268.8	1.15	145	263	2.53	230	262.3	3.15
61	268.6	1.18	146	262.8	2.48	231	262.1	3.40
62	268.3	1.22	147	262.6	2.59	232	262	3.55
63	268.2	1.23	148	262.9	2.53	233	262.1	3.40
64	268.2	1.23	149	262.7	2.59	234	262.2	3.26
65	267.9	1.27	150	262.7	2.38	235	262.2	3.26
66	267.9	1.27	151	262.7	2.48	236	262.2	3.26
67	267.8	1.29	152	262.9	2.59	237	262.3	3.15
68	268	1.26	153	262.9	2.72	238	262.3	3.15
69	267.6	1.32	154	262.7	2.65	239	262.3	3.15
70	267.4	1.35	155	262.7	2.65	240	262.1	3.40
71	267.1	1.39	156	262.7	2.59	241	262.2	3.26
72	267.1	1.39	157	262.6	2.72	242	262	3.55
73	266.8	1.45	158	262.5	2.65	243	262.2	3.26
74	266.8	1.45	159	262.6	2.53	244	262.1	3.40
75	266.9	1.43	160	262.6	2.59	245	262.3	3.15
76	266.7	1.46	161	262.6	2.72	246	262.4	3.05

77	266.7	1.46	162	262.6	2.87	247	262.4	3.05
78	266.3	1.54	163	262.6	2.65	248	262.1	3.40
79	266.2	1.56	164	262.6	2.79	249	262.1	3.40
80	266.3	1.54	165	262.5	2.79	250	262.2	3.26
81	266	1.60	166	262.4	2.79			
82	266.2	1.56	167	262.5	2.65			
83	266	1.60	168	262.5	2.65			
84	265.9	1.62	169	262.7	2.79			
85	265.9	1.62	170	262.7	2.79			

MT	**38**	**SOLUTION**	Oxygen solubility (measured)	0.0236	mol/kg
Volume of liquid	5000	ml	Oxygen solubility (theoretical)	Not calculated	mol/kg
Volume of gas phase	2571	ml	k_La	5.99	min^{-1}
Temperature	20	°C	t_s'	3	s

Time	**Pressure**	**$-P_f/P_i\ln((P-P_f)/(P'-P_f))$**	**Time**	**Pressure**	**$-P_f/P_i\ln((P-P_f)/(P'-P_f))$**	**Time**	**Pressure**	**$-P_f/P_i\ln((P-P_f)/(P'-P_f))$**
s	psig	(-)	s	psig	(-)	s	psig	(-)
1	280	0.05	26	263.3	2.50	51	262.7	3.04
2	279.6	0.07	27	263.2	2.57	52	262.4	3.51
3	279.2	0.09	28	263	2.73	53	262.5	3.33
4	278.5	0.13	29	263	2.73	54	262.4	3.51
5	277.6	0.19	30	262.8	2.93	55	262.4	3.51
6	276.6	0.25	31	262.7	3.04	56	262.5	3.33
7	275.4	0.33	32	262.8	2.93	57	262.5	3.33
8	274.3	0.41	33	262.8	2.93	58	262.7	3.04
9	273.6	0.47	34	262.8	2.93	59	262.7	3.04
10	272.4	0.57	35	262.5	3.33	60	262.6	3.18
11	271.1	0.69	36	262.4	3.51	61	262.6	3.18
12	270.3	0.78	37	262.6	3.18	62	262.6	3.18
13	269.2	0.91	38	262.4	3.51	63	262.5	3.33
14	268.5	1.01	39	262.5	3.33	64	262.4	3.51
15	267.8	1.12	40	262.5	3.33	65	262.5	3.33
16	267	1.26	41	262.5	3.33	66	262.7	3.04
17	266.3	1.40	42	262.5	3.33	67	262.7	3.04
18	266.1	1.44	43	262.5	3.33	68	262.5	3.33
19	265.5	1.59	44	262.4	3.51	69	262.6	3.18
20	265.1	1.70	45	262.5	3.33	70	262.4	3.51

21	264.5	1.90	46	262.3	3.74	71	262.5	3.33
22	264.3	1.98	47	262.5	3.33	72	262.4	3.51
23	264.1	2.06	48	262.5	3.33	73	262.4	3.51
24	263.8	2.20	49	262.6	3.18	74	262.5	3.33
25	263.6	2.31	50	262.6	3.18	75	262.6	3.18

MT	**39**		Oxygen solubility (measured)	0.018	mol/kg
Volume of liquid	5000	ml	Oxygen solubility (theoretical)	0.019	mol/kg
Volume of gas phase	2571	ml	k_La	4.10	min^{-1}
Temperature	45	°C	t_s'	3	s

Time	**Pressure**	**$-P_f/P_i\ln((P-P_f)/(P'-P_f))$**	**Time**	**Pressure**	**$-P_f/P_i\ln((P-P_f)/(P'-P_f))$**	**Time**	**Pressure**	**$-P_f/P_i\ln((P-P_f)/(P'-P_f))$**
s	psig	(-)	s	psig	(-)	s	psig	(-)
1	296.4	0.000	26	283	1.626	51	281.1	2.59
2	295.9	0.030	27	282.9	1.66	52	280.9	2.78
3	295.8	0.036	28	282.6	1.76	53	280.9	2.78
4	295.2	0.073	29	282.7	1.73	54	281	2.68
5	294.7	0.105	30	282.4	1.84	55	281.1	2.59
6	293.4	0.193	31	282.2	1.92	56	281	2.68
7	292.6	0.252	32	282.1	1.97	57	280.7	3.02
8	291.7	0.323	33	281.7	2.17	58	280.8	2.89
9	290.8	0.400	34	281.7	2.17	59	280.8	2.89
10	289.7	0.503	35	281.7	2.17	60	280.9	2.78
11	289.1	0.564	36	281.5	2.29	61	280.8	2.89
12	288.4	0.640	37	281.6	2.23	62	280.8	2.89
13	288.1	0.675	38	281.6	2.23	63	281.3	2.43
14	287.5	0.749	39	281.4	2.35	64	281.2	2.50
15	286.8	0.842	40	281.2	2.50	65	280.9	2.78
16	286.2	0.931	41	281.2	2.50	66	280.8	2.89
17	285.9	0.978	42	281.3	2.43	67	280.9	2.78
18	285.1	1.118	43	281.3	2.43	68	280.9	2.78
19	285	1.137	44	281.1	2.59	69	280.6	3.17
20	284.9	1.156	45	281.1	2.59	70	280.6	3.17

21	284.3	1.281	46	281.1	2.59	71	280.9	2.78
22	284.3	1.281	47	281.2	2.50	72	280.8	2.89
23	283.8	1.399	48	281	2.68	73	280.9	2.78
24	283.5	1.478	49	281	2.68	74	280.8	2.89
25	283.1	1.594	50	281.3	2.43	75	280.5	3.34

MT	**40**		Oxygen solubility (measured)	0.018	mol/kg
Volume of liquid	5000	ml	Oxygen solubility (theoretical)	0.019	mol/kg
Volume of gas phase	2571	ml	k_La	4.10	min^{-1}
Temperature	65	°C	t_s'	3	s

Time	**Pressure**	**$-P_f/P_i\ln((P-P_f)/(P'-P_f))$**	**Time**	**Pressure**	**$-P_f/P_i\ln((P-P_f)/(P'-P_f))$**	**Time**	**Pressure**	**$-P_f/P_i\ln((P-P_f)/(P'-P_f))$**
s	psig	(-)	s	psig	(-)	s	psig	(-)
1	292.6	0.00	26	277.4	2.10	51	276.2	3.05
2	291.5	0.06	27	277.1	2.26	52	276.2	3.05
3	290.8	0.11	28	276.9	2.39	53	276.3	2.92
4	290.1	0.15	29	276.9	2.39	54	276.1	3.20
5	289.7	0.18	30	276.8	2.46	55	275.9	3.58
6	288.8	0.24	31	276.5	2.71	56	275.9	3.58
7	288.6	0.25	32	276.5	2.71	57	276	3.37
8	287.9	0.31	33	276.5	2.71	58	276	3.37
9	286.7	0.40	34	276.7	2.54	59	276.1	3.20
10	285.8	0.48	35	276.6	2.62	60	276.2	3.05
11	284.7	0.59	36	276.3	2.92	61	276	3.37
12	283.9	0.68	37	276.2	3.05	62	275.8	3.86
13	283	0.79	38	276.3	2.92	63	276.1	3.20
14	282.4	0.87	39	276.1	3.20	64	276.2	3.05
15	281.9	0.94	40	276.1	3.20	65	275.8	3.86
16	281.5	1.00	41	276.2	3.05	66	275.9	3.58
17	280.7	1.14	42	276.3	2.92	67	276	3.37
18	280	1.27	43	276.4	2.81	68	275.9	3.58
19	279.7	1.34	44	276	3.37	69	276	3.37
20	279.1	1.49	45	276.1	3.20	70	275.7	4.25

21	278.6	1.63	46	275.9	3.58	71	275.7	4.25
22	278.2	1.76	47	276	3.37	72	275.9	3.58
23	277.9	1.87	48	276	3.37	73	275.7	4.25
24	277.7	1.96	49	276	3.37	74	275.8	3.86
25	277.6	2.00	50	276.1	3.20	75	275.7	4.25

APPENDIX C: Supporting information for model development

Appendix C.1: Sulphuric acid speciation

It was assumed that $H_2SO_{4(aq)}$ in the Fe(II) –Fe(III)- H_2SO -H_2O system would behave similar than the pure H_2SO_4-H_2O system. In water $H_2SO_{4(l)}$ dissociates according to the following two reactions:

$$H_2SO_{4(l)} \rightarrow H^+_{(aq)} + HSO_4^-{}_{(aq)} \quad \text{C.1}$$

$$HSO_4^-{}_{(aq)} \rightarrow H^+_{(aq)} + SO_4^{2-}{}_{(aq)} \quad \text{C.2}$$

Concerning these reactions, it is known that at high temperatures, $H_2SO_{4(aq)}$ acts as monoprotic acid, that is only one proton is liberated from the acid and very low levels of SO_4^{2-} exists. In a pure H_2SO_4-H_2O system, the species concentrations were calculated over the temperature range 125°C to 250°C by using the Pitzer activity coefficient model (Pitzer et al., 1977), as shown in Figure C.1. Equilibrium constants were obtained from Sippola (2012) based on the original data published by Knopf et al. (2003). The Debye-Huckel parameter, which was also required in the calculations, was obtained from Bradley and Pitzer (1979).

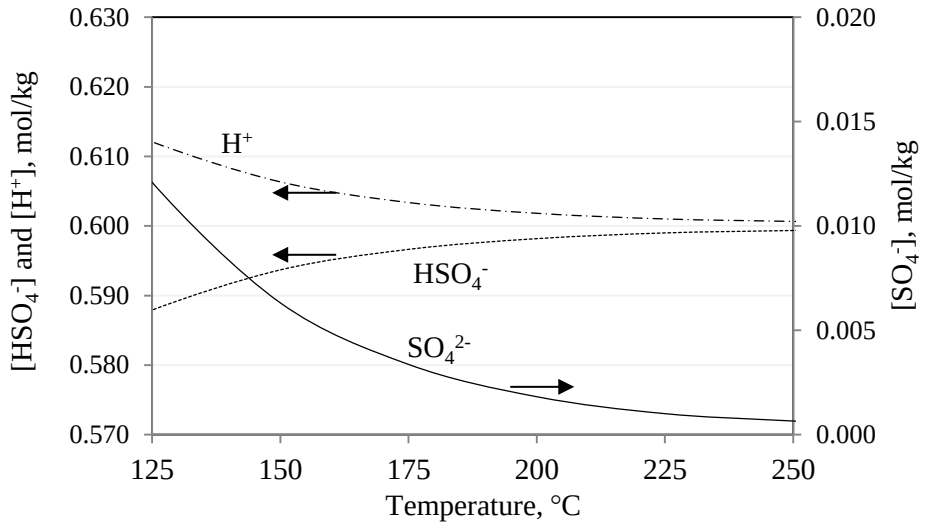

Figure C.1: Calculated species concentrations in the H_2SO_4-H_2O system from 125°C to 250°C (initial H_2SO_4 concentration 0.6 mol/kg

As seen from Figure C.1, less than 0.01 mol/kg SO_4^{2-} exists at temperatures exceeding 150°C with a solution starting with 0.6 mol/kg H_2SO_4. Above calculations thus serve as support for simulating H_2SO_4 as a monoprotic acid at the test work temperatures (180 to 220°C). In other words, Reaction C.2 was thus omitted from the reaction set. The H_2SO_4 concentrations employed during the current test work was less than 0.6 mol/kg in all cases.

Appendix C.2: Equilibrium aqueous oxygen concentration

The concentration of dissolved oxygen in the liquid phase and the gas phase is governed by Eq. C.3. Oxygen solubility ($m^*_{O_2}$ in mol/kg) may thus be related to oxygen partial pressure ($y_{O_2}P$ *or* p_{O_2} in atm) of oxygen in the gas, Henry's constant ($\mathcal{H}_{O_2}$ in atm.kg/mol) the activity of oxygen in water (γ_{O_2}) and the fugacity coefficient ($\hat{\phi}_{O_2}$) in the gas (Koretsky, 2004: 393):

$$\hat{\phi}_{O_2} y_{O_2} P = m^*_{O_2} \gamma_{O_2} \mathcal{H}_{O_2} \qquad \text{C.3}$$

Considering that oxygen is only sparingly soluble in water and the relatively low pressures involved, both the vapour phase fugacity and the activity coefficients would be close to one. Therefore Eq. C.3 may be simplified to Eq. C.4, which is well known as Henry's Law or Henry's Equation (Koretsky, 2004: 393-394):

$$p_{O_2} = m^*_{O_2} \mathcal{H}_{O_2} \qquad \text{C.4}$$

Based on standard thermodynamic relationships between heat capacity, enthalpy and entropy at constant pressure, an equation to predict the oxygen solubility in pure water has been derived by Tromans (1998a) and was validated against various sources. According to the proposed relationship, Henry's Coefficient may be expressed as a function of temperature according to Eq. C.5:

$$\frac{1}{\mathcal{H}} = exp\left(\frac{0.046T^2 + 203.35T\, ln\left(\frac{T}{298}\right) - (299.378 + 0.092T)(T - 298) - 20591}{8.3144T}\right) \qquad \text{C.5}$$

This relationship showed very good agreement with published oxygen solubility measurements up to 616 K and 60 atm. Conditions employed during this study fall within this range. The solubility of oxygen in water calculated using Henry's Law, as defined by Eq. C.5, is graphically depicted in Figure C.2 and illustrates that oxygen solubility decreases with temperature to a minimum of 95°C (i.e. 368 K) and then increases again at higher temperatures.

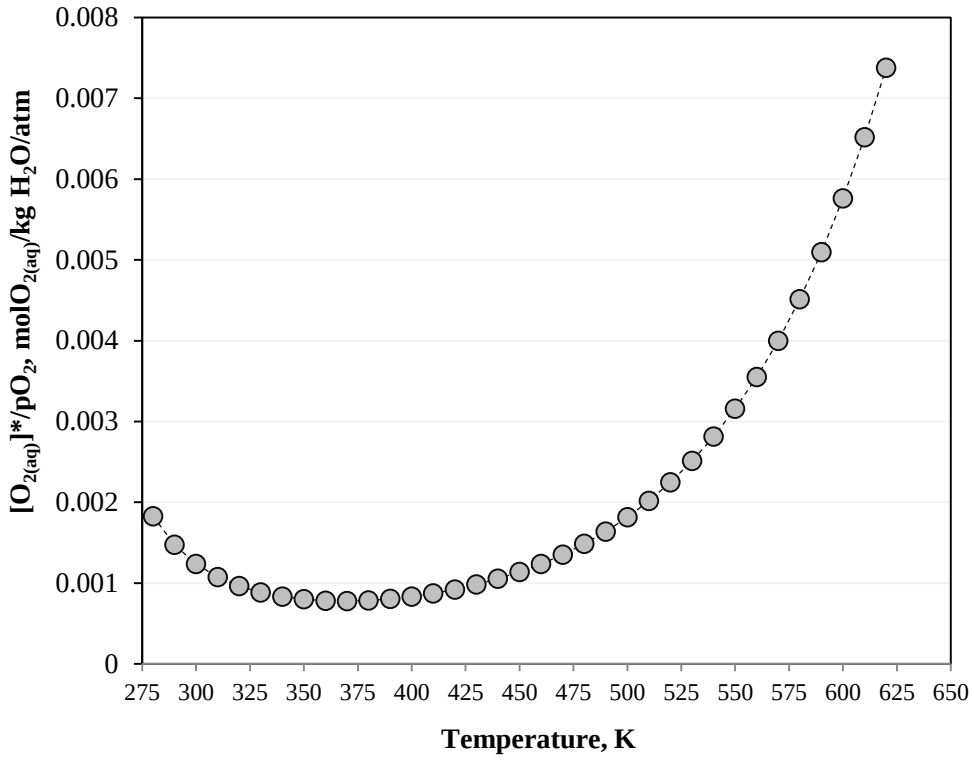

Figure C. 2: Oxygen solubility in pure water as a function of temperature (Tromans, 2000)

The aqueous solubility of oxygen is reduced in the presence of dissolved salts. Tromans (1998b) also developed a model to predict oxygen aqueous solubility as a function of the molal concentrations of 21 inorganic solutes. This model is based on the assumption that in a solution containing an inorganic solute *i*, only a fraction ψ_i of the total water content is available to interact with oxygen, the remaining fraction *(1- ψ_i)* is confined to interactions with dissolved solute ions. Therefore, the oxygen solubility in the solution is only a fraction of the solubility of oxygen in pure water as described in Eq. C.6..

$$m^*_{O_{2:i}} = \psi_i m^*_{O_{2:w}} \qquad \text{C.6}$$

The effective value for ψ may be calculated according to Eq. C.7:

$$\psi_{eff} = \psi_1 (\prod_{i=2}^{j} \psi_i)^h \qquad \text{C.7}$$

where *h* is an empirical parameter, which for the 21 electrolytes, is equal to 0.8 ±0.17. The overall effective value ψ_{eff} is dominated by the smallest factor ψ_i. The empirical function to describe ψ_i, proposed by Tromans (1998b), is presented below:

$$\varphi_i = [\frac{1}{1 + \kappa m_i{}^{Y}}]^{-\eta} \quad \text{C.8}$$

The parameters κ, Y and η are specific to each electrolyte.

A very high correlation between predicted and measured oxygen solubilities in H_2SO_4 solutions up to 1.6 mol/kg H_2SO_4 in the temperature range 300 to 475 K was observed with the use of above approach (Tromans, 1998b) and therefore the use of these empirical equations are justified for this study. Similarly, in context of the oxygen mass transfer work conducted with sodium sulphite and sulphate solutions, the relationship of Tromans (2000) showed acceptable correlation with measured oxygen solubilities in Na_2SO_3 and Na_2SO_4 systems.

The parameters used to quantify the oxygen solubility during this study are included in Table C.1.

Table C. 1: Values of coefficients and exponents for use with Equation C.8

	κ	Y	η	*Reference*
H_2SO_4	2.02	1.25	0.17	Tromans (1998b)
$MgSO_4$[a]	0.20	1.11	5.46	Tromans (1998b)
Na_2SO_4	0.63	0.91	1.44	Tromans (2000)

a – It was assumed that $FeSO_4$ and $Fe_2(SO_4)_3$ had similar parameters than $MgSO_4$

For H_2SO_4 and Fe(II), the following expressions was thus used to calculate $\psi_{H_2SO_4}$ and ψ_{FeSO_4}:

$$\psi_{H_2SO_4} = (\frac{1}{1 + 2.01628[H_2SO_4]^{1.253475}})^{0.168954} \quad \text{C.9}$$

$$\psi_{FeSO_4} = (\frac{1}{1 + 0.12[FeSO_4]^{1.108}})^{5.456} \quad \text{C.10}$$

Since it was found that $\psi_{H_2SO_4} < \psi_{FeSO_4}$ was true for all generated data points, the effective value for ψ was calculated as follows:

$$\psi_{eff} = \psi_{H_2SO_4}\psi_{FeSO_4}{}^{0.8} \quad \text{C.11}$$

Regarding $FeSO_{4(aq)}$, there are no published values for the parameters κ, Y and η. It was therefore assumed that $FeSO_{4(aq}$ has the same parameters as $MgSO_4$, since these compounds have the same Schumpe parameter in oxygen-water systems (Schumpe, 1993). This assumption was previously made by Steyl (2012: 69) and this approach was thus adopted in the current study. In addition, since there are no published values for $Fe_2(SO_4)_{3(aq)}$, it was assumed that all iron in solution is present as iron(II).

For the Na_2SO_3-Na_2SO_4 system it was assumed that the solution only consisted of Na_2SO_4 as calculated values of $\psi_{Na_2SO_4}$ and $\psi_{Na_2SO_3}$ were almost identical (corresponded within 5% at concentrations employed during this study) based on data published by Tromans (2000). Incorporation of additional complexity in the predicted oxygen solubility by taking both salts into consideration was therefore not deemed necessary.

Appendix C.3: Shrinking particle model

It was assumed that pyrite particles were spherical and that they retain their shape during shrinkage. Following the derivation provided by Levenspiel (1999: 570-579), the reaction rate (r_s) per unit surface area at the surface of a particle may be expressed as follows:

$$-\frac{1}{4\pi {R_p}^2}\frac{dN_B}{dt} = r_s MW_s \qquad \text{C.12}$$

where N_B is total amount of moles in the unreacted spherical particle, R_p is the particle radius and MW_s is the molar weight of the mineral. The change in moles of B may be related to the particle radius as follows:

$$-dN_B = -\rho_s d\left(\frac{4}{3}\pi {R_p}^3\right) = -4\pi\rho_s {R_p}^2 dR_p \qquad \text{C.13}$$

Therefore, Equation C.12 may be rewritten as shown in Equation C.14. Note that ρ_s is the molar density of the mineral.

$$-\rho_s \frac{dR_p}{dt} = r_s MW_s \qquad \text{C.14}$$

By integration between the limits $R_p = R_{po}$ at $t = 0$ and $R_p = R_p$ at $t = t$ and subsequent rearranging, the reaction time may be expressed as a function of the particle radius (R_p) according to Equation C.3.6.

$$-\rho_s \int_{R_{po}}^{R_p} dR_p = r_s MW_s \int_o^t dt \qquad \text{C.15}$$

$$\rho_s\left(R_{po} - R_p\right) = t r_s MW_s \qquad \text{C.16}$$

$$t = \frac{\rho_s}{r_s MW_s}\left(R_{po} - R_p\right) \qquad \text{C.17}$$

The observed rate constant, k_s, is subsequently defined according to Equation C.18. The inverse of the observed rate constant ($1/k_s$) represents the total time required for complete conversion, that is when the particles radius is zero ($R_p = 0$). Thus k_s is defined directly from Equation C.17.

$$k_s = \frac{r_s MW_s}{\rho_s R_{po}} \qquad \text{C.18}$$

Substitution of Equation C.18 into Equation C.17 then yields the following:

$$t = \frac{1}{k_s}\left(1 - \frac{R_p}{R_{po}}\right) \quad \text{C.19}$$

And, since that the conversion may be related to the initial radius and the radius at any point in time according to Equation C.20,

$$X = 1 - \frac{{R_p}^3}{R_{po}^3} \quad \text{C.20}$$

the conversion may be expressed as a function of time according to Equation C.22, which follows from Equation C.21.

$$tk_s = 1 - (1 - X)^{\frac{1}{3}} \quad \text{C.21}$$

$$\frac{dX}{dt} = 3k_s(1 - X)^{\frac{2}{3}} \quad \text{C.22}$$

Appendix C.4: Homogeneous iron(II) to iron(III) oxidation

The experimental data published by Ruiz, Jerez and Padilla (2016) was used to establish the rate constant of iron(II) to iron(III) oxidation in the bulk of the solution and the associated temperature dependency or activation energy. During the tests conducted by Ruiz, Jerez and Padilla (2016), a stirred batch pressure reactor was used and the reactor charged with synthetic ferrous solutions. The rate of iron(II) to iron(III) oxidation was then monitored as a function of time at temperatures ranging between 180 to 220°C.

It was assumed that the reaction rate was first order in aqueous oxygen concentration and second order in iron(II) concentration, since this rate dependency is well established (Steyl, 2012). In addition, it was assumed that the rate of reaction is negative in proton concentration to the power of 0.25. This was guided by observations in the test work conducted by Steyl (2012) (< 180°C) and (Vraĉar & Cerović, 1997)(< 200°C) and is deemed necessary if solution speciation changes are not accounted for. The assumption on the magnitude of the order had to be made due to lack of experimental data on the influence of acid concentration on the rate of iron(II) to iron(III) oxidation at temperatures employed during this study. A dynamic model was subsequently programmed in Matlab and the relevant reaction rate constants and orders regressed to the published experimental data. The set of equations to describe the oxidation process, which was solved by Matlab ODE45 solver, is presented below:

$$r_4 = k_4[Fe^{(II)}]^2[O_2][H^+]^{-0.25} \quad \text{C.23}$$

$$k_4 = k_{4R}\exp\left(-\frac{E_{A2}}{R_g}\left(\frac{1}{T}-\frac{1}{T_{4R}}\right)\right) \quad \text{C.24}$$

$$\frac{d[O_2]}{dt} = k_L a([O_2]^* - [O_2]) - 0.25r_4 \quad \text{C.25}$$

$$\frac{d[Fe(III)]}{dt} = r_4 \quad \text{C.26}$$

$$\frac{d[Fe(II)]}{dt} = -r_4 \quad \text{C.27}$$

$$\frac{d[H_2SO_4]}{dt} = -0.5r_4 \quad \text{C.28}$$

The oxygen solubility was again modelled by the relationship published by Tromans (1998b) and the initial values obtained from the experimental work conducted by Ruiz, Jerez and Padilla (2016). An arbitrary high k_La value of 5 min^{-1} was used to ensure no oxygen gas-liquid mass transfer limitations during the simulation. The rate constant (k_{4R}) and the activation energy (E_{A2}) was varied during the regression of the experimental data points. The regression was conducted by using the Matlab function '*fminsearch'* to minimise the sum of the squared errors between experimental and simulated data points until acceptable error tolerances were met. The regressed constants are indicated in Table C.2.

Table C.2: Regressed constants for iron(II) to iron(III) oxidation rate from data published by Ruiz, Jerez and Padilla (2016)

k_4	E_{A4}
kg$^{1.75}$/mol$^{1.75}$.min	kJ/mol
782.5	69

A comparison between the simulated rate and the experimental data are presented in Figure C.3. From all of the presented data it was clear that a high correlation between the simulated and experimental data was achieved. This meant that the iron(II) oxidation rate could be predicted to a reasonable accuracy with the regressed constants.

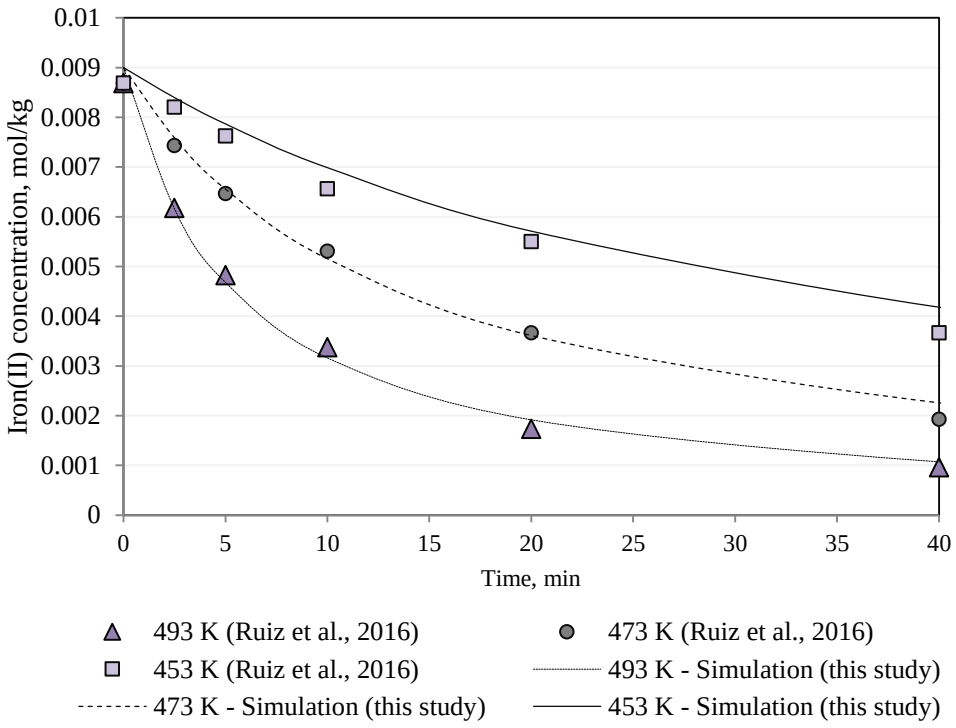

Figure C.3: (a) Rate of iron(II) conversion to iron(III) as a function of temperature: simulated rate vs. experimental data (b) Arrhenius plot based on regressed rate constants (Experimental conditions from Ruiz et al. (2016): 0.6 mol/L H_2SO_4, 690 kPa pO_2, 800 rev/min, k_La = 5 min^{-1}(assumed))

It should be noted that the authors, Ruiz, Jerez and Padilla (2016), do not explicitly state that the molar concentrations were corrected for temperature (based on the variation of solution volume with temperatures), therefore it was assumed that the solutions were prepared at 25°C and that kinetic samples were again cooled to 25°C when the molar concentrations were converted to molal concentrations during interpretation of their reported data.

Appendix C.5: Conversion between molarity and molality

The following relationship was used to convert species "j" concentration from molarity (*M*) to molality (*m*):

$$m_j = \frac{M_j(1 + \sum m_i MW_i)}{\rho_{sln} - M_j MW_j} \qquad \text{C.29}$$

where ρ_{sln} is the density of the solution and "i" denotes all other species except "j".

Appendix C.6: Solution Density of Fe(II)-Fe(III)-H_2SO_4 system

The following relationship for the density of liquid water (kg/m^3) as a function of temperature was regressed from data published in standard steam tables (Koretsky, 2004: 508-509) and is valid for the temperature range at which test work was conducted (i.e., 180-220°C):

$$\rho_w = 15.81747 + 9.87802T - 0.035239T^2 + 5.38051 \cdot 10^{-5}T - 3.2612 \cdot 10^{-8}T \quad \text{C.31}$$

Solution density data for the Fe(II)-Fe(III)-H_2SO_4-H_2O system could not be found (neither at ambient nor elevated temperatures). The solution density was thus initially estimated, for experimental planning purposes, by an empirical correlation published by Steyl (2012: 411), as shown below:

$$\frac{\rho}{\rho_w} = 1 + \frac{1}{19}[H_2SO_4] + \frac{1}{7}[Me] \quad \text{C.32}$$

This relationship provides the solution density relative to the density of water. Equation C.32 may be used to calculate the density of water at the operating temperature. In the above relationship, [Me] represents the sum of all metal species concentrations (mol/kg) in solution.

This relationship was reviewed once adequate density data as a function of metal and acid concentrations had been collected during the test work program. Microsoft Excel Solver was employed to minimise the error between the measured and predicted densities assuming that the functional form of the density empirical equation remained the same. Note that all density measurements were conducted at ambient temperature. The reviewed correlation is provided below:

$$\frac{\rho_{sln}}{\rho_w} = 1 + \frac{1}{15}[H_2SO_4] + \frac{1}{7}[Me] \quad \text{C.33}$$

The predicted densities were subsequently plotted against the measured densities as shown in Figure C.4, and as seen, a very high correlation coefficient (R-squared) value was obtained.

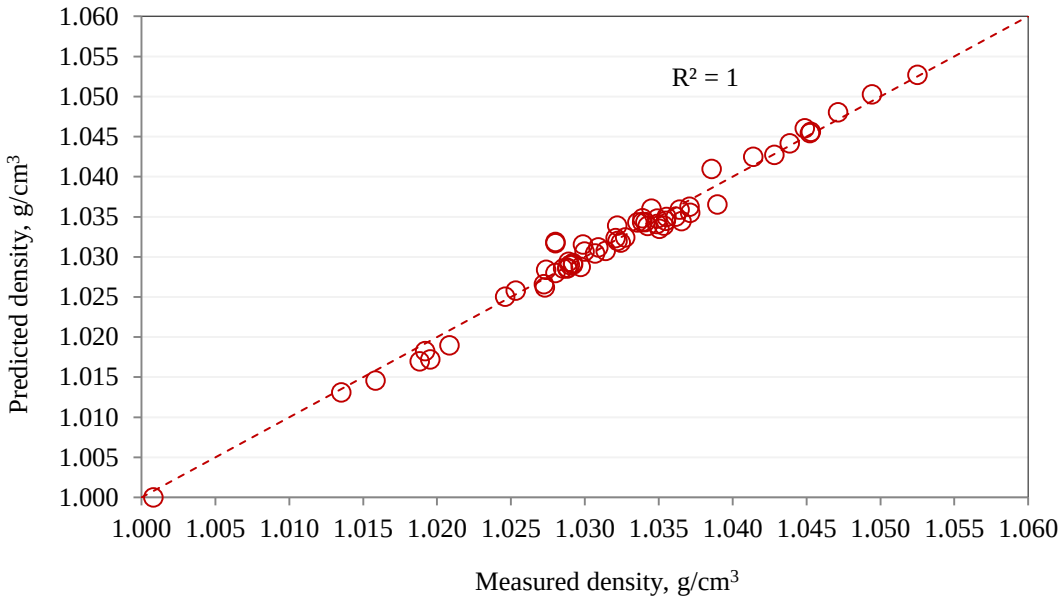

Figure C.4: Predicted densities vs measured densites (prediction based on equation C.33, measurements taken at ambient temperatures ranging between 18 to 25°C)

To evaluate the performance of both Equations C.31 and C.33 at elevated temperatures, the experimental data of a pure H_2O-H_2SO_4 system up to 100°C was obtained and compared to the model outputs.

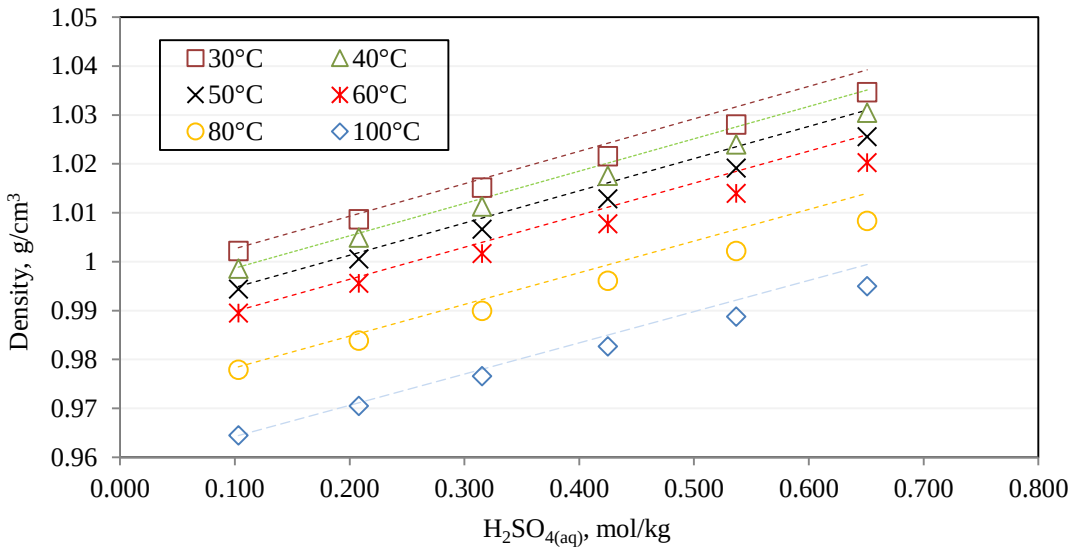

Figure C.5: Comparison of Equation A.3 modelled outputs to experimental data from 30 to 100°C (experimental data obtained from Liley et al. 1997)

As observed in Figure C.5, a relatively good correlation between the model outputs and the experimental data was obtained, which provided support for the use of Equation C.33 over the range of sulphuric acid concentrations employed (0.1-0.6 mol/kg). The slight deviation at higher sulphuric

acid concentrations were most likely attributed to nonlinear effects introduced by the presence of metal species which were accounted for in the proposed empirical relationship.

The density model of Laliberté and Cooper (2004) is commonly used by metallurgists, but is however not recommended for the current application as their empirical model was found to be inconsistent with experimental data for the Fe(II)-Fe(III)-H_2SO_4-H_2O system. The authors themselves did not recommend their empirical model for this particular system (Laliberté and Cooper, 2004).

Appendix C.7: Vapour pressure of Fe(II)-Fe(III)-H_2SO_4 system

It is known that the presence of electrolytes in water will alter the vapour pressure exerted by the solvent due to the decreased activity of water. The vapour pressure is an important parameter as it is used to calculate the partial pressure of oxygen introduced into system by subtraction from the total measured pressure. It was therefore necessary to evaluate the potential effect of solution species concentrations on water activity.

$FeSO_4$-$Fe_2(SO_4)_3$-H_2SO_4 system

The iron species concentrations were too low (< 4 g/L) to have any appreciable influence on the vapour pressure of the solution and were not considered, however due to the relatively high sulphuric acid concentrations employed, the potential influence of sulphuric acid on solution vapour pressure had to be considered.

Holmes and Mesmer (1992) published the stoichiometric osmotic coefficients of $H_2SO_{4(aq)}$ up to 200°C. The data was extrapolated to 220°C for acid concentrations ranging from 0.1 to 0.7 mol/kg to evaluate the associated water activity at these higher temperatures. The water activity was subsequently calculated according to Equation C.34. It was assumed that sulphuric acid behaved like a monoprotic acid, thus the bisulphate anion did not dissociate further (see Appendix C.1 for further discussion).

$$ln a_w = -\left(\frac{\nu m M_w}{1000}\right)\emptyset, \qquad where\ \nu = 2\ and\ \emptyset = 18\ (water) \tag{C.34}$$

The calculated results are shown in Table C.3.

Table C.3: Stoichiometric osmotic coefficients of $H_2SO_{4(aq)}$ (Holmes and Mesmer, 1992) and calculated associated water activities in the temperature region 448.15 to 493.15 K

	Φ			a_w		
H_2SO_4, m/m°	448.15 K	473.15 K	493.15 K [a]	448.15 K	473.15 K	493.15 K
0.1	0.602	0.5923	0.5813	0.998	0.998	0.998
0.2	0.5946	0.5813	0.5676	0.996	0.996	0.996
0.3	0.5932	0.5772	0.5616	0.994	0.994	0.994
0.4	0.5943	0.576	0.5813	0.991	0.992	0.992
0.5	0.5968	0.5764	0.5573	0.989	0.990	0.990
0.6	0.6001	0.5777	0.5567	0.987	0.988	0.988
0.7	0.604	0.5798	0.5574	0.985	0.985	0.986

[a] *Extrapolated*

As seen from the calculations, at H_2SO_4 molalities up to 0.7 mol/kg and temperatures ranging from 175 to 220°C, the water activity remains above 98.5%. According to Equation C.35, the solution vapour pressure will thus be 98.5-100% of the vapour pressure exerted by pure water.

$$a_w = \frac{p_s}{p_w} \qquad \text{C.35}$$

Given the above results, the pure water saturation pressure was used during the current study. The well-known Antoine Equation was used to calculate the vapour pressure of water at the operating temperature (Koretsky, 2004: 500):

$$lnp_w = 11.6834 - \frac{3816.44}{T - 46.13} \qquad \text{C.36}$$

The vapour pressure predicted by above equation was compared to the vapour pressure published in standard steam tables (see e.g., Koretsky, 2004: 507-519) and corresponded to each other within < 6 kPa for the temperature range investigated (180-210°C).

APPENDIX D: Supporting data for batch pyrite oxidation tests

Appendix D.1: Free acid and iron(II) titrations

Iron(II) titration (chromatometry)

To determine the iron(II) concentration in each of the samples removed from the reactor during the batch POX experiments, a potentiometric titration was conducted with pre-prepared solution of sodium dichromate. The redox titration is based on the reaction between iron(II) and the dichromate ion as follows (Jeffery et al; 1989: 375):

$$6Fe^{2+} + Cr_2O_7{}^{2-} + 14H^+ \leftrightarrow 2Cr^{3+} + 6Fe^{3+} + 7H_2O \qquad \text{D.1}$$

Each kinetic sample which was removed from the reactor was titrated with an automatic Metrohm Titrinoplus, per the following procedure:

Fifteen (15) ml of sample was pipetted into a 100 ml conical flask. A magnetic stirrer was added and the solution stirred. The oxidation-redox potential (ORP) was recorded with a platinum electrode as a function of the addition of 0.1 ml dichromate solution (see Table D.1 for concentrations). After each step-wise addition the solution was stirred for at least three seconds to ensure a homogeneous solution was obtained as well as to allow time for electrode response. The autotitrator generates a plot of the potential as function of reagent volume addition and stops at the end-point of the titration curve. The end-point is characterised by the steeply rising portion of the titration curve (Skoog et al., 2004: 625). Since all solutions taken from the reactor had free acid concentrations exceeding 13 g/L free H_2SO_4 at room temperature (which resulted in a solution pH ~ 1 and never above 1.5) after dichromate addition), no additional acid was added to maintain iron(III) (which start to precipitate at ~pH 2) in solution during the titration.

Experimental error: iron(II) titrations

During the initial test series which involved execution of batch POX tests on Sample C, it was realised that the titrations performed on the POX solutions were erroneous in that the iron(II) concentrations were under-analysed as a result of premature termination of the titration by the autotitrator. These titrations were repeated within 2 months after the tests were conducted. Since solutions were stored in closed containers, with almost no contact with oxygen, very little further oxidation had occurred. A comparison with more accurately conducted titrations, at a later stage, showed that the oxidation of the ferrous during storage would have at most led to a reduction in iron(II) concentration by roughly 10%, corresponding to less than 0.2 g/L difference in reported

iron(II) concentrations. As a result of the relatively low iron concentrations in solution, larger sample volumes (15 ml vs. 3 ml) were used for the titrations throughout the remainder of the study. Based on the results of 5 tests, which were conducted at different times during the experimental campaign (over 3 years), under similar experimental conditions, the iron(II) concentrations varied within 10% of one another, therefore, an experimental error of ± 10% (i.e., ~ ±0.3 g/L Fe) may be assumed for the current study.

Free acid titration

A free acid titration was also conducted on the rapidly cooled solution. Since the solutions also contained iron(III), which may interfere with the free acid titration if it starts to precipitate at ~pH 2, the iron(III) was masked by converting it to iron(II) with the addition of sodium thiosulphate ($Na_2S_2O_3.5H_2O$) and potassium iodide (KI). The two relevant reactions are shown below:

$$2Fe^{3+} + 2I^- \rightarrow 2Fe^{2+} + I_2 \qquad \text{D.2}$$

$$I_2 + 2{S_2O_3}^{2-} \rightarrow {S_4O_6}^{2-} + 2I^- \qquad \text{D.3}$$

$$2Fe^{3+} + 2{S_2O_3}^{2-} \rightarrow 2Fe^{2+} + {S_4O_6}^{2-} \textit{ (net reaction)} \qquad \text{D.2 + D.3}$$

The procedure is indirect as the reaction proceeds via the intermediate oxidation of iodide (I^-) to iodine (I_2) according to reaction D.2. The liberated iodine is then titrated with the thiosulphate ion ($S_2O_3^{2-}$) yielding the net reaction indicated by (D.2 + D.3). After the iron(III) was converted to iron(II), the solution was used for the acid titration.

The free acid titrations were conducted with the addition of a pre-prepared sodium carbonate ($NaCO_3$) solution. The free acid may then be determined by the stoichiometry of the following acid-base reaction:

$$H_2SO_4 + Na_2CO_3 \rightarrow Na_2SO_4 + H_2O + CO_2 \qquad \text{D.4}$$

The following procedure was followed for each acid titration which had been conducted:

Three (3) ml of the solution was pipetted into a 100 ml conical flask followed by 20 ml of DI water. Two heaped scoops (~ 2 g) (i.e., an unmeasured excess of potassium iodide) was added to the solution and swirled until completely dissolved. The solution yielded a dark yellow-brown colour. The thiosulfate solution was then added drop-wise until the solution became colourless indicating complete conversion of iron(III) to iron(II) (Skoog et al., 2004: 563).

A magnetic stirrer was then added and stirred until homogeneous. The sample was titrated with the addition of freshly standardised Na_2CO_3 solution using a Metrohm Titrinoplus autotitrator. The pH was measured (Ag/AgCl sat electrode) with the addition of ~ 0.5 ml solution volumes in ~ two second intervals until the pH reached 3.2.

The preparation methods for the titrants used during the iron(II) and acid titrations are included in Table D.1. In all cases analytical (AR) grade reagents were used.

Table D.1: Preparation methods of titrants for iron(II) and free acid titrations

0.0537 M sodium thiosulphate solution		
Recipe	Method	Comment
13.462 g $Na_2S_2O_3.5H_2O$	Dissolve salt with Millipore water to 1 L. Keep in glass-stoppered bottle.	Prepared such that 1 ml titrant addition will yield 1 g/L iron(III) in solution with 3 ml sample addition
0.0305 M sodium carbonate solution		
Recipe	Method	Comment
▪ 3.258 g Na_2CO_3 (0.995 wt% purity)	Dry Na_2CO_3 salt in oven at 60°C for 24 hours Dissolve salt with Millipore water to 1 L. Keep in glass-stoppered bottle.	Prepared such that 1 ml titrant addition will yield 1 g/L free H_2SO_4 in solution with 3 ml sample addition
8.953×10^{-3} M sodium dichromate solution		
Recipe	Method	Comment
▪ 2.6469 g $K_2Cr_2O_7$ (0.995 wt% purity)	Dry $K_2Cr_2O_7$ salt in oven at 60°C for 24 hours. Dissolve salt with Millipore water to 1 L. Keep in glass-stoppered bottle.	Prepared such that 1 ml titrant addition will yield 0.08 g/L iron(II) in solution with 15 ml sample addition

All stock solutions of the titrants were checked against pre-prepared solutions containing 5, 10 and 50 g/L H_2SO_4 as well as 1, 2 and 5 g/L ferrous containing solutions.

Appendix D.2: Log sheets: Sample C

Test series 3: PO4 – 650 kPa pO_2

Test	Mass of solids added	Mass of water added	Average temperature	Steam pressure (calc)	Average pressure	pO_2	Residence Time	Acid addition	Impeller Speed	Impeller Arrangement	MgO addition	$Fe_2(SO_4)_3$ addition
	g	g	°C	bar	bar	kPa	min	g	rev/min		g	g
C1	45.2	4283	201.9	15.39	21.18	595	10	149.6	700	B	0.00	0.00
C4	45.27	4285	201.9	15.37	21.90	670	5	150.1	700	C	1.02	0.00
C5	44.55	4283	202.0	15.41	21.81	656	10	150.1	700	C	1.01	0.00
C6	45.03	4285	200.9	15.06	21.50	661	15	149.7	700	C	1.01	0.00
C7	44.54	4284	201.6	15.29	21.78	666	20	150.3	700	C	1.04	0.00

Test	Residence Time	Volume of solution out (calc)	Density of solution	Mass of solution removed (calc)	Fe(II)	Fe(III) (calc)	Fe(total)	H_2SO_4	Al	Si	Fe(II)	Fe(III) (calc)	H_2SO_4
	min	ml	g/cm3	g	mg/L	mg/L	mg/L	mg/L	mg/L	mg/L	mol/kg	mol/kg	mol/kg
C1	10	3900	1.034	4031	1840	840	2680	39902	26.00	99.00	0.030	0.014	0.370
C4	5	3850	1.029	3961	1037	633	1670	35430	19.50	66.50	0.017	0.010	0.325
C5	10	3873	1.034	4005	1814	1106	2920	39780	17.00	44.00	0.029	0.018	0.367
C6	15	4051	1.034	4190	1217	2128	3345	36896	25.00	99.50	0.021	0.036	0.356
C7	20	3900	1.035	4039	538	2942	3480	37331	24.00	111.00	0.009	0.048	0.347

	Residence Time	Mass out (calc)	Residue composition, wt%				Accountability, %			
Test	min	g	Al	Si	Fe	S_2^{2-}	Al	Si	Fe	Total S
Head	-	-	4.17	12.46	29.43	32.02				
C1	10	22.51	7.33	24.75	13.55	12.35	93	106	102	98
C4	5	38.03	4.88	13.80	27.90	31.29	102	98	128	100
C5	10	20.00	7.76	24.00	12.90	17.51	87	90	106	101
C6	15	15.71	11.70	31.85	0.78	0.59	103	96	103	97
C7	20	15.37	11.80	32.20	0.32	0.17	103	97	104	96

	Residence Time	Oxidation extent (%)				
Test	min	Method 1	Method 2	Method 3	Method 4	Average
C1	10	79	80	77	81	79
C4	5	48	50	20	18	49
C5	10	86	87	80	75	87
C6	15	102	100	99	99	101
C7	20	104	104	100	100	104

Test series 1: PO1 & PO2 - 180°C

Test	Mass of solids added	Mass of water added	Average temperature	Average pressure	pO_2	Residence Time	Acid addition	Impeller Speed	Impeller Arrangement	MgO addition	$Fe_2(SO_4)_3$ addition
	g	g	°C	bar	kPa	min	g	rev/min		g	g
C8	45.22	4392	181.12	16.325	7.01	10	150.5	700	C	0.98	0.00
C9	44.78	4393	181.54	16.360	695	15	149.7	700	C	1.03	0.00
C10	46.03	4392	181.53	16.136	673	20	149.7	700	C	1.02	0.00
C11	45.6	4393	181.57	16.224	681	30	149.4	700	C	1.02	0.00
C32	44.68	4378	181.84	16.41	693	15	149.9	600	C	0.25	0.00
C20	45.59	4379	179.76	16.70	771	30	149.7	600	C	0.48	0.00
C19	45.09	4378	181.65	16.28	684	45	149.4	600	C	0.50	0.00
C18	44.23	4381	181.70	16.16	671	60	149.7	600	C	0.50	0.00

Test	Residence Time	Volume of solution out (calc)	Density of solution	Mass of solution removed (calc)	Fe(II)	Fe(III) (calc)	Fe(total)	H_2SO_4	Al	Si	Fe(II)	Fe(III) (calc)	H_2SO_4
	min	ml	g/cm3	g	mg/L	mg/L	mg/L	mg/L	mg/L	mg/L	mol/kg	mol/kg	mol/kg
C8	10	4200	1.025	4303	592	259	850.50	33251	19.50	13.00	0.010	0.004	0.324
C9	15	4200	1.025	4306	756	394	1150.00	33251	20.00	27.00	0.013	0.007	0.324
C10	20	4200	1.027	4315	965	515	1480.00	35750	19.50	36.00	0.017	0.009	0.349

C11	30	4200	1.029	4323	1316	914	2230.00	34263	23.00	55.00	0.023	0.016	0.334
C32	15	4232	1.027	4347	840	190	1030.00	34867	14.00	34.00	0.015	0.003	0.344
C20	30	4233	1.029	4357	1610	405	2015.00	34756	18.50	28.00	0.028	0.007	0.343
C19	45	4324	1.028	4445	1608	1202	2810.00	35763	18.00	38.00	0.028	0.021	0.360
C18	60	4200	1.028	4318	792	2138	2930.00	35102	19.00	37.00	0.014	0.037	0.343
	Final						3100						

	Residence Time	Mass out (calc)	Residue composition, wt%				Accountability, %			
Test	min	g	Al	Si	Fe	S_2^{2-}	Al	Si	Fe	Total S
Head	-	-	4.17	12.46	29.43	32.02	0	0	0	0
C8	10	37.00	4.51	13.65	29.75	29.80	94	92	111	97
C9	15	32.25	4.65	14.20	26.90	28.30	85	85	103	95
C10	20	32.00	5.17	15.90	27.30	24.45	93	94	114	100
C11	30	23.90	6.07	18.25	22.60	22.70	83	83	113	97
C32	15	34.55	5.02	18.25	27.10	29.20	96	101	104	98
C20	30	28.13	6.75	18.55	19.60	21.90	104	94	105	97
C19	45	17.97	10.10	30.10	7.47	8.87	101	99	102	98
C18	60	15.24	11.75	34.50	1.27	1.08	101	98	96	94

	Residence Time	Oxidation extent (%)				
Test	min	Method 1	Method 2	Method 3	Method 4	Average
C8	10	27	27		23	27
C9	15	37	37	34	36	37
C10	20	47	48		45	48
C11	30	71	72	59	62	72
C32	15	33	33	29	29	33
C20	30	64	65	59	58	64
C19	45	92	91	90	89	91
C18	60	95	95	99	99	95

Test series 1: PO3 & PO5 - 191°C and 211°C

Test	Mass of solids added	Mass of water added	Average temperature	Average pressure	pO2	Residence Time	Acid addition	Impeller Speed	Impeller Arrangement	MgO addition	$Fe_2(SO_4)_3$ addition
	g	g	°C	bar	kPa	min	g	rev/min		g	g
C46	46.45	4209.87	191.01	19.83	797	55	150.0	600	C	0.02	0.23
C47	45.46	4196.60	210.93	24.70	622	21	149.7	600	C	0.05	0.23

Test	Residence time	Volume of solution out (calc)	Density of solution	Mass of solution removed (calc)	Fe(II)	Fe(III) (calc)	Fe(total)	H_2SO_4	Al	Si	Fe(II)	Fe(III) (calc)	H_2SO_4
	Min	ml	g/cm3	g	mg/L	mg/L	mg/L	mg/L	mg/L	mg/L	mol/kg	mol/kg	mol/kg
C46	5	39	1.027	40	960	240	1200	29882	16.00	38.00	0.015	0.004	0.268
	10	28	1.029	29	1630	290	1920	29884	18.00	54.00	0.026	0.005	0.268
	17	35	1.034	36	2360	680	3040	32137	20.00	77.00	0.037	0.011	0.288
	27	27	1.036	28	1070	2610	3680	30318	21.00	93.00	0.017	0.041	0.272
	40	35	1.036	36	440	3350	3790	33814	22.00	95.00	0.007	0.053	0.303
	55	3537	1.034	3658	220	3530	3750	34971	23.00	95.00	0.003	0.056	0.313
C47	2	31	1.031	32	1570	260	1830	31453	18.00	55.00	0.024	0.004	0.269
	4	32	1.034	33	2590	260	2850	31934	20.00	75.00	0.039	0.004	0.273
	6	25	1.038	26	3140	540	3680	35447	21.50	94.00	0.047	0.008	0.303
	9	26	1.038	27	1510	2190	3700	32573	21.50	93.00	0.023	0.033	0.278

	14	28	1.039	29	720	3210	3930	34908	23.00	101.00	0.011	0.048	0.298
	21	3375	1.033	3486	320	3420	3740	36414	23.00	96.00	0.005	0.051	0.311

	Residence time		Residue composition, wt%				Accountability, %			
Test	min	Mass out (calc), g	Al	Si	Fe	S_2^{2-}	Al	Si	Fe	Total S
Head	-	-	4.17	12.46	29.43	32.02				
C46	55	14.60	11.30	33.60	0.52	0.17	91	93	101	96
C47	21	13.33	10.40	32.80	0.32	0.13	78	84	96	94

	Residence Time	Oxidation extent (%)				
Test	min	Method 1	Method 2	Method 3	Method 4	Average
C46	5		32			32
	10		51			51
	17		81			81
	27		98			98
	40		101			101
	55		100			100

	Residence Time	Oxidation extent (%)				
Test	min	Method 1	Method 2	Method 3	Method 4	Average
C47	2		49			49
	4		76			76
	6		98			98
	9		99			99
	14		105			105
	21		100			100

Test series 3: PO11 – 0.115 mol//kg H_2SO_4

Test	Mass of solids added	Mass of water added	Average temperature	Average pressure	pO2	Residence Time	Acid addition	Impeller Speed	Impeller Arrangement	MgO addition	$Fe_2(SO_4)_3$ addition
	g	g	°C	bar	kPa	min	g	rev/min		g	g
C12	44.58	4318	201.82	19.92	473	5	49.9	600	C	0.49	0.00
C13	44.71	4318	201.92	20.30	507	10	49.7	600	C	0.49	0.00
C14	45.41	4318	201.81	20.25	506	15	49.7	600	C	0.50	0.00

Test	5	Volume of solution out (calc)	Density of solution	Mass of solution removed (calc)	Fe(II)	Fe(III) (calc)	Fe(total)	H_2SO_4	Al	Si	Fe(II)	Fe(III) (calc)	H_2SO_4
	10	ml	g/cm3	g	mg/L	mg/L	mg/L	mg/L	mg/L	mg/L	mol/kg	mol/kg	mol/kg
C12	5	4004	1.014	4058	1160	405	1565	13180	5.50	27.50	0.019	0.007	0.125
C13	10	3889	1.019	3963	1880	1220	3100	14917	8.60	33.00	0.030	0.020	0.137
C14	15	4047	1.019	4123	765	1725	2490	15363	9.50	35.00	0.013	0.029	0.147

	Residence Time		Residue composition, wt%				Accountability, %			
Test	min	Mass out (calc), g	Al	Si	Fe	S_2^{2-}	Al	Si	Fe	Total S
C12	5	29.25	5.56	17.60	22.20	26.50	89	95	97	104
C13	10	18.62	9.59	29.70	5.65	6.66	98	102	100	101
C14	15	21.45	8.38	25.70	9.66	0.57	99	102	93	102

	Residence Time	Oxidation extent (%)				
Test	min	Method 1	Method 2	Method 3	Method 4	Average
C12	5	47.81	47	50.46	46	47
C13	10	91.96	92.40	91.97	91	92
C14	15				99	99

Test series 2: PO9 – 516 kPa pO_2

Test	Mass of solids added	Mass of water added	Average temperature	Average pressure	pO2	Residence Time	Acid addition	Impeller Speed	Impeller Arrangement	MgO addition	$Fe_2(SO_4)_3$ addition
	g	g	°C	bar	kPa	min	g	rev/min		g	g
C17	44.04	4271	201.31	20.25	522	5	149.6	600	C	0.50	0.00
C16	44.27	4272	201.31	20.10	507	10	149.9	600	C	0.50	0.00
C15	44.58	4273	201.50	20.12	503	15	149.9	600	C	0.50	0.00
C30	45.78	4273	201.64	20.45	532	20	149.9	600	C	0.50	0.00

Test	Residence Time	Volume of solution out (calc)	Density of solution	Mass of solution removed (calc)	Fe(II)	Fe(III) (calc)	Fe(total)	H_2SO_4	Al	Si	Fe(II)	Fe(III) (calc)	H_2SO_4
	min	ml	g/cm3	g	mg/L	mg/L	mg/L	mg/L	mg/L	mg/L	mol/kg	mol/kg	mol/kg
C17	5	4051	1.028	4164	995	245	1240	36110	16.00	41.00	0.017	0.004	0.349
C16	10	3952	1.030	4071	1508	442	1950	38550	19.00	45.00	0.025	0.007	0.364
C15	15	4095	1.032	4227	2110	770	2880	35822	19.00	44.50	0.036	0.013	0.350
C30	20	4035	1.035	4176	1067	2289	3355	38151	20.00	33.00	0.018	0.039	0.367
	Final						3350						

	Residence Time	Mass out (calc)	Residue composition, wt%				Accountability, %			
Test	min	g	Al	Si	Fe	S_2^{2-}	Al	Si	Fe	Total S
C17	5	34.34	5.09	15.20	25.00	26.40	99	98	105	98
C16	10	27.92	5.81	20.40	19.60	23.30	92	106	101	99
C15	15	19.73	9.37	25.95	10.35	13.75	104	95	105	95
C30	20	17.13	10.80	32.15	1.09	1.09	101	99	102	98

	Residence Time	Oxidation extent (%)				
Test	min	Method 1	Method 2	Method 3	Method 4	Average
C17	5	39	37	34	36	38
C16	10	59	58	58	54	59
C15	15	90	86	84	81	88
C30	20	100	98	99	99	99

Test series 3: PO12 – 0.59 mol/kg H_2SO_4

Test	Mass of solids added	Mass of water added	Average temperature	Average pressure	pO_2	Residence Time	Acid addition	Impeller Speed	Impeller Arrangement	MgO addition	$Fe_2(SO_4)_3$ addition
	g	g	°C	bar	kPa	min	g	rev/min		g	G
C23	45.73	4128	201.13	20.62	566	5	249.7	600	C	0.50	0.00
C22	45.49	4128	201.22	20.49	550	10	249.8	600	C	0.50	0.00
C21	45.7	4128	201.56	20.21	550	15	249.9	600	C	0.50	0.00
C31	44.78	4128	201.28	20.69	567	5	250.7	600	C	0.51	0.00

Test	min	Volume of solution out (calc)	Density of solution	Mass of solution removed (calc)	Fe(II)	Fe(III) (calc)	Fe(total)	H_2SO_4	Al	Si	Fe(II)	Fe(III) (calc)	H_2SO_4
	5	ml	g/cm^3	g	mg/L	mg/L	mg/L	mg/L	mg/L	mg/L	mol/kg	mol/kg	mol/kg
C23	5	3969	1.042	4135	1043	197	1240	57275	18.00	33.00	0.018	0.003	0.548
C22	10	4042	1.045	4223	1650	420	2070	58935	22.00	39.00	0.028	0.007	0.574
C21	15	3939	1.047	4124	2128	727	2855	59051	23.00	41.00	0.035	0.012	0.561
C31	5	4078	1.045	4263	1018	172	1190	61283	18.00	47.50	0.018	0.003	0.603
	Final						3350						

	Residence Time		Residue composition, wt%				Accountability, %			
Test	min	Mass out (calc), g	Al	Si	Fe	S_2^{2-}	Al	Si	Fe	Total S
C23	5	34.03	4.92	14.00	26.90	1.09	92	86	105	95
C22	10	27.58	6.39	18.50	20.50	30.40	98	93	105	95
C21	15	20.33	9.02	26.70	9.93	11.80	101	98	99	92
C31	5	30.73	6.14	16.55	27.00	30.75	105	95	100	100

	Residence Time	Oxidation extent (%)				
Test	min	Method 1	Method 2	Method 3	Method 4	Average
C23	5	37	37	32	29	37
C22	10	62	61	58	56	62
C21	15	84	84	85	84	84
C31	5	37	35	37	34	36

Test series 3: PO6 – 706 kPa pO_2

Test	Mass of solids added	Mass of water added	Average temperature	Average pressure	pO_2	Residence Time	Acid addition	Impeller Speed	Impeller Arrangement	MgO addition	$Fe_2(SO_4)_3$ addition
	g	g	°C	bar	kPa	min	g	rev/min		g	G
C43	44.2	4173	201.86	21.88	717	2	150.0	600	C	0.05	0.45
C44	45.39	4172	201.83	22.23	752	2	149.8	600	C	0.05	0.44
C26	45.63	4171	199.94	21.48	677	5	149.8	600	C	0.50	0.00
C25	45.72	4172	201.60	21.58	687	10	149.8	600	C	0.50	0.00
C24	45.65	4172	201.70	21.67	696	15	149.9	600	C	0.50	0.00

Test	min	Volume of solution out (calc)	Density of solution	Mass of solution removed (calc)	Fe(II)	Fe(III) (calc)	Fe(total)	H_2SO_4	Al	Si	Fe(II)	Fe(III) (calc)	H_2SO_4
	2	ml	g/cm3	g	mg/L	mg/L	mg/L	mg/L	mg/L	mg/L	mol/kg	mol/kg	mol/kg
C43	2	4000	1.030	4122	860	220	1080	38665	16.00	15.00	0.014	0.004	0.353
C44	2	4000	1.029	4117	830	180	1010	37171	16.00	15.00	0.014	0.003	0.355
C26	5	3882	1.127	4376	1239	251	1490	35973	16.00	33.00	0.020	0.004	0.333
C25	10	4111	1.032	4242	2091	609	2700	37003	18.00	35.00	0.036	0.011	0.363
C24	15	4034	1.035	4175	1108	2167	3275	36648	20.50	38.50	0.019	0.037	0.353
	Final						3350						

	Residence Time		Residue composition, wt%				Accountability, %			
Test	min	Mass out (calc), g	Al	Si	Fe	S_2^{2-}	Al	Si	Fe	Total S
C43	2	35.00	4.88	14.70	27.25	29.80	93	92	103	99
C44	2	35.57	4.79	14.80	27.50	30.30	93	94	103	99
C26	5	31.56	5.36	15.80	25.10	24.40	92	90	102	95
C25	10	22.08	8.26	25.10	12.90	12.10	100	100	104	97
C24	15	16.63	11.10	33.05	1.33	1.38	101	99	100	95

	Residence Time	Oxidation extent (%)				
Test	min	Method 1	Method 2	Method 3	Method 4	Average
C43	2	32	32	29	29	32
C44	2	30	30	27	26	30
C26	5	43	44	41	47	44
C25	10	82	81	79	82	82
C24	15	98	98	98	98	98

Test series 3: PO10 – 1109 kPa pO_2

Test	Mass of solids added	Mass of water added	Average temperature	Average pressure	pO2	Residence Time	Acid addition	Impeller Speed	Impeller Arrangement	MgO addition	$Fe_2(SO_4)_3$ addition
	g	g	°C	bar	kPa	min	g	rev/min		g	G
C29	46.01	4172	200.64	26.24	1144	4	149.1	600	C	0.50	0.00
C28	46.07	4172	201.65	26.15	1102	8	149.7	600	C	0.50	0.00
C27	45.82	4172	201.61	25.92	1080	12	149.8	600	C	0.50	0.00

Test	min	Volume of solution out (calc)	Density of solution	Mass of solution removed (calc)	Fe(II)	Fe(III) (calc)	Fe(total)	H_2SO_4	Al	Si	Fe(II)	Fe(III) (calc)	H_2SO_4
	4	ml	g/cm3	g	mg/L	mg/L	mg/L	mg/L	mg/L	mg/L	mol/kg	mol/kg	mol/kg
C29	4	3931	1.031	4053	1649	621	2270	36923	17.00	50.00	0.027	0.010	0.346
C28	8	4020	1.035	4161	1391	1959	3350	37234	19.00	53.00	0.023	0.033	0.357
C27	12	4056	1.134	4600	572	2808	3380	36825	20.00	50.00	0.010	0.048	0.356
	Final						3350						

	Residence Time	Mass out (calc)	Residue composition, wt%				Accountability, %			
Test	min	g	Al	Si	Fe	S_2^{2-}	Al	Si	Fe	Total S
C29	4	27.38	6.75	19.90	19.40	21.30	100	98	105	96
C28	8	16.41	11.30	33.50	0.55	0.26	101	99	100	95
C27	12	16.37	11.20	33.55	1.06	1.13	100	100	103	97

	Residence Time	Oxidation extent (%)				
Test	min	Method 1	Method 2	Method 3	Method 4	Average
C29	4	66	68	61	60	67
C28	8	99	100	99	100	100
C27	12	102	101	99	99	101

Evaluate possible pre-oxidation during heating period

Test	Mass of solids added	Mass of water added	Average temperature	Average pressure	pO_2	Residence Time	Acid addition	Impeller Speed	Impeller Arrangement	MgO addition	$Fe_2(SO_4)_3$ addition
	g	g	°C	bar	kPa	min	g	rev/min		g	g
C33	45.19	4172	200.00	0.00	0	0	0.0	600	C	0.51	0.00

Test	Residence time	Volume of solution out (calc)	Density of solution	Mass of solution removed (calc)	Fe(II)	Fe(III) (calc)	Fe(total)	H_2SO_4	S	Al	Si	Fe(II)	Fe(III) (calc)	H_2SO_4
	min	ml	g/cm3	g	mg/L	mg/L	mg/L	mg/L	mg/L	mg/L	mg/L	mol/kg	mol/kg	mol/kg
C33	0	4119	1.001	4122	0	0	0	0	77.00	0.00	0.00	0.000	0.000	0.000

	Residence time		Residue composition, wt%				Accountability, %			
Test	min	Mass out (calc), g	Al	Si	Fe	S_2^{2-}	Al	Si	Fe	Total S
C33	0	42.71	4.35	13.43	28.50	30.80	103	102	92	92

	Residence Time	Oxidation extent (%)				
Test	min	Method 1	Method 2	Method 3	Method 4	Average
C33	0	0	0	8	9	0

PO7: Evaluate effect of $Fe_2(SO_4)_3$ addition

Test	Mass of solids added	Mass of water added	Average temperature	Average pressure	pO2	Residence Time	Acid addition	Impeller Speed	Impeller Arrangement	MgO addition	$Fe_2(SO_4)_3$ addition
	g	g	°C	bar	kPa	min	g	rev/min		g	g
C34	45.67	4172	201.69	21.76	705	5	150.1	600	C	0.51	0.446
C35	45.68	4171	201.69	21.30	690	10	149.8	600	C	0.45	0.446

Test	Residence Time	Volume of solution out (calc)	Density of solution	Mass of solution removed (calc)	Fe(II)	Fe(III) (calc)	Fe(total)	H_2SO_4	Al	Si	Fe(II)	Fe(III) (calc)	H_2SO_4
	min	ml	g/cm3	g	mg/L	mg/L	mg/L	mg/L	mg/L	mg/L	mol/kg	mol/kg	mol/kg
C34	5	3895	1.030	4011	1327	228	1555	38665	18.00	57.00	0.022	0.004	0.359
C35	10	3645	1.034	3769	2145	511	2655	39959	23.00	113.00	0.033	0.008	0.347
	Final						3350						

	Residence Time		Residue composition, wt%				Accountability, %			
Test	min	Mass out (calc), g	Al	Si	Fe	S_2^{2-}	Al	Si	Fe	Total S
C34	5	31.11	5.49	16.00	24.90	26.90	93	91	103	99
C35	10	25.77	7.98	22.50	14.80	17.90	112	109	100	95

	Residence Time	Oxidation extent (%)				
Test	min	Method 1	Method 2	Method 3	Method 4	Average
C34	5	45	47	42	43	46
C35	10	72	80	72	68	76

Evaluate influence of lignosulphonate addition

Test	Mass of solids added	Mass of water added	Average temperature	Average pressure	pO_2	Residence Time	Acid addition	Impeller Speed	Impeller Arrangement	MgO addition	$Fe_2(SO_4)_3$ addition
	g	g	°C	bar	kPa	min	g	rev/min		G	g
C36	46.55	4173	201.54	21.30	659	5	149.9	600	C	0.51	0.00
C37	45.32	4173	201.69	22	705	10	149.1	600	C	0.50	0.00

Test	Residence Time	Volume of solution out (calc)	Density of solution	Mass of solution removed (calc)	Fe(II)	Fe(III) (calc)	Fe(total)	H_2SO_4	Al	Si	Fe(II)	Fe(III) (calc)	H_2SO_4
	min	ml	g/cm3	g	mg/L	mg/L	mg/L	mg/L	mg/L	mg/L	mol/kg	mol/kg	mol/kg
C36	5	3900	1.029	4013	1083	197	1280	37960	21.00	76.00	0.018	0.003	0.353
C37	10	3962	1.032	4090	1860	370	2230	34690	22.00	100.00	0.031	0.006	0.328
	Final						3350						

	Residence Time		Residue composition, wt%				Accountability, %			
Test	min	Mass out (calc), g	Al	Si	Fe	S_2^{2-}	Al	Si	Fe	Total S
C36	5	31.35	5.92	17.10	23.40	28.40	100	98	90	97
C37	10	24.00	7.19	20.50	17.60	23.68	96	94	98	92

	Residence Time	Oxidation extent (%)				
Test	min	Method 1	Method 2	Method 3	Method 4	Average
C36	5	36	38	46	40	37
C37	10	66	67	68	61	66

PO8: Reduced MgO addition 0.1 MgO

Test	Mass of solids added	Mass of water added	Average temperature	Average pressure	pO2	Residence Time	Acid addition	Impeller Speed	Impeller Arrangement	MgO addition	$Fe_2(SO_4)_3$ addition
	g	g	°C	bar	kPa	min	g	rev/min		g	g
C38	46.22	4173	201.12	22	694	5	149.4	600	C	0.10	0.00
C39	47.73	4172	200.94	22	682	10	149.3	600	C	0.10	0.00

Test	10	Volume of solution out (calc)	Density of solution	Mass of solution removed (calc)	Fe(II)	Fe(III) (calc)	Fe(total)	H_2SO_4	Al	Si	Fe(II)	Fe(III) (calc)	H_2SO_4
	Residence Time	ml	g/cm3	g	mg/L	mg/L	mg/L	mg/L	mg/L	mg/L	mol/kg	mol/kg	mol/kg
C38	5	3700	1.031	3814	1322	173	1495	38608	16.00	13.00	0.020	0.003	0.341
C39	10	3800	1.034	3929	2259	331	2590	40327	20.00	16.00	0.036	0.005	0.366
	Final						3350						

	Residence Time		Residue composition, wt%				Accountability, %			
Test	min	Mass out (calc), g	Al	Si	Fe	S_2^{2-}	Al	Si	Fe	Total S
C38	5	32.00	5.16	15.70	25.70	29.10	89	88	101	95
C39	10	24.00	7.24	22.00	16.50	18.90	91	90	98	97

	Residence Time	Oxidation extent (%)				
Test	min	Method 1	Method 2	Method 3	Method 4	Average
C38	5	41	45	40	37	43
C39	10	70	77	72	70	74

PO13 – 1031 kPa pO_2

Test	Mass of solids added	Mass of water added	Average temperature	Steam pressure (calc)	Average pressure	pO2	Residence Time	Acid addition	Impeller Speed	Impeller Arrangement	MgO addition	$Fe_2(SO_4)_3$ addition
	g	g	°C	bar	bar	kPa	min	g	rev/min		g	g
C42	44.95	4174	201.85	25.51	15.37	1031	30	149.68	600	C	0.05	0.4417

Test	Residence time	Volume of solution out (calc)	Density of solution	Mass of solution removed (calc)	Fe(II)	Fe(III) (calc)	Fe(total)	H_2SO_4	Al	Si	Fe(II)	Fe(III) (calc)	H_2SO_4
	min	ml	g/cm3	g	mg/L	mg/L	mg/L	mg/L	mg/L	mg/L	mol/kg	mol/kg	mol/kg
C42	4	37.08	1.031	38.24	2111	104	2215	37496	17.50	0.00	0.035	0.0017	0.351
	8	38.84	1.036	40.25	2262	1048	3310	40454	20.00	0.00	0.037	0.0172	0.378
	12	44.20	1.037	45.84	1206	2234	3440	40911	20.00	0.00	0.020	0.0366	0.383
	16	40.44	1.038	41.98	754	2826	3580	40000	23.00	0.00	0.012	0.0464	0.374
	20	47.66	1.038	49.48	603	2917	3520	41877	24.00	0.00	0.010	0.0479	0.392
	25	3604.74	1.034	3725.85	603	2837	3440	41698	22.00	0.00	0.010	0.0465	0.390
	Final						3530						

	Residence time		Residue composition, wt%				Accountability, %			
Test	min	Mass out (calc), g	Al	Si	Fe	S_2^{2-}	Al	Si	Fe	Total S
C42	25	13.33	9.42	19.33	0.81	0.10	71	62	99	94

	Residence Time	Oxidation extent (%)				
Test	min	Method 1	Method 2	Method 3	Method 4	Average
C42	4		63			63
	8		94			94
	12		97			97
	16		101			101
	20		100			100
	25		97			97

Appendix D.3: Log sheets: Sample D

PO14

Test	Mass of solids added	Mass of water added	Average temperature	Average pressure	pO_2	Residence Time	Acid addition	Impeller Speed	Impeller Arrangement	MgO addition	$Fe_2(SO_4)_3$ addition
	g	g	°C	bar	kPa	min	g	rev/min		g	g
D33	37.56	4275.41	201.44	21.10	603.44	0.25	149.95	600	C	0.05	0.448
D34	37.39	4272.63	201.60	20.82	570.43	1.00	150.31	600	C	0.05	0.448
D35	37.48	4275.53	201.80	21.59	640.48	3.00	150.74	600	C	0.05	0.448
D3	38.12	4272.95	201.51	21.83	673.97	5.00	149.62	600	C	0.50	0.000
D39	37.52	4273.96	201.63	21.77	664.54	6.50	149.55	600	C	0.05	0.445
D36	38.3	4270.96	201.93	22.06	682.96	7.50	149.81	600	C	0.05	0.449
D2	37.5	4272.10	200.91	21.84	694.94	10.00	149.22	600	C	0.50	0.000
D38	37.53	4275.23	202.23	21.80	646.58	12.50	149.86	600	C	0.05	0.448
D20	37.66	4271.81	201.99	21.52	627.26	15.00	149.61	600	C	0.5	0.000
D1	37.66	4271.46	201.34	21.74	671.16	20.00	149.60	600	C	0.50	0.000
D8	38.29	4272.45	201.39	21.68	663.10	5.00	150.39	600	C	0.5	0.000
D22	36.5	4272.15	201.99	21.70	644.61	15.00	149.59	600	C	0.5	0.000
D30	37.8	4272.00	201.44	22.05	698.28	30.00	149.74	600	C	0.05	0.448

	Residence Time		Residue composition, wt%				Accountability, %			
Test	min	Mass out (calc), g	Al	Si	Fe	S_2^{2-}	Al	Si	Fe	Total S
Head	-	-	2.40	8.95	35.55	40.13				
D33	0.25	34.44	2.22	8.56	35.00	37.35	90	90	105	97
D34	1	32.55	2.45	8.55	33.77	37.08	95	86	102	97
D35	3	28.50	2.75	9.36	32.20	36.80	94	83	103	96
D3	5	24.51	3.63	13.25	29.90	32.75	103	98	98	101
D39	6.5	21.69	0.00							
D36	7.5	20.07	4.18	14.70	25.70	29.26	99	89	102	97
D2	10	14.17	6.21	22.40	16.50	19.00	103	97	100	96
D38	12.5	12.00	6.46	25.10	13.90	16.20	93	95	102	95
D20	15	9.90	7.39	27.30	6.16	9.08	85	79	100	100
D1	20	9.31	9.77	34.55	0.83	0.39	107	98	102	97
D8	5	23.68	3.04	11.50	30.00	36.40	84	83	100	100
D22	15	12.55	6.91	24.80	4.39	5.99	105	95	100	100
D30	30	10.55	7.76	31.72	5.94	6.43	100	101	109	104

Test	Residence Time	Volume of solution (calc)	Density of solution	Mass of solution removed (calc)	Fe(II)	Fe(III) (calc)	Fe(total)	H_2SO_4	Al	Si	Fe(II)	Fe(III) (calc)	H_2SO_4
	min	ml	g/cm3	g	mg/L	mg/L	mg/L	mg/L	mg/L	mg/L	mol/kg	mol/kg	mol/kg
D33	0.25	4050	1.026	4153	390	102	492	34600	12.00	20.00	0.007	0.002	0.3342
D34	1.00	3900	1.027	4004	612	57	669	36850	14.00	24.00	0.010	0.001	0.3286
D35	3.00	3900	1.029	4013	1014	136	1150	37000	16.00	27.00	0.017	0.002	0.3441
D3	5.00	4081	1.025	4185	1213	252	1465	36427	13.50	26.00	0.021	0.004	0.3547
D39	6.50	3900	1.031	4022	1590	360	1950	38801	15.00	33.00	0.025	0.006	0.3460
D36	7.50	3900	1.033	4027	1926	314	2240	38990	19.00	28.00	0.031	0.005	0.3477
D2	10.00	3878	1.033	4006	1054	1776	2830	38628	13.00	17.00	0.017	0.029	0.3575
D38	12.50	3900	1.035	4037	2406	644	3050	39550	17.00	45.00	0.038	0.010	0.3526
D20	15.00	4008	1.037	4157	1832	1428	3260	39653	13.00	19.50	0.031	0.024	0.3794
D1	20.00	4098	1.035	4241	975	2355	3330	37300	14.00	19.50	0.017	0.040	0.3648
D8	5.00	3992	1.032	4120	1395	220	1615	38768	13.00	33.50	0.023	0.004	0.3693
D22	15.00	4076	1.036	4223	2119	931	3050	39680	12.00	0.00	0.036	0.016	0.3860
D30	30.00	3783	1.036	3920	407	3313	3720	42989	23.00	20.00	0.006	0.053	0.3881
	Final						3540						

	Residence Time	Oxidation extent (%)				
Test	min	Method 1	Method 2	Method 3	Method 4	Average
D33	0	15	14	10	15	14
D34	1	20	19	17	20	19
D35	3	34	32	31	30	33
D3	5	44	44	46	48	44
D39	7	57	59	100	100	58
D36	8	64	67	62	62	66
D2	10	82	85	82	83	84
D38	13	89	92	87	87	90
D20	15	96	98	96	95	97
D1	20	102	100	99	100	101
D8	5	47	48	48	45	48
D22	15	96	92	96	96	94
D30	30	105	112	95	96	108

PO15

Test	Mass of solids added	Mass of water added	Average temperature	Average pressure	pO_2	Residence Time	Acid addition	Impeller Speed	Impeller Arrangement	MgO addition	$Fe_2(SO_4)_3$ addition
	g	g	°C	bar	kPa	min	g	rev/min		g	g
D6	38.03	4272.54	200.67	25.41	1059.94	5.00	149.73	600	C	0.5	0
D17	39.13	4272.39	201.96	25.30	1006.50	7.50	149.99	600	C	0.5	0
D7	37.33	4272.25	201.64	25.28	1014.42	10.00	149.03	600	C	0.5	0

Test	Residence Time	Volume of solution (calc)	Density of solution	Mass of solution removed (calc)	Fe(II)	Fe(III) (calc)	Fe(total)	H_2SO_4	Al	Si	Fe(II)	Fe(III) (calc)	H_2SO_4
	min	ml	g/cm3	g	mg/L	mg/L	mg/L	mg/L	mg/L	mg/L	mol/kg	mol/kg	mol/kg
D6	5.00	3969	1.728	6856	1728	502	2230	37996	12.00	23.00	0.029	0.008	0.360
D17	7.50	3840	1.037	3982	2541	809	3350	40389	19.00	184.0	0.041	0.013	0.370
D7	10.00	3947	1.032	4074	1139	2161	3300	37996	14.00	25.00	0.019	0.036	0.358
	Final						3540						

	Residence Time		Residue composition, wt%				Accountability, %			
Test	min	Mass out (calc), g	Al	Si	Fe	S_2^{2-}	Al	Si	Fe	Total S
Head	-	-	2.40	8.95	35.55	40.13				
D6	5	20.66	4.06	16.25	25.30	28.70	97	101	104	97

D17	7.5	10.68	6.89	26.10	12.70	16.40	86	100	102	98
D7	10	9.83	8.08	34.50	2.75	2.31	95	104	100	95

	Residence Time	Oxidation extent (%)				
Test	min	Method 1	Method 2	Method 3	Method 4	Average
D6	5	65	63	61	61	64
D17	8	92	95	90	89	94
D7	10	98	93	98	98	96

PO16

Test	Mass of solids added	Mass of water added	Average temperature	Average pressure	pO_2	Residence Time	Acid addition	Impeller Speed	Impeller Arrangement	MgO addition	$Fe_2(SO_4)_3$ addition
	g	g	°C	bar	kPa	min	g	rev/min		g	g
D16	38.8	4273.26	201.82	20.02	482.49	5.00	150.70	600	C	0.50	0.00
D5	37.93	4274.83	201.25	20.05	504.85	10.00	149.18	600	C	0.50	0.00
D4	37.46	4273.25	201.40	19.95	489.35	15.00	149.76	600	C	0.50	0.00
D15	39.04	4271.99	201.96	20.31	504.34	17.50	149.70	600	C	0.50	0.00
D23	36.03	4272.89	202.52	19.77	434.51	20.00	149.47	600	C	0.50	0.00

Test	Residence Time	Volume of solution (calc)	Density of solution	Mass of solution removed (calc)	Fe(II)	Fe(III) (calc)	Fe(total)	H_2SO_4	Al	Si	Fe(II)	Fe(III) (calc)	H_2SO_4
	min	ml	g/cm3	g	mg/L	mg/L	mg/L	mg/L	mg/L	mg/L	mol/kg	mol/kg	mol/kg
D16	5.00	3986	1.029	4101	1473	0	1320	37249	19.00	163.0	0.025	0.025	0.354
D5	10.00	3908	1.027	4014	1646	1023	1890.00	37813	15.00	27.00	0.000	0.000	0.000
D4	15.00	3922	1.031	4042	2233	687	2920.00	39424	15.00	28.00	0.037	0.037	0.369
D15	17.50	3900	1.036	4042	2517	1023	3540.00	39117	20.50	187.50	0.041	0.041	0.364
D23	20.00	4028	1.032	4157	2504	636	3140.00	41815	16.00	29.50	0.042	0.042	0.402
	Final						3540						

	Residence Time		Residue composition, wt%				Accountability, %			
Test	min	Mass out (calc), g	Al	Si	Fe	S_2^{2-}	Al	Si	Fe	Total S
Head	-	-	2.40	8.95	35.55	40.13				
D16	5	26.90	2.86	9.99	34.20	36.70	91	96	105	99
D5	10	0.00	3.97	14.40	28.20	32.30	103	97	101	96
D4	15	12.37	7.26	24.30	14.85	20.30	106	93	100	97
D15	17.5	11.66	6.95	25.50	12.10	16.45	95	106	110	98
D23	20	12.50	6.27	25.30	13.60		98	102	112	

	Residence Time	Oxidation extent (%)				
	min	Method 1	Method 2	Method 3	Method 4	Average
D16	5	38	37	33	37	38
D5	10	55	53	54	53	54
D4	15	86	82	86	85	84
D15	18	99	100	90	88	100
D23	20	99	94	87	n/a	96

PO17

Test	Mass of solids added	Mass of water added	Average temperature	Average pressure	pO_2	Residence Time	Acid addition	Impeller Speed	Impeller Arrangement	MgO addition	$Fe_2(SO_4)_3$ addition
	g	g	°C	bar	kPa	min	g	rev/min		g	g
D11	37.78	4229.09	201.44	21.58	651.20	5.00	249.56	600	C	0.50	0.00
D10	37.75	4228.96	201.76	21.70	652.90	10.00	249.58	600	C	0.50	0.00
D9	38.56	4229.39	201.51	21.82	672.97	15.00	250.37	600	C	0.50	0.00

Test	Residence Time	Volume of solution (calc)	Density of solution	Mass of solution removed (calc)	Fe(II)	Fe(III) (calc)	Fe(total)	H_2SO_4	Al	Si	Fe(II)	Fe(III) (calc)	H_2SO_4
	min	ml	g/cm3	g	mg/L	mg/L	mg/L	mg/L	mg/L	mg/L	mol/kg	mol/kg	mol/kg
D11	5.00	4181	1.045	4371	1190	260	1450.00	60461	14.00	35.00	0.021	0.021	0.609
D10	10.00	4055	1.049	4255	1993	487	2480.00	63369	15.00	39.00	0.034	0.034	0.619
D9	15.00	3965	1.052	4174	2193	1097	3290.00	63991	17.00	40.00	0.037	0.037	0.612
	Final						3540						

	Residence Time		Residue composition, wt%				Accountability, %			
Test	min	Mass out (calc), g	Al	Si	Fe	S_2^{2-}	Al	Si	Fe	Total S
Head	-	-	2.40	8.95	35.55	40.13				
D11	5	22.13	2.71	10.50	33.30	36.80	72	73	100	100
D10	10	14.69	4.56	17.70	22.90	25.87	81	82	100	100
D9	15	11.76	7.20	28.30	8.32	11.00	99	101	104	98

Test	Residence Time	Oxidation extent (%)				
	min	Method 1	Method 2	Method 3	Method 4	Average
D11	5	45	41	45	45	43
D10	10	75	70	75	75	72
D9	15	95	93	93	92	94

PO18

Test	Mass of solids added	Mass of water added	Average temperature	Average pressure	pO_2	Residence Time	Acid addition	Impeller Speed	Impeller Arrangement	MgO addition	$Fe_2(SO_4)_3$ addition
	g	g	°C	bar	kPa	min	g	rev/min		g	g
D14	38.38	4318.45	202.17	21.63	631.65	5.00	50.00	600	C	0.49	0.00
D13	39.14	4319.22	202.12	21.57	627.69	10.00	49.77	600	C	0.51	0.00
D12	37.41	4318.93	202.03	21.63	637.16	15.00	48.93	600	C	0.50	0.00

Test	Residence Time	Volume of solution (calc)	Density of solution	Mass of solution removed (calc)	Fe(II)	Fe(III) (calc)	Fe(total)	H_2SO_4	Al	Si	Fe(II)	Fe(III) (calc)	H_2SO_4
	min	ml	g/cm3	g	mg/L	mg/L	mg/L	mg/L	mg/L	mg/L	mol/kg	mol/kg	mol/kg
D14	5.00	4011	1.016	4075	1626	244	1870.00	14411	5.20	25.00	0.027	0.027	0.136
D13	10.00	4019	1.021	4102	1838	1312	3150.00	16116	8.30	29.00	0.031	0.031	0.153
D12	15.00	4129	1.020	4210	705	1800	2505.00	15951	8.35	30.00	0.012	0.012	0.155
	Final						3540						

	Residence Time		Residue composition, wt%				Accountability, %			
Test	min	Mass out (calc), g	Al	Si	Fe	S_2^{2-}	Al	Si	Fe	Total S
Head	-	-	2.40	8.95	35.55	40.13				
D14	5	21.54	3.87	16.50	28.50	30.00	93	106	100	97
D13	10	12.82	6.40	28.50	9.88	7.92	91	108	100	100
D12	15	15.96	5.05	21.45	17.05	2.86	94	106	98	101

	Residence Time	Oxidation extent (%)				
	min	Method 1	Method 2	Method 3	Method 4	Average
D14	5	54.98	53	55.02	58.05	54
D13	10	90.97	89	90.90	93.54	90
D12	15	77.78	71	79.53	96.88	74

PO20

Test	Mass of solids added	Mass of water added	Average temperature	Average pressure	pO_2	Residence Time	Acid addition	Impeller Speed	Impeller Arrangement	MgO addition	$Fe_2(SO_4)_3$ addition
	g	g	°C	bar	kPa	min	g	rev/min		g	g
D24	36.55	4271.33	201.81	21.76	657.42	30.00	149.93	600	C	0.05	0.00

Test	Residence Time	Volume of solution (calc)	Density of solution	Mass of solution removed (calc)	Fe(II)	Fe(III) (calc)	Fe(total)	H_2SO_4	Al	Si	Fe(II)	Fe(III) (calc)	H_2SO_4
	min	ml	g/cm3	g	mg/L	mg/L	mg/L	mg/L	mg/L	mg/L	mol/kg	mol/kg	mol/kg
D24	5.00	40	1.027	42	1715	0	1715	30861	15	43	0.0289	0.0000	0.30
	10.00	34	1.034	36	2865	195	3060	36581	31	81	0.0457	0.0031	0.30
	15.00	33	1.037	34	1809	1871	3680	37339	21	98	0.0289	0.0299	0.37
	20.00	38	1.037	39	1055	2465	3520	36144	19	91	0.0168	0.0393	0.37
	25.00	42	1.037	44	754	2966	3720	38367	21	106	0.0120	0.0473	0.39
	30.00	3807	1.036	3946	603	2947	3550	36230	20	97	0.0096	0.0470	0.36
	Final						3720						

	Residence Time		Residue composition, wt%				Accountability, %			
Test	min	Mass out (calc), g	Al	Si	Fe	S_2^{2-}	Al	Si	Fe	Total S
Head	-	-	2.40	8.95	35.55	40.13				
D24	30	9.86	9.35	27.20	1.36	0.05	100	89	96	92

	Residence Time	Oxidation extent (%)				
	min	Method 1	Method 2	Method 3	Method 4	Average
D24	5		46			46
	10		82			82
	15		99			99
	20		95			95
	25		100			100
	30		95			95

PO21

Test	Mass of solids added	Mass of water added	Average temperature	Average pressure	pO_2	Residence Time	Acid addition	Impeller Speed	Impeller Arrangement	MgO addition	$Fe_2(SO_4)_3$ addition
	g	g	°C	bar	kPa	min	g	rev/min		g	g
D25	37.84	4275.4	201.7875	21.77	659.06	30	149.09	600	C	0.05	0.00

Test	Residence Time	Volume of solution (calc)	Density of solution	Mass of solution removed (calc)	Fe(II)	Fe(III) (calc)	Fe(total)	H_2SO_4	Al	Si	Fe(II)	Fe(III) (calc)	H_2SO_4
	min	ml	g/cm3	g	mg/L	mg/L	mg/L	mg/L	mg/L	mg/L	mol/kg	mol/kg	mol/kg
D25	5.00	37	1.030	38	1845.0	0	1845.00	36922	13.00	18.00	0.032	0.000	0.34
	10.00	40	1.036	41	2864.8	335	3200.00	41932	13.00	21.00	0.046	0.005	0.38
	15.00	36	1.038	37	1658.6	1921	3580.00	40219	15.00	22.00	0.027	0.031	0.37
	20.00	37	1.037	39	1055.5	2485	3540.00	40851	14.00	22.00	0.017	0.040	0.38
	25.00	40	1.037	41	753.9	2816	3570.00	42023	15.00	22.00	0.012	0.045	0.39
	30.00	3850	1.037	3991	603.1	2867	3470.00	40210	16.00	22.00	0.010	0.046	0.37
	Final						3720						

	Residence Time		Residue composition, wt%				Accountability, %			
Test	min	Mass out (calc), g	Al	Si	Fe	S_2^{2-}	Al	Si	Fe	Total S
Head	-	-	2.40	8.95	35.55	40.13				
D25	30.00	8.52	11.10	36.70	0.22	0.11	106.42	91.00	96	94.37

	Residence Time	Oxidation extent (%)				
D25	min	Method 1	Method 2	Method 3	Method 4	Average
	5		52			52
	10		90			90
	15		101			101
	20		100			100
	25		101			101
	30		98			98

PO19

Test	Mass of solids added	Mass of water added	Average temperature	Average pressure	pO_2	Residence Time	Acid addition	Impeller Speed	Impeller Arrangement	MgO addition	$Fe_2(SO_4)_3$ addition
	g	g	°C	bar	kPa	min	g	rev/min		g	g
D27	76.00	4253.65	201.03	21.86	693.42	5.00	150.58	600	C	0.05	0.45
D26	75.68	4252.36	201.77	21.81	663.41	15.00	149.76	600	C	0.05	0.44

Test	Residence Time	Volume of solution (calc)	Density of solution	Mass of solution removed (calc)	Fe(II)	Fe(III) (calc)	Fe(total)	H_2SO_4	Al	Si	Fe(II)	Fe(III) (calc)	H_2SO_4
	min	ml	g/cm3	g	mg/L	mg/L	mg/L	mg/L	mg/L	mg/L	mol/kg	mol/kg	mol/kg
D27	5.00	3994	1.030	4113	2262	695	1920.00	39070	29.00	37.00	0.038	0.038	0.374
D26	15.00	4011	1.041	4176	4071	695	5235.00	43627	34.00	41.00	0.069	0.069	0.420
	Final						7080						

	Residence Time		Residue composition, wt%				Accountability, %			
Test	min	Mass out (calc), g	Al	Si	Fe	S_2^{2-}	Al	Si	Fe	Total S
D27	5	55.90	3.04	10.40	34.00	37.20	100	88	99	97
D26	15	27.32	5.58	20.25	20.05	22.52	91	84	98	99

	Residence Time	Oxidation extent (%)				
	min	Method 1	Method 2	Method 3	Method 4	Average
D27	5	28	16	30	32	22
D26	15	78	70	80	80	74

DD40 & DD41

Test	Mass of solids added	Mass of water added	Average temperature	Average pressure	pO_2	Residence Time	Acid addition	Impeller Speed	Impeller Arrangement	MgO addition	$Fe_2(SO_4)_3$ addition
	g	g	°C	bar	kPa	min	g	rev/min	C	g	g
DD40	32.15	4276.21	202.06	21.99	671.43	7.50	149.70	600	C	0.05	0.45
DD41	32.28	4276.42	202.11	21.76	646.76	3.00	149.61	600	C	0.05	0.45

Test	Residence Time	Volume of solution (calc)	Density of solution	Mass of solution removed (calc)	Fe(II)	Fe(III) (calc)	Fe(total)	H_2SO_4	Al	Si	Fe(II)	Fe(III) (calc)	H_2SO_4
	min	ml	g/cm3	g	mg/L	mg/L	mg/L	mg/L	mg/L	mg/L	mol/kg	mol/kg	mol/kg
DD40	7.50	3950	1.031	4072	1974	256	2230.00	36800	11.00	61.00	0.031	0.004	0.332
DD41	3.00	3850	1.028	3959	1188	62	1250.00	37600	11.00	52.00	0.018	0.001	0.331

Test	Residence Time		Residue composition, wt%				Accountability, %			
	min	Mass out (calc), g	Al	Si	Fe	S_2^{2-}	Al	Si	Fe	Total S
DD40	7.5	13.00	3.02	11.20	33.10	36.10	93	97	101	92
DD41	3	22.50	2.15	6.61	39.80	43.00	112	96	106	94

Test	Residence Time	Oxidation extent (%)				
	min	Method 1	Method 2	Method 3	Method 4	Average
DD40	8	68		67	69	68
DD41	3	37		31	36	37

Appendix D.4: Log sheets: Sample E

PO22

Test	Mass of solids added	Mass of water added	Average temperature	Average pressure	pO_2	Residence Time	Acid addition	Impeller Speed	Impeller Arrangement	MgO addition	$Fe_2(SO_4)_3$ addition
	g	g	°C	bar	kPa	min	g	rev/min		g	g
E3	53.52	4283.34	202.07	21.72	644.54	10.00	149.35	600	C	0.50	0.00
E4	53.71	4283.36	201.91	21.47	625.02	15.00	149.45	600	C	0.50	0.00
E2	54.86	4283.41	201.16	21.52	654.41	20.00	149.77	600	C	0.50	0.00
E1	55.34	4282.28	201.76	21.98	680.29	30.00	149.64	600	C	0.50	0.00

Test	Residence Time	Volume of solution out (calc)	Density of solution	Mass of solution removed (calc)	Fe(II)	Fe(III) (calc)	Fe(total)	H_2SO_4	Al	Si	Fe(II)	Fe(III) (calc)	H_2SO_4
	min	ml	g/cm3	g	mg/L	mg/L	mg/L	mg/L	mg/L	mg/L	mol/kg	mol/kg	mol/kg
E3	10.00	3913	1.036	4052	2525	435	2960	39940	18	0	0.041	0.007	0.3721
E4	15.00	3950	1.036	4090	3103	738	3840	37910	18	0	0.051	0.012	0.356
E2	20.00	4000	1.043	4171	1000	4590	5590	41140	19	24	0.017	0.077	0.392
E1	30.00	3950	1.043	4120	434	5216	5650	39303	22	28	0.007	0.086	0.370
						5580							

	Residence Time		Residue composition, wt%				Accountability, %			
Test	min	Mass out (calc), g	Al	Si	Fe	S_2^{2-}	Al	Si	Fe	Total S
Head	-	-	1.00	5.70	40.10	45.20				
E3	10.00	26.00	1.67	9.10	34.90	43.55	94	78	96	96.84
E4	15.00	23.00	2.01	11.70	27.80	30.90	99.31	87.90	100.11	91.26
E2	20.00	7.50	5.88	36.00	3.08	3.21	93.42	88.64	101.80	99.11
E1	30.00	7.50	5.92	36.95	2.15	1.22	95.93	91.36	101.30	96.02

	Residence Time	Oxidation extent (%)				
Test	min	Method 1	Method 2	Method 3	Method 4	Average
E3	10.00	54.0	53.0	57.7	53.2	53.5
E4	15.00	70.4	68.8	70.3	70.7	69.6
E2	20.00	100.8	100.2	99.0	99.0	100.5
E1	30.00	100.6	101.3	99.3	99.6	100.9

PO26

Test	Mass of solids added	Mass of water added	Average temperature	Average pressure	pO_2	Residence Time	Acid addition	Impeller Speed	Impeller Arrangement	MgO addition	$Fe_2(SO_4)_3$ addition
	g	g	°C	bar	kPa	min	g	rev/min		g	g
E7	53.84	4283.33	201.52	23.56	846.69	5.00	149.8	600.00	C	0.50	0.00
E6	54.54	4282.19	201.90	23.65	843.08	10.00	149.20	600.00	C	0.50	0.00
E5	53.59	4283.64	201.94	23.56	833.40	15.00	149.4	600.00	C	0.50	0.00

Test	Residence Time	Volume of solution out (calc)	Density of solution	Mass of solution removed (calc)	Fe(II)	Fe(III) (calc)	Fe(total)	H_2SO_4	Al	Si	Fe(II)	Fe(III) (calc)	H_2SO_4
	min	ml	g/cm3	g	mg/L	mg/L	mg/L	mg/L	mg/L	mg/L	mol/kg	mol/kg	mol/kg
E7	5.00	3889	1.032	4014	1825	535	2360	39260	23	104	0.030	0.009	0.363
E6	10.00	3766	1.039	3912	2926	1284	4210	42514	24	156	0.046	0.020	0.381
E5	15.00	3813	1.044	3980	2283	3197	5480	42632	24	184	0.036	0.051	0.387
						5580							

	Residence Time		Residue composition, wt%				Accountability, %			
Test	min	Mass out (calc), g	Al	Si	Fe	S_2^{2-}	Al	Si	Fe	Total S
Head	-	-	1.00	5.70	40.10	45.20				
E7	5.00	33.00	1.26	8.01	37.95	39.60	93.54	99.31	100.52	95.58
E6	10.00	20.12	2.26	13.80	29.40	35.20	99.95	108.22	99.55	97.11
E5	15.00	8.00	5.48	31.90	7.76	9.14	98.88	106.51	100.12	96.72

Test	Residence Time	Oxidation extent (%)				
	min	Method 1	Method 2	Method 3	Method 4	Average
E7	5.00	42.5	42.3	42.0	46.3	42.4
E6	10.00	72.5	75.4	73.0	71.3	74.0
E5	15.00	97.2	98.2	97.1	97.0	97.7

PO23

Test	Mass of solids added	Mass of water added	Average temperature	Average pressure	pO2	Residence Time	Acid addition	Impeller Speed	Impeller Arrangement	MgO addition	$Fe_2(SO_4)_3$ addition
	g	g	°C	bar	kPa	min	g	rev/min		g	g
E21	54.23	4283.64	201.20	21.81	682.37	2.00	149.37	700.00	C	0.50	0.45
E8	55.65	4283.30	200.94	21.54	664.29	5.00	149.00	700.00	C	0.50	0.00
E9	53.78	4283.85	201.46	21.15	607.95	10.00	149.32	700.00	C	0.50	0.00
E10	54.29	4283.06	201.02	21.42	649.31	15.00	149.76	700.00	C	0.50	0.00
E22	56.84	4283.00	200.62	21.78	698.38	25.00	149.73	700.00	C	0.05	0.45

Test	Residence Time	Volume of solution out (calc)	Density of solution	Mass of solution removed (calc)	Fe(II)	Fe(III) (calc)	Fe(total)	H_2SO_4	Al	Si	Fe(II)	Fe(III) (calc)	H_2SO_4
	min	ml	g/cm3	g	mg/L	mg/L	mg/L	mg/L	mg/L	mg/L	mol/kg	mol/kg	mol/kg
E21	2.00	3800	1.028	3906	838	182	1020	36578	14	32	0.013	0.003	0.372
E8	5.00	3860	1.030	3975	1433	177	1610	38616	17	15	0.023	0.003	0.355
E9	10.00	3950	1.034	4086	2487	433	2920	40229	20	19	0.041	0.007	0.378
E10	15.00	3850	1.041	4009	3274	1326	4600	43340	22	20	0.053	0.021	0.397
E22	25.00	3800	1.046	3973	850	5305	6155	42585	29	24	0.014	0.084	0.385
						5580							

	Residence Time		Residue composition, wt%				Accountability, %			
Test	min	Mass out (calc), g	Al	Si	Fe	S_2^{2-}	Al	Si	Fe	Total S
Head	-	-	1.00	5.70	40.10	45.20				
E21	2.00	45.00	1.06	5.88	40.00	44.50	97.77	89.53	100.60	94.51
E8	5.00	42.00	1.02	6.53	38.55	34.20	88.77	88.29	100.40	92.84
E9	10.00	34.00	1.46	8.44	35.50	34.47	103.40	92.83	105.77	97.70
E10	15.00	18.00	2.74	17.10	24.30	27.10	106.45	101.95	101.44	98.59
E22	25.00	7.10	5.73	37.40	1.97	2.14	90.63	84.77	103.23	98.10

Test	Residence Time	Oxidation extent (%)				
	min	Method 1	Method 2	Method 3	Method 4	Average
E21	2.00	17.8	17.8	17.2	18.3	17.8
E8	5.00	27.8	28.4	27.4	42.9	28.1
E9	10.00	51.7	51.9	45.9	53.4	51.8
E10	15.00	81.3	82.0	79.9	80.1	81.7
E22	25.00	102.6	110.3	99.4	99.4	106.5

PO25

Test	Mass of solids added	Mass of water added	Average temperature	Average pressure	pO_2	Residence Time	Acid addition	Impeller Speed	Impeller Arrangement	MgO addition	$Fe_2(SO_4)_3$ addition
	g	g	°C	bar	kPa	min	g	rev/min		g	g
E13	55.25	4283.05	200.67	19.70	488.71	8.00	149.72	600.00	C	0.50	0.00
E12	54.94	4284.5	201.15	19.82	484.92	16.00	149.43	600.00	C	0.50	0.00
E11	54.98	4283.88	200.93	19.67	477.88	24.00	149.71	600.00	C	0.50	0.00
E23	58.08	4285.06	201.88	19.76	454.89	40.00	150.06	600.00	C	0.05	0.45

Test	Residence Time	Volume of solution out (calc)	Density of solution	Mass of solution removed (calc)	Fe(II)	Fe(III) (calc)	Fe(total)	H_2SO_4	Al	Si	Fe(II)	Fe(III) (calc)	H_2SO_4
	min	ml	g/cm3	g	mg/L	mg/L	mg/L	mg/L	mg/L	mg/L	mol/kg	mol/kg	mol/kg
E13	8.00	3850.00	1.030	3964	1268	282	1550	39121	18	29	0.020	0.005	0.359
E12	16.00	3900.00	1.034	4032			2790	40019	20	31	0.058	-0.012	0.371
E11	24.00	3900.00	1.040	4057	3314	1276	4590	43904	22	34	0.054	0.021	0.408
E23	40.00	3800.00	1.048	3981	650	5510	6160	41676	30	24	0.010	0.087	0.377
						5580							

	Residence Time		Residue composition, wt%				Accountability, %			
Test	min	Mass out (calc), g	Al	Si	Fe	S_2^{2-}	Al	Si	Fe	Total S
Head	-	-	1.00	5.70	40.10	45.20				
E13	8.00	42.00	1.25	6.94	39.70	40.41	107.57	96.10	102.19	96.11
E12	16.00	29.00	1.36	8.67	38.40	39.69	85.50	83.68	99.38	93.53
E11	24.00	17.00	2.79	18.00	27.55	34.20	101.87	101.87	102.44	101.30
E23	40.00	8.50	5.65	36.80	1.43	1.47	102.32	97.24	101.03	96.16

Test	Residence Time	Oxidation extent (%)				
	min	Method 1	Method 2	Method 3	Method 4	Average
E13	8.00	26.9	27.3	24.7	32.0	27.1
E12	16.00	49.1	49.6	49.7	53.9	49.3
E11	24.00	81.2	81.8	78.8	76.6	81.5
E23	40.00	100.5	110.4	99.5	99.5	105.5

PO24

Test	Mass of solids added	Mass of water added	Average temperature	Average pressure	pO_2	Residence Time	Acid addition	Impeller Speed	Impeller Arrangement	MgO addition	$Fe_2(SO_4)_3$ addition
	g	g	°C	bar	kPa	min	g	rev/min		g	g
E16	54.85	4389.88	181.64	16.12	668.40	25.00	149.91	600.00	C	0.50	0.00
E15	55.03	4390.83	181.74	16.13	667.15	50.00	149.72	600.00	C	0.50	0.00
E14	54.84	4389.79	181.72	16.13	667.64	84.00	149.72	600.00	C	0.50	0.00

Test	Residence Time	Volume of solution out (calc)	Density of solution	Mass of solution removed (calc)	Fe(II)	Fe(III) (calc)	Fe(total)	H_2SO_4	Al	Si	Fe(II)	Fe(III) (calc)	H_2SO_4
	min	ml	g/cm3	g	mg/L	mg/L	mg/L	mg/L	mg/L	mg/L	mol/kg	mol/kg	mol/kg
E16	25.00	4200.00	1.030	4325	1526	294	1820	37950	17	30	0.026	0.005	0.370
E15	50.00	4000.00	1.037	4149	2722	1318	4040	40456	20	35	0.044	0.021	0.376
E14	84.00	3637.73	1.043	3793	691	4874	5565	39591	22	35	0.010	0.072	0.335
						5166							

	Residence Time		Residue composition, wt%				Accountability, %			
Test	min	Mass out (calc), g	Al	Si	Fe	S_2^{2-}	Al	Si	Fe	Total S
Head	-	-	1.00	5.70	40.10	45.20				

E16	25.00	36.00	1.27	7.76	39.20	40.17	96.04	93.38	98.91	98.19
E15	50.00	22.00	1.90	11.50	26.40	31.64	90.50	85.12	99.55	97.49
E14	84.00	10.00	4.68	32.40	9.86	12.00	99.64	107.77	96.54	89.80

Test	Residence Time	Oxidation extent (%)				
	min	Method 1	Method 2	Method 3	Method 4	Average
E16	25.00	34.8	34.7	35.8	41.7	34.8
E15	50.00	73.2	77.7	73.7	72.0	75.5
E14	84.00	92.1	107.2	95.5	95.2	99.6

Appendix D.5: Log sheets: Sample F

PO28

Test	Mass of solids added	Mass of water added	Average temperature	Average pressure	Steam pressure	pO_2	Residence Time	Acid addition	Impeller Speed	Impeller Arrangement	MgO addition	$Fe_2(SO_4)_3$ addition
	g	g	°C	bar	bar	kPa	min	g	rev/min		g	g
F1	28.83	4301.83	201.78	21.87	15.34	668.94	42.00	149.67	600	C	0.0554	0.4456

Test	Residence Time	Volume of solution out (calc)	Density of solution	Mass of solution removed (calc)	Fe(II)	Fe(III) (calc)	Fe(total)	H_2SO_4	Al	Si	Fe(II)	Fe(III) (calc)	H_2SO_4
	min	ml	g/cm^3	g	mg/L	mg/L	mg/L	mg/L	mg/L	mg/L	mol/kg	mol/kg	mol/kg
F1	7.00	30	1.035	30.06	1370	535	1905.00	36311	6.00	0.00	0.0220	0.0086	0.3314
	14.00	35	1.035	35.32	2070	990	3060.00	39866	7.00	22.00	0.0332	0.0159	0.3638
	21.00	36	1.034	36.25	980	2280	3260.00	40842	6.80	23.00	0.0157	0.0365	0.3727
	28.00	31	1.035	30.89	510	2800	3310.00	40739	7.50	28.00	0.0082	0.0449	0.3718
	35.00	31	1.036	30.69	340	3140	3480.00	40681	8.10	31.00	0.0054	0.0503	0.3713
	42.00	3688	1.034	3803.70	270	3130	3400.00	38044	6.20	29.00	0.0043	0.0502	0.3472
Final							3400.00						

	Residence Time	Oxidation extent (%)				
Test	min	Method 1	Method 2	Method 3	Method 4	Average
F1	7		56			56
	14		90			90
	21		96			96
	28		97			97
	35		102			102
	42		100			100

PO27

Test	Mass of solids added	Mass of water added	Average temperature	Average pressure	Steam pressure	pO_2	Residence Time	Acid addition	Impeller Speed	Impeller Arrangement	MgO addition	$Fe_2(SO_4)_3$ addition
	g	g	°C	bar	bar	kPa	min	g	rev/min		g	g
F2	28.43	4302.00	201.82	19.95	15.36	475.90	48.00	149.56	600	C	0.0506	0.4490

	Residence Time	Oxidation extent (%)				
Test	min	Method 1	Method 2	Method 3	Method 4	Average
F2	8		46			46
	16		83			83
	24		97			97
	32		104			104
	40		104			104
	48		100			100

Test	Residence Time	Volume of solution out (calc)	Density of solution	Mass of solution removed (calc)	Fe(II)	Fe(III) (calc)	Fe(total)	H_2SO_4	Al	Si	Fe(II)	Fe(III) (calc)	H_2SO_4
	min	ml	g/cm^3	g	mg/L	mg/L	mg/L	mg/L	mg/L	mg/L	mol/kg	mol/kg	mol/kg
F2	8.00	28.00	1.034	28.49	1230.00	360.0	1590.00	36178	4.90	0.00	0.02	0.0058	0.3326

	16.00	34.00	1.033	33.74	2260.00	580.0	2840.00	41074	6.70	18.00	0.04	0.0094	0.3777
	24.00	33.00	1.035	33.48	1740.00	1590.0	3330.00	43143	7.00	28.00	0.03	0.0257	0.3967
	32.00	34.00	1.035	33.55	890.00	2680.0	3570.00	41876	7.50	36.00	0.01	0.0433	0.3850
	40.00	35.50	1.035	35.60	570.00	2980.0	3550.00	42819	7.80	37.00	0.01	0.0481	0.3937
	48.00	3715.04	1.032	3796.14	330.00	3090.0	3420.00	42985	7.30	33.00	0.01	0.0499	0.3952
Final							3420.00						

PO29

Test	Mass of solids added	Mass of water added	Average temperature	Average pressure	Steam pressure	pO_2	Residence Time	Acid addition	Impeller Speed	Impeller Arrangement	MgO addition	$Fe_2(SO_4)_3$ addition
	g	g	°C	bar	bar	kPa	min	g	rev/min		g	g
F3	28.75	4302.10	201.93	26.50	15.39	1127.37	30.00	149.66	600	C	0.0496	0.4468

Test	Residence Time	Volume of solution out (calc)	Density of solution	Mass of solution removed (calc)	Fe(II)	Fe(III) (calc)	Fe(total)	H_2SO_4	Al	Si	Fe(II)	Fe(III) (calc)	H_2SO_4	
	min	ml	g/cm^3	g	mg/L	mg/L	mg/L	mg/L	mg/L	mg/L	mol/kg	mol/kg	mol/kg	
F3	5.00	34.21	1.030	35.23	1250.00	725.00	1975.00	32764	8.45	40.00	0.0192	0.0111	0.2863	
	10.00	40.14	1.031	41.40	1410.00	1410.00	2820.00	43132	8.50	55.00	0.0216	0.0216	0.3769	
	15.00	33.35	1.036	34.55	930.00	2380.00	3310.00	46602	11.00	69.00	0.0143	0.0365	0.4072	
	20.00	38.88	1.037	40.31	360.00	3160.00	3520.00	48095	10.00	68.00	0.0055	0.0485	0.4203	
	25.00	36.20	1.037	37.53	310.00	3270.00	3580.00	47851	11.00	70.00	0.0048	0.0502	0.4182	
	30.00	3504.43	1.032	3604.77	190.00	3315.00	3505.00	47926	10.00	64.00	0.0029	0.0509	0.4188	
Final							3505.00							

	Residence Time	Oxidation extent (%)				
Test	min	Method 1	Method 2	Method 3	Method 4	Average
F3	5		56			56
	10		80			80
	15		94			94
	20		100			100
	25		102			102
	30		100			100

Appendix E: Chemical and mineralogical analysis

All chemical and mineralogical analyses were performed by MINTEK's Analytical Services and Mineralogical Divisions. The procedures which were employed are summarised below.

ICP-OES (solutions)	Produced aerosol is conveyed into argon plasma where electrons are excited. The emission spectrum is measured by a spectrometer when the excited electrons drop to their ground state – each element having its own unique spectrum with the intensity dependent on the concentration. The initial concentrations of the elements were then calculated based on the known volume of sample introduced to the ICP-OES instrument.
ICP-OES (solids)	Sodium peroxide and sodium carbonate was added to the sample. The mixture was fused followed by leaching in distilled water. Hydrochloric acid was subsequently added and the solution read by ICP-OES.
Elemental S	Elemental sulphur was determined by selectively dissolving it in trichloroethylene at an elevated temperature. The resulting solution was subsequently heated and the trichloroethylene evaporated off. The elemental sulphur, which stayed behind, was weighed and the concentration of elemental sulphur in the original sample calculated.
Sulphate S	The sulphate sulphur content of the sample was determined after the elemental sulphur was removed by trichloroethylene (see above procedure). Sulphate was determined by dissolution in sodium carbonate solution. After filtration, the sulphate was precipitated from the solution by addition of barium chloride and the resulting precipitate weighed. The concentration of sulphate in the original sample was then calculated.
Sulphide S	The sulphide sulphur in the sample was only determined after both elemental sulphur and sulphate sulphur had been removed. The residue was analysed by combustion in a CS Analyser. The sample was heated in a furnace where the sulphur is burned off. Sulphur is carried into a stream of oxygen where it is converted to sulphur dioxide. The sulphur dioxide gas was analysed with an infrared (IR) detector. The instrument was calibrated by using known standards.
Total S	Total sulphur was also determined by combustion in a CS Analyser. Similar to the procedure supplied for sulphide sulphur, the sample, without undergoing any pre-treatment, was heated in a furnace where the sulphur is burned off. The sulphur is contacted with oxygen where it is converted to sulphur dioxide. The sulphur dioxide gas was analysed with an infrared detector. The instrument was calibrated by using known standards. The total sulphur, which is independently measured, must equal the sum of all other sulphur species: $$Total\ Sulphur = Elemental\ sulphur + sulphate\ sulphur + sulphide\ sulphur$$
XRD	A representative portion of the sample was micronized using a McCrone mill. The bulk mineral composition was subsequently obtained by performing XRD on it. The TOPAS® software package was employed to quantity the relative contribution of minerals (be mass) by using the Rietveld refinement method. The detection limit is 1 wt%.
SEM	A representative portion of the sample was mounted into a polished section. A Zeiss Scanning Electron Microscope with Energy Dispersive X-Ray microanalysis (EDS) was used to identify and differentiate between the different mineral phases. Elemental mapping analysis was conducted on selected areas of the polysection and backscattered electron images (BSE) obtained to show the different mineral compounds and how they are associated. Major elements present in the samples were selected for the mapping.
PSD	Particle size distributions of the different samples were determined using a Saturn DigiSizer laser diffraction particle size analyser, which provided the size distribution based on the volume of the individual particles. A representative portion of the sample was introduced to the sampling chamber of the instrument. The analysis is based on the scattering pattern which is obtained when

	a beam of light is passed through the sampling chamber. Background measurements were performed prior to each measurement to ensure air bubbles, which may interfere with the analysis, are removed.

APPENDIX F: Model MATLAB code

Provided in electronic format.